

University of Memphis

## University of Memphis Digital Commons

---

Electronic Theses and Dissertations

---

2021

### Development of Robust and Dynamic Control Solutions for Energy Storage Enabled Hybrid AC/DC Microgrids

Morteza Daviran Keshavarzi

Follow this and additional works at: <https://digitalcommons.memphis.edu/etd>

---

#### Recommended Citation

Daviran Keshavarzi, Morteza, "Development of Robust and Dynamic Control Solutions for Energy Storage Enabled Hybrid AC/DC Microgrids" (2021). *Electronic Theses and Dissertations*. 2510.  
<https://digitalcommons.memphis.edu/etd/2510>

This Dissertation is brought to you for free and open access by University of Memphis Digital Commons. It has been accepted for inclusion in Electronic Theses and Dissertations by an authorized administrator of University of Memphis Digital Commons. For more information, please contact [khggerty@memphis.edu](mailto:khggerty@memphis.edu).

DEVELOPMENT OF ROBUST AND DYNAMIC CONTROL SOLUTIONS FOR  
ENERGY STORAGE ENABLED HYBRID AC/DC MICROGRIDS

by

Morteza Daviran Keshavarzi

A Dissertation

Submitted in Partial Fulfillment of the

Requirements for the Degree of

Doctor of Philosophy

Major: Electrical and Computer Engineering

The University of Memphis

August 2021

## **DEDICATION**

I would love to dedicate this Ph.D. dissertation to my Mother, and the rest of my great family who compassionately supported me from overseas, throughout my studies abroad.

## **ACKNOWLEDGEMENT**

I am sincerely grateful to my supervisor Dr. Mohd. Hasan Ali for his invaluable guidance and continuous support during my Ph.D. study at the University of Memphis. His insightful advice and great experience encouraged me in all aspects of my academic life. My gratitude extends to the Department of Electrical & Computer Engineering for their funding support.

I would also like to warmly appreciate the committee members Dr. Eddie Jacobs, Dr. Sajjan Shiva, and Dr. John Hochstein who accepted to take part in the committee, and for their valuable time and advice.



## PREFACE

After more than 10 years serving as an electrical engineer in the power and energy industry, I came back to academia to push the boundaries of my knowledge and grow my capabilities. My industry background in power systems and my passion to focus on microgrid power systems motivated me to conduct this research. The outcome of this research has been published in three journal articles (two under review), three conference papers, and one book chapter. The contents of this dissertation include all these publications which are listed below:

Chapter 2: M Hasan Ali and M. Daviran Keshavarzi, “Mixed AC/DC System Stability Under Uncertainty,” in *Emerging Power Converters for Renewable Energy and Electric Vehicles*, CRC Press, Taylor & Francis Group, 2021.

Chapter 3: M. D. Keshavarzi and M. H. Ali, “FRT Capability Enhancement of Autonomous AC/DC Hybrid Microgrid by Coordinated MSDBR and Interlinking Converter Control Strategy,” in *2019 IEEE Power & Energy Society Innovative Smart Grid Technologies Conference (ISGT)*, Feb. 2019, pp. 1–5, and

M. Daviran Keshavarzi and M. H. Ali, “Disturbance Resilience Enhancement of Islanded Hybrid Microgrid Under High Penetration of Renewable Energy Resources by BESS,” in *IEEE Transmission & Distribution*, 2020, pp. 1–5

Chapter 4: M. Daviran Keshavarzi and M. H. Ali, “A Novel Bidirectional DC-DC Converter for Dynamic Performance Enhancement of Hybrid AC/DC Microgrid,” *Electronics*, vol. 9, no. 10, p. 1653, Oct. 2020,

Chapter 5: M. Daviran Keshavarzi and M. Hasan Ali, “Influence of Battery Energy Storage Location on the Dynamic Performance of Hybrid AC/DC Microgrid,” in *2020 2nd International Conference on Smart Power & Internet Energy Systems (SPIES)*, Sep. 2020, pp. 182–187, and

M. Daviran Keshavarzi and M. Hasan Ali, “Performance Analysis of Hybrid AC/DC Microgrid Under Influence of Battery Energy Storage Location”, *Int. Trans. on Electrical Energy Systems*, John Wiley & Sons, 2021 (under the second round of review).

Chapter 6: M. Daviran Keshavarzi and M. Hasan Ali, “Dynamic Performance Enhancement of Power Grids by Operating Solar Photovoltaic (PV) System as Supercapacitor Energy Storage”, *Energies*, 2021 (under review).

## ABSTRACT

Hybrid microgrids (HMGs) that incorporate the functionalities of both AC and DC load/generation systems are gradually evolving from the concept stage to real-world practice. HMGs can reduce power losses due to decreased requirement of conversions from AC to DC and vice versa. HMGs, particularly in islanded operations, are prone to instability and power fluctuations due to the intermittent nature of renewable energy sources (RES) and the stochastic behavior of the loads. It is imperative to damp system oscillations with faster dynamics and reliable controllers. Converter-interfaced energy storage systems (ESS) are well demonstrated to be the most reliable, technically feasible, and economically viable solutions to manage voltage/frequency deviations and to enhance the dynamic performance of microgrids.

The problem of control and power management of microgrids has been well studied in recent years, and various methodologies have been proposed. However, there are technological gaps in the HMGs area yet to be addressed. This dissertation aims to develop robust control solutions to enhance the resiliency and stability of hybrid AC/DC microgrids against grid disturbances.

Among all ESS, the battery energy storage system (BESS) is the most cost-effective and widely accepted technology. This work explores the influence of the BESS operation and proposes novel methodologies to improve the fault ride-through (FRT) capability and disturbance resiliency of microgrids involving complex dynamics characteristics. In addition, this study proposes a novel bidirectional DC-DC converter for energy storage applications in DC and hybrid microgrids. The new converter has a symmetrical configuration that allows designing one controller for both directions. The design approach is based on the linearization and frequency response of the system.

Furthermore, a new grid-connected photovoltaic-supercapacitor (PV-SC) energy storage system is proposed where a minimum number of power components are used to implement both

functionalities. The proposed PV-SC system improves the dynamic performance of the connected grid system during the daytime, nighttime, and cloudy situations.

Appropriate design methodologies and mathematical models have been developed in simulation environments with the maximum possible details to obtain the highest accuracy for linearized models. Simulation results demonstrate the validity and effectiveness of the proposed approaches and show better performance than conventional methods.

# TABLE OF CONTENTS

Content	Page
List of Tables .....	<b>Error! Bookmark not defined.</b>
List of Figures .....	<b>Error! Bookmark not defined.</b>
Abbreviations .....	xviii
Chapter 1 Introduction .....	1
1.1 Background .....	1
1.2 Motivation .....	3
1.3 Objectives .....	5
1.4 Novelty of the Proposed Work .....	6
1.5 Organization of this Dissertation .....	7
Chapter 2 Literature Review .....	8
2.1 Introduction .....	8
2.2 Structure of the Hybrid Microgrid .....	9
2.2.1 Power Converters .....	11
2.3 Control Strategies in HMG .....	14
2.3.1 Primary control techniques .....	17
2.3.1.1 VSC control system in dq reference frame .....	20
2.3.1.2 DC-DC converter control schemes .....	33
2.3.1.3 Interlinking Converter .....	37
2.4 Fault Ride Through Capability of HMGs .....	38
2.5 Disturbance Resiliency of HMGs .....	40
2.6 A Survey on Conventional Bidirectional DC-DC Converter .....	41
2.7 Energy Storage Location in HMGs .....	44
2.8 Evaluation of PV Operating as PV-Supercapacitor Energy Storage .....	46
2.9 Chapter Conclusion .....	48
Chapter 3 Disturbance Resiliency and Fault Ride Through Capability of Hybrid Microgrids ....	49
3.1 Introduction .....	49
3.2 Fault ride through evaluation of the Hybrid AC/DC Microgrids .....	49
3.2.1 HMG Structure and Control systems for FRT Evaluation .....	50
3.2.2 Proposed MSDBR-ILC Coordinated Control Algorithm .....	52
3.2.2.1 MSDBR control algorithm .....	52

3.2.2.2 Coordination control with ILC .....	55
3.2.3 Performance Evaluation and analysis .....	56
3.2.3.1 Effectiveness of Proposed FRT Scheme During 3LG Fault.....	56
3.2.3.2 Effectiveness of Proposed FRT Scheme During 1LG Fault.....	56
3.2.3.3 Index-based performance evaluation.....	58
3.3 Disturbance Resilience Enhancement of Islanded Hybrid Microgrid Using Energy Storage	59
3.3.1 HMG Structure and Control systems .....	60
3.3.1.1 AC subgrid.....	60
3.3.1.2 DC subgrid.....	62
3.3.1.3 ILC.....	63
3.3.2 BESS and Coordinated LVRT Scheme.....	63
3.3.2.1 BESS control .....	63
3.3.2.2 Coordinated LVRT Scheme in DFIG .....	65
3.3.3 Performance Evaluation and analysis .....	66
3.3.3.1 Step load change analysis .....	66
3.3.3.2 Power generation variation analysis .....	67
3.3.3.3 Fault analysis .....	67
3.3.3.4 Index-Based Performance Evaluation .....	67
3.4 Chapter Conclusion.....	70
3.5 Chapter Appendix .....	71
3.5.1 System parameters for both studies.....	71
3.5.2 Parameters of the system controllers:.....	72
Chapter 4 A Novel Bidirectional DC-DC Converter for Energy Storage Applications .....	73
4.1 Introduction.....	73
4.2 Proposed DC-DC Converter for BESS System .....	75
4.2.1 Principle of Operation .....	75
4.2.1 Converter Transfer Functions .....	80
4.2.3 Estimation of the Equivalent Load Resistance.....	82
4.2.4 Power Stage Adjustment .....	85
4.3 Control System.....	88
4.3.1 Proposed Converter Controller.....	88
4.3.1.1 Current Control Mode .....	88
4.3.1.2 Voltage Control Mode .....	92

4.3.2 Conventional BDC Controller.....	96
4.4 Simulation Results .....	97
4.5 Chapter Conclusion.....	100
Chapter 5 Performance Analysis of Hybrid Microgrids Under Influence of Energy Storage Location .....	102
5.1 Introduction.....	102
5.2 HMG case studies and their configurations .....	103
5.2.1 Case Study I: An Industrial HMG.....	103
5.2.2 Case Study II: A Fully Converter-based HMG .....	106
5.3 BESS Modelling .....	107
5.3.1 Battery Model.....	107
5.3.2 AC BESS.....	109
5.3.3 DC BESS.....	111
5.4 Simulation Results and Discussion.....	112
5.4.1 Case Study I analysis .....	113
5.4.1.1 Islanding .....	113
5.4.1.2 Random fluctuation in wind speed .....	114
5.4.1.3 Disruption in dynamic load .....	115
5.4.1.4 Random variation of solar irradiance .....	116
5.4.1.5 Fault analysis and LVRT evaluation .....	117
5.4.2 Case Study II Analysis .....	119
5.4.2.1 Load/generation variation in DCg. ....	120
5.4.2.2 Load/generation variation in ACg. ....	121
5.4.2.3 Fault event and LVRT analysis .....	121
5.4.3 Index-based performance analysis.....	124
5.4 Chapter Conclusion.....	126
5.5 Chapter Appendix .....	128
Chapter 6 Solar Photovoltaic (PV) System as Supercapacitor Energy Storage.....	130
6.1 Introduction.....	130
6.2 Proposed PV-Supercapacitor Energy Storage (SES) System Modeling.....	131
6.2.1 Principle of Operation .....	131
6.2.2 Operation Algorithm .....	133
6.3 Components models and control systems .....	135

6.3.1 PV .....	135
6.3.2 Supercapacitor .....	137
6.3.3 Bidirectional DC-DC Converter .....	138
6.3.4 VSC, Load and Transmission Line .....	141
6.4 Control systems.....	142
6.4.1 BDC control .....	142
6.4.2 VSC Control.....	144
6.5 Nonlinear Mathematical Model and Small-Signal Analyses.....	145
6.5.1 NMM.....	145
6.5.2 Small-Signal Analyses .....	146
6.6 Simulation Results and Discussions .....	149
6.6.1 Validation of dynamic accuracy of NMM .....	150
6.6.2 Effectiveness of Proposed PVSC System to Maintain Voltage Stability .....	152
6.6.3 Stepwise Load Variation and Weak Integration to Grid .....	154
6.6.4 Performance Comparison Between the Proposed PVSC and Conventional SC.....	155
6.6.5 Cost-Effectiveness of the Proposed Approach.....	158
6.7 Chapter Conclusion.....	159
Chapter 7 Conclusion, Contributions, and Future Work .....	160
7.1 Conclusion and Contributions .....	160
7.2 Future Work .....	162
Bibliography .....	164



## LIST OF TABLES

Table	Page
Table 3.1. Index-based performance evaluation .....	59
Table 3.2. Index-based performance evaluation .....	68
Table 3.3 System data for power stage .....	72
Table 4.1. Comparison between proposed, conventional, and other bidirectional DC-DC converters (BDCs). .....	75
Table 4.2 Parameters of the proposed BDC.....	85
Table 4.3. Conventional BDC parameters. ....	97
Table 4.4 Grid parameters.....	98
Table 5.1 DERs' role in Case study II .....	108
Table 5.2 index values of disturbances for key parameters of the HMG in Case study I.....	126
Table 5.3 Index values of disturbances happening in ACg for key parameters of the HMG in Case study II .....	126
Table 5.4 Index values of disturbances happening in DCg for key parameters of the HMG in Case study II .....	126
Table 5.5 System parameters in the case study I .....	128
Table 5.6 BESS parameters in the case study I .....	128
Table 5.7 Initial values in the case study I.....	128
Table 5.8 System parameters in the case study II.....	129
Table 5.9 BESS parameters in the case study II .....	129
Table 5.10 Initial values in the case study II .....	129
Table 6.1 Parameters of the PVSC system under the study.....	150
Table 6.2 PV parameters.....	150
Table 6.3 SC parameters .....	150

## LIST OF FIGURES

Figure	Page
Figure 2.1	Typical structure of hybrid microgrid..... 10
Figure 2.2	HMG including subgrids with different ratings..... 11
Figure 2.3	Microgrid clusters based on (a) AC or (b) DC distribution systems ..... 11
Figure 2.4	DC-DC converter topologies for microgrid applications..... 12
Figure 2.5	A two-level three-phase VSC ..... 13
Figure 2.6	Centralized hierarchical control of HMG; dashed lines represent communication links 15
Figure 2.7	An example of a distributed control scheme..... 16
Figure 2.8	Droop control for active power-sharing in a two DER AC microgrid ..... 19
Figure 2.9	The dynamic model of the VSC power stage ..... 22
Figure 2.10	The control diagram of a grid forming VSC ..... 24
Figure 2.11	equivalent model of the current closed-loop ..... 25
Figure 2.12	Simplified linearized system of VSC control equal to voltage and current loops 26
Figure 2.13	A droop-controlled AC microgrid equipped with centralized secondary control 28
Figure 2.14	centralized secondary voltage and frequency control ..... 29
Figure 2.15	The control diagram of a grid feeding VSC ..... 31
Figure 2.16	The standard structure of the PLL..... 31
Figure 2.17	d axis reference current generating in DC-link voltage control scheme ..... 32
Figure 2.18	an equivalent linearized model of the DC-link voltage control dynamics ..... 32
Figure 2.19	plant model of the DC-DC converter control schemes; (a) voltage control, (b) current control 35
Figure 2.20	DC-DC converter dual-loop control..... 37
Figure 2.21	Basic schematic of the PV system with BES ..... 47
Figure 2.22	Supercapacitor energy storage unit. .... 47
Figure 3.1	Hybrid AC/DC Microgrid structure under the study. .... 50
Figure 3.2	ILC control block diagram..... 52
Figure 3.3	Per-phase fault detection logic diagram..... 53
Figure 3.4	Block diagram of q-axis outer loop in ILC control system. .... 55

Figure 3.5	system dynamic response to a 3LG fault at point F. Red (without FRT), Blue (with FRT).	57
Figure 3.6	The total power dissipated by MSDBR during a 3LG fault. ....	57
Figure 3.7	System dynamic response to a 1LG fault at point F. Red (without FRT), Blue (with FRT).	58
Figure 3.8	Hybrid AC/DC Microgrid structure under the study. ....	61
Figure 3.9	DG speed governor model. ....	61
Figure 3.10	BESS control block diagram ....	64
Figure 3.11	Step load change in Load <sub>1</sub> (case A1) ; (a) ACg frequency, (b) ACg voltage magnitude and (c) BESS power in case of W ....	68
Figure 3.12	Step load changes in DC Load (case A2); (a) ACg frequency, (b) ACg voltage magnitude, (c) ILC and BESS power in case of W ....	69
Figure 3.13	Wind speed fluctuation (case B1): (a) ACg frequency, (b) ACg voltage magnitude and (c) DFIG and BESS power in case of W ....	69
Figure 3.14	Solar irradiance variation (case B2): (a) ACg frequency, (b) ACg voltage magnitude, (c) PV and BESS output power in case of W ....	70
Figure 3.15	Fault analysis (cases C1 and C2); (a) and (b) ACg frequency, (b) and (c) ACg voltage magnitude during ACg and DCg faults respectively. ....	70
Figure 4.1	Conventional bidirectional DC-DC converter. ....	73
Figure 4.2	Proposed bidirectional DC-DC converter. ....	74
Figure 4.3	Hybrid microgrid under the study ....	75
Figure 4.4	Discharge mode circuit. (a) Current flow diagram; (b) equivalent circuit. ....	77
Figure 4.5	Charge mode circuit. (a) Current flow diagram; (b) equivalent circuit. ....	78
Figure 4.6	Inductor currents and <b>S3–S4</b> switching conditions during power a flow direction change.	79
Figure 4.7	Equivalent Boost converter circuit; <b>e1</b> and <b>e2</b> represent input and output voltages, respectively and <b>RI</b> represents the converter equivalent load in each mode. ....	80
Figure 4.8	Converter connection network. · stands for charge mode operating parameters. ....	83
Figure 4.9	Load resistance variation for the test case presented in Table 4.2. ....	85
Figure 4.10	Bode plot of unadjusted converter for open-loop <b>G11s</b> with zoomed-in magnitude.	86
Figure 4.11	Bode plot of the adjusted converter for open-loop <b>G11s</b> . ....	88
Figure 4.12	Current controller block diagram of the proposed converter. (a) Closed-loop small-signal model based on the discharge mode parameters for reference; (b) plant model. ....	89

Figure 4.13	Bode plots of duty ratio-to-inductor current <b><math>G_{21s}</math></b> . (a) uncompensated charge mode gain; (b) compensated charge mode gain. ....	90
Figure 4.14	Bode plots of duty ratio-to-output voltage <b><math>v_2</math></b> , <b><math>G_{11s}</math></b> . (a) Uncompensated charge mode; (b) compensated charge mode. ....	94
Figure 4.15	Voltage controller block diagram of the proposed converter. (a) Closed-loop small-signal model based on the discharge mode parameters as the reference; (b) plant model.	95
Figure 4.16	Battery voltage vs. state of charge (SoC) for different loading conditions. ....	96
Figure 4.17	Conventional BDC control systems used for comparison analysis. (a) Current control; (b) voltage control. ....	97
Figure 4.18	Converter response to pulsed DC load change for Case I with voltage control mode.	99
Figure 4.19	Inductor currents in voltage control mode for Case I. ....	99
Figure 4.20	Converter response to pulsed DC load changes for Case I with the current controller.	100
Figure 4.21	System response to power generation variation in DER1 in Case II with BDC in voltage control.	101
Figure 5.1	Hybrid AC/DC microgrid in Case Study I. ....	103
Figure 5.2	ILC control system for Case I with both BESSs and Case II with ACB only. ....	105
Figure 5.3	Case II Hybrid microgrid; DER1 and DER4 are the candidate locations for BESS	106
Figure 5.4	Power stage and control diagram of non-BESS DERs in ACg in Case II [30]. <b><math>V_{aci}</math></b> is the terminal voltage and <b><math>i \in 1, 2</math></b> . ....	107
Figure 5.5	Power stage and control diagram of non-BESS DERs in DCg in Case II. <b><math>V_{dcj}</math></b> is the terminal voltage and <b><math>j \in 3, 4</math></b> . ....	108
Figure 5.6	The VSC control diagram used in ACB control in Case I. ....	110
Figure 5.7	The VSC control diagram used in ACB, and ILC when operating with DCB in Case study II. ....	111
Figure 5.8	Power stage block diagram of DC-DC converter utilized in DCB [1] in both cases. <b><math>v_2</math></b> is the DCB output terminal that is connected to DCg PCC and <b><math>V_{dc4}</math></b> in the Case I and Case II, respectively. ....	112
Figure 5.9	Control system diagram of the bidirectional DC-DC converter. <b><math>v_2</math></b> is the DCB output terminal voltage that is connected to DCg PCC and <b><math>V_{dc4}</math></b> in Case I and II, respectively	112
Figure 5.10	System response to Islanding incidence simulation in Case I; (a) ACg frequency ( <b><math>Hz</math></b> ), (b) ACg voltage (pu), (c) DCg Voltage ( <b><math>V</math></b> ), (d) BESS power ( <b><math>kW</math></b> ) and (e) ILC power ( <b><math>kW</math></b> ).	114

Figure 5.11	Disturbance in wind speed in Case I; (a) ACg frequency ( <b>Hz</b> ), (b) ACg voltage (pu), (c) BESS output power ( <b>kW</b> ), and (d) WTG output power ( <b>kW</b> ).....	115
Figure 5.12	The step change in frequency-dependent load in Case study I; (a) ACg frequency ( <b>Hz</b> ), (b) DCg voltage ( <b>V</b> ), (c) BESS output power ( <b>kW</b> ), and (d) Mechanical torque of induction motor ( <b>N.m</b> ).....	116
Figure 5.13	Random variation of Solar Irradiance; (a) ACg frequency ( <b>Hz</b> ), (b) DCg voltage ( <b>V</b> ), (c) BESS output power ( <b>kW</b> ) and (d) PV output power ( <b>kW</b> ) .....	118
Figure 5.14	Dynamic response to a 3LG fault event in ACg of Case I; (a) ACg frequency ( <b>Hz</b> ), (b) ACg voltage (pu), (c) DCg voltage ( <b>V</b> ).....	119
Figure 5.15	Dynamic response to fault event in DCg in Case I; (a) ACg frequency, (b) ACg voltage, (c) DCg voltage. ....	120
Figure 5.16	Load/generation variation in DCg in Case II, (a) AC link frequency ( <b>Hz</b> ), (b) AC link voltage magnitude (pu), (c) DC link voltage ( <b>V</b> ), and (d) BESS output power ( <b>kW</b> ). ....	122
Figure 5.17	Load/generation variation in ACg in Case II, (a) AC link frequency ( <b>Hz</b> ), (b) AC link voltage magnitude (pu), (c) DC link voltage ( <b>V</b> ) and (d) BESS output power ( <b>kW</b> ). ....	123
Figure 5.18	Evaluation of fault event in Case II. (a) AC link frequency ( <b>Hz</b> ), (b) AC link voltage magnitude (pu), (c) DC link voltage ( <b>V</b> ), and (d) BESS output power ( <b>kW</b> ).....	124
Figure 5.19	BESS output power for high impedance faults occurring in both subgrids of Case II with different values of resistances to emulate different levels of voltage sags; (a) <b>R<sub>fac</sub> = 120mΩ</b> , <b>R<sub>fdc</sub> = 1.25Ω</b> (b) <b>R<sub>fac</sub> = 150mΩ</b> , <b>R<sub>fdc</sub> = 1.5Ω</b> and (c) <b>R<sub>fac</sub> = 180mΩ</b> , <b>R<sub>fdc</sub> = 2Ω</b> , where <b>R<sub>fac</sub></b> and <b>R<sub>fdc</sub></b> represent fault resistance of ACg and DCg faults, respectively. ....	125
Figure 6.1	Proposed PV-Supercapacitor energy storage system (power stage).....	133
Figure 6.2	The control algorithm of the proposed PVSC system during daytime .....	136
Figure 6.3	Figure 5. PV module equivalent circuit, a) current source model, Thevenin equivalent	137
Figure 6.4	P-V characteristics of the PV array under the study, for different levels of irradiance and rated temperature ( <b>25°C</b> ).....	138
Figure 6.5	Supercapacitor model, (a) circuit model, and (b) nonlinear model diagram .....	139
Figure 6.6	Equivalent circuit model for power stage of the BDC and VSC .....	140
Figure 6.7	Diagram of the nonlinear model of the BDC combined with: (a) PV and (b) SC models.	141
Figure 6.8	The complete dynamic model of the VSC, load and transmission line represented in <b>αβ</b> frame	142
Figure 6.9	BDC control diagram when operating with SC .....	143

Figure 6.10	BDC control system when connected to PV. ....	144
Figure 6.11	The VSC control system diagram .....	144
Figure 6.12	Nonlinear Mathematical Model of the proposed PVSC system .....	147
Figure 6.13	Replacement of dominant poles of the linearized PVSC system for variation of active power droop $0.01 < md < 0.1$ .....	148
Figure 6.14	pole map of the PVSC small-signal model for the variation of DC-DC control system parameters; (a) variation of $kic1$ and (b) variation of $kiv1$ . ....	149
Figure 6.15	Pole displacement map in response to integral gain variation in VSC voltage control ( $kiv2$ ) loops, $188 < kiv2 < 560$ . ....	149
Figure 6.16	Comparison of NMM to that of the DSM for a step change in AC nominal voltage; (a) $vc$ and (b) $mdq$ .....	151
Figure 6.17	Comparison of NMM dynamics to that of the DSM for a step change in DC link reference voltage $vdc$ .....	151
Figure 6.18	Comparison of NMM dynamics to that of the DSM for step change in $PVSC$ *	152
Figure 6.19	DC link voltage during the changeover between PV and SC .....	153
Figure 6.20	SC terminal voltage during the changeover between PV and SC; $vpvt$ – refers to the PV voltage at the changeover moment. ....	153
Figure 6.21	Performance evaluation of proposed PVSC compared to regular PV system during voltage disruption in main grid; (a) VSC output voltage, (b) VSC output frequency.....	154
Figure 6.22	Stepwise load variation and weak integration to grid .....	155
Figure 6.23	Islanded microgrid representation with the BPS and BPS-SC. The open dashed lines represent BPS, and the closed dashed lines represent BPS-SC.....	156
Figure 6.24	Step load change in local load. (a) and (b) grid voltage and frequency at load point and (c) load power. ....	157
Figure 6.25	Output active power in PV energy storage systems for load change disturbance.	157
Figure 6.26	Fault analysis evaluation, (a) and (b) grid voltage and frequency at load point, and (c) load power. ....	158

## **Abbreviations**

AC	Alternative Current
ACg	AC sub-grid
ACB	AC grid BESS
DCB	DC grid BESS
DC	Direct Current
DCg	DC sub-grid
RES	Renewable Energy Sources
HMG	Hybrid AC/DC Microgrid
ESS	Energy Storage System
BESS	Battery Energy Storage System
DER	Distributed Energy Resource
ILC	Interlinking Converter
MPP	Maximum Power Point
MPPT	Maximum Power Point Tracking
PCC	Point of Common Coupling
PV	Photovoltaic
SC	Supercapacitor
PV-SC	PV-Supercapacitor
WTG	Wind Turbine Generator
DG	Diesel Generator
DFIG	Doubly Fed Induction Generator
FRT	Fault Ride-Through
LVRT	Low Voltage Ride Through
VSC	Voltage-Sourced Converter
SoC	State of Charge
PI	Proportional-Integral

PLL	Phase Locked Loop
PMS	Power Management System
PWM	Pulse Width Modulation
MRW	Modulation Reference Waveform
IGBT	Insulated-Gate Bipolar Transistor
MOSFET	Metal-Oxide-Semiconductor Field-Effect Transistor
MAS	Multi-agent Systems
NRF	Natural Reference Frame
RRF	Rotating Reference Frame
SRF	Stationary Reference Frame
ESR	Equivalent Series Resistance
SDBR	Series Dynamic Braking Resistor
MSDBR	Modulated Series Dynamic Braking Resistor
ROCOF	Rate of Change of Frequency
LCL	Inductor(L)-Capacitor(C)-Inductor(L)
SES	Supercapacitor Energy Storage
BES	Battery Energy Storage
BDC	Bidirectional DC-DC Converter
PV-SES	PV- Supercapacitor Energy Storage
BPS	Basic PV System
RSC	Rotor Side Converter
GSC	Grid Side Converter
CCM	Continuous Conduction Mode
DCM	Discontinuous Conduction Mode
DDA	Distribution Detection Algorithm
DSM	Detailed Switching Model
NMM	Nonlinear Mathematical Model





# Chapter 1 Introduction

## 1.1 Background

Micro-grids are limited-size electrical power systems operating in medium and low voltage levels. Traditionally, the communities and customers located in the remote territories are fed by isolated power systems that rely on their energy resources with generating units, mostly with the conventional type of generators and fossil fuels. In the recent two decades, the concept of microgrids developed from those conventional power systems including diverse energy resources such as renewables and energy storage units. The microgrid concept assumes a group of loads and distributed resources as a single controllable unit [1].

The aim of operating these grids is to generate and transmit the required energy from diverse distributed energy resources (DERs) to the loads inside the grid or the hosting grid independent of the main grid ensuring high-reliability levels. Microgrids are recognized as the best solution to handle natural disasters that might cripple conventional super grids. The late power outages in October 2019 in California [2] due to the wildfire and the recent power crisis in February 2021 in Texas [3] due to the winter storm, once again manifested that how the resiliency of the super grids can be compromised during natural disasters leaving millions of people without electricity.

Microgrids are conventionally developed for AC power systems. However, the ever-increasing demand for electric power by DC loads in the modern environment (e.g., data centers, computers, electronic devices, electric vehicle charging stations, etc.) along with the recent advancement in DC power generation, energy storage, and power conversion technologies, has made it attractive to develop DC microgrids, where the DC loads and DERs can be directly interconnected without the need to converting to AC. Nevertheless, in the current trend of the power industry, the

sole operation of DC or AC microgrids might not be economically or technically viable where there is a considerable number of loads and DERs in both forms, and hence two forms of the microgrids should get support from each other.

The Hybrid AC/DC Microgrids (HMGs) emerged by interconnecting two types of the aforementioned microgrids. HMGs are utilized to serve both AC and DC power systems inside a limited area with a higher level of reliability and flexibility, avoiding frequent conversion from AC to DC and vice versa, and hence increasing power efficiency. Two sub-grids are connected by interlinking converters (ILC) to exchange power and support each other [4]. HMGs, facilitate the operation of renewable energy systems while providing service to conventional AC and DC loads and power systems [5]. Like the conventional AC and recently developed DC microgrids, in HMGs where a significant amount of power is supplied by intermittent renewable energy resources (RESs), specifically operated in islanded mode, rely on energy storage systems (ESS) for continuous operation. The energy storage is traditionally collocated with intermittent RES to provide a continuous supply of energy, i.e., storing energy when the renewable generation is higher than the demand, and supplying energy when the demand is higher than the renewable generation, yielding an optimized RES generation capacity. The recent advancement in energy storage technologies such as utility-scale batteries and supercapacitors has made it technically feasible to exploit the energy storage in power distribution grids, e.g., microgrids not only for providing ancillary services but also for improving grid resiliency during contingencies and disturbances.

During the last two decades, the power electronic-based power converters revolutionized the way power systems generate, transmit, store, and deliver electric power. The current trend of AC, DC, and hybrid microgrids owes its development to technological advancements made in power electronic devices. High-speed high-power switching devices like insulated gate bipolar transistors

(IGBT) and metal oxide semiconductor field-effect transistors (MOSFET) and power diodes are widely employed in power converters. The converters are used to transfer the power and/or control the flow of power between two voltage levels or current forms (i.e., DC and AC). For instance, the DC-DC converters are used to connect two systems with two or more voltage levels. While DC-AC (or AC-DC) converters bridge a DC system with an AC system. In modern microgrids, power converters are essential parts of the power system and have a vital role in real-time control and continuous power management of the grid.

The challenges that microgrid operators face relatively differ from those in super grids. Due to their limited capacity of generation reserve and ubiquitous power converters, HMGs and conventional microgrids have smaller inertia and generation support compared to large power grids. In addition, due to the smaller scale of generation, the problem of fault ride-through (FRT) and low voltage ride-through (LVRT) in islanded microgrids might be challenging. Furthermore, the non-dispatchable and intermittent nature of distributed renewable energies constitutes the risk of a power outage. Also, due to the increased uptake of power converters in every aspect of microgrid power systems, the power quality issues and harmonic performance of HMGs demand more research. Consequently, the stability of the grid is easily jeopardized during large disturbances (e.g., grid faults, load/generation disruptions, etc.).

The study conducted in this dissertation aims to explore some of those challenges and develop robust and dynamic solutions for energy storage-enabled hybrid microgrids. The following subsections briefly outline the motivation for this research and discuss the objectives pursued by the researcher.

## **1.2 Motivation**

The paradigm of the microgrid along with the evolution of the smart grid is a relatively new

idea that has been developing in electric power research institutes over the last two decades [1]. On the other hand, the conventional power grid generation, transmission, and distribution infrastructures are well developed with huge investments during the last century. Therefore, the evolution toward the new concept would not be an easy and quick step and it needs a lot of research to develop and fabricate a flawless and state-of-the-art system that is worth shifting from the conventional environment to the new idea. Although the concept is relatively mature now, there are still gaps between research concepts and practical systems that require more research with detailed insights.

The dynamic performance and power management of the microgrids (particularly HMGs in islanded operation or located in isolated areas) are the most vital aspects of the concept that need continuous research [6]. As the level of penetration of renewable energies is elevating, the dynamic performance of the microgrids is compromised due to the low inertia power generation [7]. The renewables should be collocated with the energy storage to minimize the power fluctuation [8]. Then the distributed energy storage requires power balancing to achieve a balanced charge/discharge process to avoid premature aging of storage (e.g., batteries) during primary frequency control [9]. Some researchers proposed a hybrid energy storage system (HESS) comprised of a battery energy storage system (BESS) and high-power density super capacitor-based storage to improve the battery life cycle [10]. The general points that invoke motivations in this field are:

- The FRT capability of the islanded HMG is not explored properly so far.
- Disturbance resiliency of the HMG including dynamic loads and grid following energy storage still needs consideration to explore.
- The impact of BESS location in AC or DC subgrid on the dynamic performance of a small-sized HMG has not been analyzed yet.

- The conventional bidirectional DC-DC converter for energy storage application in microgrids needs improvement to enhance the system response to DC bus under/overvoltage.
- A BESS capable of handling different disturbances (e.g., load variation, renewables intermittency, grid faults, communication delay, etc.) is of interest.
- The conventional PV system can be revised and integrated with a high-power density energy storage (like a supercapacitor) with a minimum number of power converters to improve the system's dynamic performance and, hence saving capital costs.

The research of the dynamic performance of HMG intrinsically involves complexity and computational challenge. Microgrids incorporate various systems with different dynamic properties that seek accurate simulation or real-time emulation to evaluate proposed control effectiveness. The computer simulation with averaged models cannot effectively portrait the power electronics-dominated system with highly nonlinear dynamics, particularly integrated with high inertia systems. Recent research works implement some experimental setups to emulate part of the microgrids [11]. However, they are only power electronics devices that do not incorporate multi dynamics of low/high inertia systems (i.e., conventional synchronous generators, wind turbines, etc.). In this research, for simulation purposes, high-order models and detailed switching electronics devices with ultra-high sampling frequencies compared to current research have been used, to exhibit the system nonlinearities as much as possible. This requires higher computational capabilities with longer simulation times. In addition, the nonlinear nature of these systems usually invalidates the control system parameters that are designed based on analytical methods. Therefore, a process of heuristic or trial and error would be needed to implement a well-tuned control system.

### **1.3 Objectives**

The objectives of this research are to address issues and findings outlined in the motivation

section as far as possible. The following objectives are sought in this research:

- This research aims at devising new methodologies based on inverter/converter interfaced AC/DC DERs and BESS to improve transient stability and overall dynamic performance of the HMG ensuring flexible load demand response and continuity of the service in the presence of multi dynamics DERs and frequency-dependent dynamic loads.
- The resiliency and FRT capability of energy storage enabled, and islanded HMGs are to be explored and improved. Also, the performance of HMGs will be evaluated to examine the impact of the BESS location.
- The structure of bidirectional DC-DC converter for energy storage applications will be improved to enhance the dynamic performance of DC microgrids and DC subgrid of HMGs.
- The performance and cost-effectiveness of grid-connected PV generating systems will be improved.

#### **1.4 Novelty of the Proposed Work**

The novelties of this work are aligned with the solutions for issues outlined in the research motivation and objective sections. In summary:

- A coordinated control scheme of ILC and series dynamic braking resistor with a fault detection algorithm is proposed for FRT capability enhancement of the entire HMG including AC and DC BESS.
- A revers-droop control method is proposed to be employed in the grid following BESS along with a coordinated LVRT scheme in a doubly-fed induction generator (DFIG) based wind turbine generator system to improve the resiliency of the HMG against various disturbances.

- The influence of the BESS location (AC or DC grid) on the dynamic performance of the HMG is evaluated that is useful for BESS siting and system operator to know about the HMG operation with a single BESS at a time.
- A novel bidirectional DC/DC converter for BESS application is proposed that improves converter's gain and dynamic response to DC bus voltage variations.
- An integrated grid-connected PV-Supercapacitor (PV-SC) system is proposed to merge two DC-DC converters, that are separately used for PV and energy storage, into one bidirectional converter to save the capital cost of the system, and a control algorithm is designed for this system.

## **1.5 Organization of this Dissertation**

This dissertation is composed of 6 chapters. Chapter 2 conducts a literature review and provides a detailed background of microgrid structures, main components, and control systems. The contents of chapter 3 to chapter 6 encompass the main research that was published in journals and conferences. Chapter 3 explores the methods of improving FRT capability and disturbance resiliency in HMG. Chapter 4 presents a novel bidirectional DC-DC converter for energy storage applications. Chapter 5 evaluates the influence of BESS location on the dynamic performance of the HMG. Chapter 6 discusses the integrated PV-SC and explores its impact on the performance of a grid-connected PV system. Finally, chapter 7 concludes the results of this research, presents key findings, and wraps up the dissertation with some recommendations for future research.



## Chapter 2 Literature Review

### 2.1 Introduction

AC/DC power systems, especially HMGs are getting wider attention to the power community worldwide [4],[12],[13]. HMGs are electrical distribution networks that serve both AC and DC power systems, with higher reliability and efficiency levels by incorporating autonomous control systems [1]. The purpose of operating these grids is to supply energy from DERs, e.g., wind turbines, photovoltaic (PV) arrays, diesel generators, etc., to the loads independent of the main utility grid in a relatively small area of coverage such as remote towns, university campuses, hospitals, military bases, ships, etc. However, they can operate grid-connected to exchange power with the main grid to either support the grid or get supported by the grid. In an HMG system, operational functionalities of both AC and DC currents are combined to avoid frequent conversions from AC to DC and DC to AC to minimize energy losses and directly feed dc loads from DC primary sources [14]. However, the uncertain or intermittent nature of renewable resources constitutes the risk of a power outage for sensitive loads inside the microgrid. The technical development has made it feasible to collocate energy storage (ES) systems to enhance power quality as well as grid reliability. In HMGs, an ES is an essential component that is mainly used for peak shaving and minimization of power and frequency fluctuations resulting from solar irradiance variation or wind speed change. Improving the resiliency and transient stability during large/small-signal disturbances in an islanded HMG comprising different DERs exhibiting diverse dynamic characteristics is a challenging task [15].

The purpose of this chapter is to provide a literature review and to discuss new and conventional methods that provide overall stability and control improvements in hybrid AC/DC

microgrids. Typically, auxiliary control devices are used to improve the transient stability of the microgrid, incurring extra costs. However, it is interesting to explore whether an existing component of the microgrid such as BESS or HESS can be utilized for resiliency enhancement [15] during large-signal disturbances in an HMG system. If an existing component, like BESS, can be used to improve the resiliency of the HMG, then the cost of many auxiliary devices can be saved. The control philosophy has different roles in islanded and grid-connected modes of microgrids. To regulate the bus voltage and AC microgrid frequency during the grid disturbances (i.e., load change and intermittent DER), the required controller drives a voltage-sourced converter (VSC) to inject and/or absorb active and reactive power, respectively.

## **2.2 Structure of the Hybrid Microgrid**

The conventional form of AC and DC microgrids have been separately developed over the past years. HMGs are only the new generations of combined AC and DC subgrids that are integrated through ILCs [16]. In this way, DC loads (e.g., electronic devices, the computer servers, etc.) and DERs with DC (e.g., Photovoltaic Panels (PV), fuel cells, etc.) can be directly connected to DC subgrid while the AC subgrid serves the AC loads and DERs with AC currents (e.g. wind turbines, microturbines, diesel generators, etc.). Nevertheless, AC and DC systems can be connected to DC and AC systems, respectively through power converters as required. Figure 2.1 shows a typical structure of an HMG. DC-DC converters and VSCs are two integral parts of every HMG to control the flow of power between various voltage levels and forms (AC/DC) as well as tracking the maximum power point in renewable energy sources (RES). Later, we will discuss how these power electronic-based converters are exploited to control the dynamic behavior of the HMG during grid disturbances. HMGs are reasonable solutions to connect microgrids with different ratings to integrate a variety of loads and DERs with dissimilar ratings. Figure 2.2 shows HMG

topologies in which a subgrid is interfaced between two subgrids with unequal ratings. In addition, depending on the application, location, and extent of the microgrid coverage, it might have several HMG subgrids (called clusters) which are interconnected throughout the AC or DC power distribution system. Figure 2.3(a) displays a microgrid cluster formed by an AC distribution system [17] while Figure 2.3(b) shows a cluster based on the DC distribution system [18]. Each subgrid inside the cluster is capable of autonomous operation. Besides, a cluster can host any type of AC, DC, or hybrid subgrid.

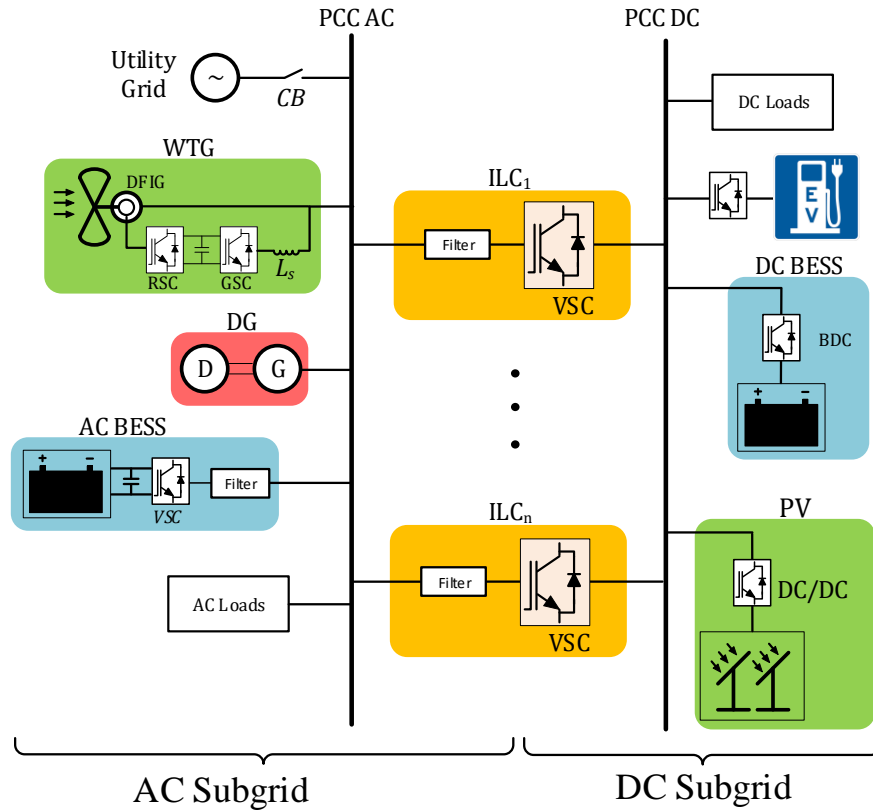


Figure 2.1 Typical structure of hybrid microgrid

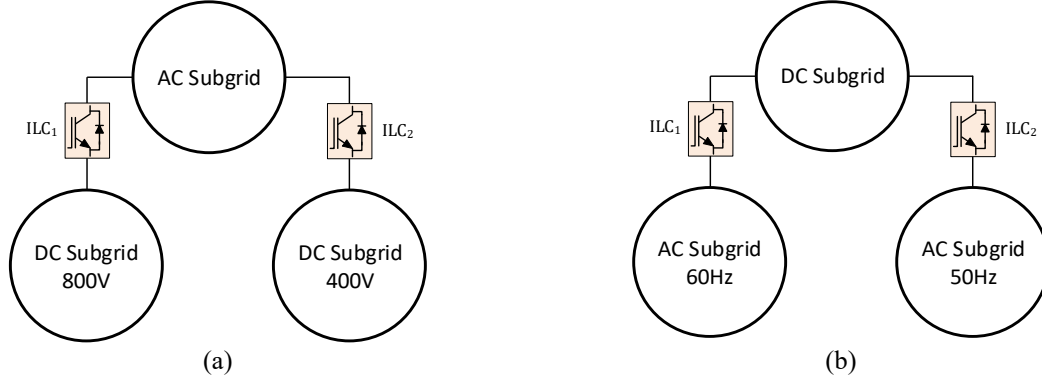


Figure 2.2 HMG including subgrids with different ratings

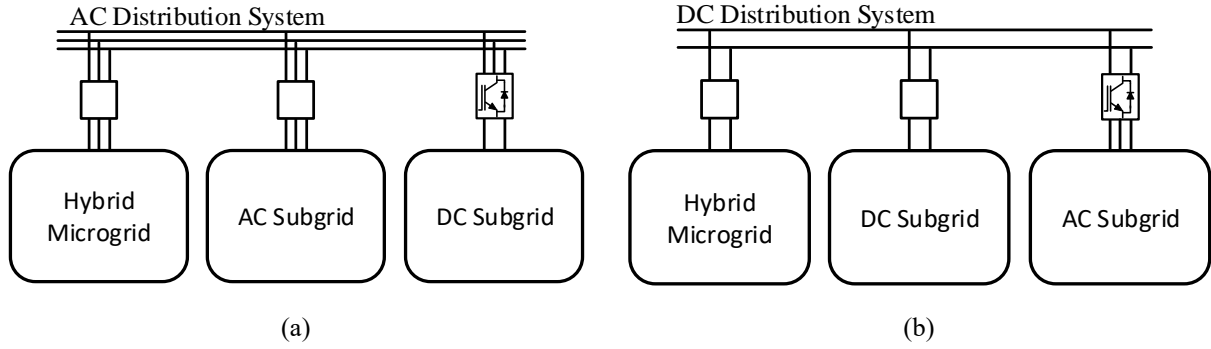


Figure 2.3 Microgrid clusters based on (a) AC or (b) DC distribution systems

Although HMGs operate autonomously in a remote location, they can operate in a grid-connected mode where there is access to the main grid to either support the grid or get supported by the grid. They should be able to island and continue the service as quickly as possible when there is a fault or abnormal situation in the main grid. In this context, HMGs are promising solutions for high-quality and reliable electric power when there are uncertainties with the main grid.

### 2.2.1 Power Converters

DC-DC converters usually interface the DC DERs and energy storage with the DC subgrid to control the flow of power and DC subgrid voltage. For instance, a boost converter (Figure 2.4 a) is used to interface a PV with a DC subgrid through a step-up conversion. In this case, the PV terminal voltage is lower than the DC subgrid voltage. If the PV voltage is higher than the DC

subgrid voltage, a buck converter (Figure 2.4 b) would be used to step down the voltage. Energy storage like BESS needs a bidirectional DC-DC converter (BDC) (Figure 2.4c) which is controlled to absorb the power and charge the battery during DC subgrid overvoltage (or oversupply of renewable DERs) and to inject the power and discharge the battery during undervoltages (or under-supply of renewable DERs). In practice, the battery voltage is less than the DC subgrid voltage, which needs a boost (step-up) operation for the discharge process and a buck (step-down) operation for the charging process. Specific loads like Electric Vehicle (EV) charging stations need a DC-DC converter to control the charging process and match the DC subgrid voltage with the vehicle battery voltage. In Figure 2.4,  $S_{boost}$  and  $S_{buck}$  are power electronic switches (IGBT/MOSFET) driven by high-frequency Pulse Width Modulation (PWM) switching techniques [19]. The pulse width or the duty ratio ( $d$ ) defines the converter gain in each operation mode. Depending on the application, the value of duty ratio is controlled based on the control scheme by voltage/current loops to control the grid voltage, flow of power, or the charge/discharge process of the energy storage. Part 2.3.1.2 discusses an overview of the DC-DC converter controller and derivation of their averaged transfer functions. In addition, a detailed survey on the bidirectional converter is discussed in section 2.6.

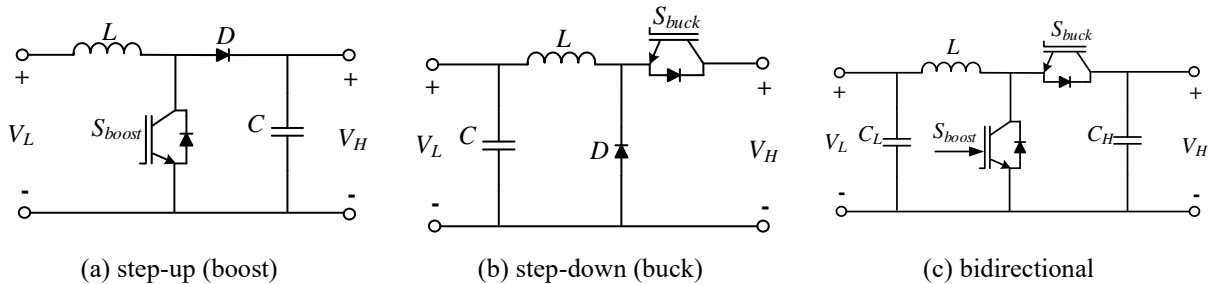


Figure 2.4 DC-DC converter topologies for microgrid applications

The VSC connects the DC DERs, energy storage, and ILC to the AC subgrid [20][21][22]. When transferring power from the DC link to the AC side, it works as an inverter, and when

exchanging power from the AC side to the DC link, it works as a rectifier. Figure 2.5 shows the power stage of a two-level, three-phase VSC along with the AC filter and DC-link capacitive filter. It is called two-level because the output AC terminals can have either of the  $-V_{dc}$  or  $V_{dc}$  values at a time. The power electronic switches are driven by a sinusoidal PWM (SPWM) to generate a sinusoidal waveform at the AC side. The pulse width is controlled by a modulation reference waveform (MRW), while the output pulse amplitude is equal to the DC-link voltage. During the time that power switches are OFF the current flows from AC side to DC side through anti-parallel diodes if the AC side amplitude is greater than the DC-link voltage at the same time. The MRW is generated by the modulation index, which varies in the range  $[0,1]$ , and carrier frequency, which is the SPWM switching frequency. The DC-link may be connected to DERs with DC voltage, energy storage or the DC bus of the DC subgrid in case if used in ILC. Due to the switching operation, the input/output currents have switching harmonics. The AC filter restricts the harmonics in AC side current while the capacitor (C) filters the ripples in the DC-link voltage. In order to increase the harmonic performance, the VSC is equipped with more than two levels, and the LC filter has another inductor in series with the output current  $I_g$  which makes it an LCL filter. In the next part we will discuss more details about the VSC.

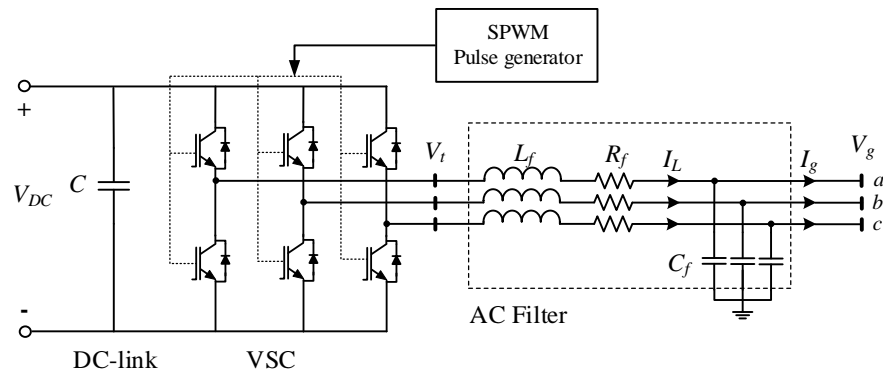


Figure 2.5 A two-level three-phase VSC

### 2.3 Control Strategies in HMG

Various control strategies have been proposed for microgrid control. Multi-level hierarchical control, which has been a standard approach, is suitable for the operability of the grids with distributed generations as it allows control of local and global variables such as frequency and voltage to guarantee power-sharing among DERs to generate a desired steady-state power [23]. The traditional hierarchical architecture has three control levels: Primary, Secondary, and tertiary. Each level has its control objectives and specific bandwidth to ensure decoupled performance. The primary layer performs load sharing and provides ancillary protection and stability control to the local devices. An example of the primary level is the most common decentralized droop control technique [24][25][26]. All the local measurements and controllers are at this control level. This level has the highest speed of response (bandwidth) since it is immediately attached to the devices with no communication interfaces.

The secondary level is responsible for compensating voltage/frequency deviations made by the primary control. This level has a relatively slower dynamic in comparison with the primary level as it requires an intermediate timescale to respond to frequency/voltage deviations and is usually implemented in control centers linked with communication channels.

Lastly, the tertiary control level, which is also called HMG Power Management System (PMS) performs supervisory management on solving the Optimal Power Flow (OPF) problem and calculating power references for DERs considering economic objectives. This level has much slower dynamics as it needs to receive data from local measurement devices, perform the control objectives in a longer timescale (compared with lower levels) and send back the reference setpoints through the low-bandwidth communication links.

In practice, the tertiary level is merged into the secondary level to form an equivalent two-level

control architecture [27]. The upper level is usually implemented in a centralized and distributed configuration. Each topology has its application and advantages.

The traditional centralized model of a converter-based HMG control is shown in Figure 14.6 that has two equivalent layers. All the DERs and devices are directly connected to the control center through communication links forming a star topology. Although relatively simple to implement, it has several drawbacks and limitations, as listed below:

- requires a substantial communication system between the control center and all DERs and devices which incurs a considerable cost in geographically scattered HMGs with several critical buses.
- its security and accuracy are compromised as the entire HMG relies on one control center.
- This approach is suitable for HMGs with critical demand-supply balance and a fixed structure with no plug-and-play capability [28].
- It is not ideal for distributed energy storage applications as it does not consider storage capacity and state of charge (SoC) [27].

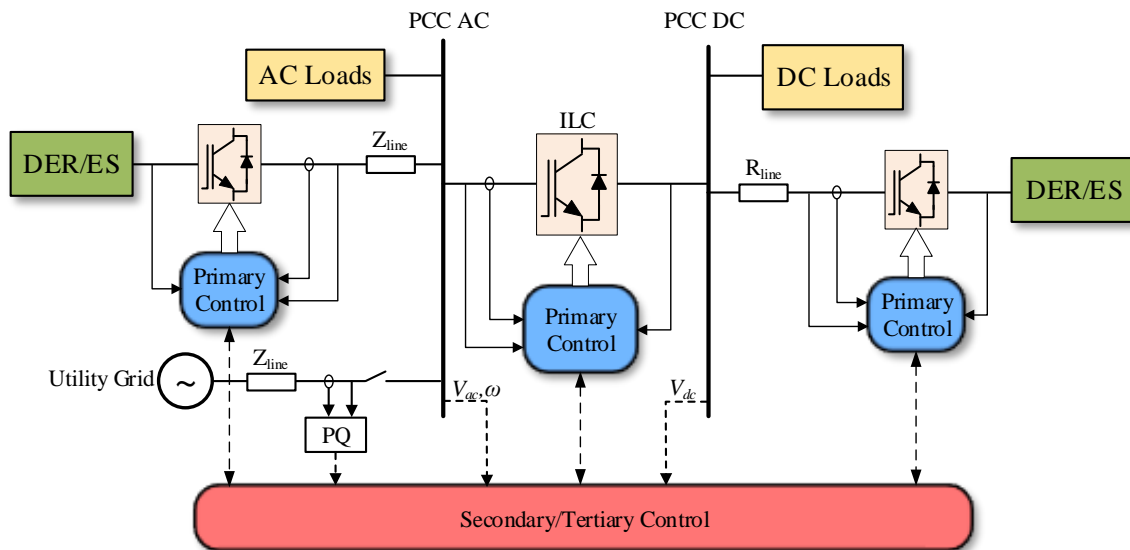


Figure 2.6 Centralized hierarchical control of HMG; dashed lines represent communication links



The distributed control architecture has been recently proposed to provide a flexible, efficient, and reliable operation based on a sparse communication network eliminating mere reliance on the control center. Figure 2.7 illustrates an example of a distributed control scheme for a converter-based HMG. This scheme is more suitable for spatially dispersed HMGs with several critical buses. In a distributed control architecture, the local controller can communicate with each other to define or decide the secondary control actions. The communication system is flexible from all-to-all link to neighbor-to-neighbor connection. The secondary control action is determined based on the averaging or consensus techniques in a multi-agent systems (MAS) framework. A MAS is a composition of multiple intelligent agents that have access to the local information and exchange information with each other to pursue several global and local objectives. In this scheme, the physical secondary/tertiary layer can be removed as the agents can establish the virtual secondary layer in the primary control level.

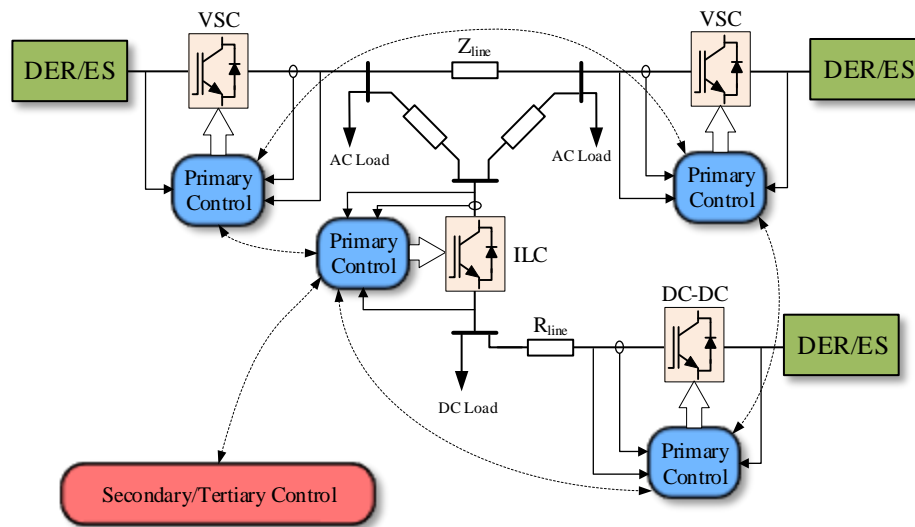


Figure 2.7 An example of a distributed control scheme

In the secondary averaging technique, each DER determines the secondary compensating terms based on the average value of some or all the other DERs. The real-time global average

asymptotically tracks the control reference within a certain timescale. For instance, the average value of the frequency in an AC subgrid is the arithmetic mean of all other DERs. This process is a little different in the case of the local variables like voltage. In this case, the output reactive power of other DERs also participates in the averaging [23].

In the cooperative consensus algorithm, the autonomous agents (i.e., DERs) share the information with other agents in a neighbor-to-neighbor configuration within a sparse communication structure. At the secondary level DERs achieve accurate load sharing through global voltage/frequency restoration while at the tertiary level agents solve the problem of optimal power flow by iteratively solving limited size subproblems and share the results with neighbors [27]. The consensus technique reduces the communication links and can get adapted to different microgrid topologies. However, even with the sparse communication links, this topology mainly depends on the communication system implying that the system gets more complicated as the number of DERs grows.

### ***2.3.1 Primary control techniques***

The primary control is based on local measurement and information. DERs use the voltage, frequency, power, etc. signals and primary setpoints to establish a decentralized control with no information received from other HMG devices. The most common type of primary control for load sharing is droop control which has been used in conventional synchronous generator-based power systems for a long time. It generates the reference signals applied to controllers, and the idea is that generating sources drop their frequency and voltage from the rated value to share a common load. The load sharing depends on the droop coefficients, which are determined based on the DRE rating. For DERs operating in AC subgrid, the reference values are determined by  $P - \omega$  and  $Q - V$  relationships:

$$\begin{aligned}\omega_i &= \omega^* - m_i P_{oi} \\ V_i &= V^* - n_i Q_{oi}\end{aligned}\tag{2. 1}$$

where  $\omega_i$  and  $\omega^*$  are the  $i$ th DER's reference angular frequency and its setpoint value,  $V_i$  and  $V^*$  are the  $i$ th DER's reference voltage magnitude and its setpoint value,  $m_i$  and  $n_i$  are active and reactive power droop coefficients respectively.  $P_{oi}$  and  $Q_{oi}$  are the output active and reactive power of each DER given in (2.2) based on the network parameters [29][30]:

$$\begin{aligned}P_{oi} &= \frac{V_i}{R_i^2 + X_i^2} [R_i(V_i - V_g \cos \varphi_i) + X_i V_g \sin \varphi_i] \\ Q_{oi} &= \frac{V_i}{R_i^2 + X_i^2} [-R_i V_g \sin \varphi_i + X_i(V_i - V_g \cos \varphi_i)]\end{aligned}\tag{2. 2}$$

where  $R$  and  $X$  are components of the line impedance connecting the DER to the bus with the voltage  $V_g$  [see Figure 2.8(a) for a two DER system],  $V_i$  is the DER output voltage,  $\varphi_i$  is the phase difference between  $V_g$  and  $V_i$ . Figure 2.8(b) shows this simple concept for sharing a common load  $P_L = P_1 + P_2$  between two parallel DERs displayed in Figure 2.8(a). In this case  $m_1 P_1 = m_2 P_2$  and  $\frac{m_1}{m_2} = \frac{P_1}{P_2}$  which implies that the load is proportionally shared to droop coefficients. The  $P - \omega$  and  $Q - V$  droop techniques work because a good decoupling exists between active and reactive powers such that active and reactive powers are proportional to DER's phase angle (or angular frequency) and voltage magnitude. In the practical medium and high voltage distribution systems, the lines connecting the DERs are mostly inductive implying that the ratio of  $\frac{X}{R} > 1$  holds for lines reactance ( $X$ ) and resistances ( $R$ ). This ensures that a good decoupling exists between active and reactive powers. If the inductive part of the line is higher than the resistive part such that the resistive part can be neglected, the active and reactive powers are simplified to:

$$P_{oi} \simeq \frac{1}{X_i} V_i V_g \sin \varphi_i$$

$$Q_{oi} \simeq \frac{V_i}{X_i} (V_i - V_g \cos \varphi_i)$$
(2.3)

However, if the inductive content of the distribution lines is less than the resistive part (i.e.,  $\frac{X}{R} < 1$ ), as in low voltage distribution systems, the  $P - \omega$  and  $Q - V$  droop would not make an accurate power-sharing. The active and reactive powers in a resistive distribution network will approximately be simplified to:

$$P_{oi} \simeq \frac{V_i}{R_i} (V_i - V_g \cos \varphi_i)$$

$$Q_{oi} \simeq \frac{-1}{R_i} V_i V_g \sin \varphi_i$$
(2.4)

In this case, a  $P - V$  and  $Q - \omega$  droop technique might be used (i.e.  $\omega_i = \omega^* + m_i Q_{oi}$  and  $V_i = V^* - n_i P_{oi}$ ). In general, to eliminate the dependency of the power-sharing on line impedance, a virtual output impedance method is employed, which is briefly discussed later in this section.

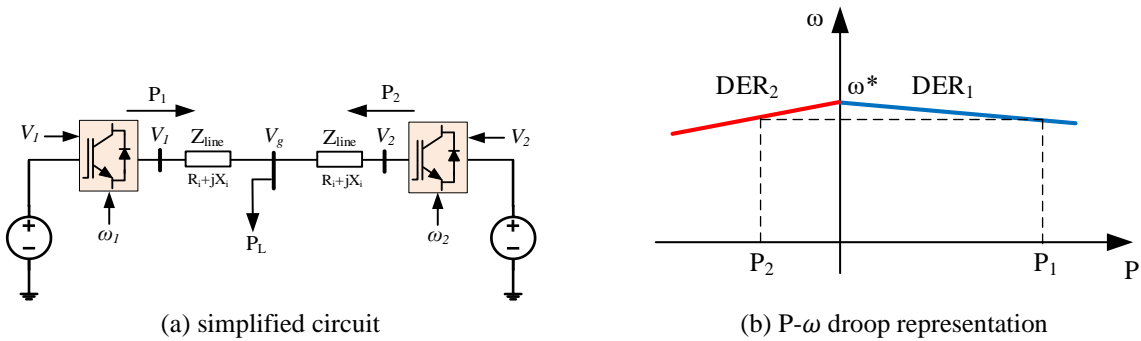


Figure 2.8 Droop control for active power-sharing in a two DER AC microgrid

A similar droop control technique is employed for the DC subgrid primary control, which is called  $V - I$  droop by applying a virtual resistance:

$$V_{dcj} = V_{dc}^* - R_{vj}I_{oj} \quad (2.5)$$

where  $V_{dcj}$  and  $V_{dc}^*$  are the  $j$ th DER's output reference and DC subgrid's nominal voltage,  $R_{vj}$  is the virtual impedance and  $I_{oj}$  is the DER output current.

#### 2.3.1.1 VSC control system in $dq$ reference frame

In a VSC-based HMG, the DER power converters in the AC subgrid and ILC can be controlled to achieve certain control objectives. In fact, this capability is a remarkable competency of the modern HMGs (and AC microgrids) compared to the conventional power systems as they flexibly integrate the distributed RES and energy storage. The control scheme can be implemented in the natural reference frame (NRF) or  $abc$ , stationary reference frame (SRF), or  $\alpha\beta$  and rotating reference frames (RRF) or  $dq$ . The NRF is challenging to implement as it deals with complex sinusoidal signals and decoupling the active and reactive currents is impossible. SRF deals with decoupled sinusoidal signals ( $\alpha\beta$ ) and hence can be used for harmonic control using proportional resonance (PR) controllers and virtual impedance implementation. However, the RRF converts three-phase sinusoidal signals to two DC direct and quadrature ( $dq$ ) axes which can be easily used in linear control type controllers like Proportional-Integral (PI) compensators. If decoupled effectively, the  $dq$  control provides accurate active and reactive power control along with droop control. The VSC can be operated in grid-forming, grid-following (or grid-feeding), and DC voltage control modes depending on the application and the control objectives in HMG. In the grid-forming mode, VSC controls the AC subgrid voltage and frequency and operates in the islanded mode of the microgrid. The reference values of voltage magnitude and angular frequency (or phase angle) are generated by the droop technique if more than one grid-forming VSC operates in the grid. The dynamic modeling of the power stage of a VSC starts by writing the KVL equations for the inductor current in  $abc$  frame and then converting them into RRF to acquire a  $dq$  decoupled control stage. It is

assumed that VSC terminal voltage  $V_t$  is an averaged value of the DC side and PWM switching operation. From Figure 2.5 we have:

$$\mathbf{v}_t = L_f \frac{d\mathbf{i}_L}{dt} + R_f \mathbf{i}_L + \mathbf{v}_g \quad (2.6)$$

where

$$\mathbf{v}_t = \begin{bmatrix} V_{ta} \\ V_{tb} \\ V_{tc} \end{bmatrix} \mathbf{i}_L = \begin{bmatrix} I_{La} \\ I_{Lb} \\ I_{Lc} \end{bmatrix} \mathbf{v}_g = \begin{bmatrix} V_{ga} \\ V_{gb} \\ V_{gc} \end{bmatrix} \quad (2.7)$$

Transforming (2.6) directly from  $abc$  frame to  $dq$  frame (RRF) it yields:

$$\mathbf{v}_{tdq} = L_f \frac{d\mathbf{i}_{Ldq}}{dt} + j\omega L_f \mathbf{i}_{Ldq} + R_f \mathbf{i}_{Ldq} + \mathbf{v}_{gdq} \quad (2.8)$$

$$\mathbf{v}_{tdq} = \begin{bmatrix} v_{td} \\ v_{tq} \end{bmatrix} \mathbf{i}_{Ldq} = \begin{bmatrix} i_{Ld} \\ i_{Lq} \end{bmatrix} \mathbf{v}_{gdq} = \begin{bmatrix} v_{gd} \\ v_{gq} \end{bmatrix} \quad (2.9)$$

assuming that the  $d$ -axis in  $dq$  frame is aligned with the  $a$ -phase in  $abc$  frame. The transformation matrix for any variable  $X$  from  $abc$  frame to  $dq$  frame is given by the Park transformation as follows [31]:

$$\begin{aligned} X_{dq} &= \mathbf{T} X_{abc} \\ \mathbf{T} &= \frac{3}{2} \begin{bmatrix} \cos \theta_s & \cos \left( \theta_s - \frac{2\pi}{3} \right) & \cos \left( \theta_s + \frac{2\pi}{3} \right) \\ -\sin \theta_s & -\sin \left( \theta_s - \frac{2\pi}{3} \right) & -\sin \left( \theta_s + \frac{2\pi}{3} \right) \end{bmatrix} \end{aligned} \quad (2.10)$$

where  $\theta_s$  is the angle difference between  $dq$  and  $abc$  frames.  $\mathbf{T}^{-1}$  is used to transform  $dq$  frame variables to  $abc$  frame. It should be noted that by the operation of the phase-locked loop (PLL) in the steady state,  $\theta_s = 0$  and the  $d$ -axis is fully aligned with  $a$ -phase. Assuming that  $X_{dq} = X_d + jX_q$ , equation (2.8) can be expressed in  $d$  and  $q$  axes for inductor current dynamics by decomposing into real and imaginary terms we obtain:

$$\begin{aligned}
L_f \frac{di_{Ld}}{dt} &= v_{td} + \omega L_f i_{Lq} - R_f i_{Ld} - v_{gd} \\
L_f \frac{di_{Lq}}{dt} &= v_{tq} - \omega L_f i_{Ld} - R_f i_{Lq} - v_{gd}
\end{aligned}
\tag{2.11}$$

The PLL functionality will be briefly discussed in the next parts. Equation (2.11) expresses the mathematical model of the inductor dynamics in terms of converter terminal and grid voltages as converter reference generating and disturbance signals. The dynamics of capacitor voltage can also be derived similarly by writing the KCL for capacitor node in Figure 2.5:

$$C_f \frac{dv_g}{dt} = \mathbf{i}_L - \mathbf{i}_g \tag{2.12}$$

where  $\mathbf{i}_g = [I_{ga} \ I_{gb} \ I_{gc}]^T$ . Transforming to  $dq$  space and decoupling the real and imaginary terms it holds:

$$\begin{aligned}
C_f \frac{dv_{gd}}{dt} &= \omega C_f v_{gq} + i_{Ld} - i_{gd} \\
C_f \frac{dv_{gq}}{dt} &= -\omega C_f v_{gd} + i_{Lq} - i_{gq}
\end{aligned}
\tag{2.13}$$

Combining (2.11) and (2.13) results in the averaged dynamic model of the power stage of the VSC shown in Figure 2.9.  $v_{td}$  and  $v_{tq}$  are the averaged  $dq$  values of VSC terminal voltage at AC side that are generated by the modulation index  $u$  :

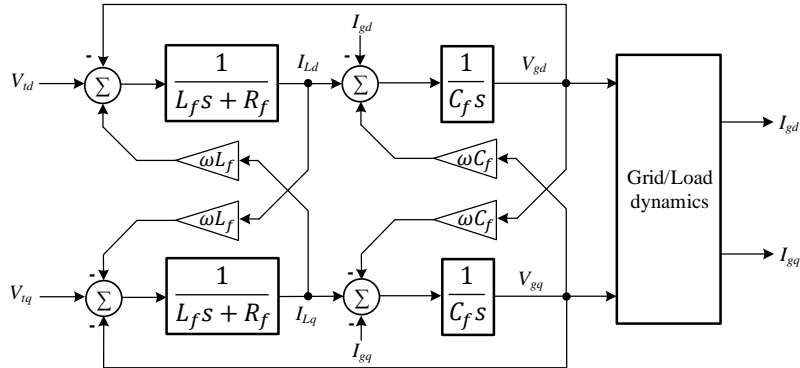


Figure 2.9 The dynamic model of the VSC power stage

$$\mathbf{v}_t = \mathbf{u} \frac{V_{dc}}{2}, \mathbf{u}^T = [u_a \quad u_b \quad u_c] \quad (2.14)$$

$$\begin{aligned} u_a &= u(t) \cos(\omega t + \theta_0) \\ u_b &= u(t) \cos\left(\omega t + \theta_0 - \frac{2\pi}{3}\right) \\ u_c &= u(t) \cos\left(\omega t + \theta_0 + \frac{2\pi}{3}\right) \end{aligned} \quad (2.15)$$

$$0 \leq u(t) \leq 1$$

where  $\theta_0$  is the initial and/or arbitrary phase angle of the VSC and  $\mathbf{u}$  is the vector of the variable modulation indexes generated by the control system.

$$\begin{aligned} u_{dq} &= u_d + ju_q \\ u(t) &= \sqrt{u_d^2 + u_q^2} \end{aligned} \quad (2.16)$$

where  $u_d$  and  $u_q$  are respectively  $d$ - and  $q$ -axis reference generating signals from the control system. They are generally DC signals in the steady-state operation that are perturbed during transients.  $\omega t$  is the phase angle generated by either droop control for a grid-forming or by the PLL for a grid-following VSC. In the general form we have:

$$\omega t = \theta_s = \int \omega(t) dt \quad (2.17)$$

where  $\omega(t)$  is treated as the time-varying angular frequency generated by droop equations or detected by the PLL. Grid/load dynamics in Figure 2.9 is the equivalent model of the VSC external network connected to  $V_g$  terminal. In the case of a stand-alone VSC and its load, the load current is simply equal to  $I_g$ . While in the networked microgrids with the operation of several DERs and other grid components, the load is shared between DERs. In general form, load dynamics are modeled by the state-space representation in which the dynamics of different DERs and grid components can be combined to form a multi-input multi-output (MIMO) system [32][33][6].



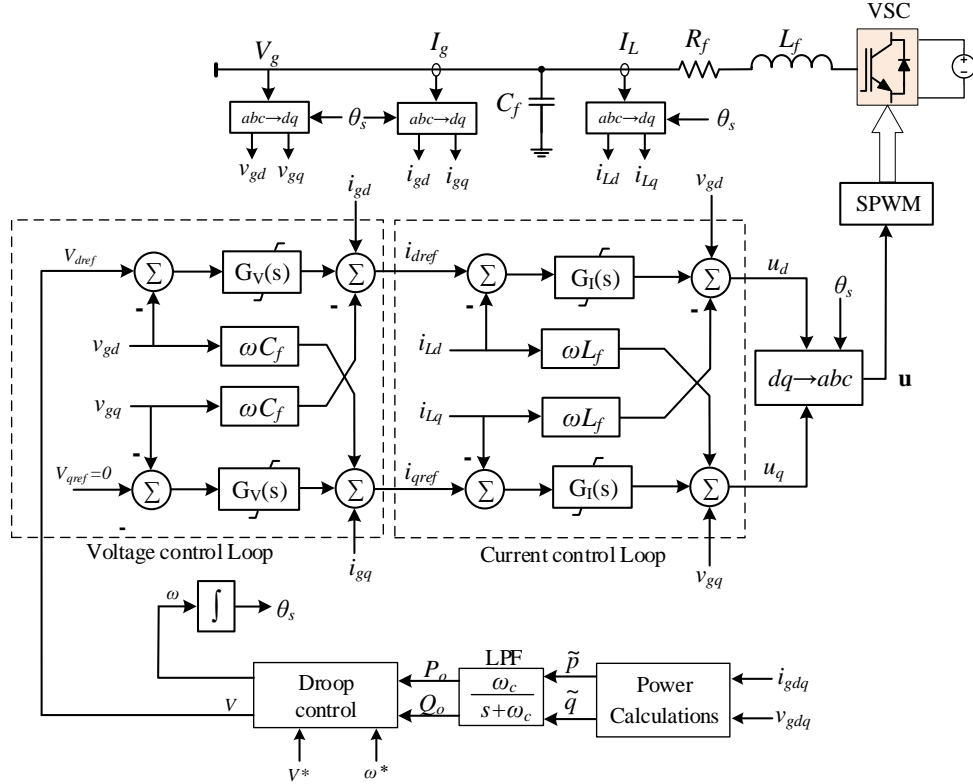


Figure 2.10 The control diagram of a grid forming VSC

Figure 2.10 shows a VSC control diagram in grid-forming mode implemented in the RRF. The VSC is modeled as an independent averaged ac source discussed earlier. The control has two inner loops of current and voltage control [20]. The voltage control loop generates current references using the droop calculations.  $G_I(s)$  and  $G_V(s)$  are PI controllers tuned based on the converter time response and output filter dynamics. The current loop's bandwidth is assumed to be faster than the voltage control loop by at least one decade in frequency response measure. In this way, it can be ensured that during the current loop transients the PI outputs in the voltage loop do not change significantly. The  $dq$  components of the measured voltage ( $V_g$ ) and currents ( $I_L, I_g$ ) are calculated using the Park transformation ( $abc \rightarrow dq$ ) in (2.10). Usually, low pass filters are used to suppress the switching harmonics from the measured signals which are neglected for simplicity. The current control loop has the following mathematical form:

$$\begin{aligned}
u_d &= k_{pI}(i_{dref} - i_{Ld}) + k_{iI} \int (i_{dref} - i_{Ld})dt + v_{gd} - \omega L i_{Lq} \\
u_q &= k_{pI}(i_{qref} - i_{Lq}) + k_{iI} \int (i_{qref} - i_{Lq})dt + v_{gq} + \omega L i_{Ld}
\end{aligned} \tag{2.18}$$

where  $i_{dref}$  and  $i_{qref}$  are the reference values of inductor  $dq$  current generated by the voltage control loop [see (2.21)] and  $k_{pI}$  and  $k_{iI}$  are the proportional and integral coefficients of the controller respectively. Feed-forward terms  $(v_{gdq}, \omega L i_{Ld}, -\omega L i_{Lq})$  are added to  $u_d$  and  $u_q$  to cancel the effect of  $V_g$  and  $I_L$  to decouple the  $d$  and  $q$  axes to be able to control two axes independently. However, perfect decoupling might not be practically achieved with these feed-forward terms in (2.18) due to the harmonics and measurement errors. Reference [34] provides a method based on multivariable-PI current control with a superior disturbance rejection approach to gain a fully decoupled control, specifically in an asymmetrical loads situation. Assuming fully decoupled, the equivalent model of the current control closed-loop takes the form shown in Figure 2.11.

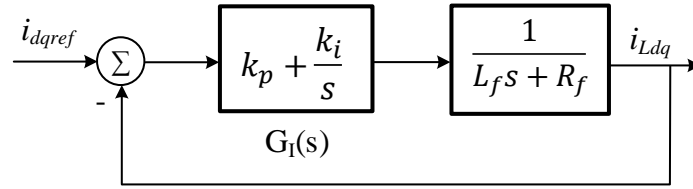


Figure 2.11 equivalent model of the current closed-loop

$k_{pI}$  and  $k_{iI}$  can be selected based on the desired response time  $\mathcal{T}$  of the converter in current loop.

We have [20]:

$$k_{pI} = \frac{L_f}{\mathcal{T}}, k_{iI} = \frac{R_f}{\mathcal{T}} \tag{2.19}$$

Then current control closed-loop acts as a first order low pass filter with the time constant  $\mathcal{T}$  i.e.:

$$i_{Ldq} = \frac{1}{\mathcal{T}s + 1} i_{dqref} \tag{2.20}$$

The voltage control loop has the following mathematical form:

$$\begin{aligned}
i_{dref} &= K(v_{dref} - v_{gd}) + K\sigma \int (v_{dref} - v_{gd})dt + i_{gd} - \omega C v_{gq} \\
i_{qref} &= K(v_{qref} - v_{gq}) + K\sigma \int (v_{qref} - v_{gq})dt + i_{gq} + \omega C v_{gd}
\end{aligned} \tag{2. 21}$$

where  $v_{dref}$  is generated by droop control and  $v_{qref} = 0$  corresponds to the fact that in steady-state the converter is driven to have  $v_{gq} = 0$ . Like the current control loop, the feed-forward terms are added to cancel the effect of grid/load dynamics and to achieve a decoupled  $d$  and  $q$  axes.  $K$  and  $K\sigma$  are the proportional and integral coefficients of the PI controller respectively. If  $\mathcal{T}$  is small enough, the current control can be considered as an inner loop with a high bandwidth whose transients do not have a significant impact on the outer loop (voltage control) over a wide range of frequencies. On the other hand,  $\mathcal{T}$  should be large enough that the bandwidth of the closed-loop system ( $\frac{1}{\mathcal{T}}$ ) is notably smaller (at least one decade) than the switching frequency ( $2\pi f_s$ ). Therefore, the combination of the inductor current and capacitor voltage loop represents two linear and independent systems with  $i_{dqref}$  as input control and  $v_{gdq}$  as output variables are shown in figure 2.12.

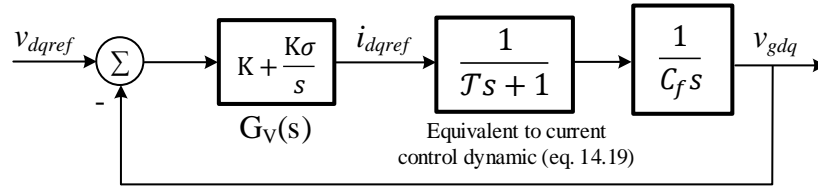


Figure 2.12 Simplified linearized system of VSC control equal to voltage and current loops

For such a system, that has two poles at origin (i.e.  $s = 0$ ) and one real pole ( $s = -1$ ) in its loop gain, control parameters of  $G_V(s)$  are determined based on the phase margin criteria [20] [35]. The loop gain in figure 2.12 has a double pole at origin and one real pole at  $s = -\frac{1}{\mathcal{T}}$ . The control objectives are based on the desired phase margin  $\rho_m$  that is kept in its maximum value at the frequency  $\omega_m$ . If the gain crossover frequency of the loop is chosen as  $\omega_m$ , then we have:

$$\rho_m = \arcsin\left(\frac{1 - \mathcal{T}\sigma}{1 + \mathcal{T}\sigma}\right)$$

$$\omega_m = \sqrt{\frac{\sigma}{\mathcal{T}}}$$
(2. 22)

Then the gain coefficient  $K$  must satisfy the unity gain of the loop at  $\omega_m$  it holds:

$$K = \omega_m C_f$$
(2. 23)

The phase margin is typically selected between  $30^\circ$  to  $75^\circ$ . In figure 2.10, the power calculation block computes the unfiltered active and reactive power components directly from  $dq$  voltage and current measurements:

$$\tilde{p} = \frac{3}{2} [v_{gd} i_{gd} + v_{gq} i_{gq}]$$

$$\tilde{q} = \frac{3}{2} [-v_{gd} i_{gq} + v_{gq} i_{gd}]$$
(2. 24)

In the steady state that the output tracks the references,  $v_{gq} = 0$  and the second terms of (2.24) converge to zero. Then the active and reactive powers will be proportional to  $i_{gd}$  and  $i_{gq}$  respectively. The low pass filter (LPF) block suppresses switching harmonics.  $\omega_c$  is the cut-off frequency of the filter that is selected one decade below the power frequency.

$$P_o = \frac{\omega_c}{s + \omega_c} \tilde{p}$$

$$Q_o = \frac{\omega_c}{s + \omega_c} \tilde{q}$$
(2. 25)

The grid forming VSC is suitable for DERs with controllable (or dispatchable) power sources like energy storage, fuel cells, conventional generators (AC or DC), or a combination of RES and energy storage in the islanded operation of AC subgrid. If several parallel DERs use grid forming VSCs with primary droop control, the values of grid voltage and frequency would have steady-state deviations from nominal ratings. Hence, the secondary control may restore the voltage and

frequency in the AC subgrid. There are several approaches to implement the secondary control based on the type of the architecture of the secondary layer hierarchy, i.e. the distributed or centralized considering various objectives [36][37][38][39]. As it was mentioned earlier, the centralized configuration collects the information from all DERs and communicates to the primary control of each DER to send corrective voltage and frequency signals. One approach is to measure the PCC voltage magnitude and frequency and propagate a common corrective signal to all DERs [21][40]. However, this configuration is only suitable for a grid of DERs with relatively equal ratings that share common loads located at the same bus as shown in figure 2.13. In addition, local loads will experience voltage magnitudes a little higher than the rated value. On the other hand, it is simple and does not rely on the configuration, and detailed model of the microgrid. The communication is relatively sparse and simple. Other approaches are based on the weighted sum of the voltage and frequency of all DERs [41] or to compensate the voltage magnitudes through accurate reactive power-sharing. However, these topologies demand extensive communication links compared to the previous one.

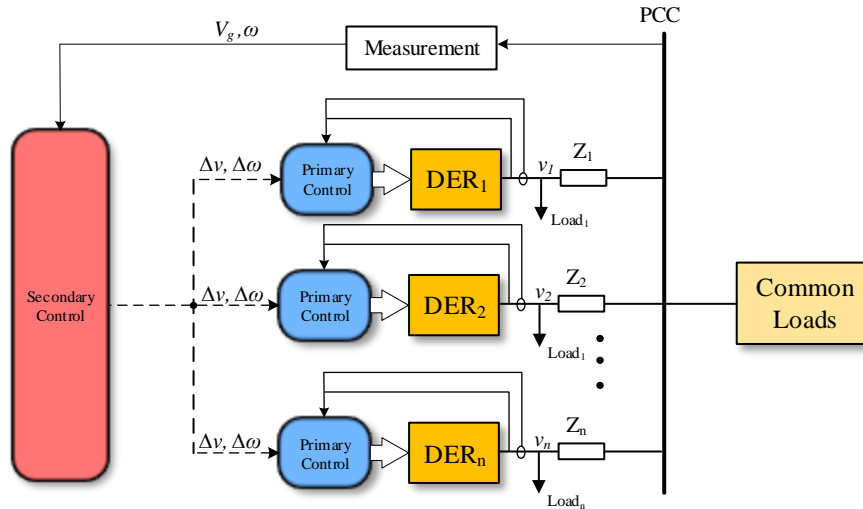


Figure 2.13 A droop-controlled AC microgrid equipped with centralized secondary control

The PCC voltage and frequency are compared with the reference values, and error signals are

passed through PI compensators. The PI controller is the most popular among the other types [42]. The output signals are sent to primary control of all DERs via low bandwidth communication medium in time intervals that are usually in the order of few milliseconds. Figure 2.14 shows a simple secondary control based on this topology.  $G_{sv}(s)$  and  $G_{sf}(s)$  are PI controllers and  $V_g^*$  and  $\omega^* = 2\pi f^*$  are the reference voltage magnitude and frequency of the system. A sampling unit can be a sample and hold circuit implemented either in discretized or analog space depending on the communication system type. Modern communication systems use discretized values. corrective signals have the mathematical form:

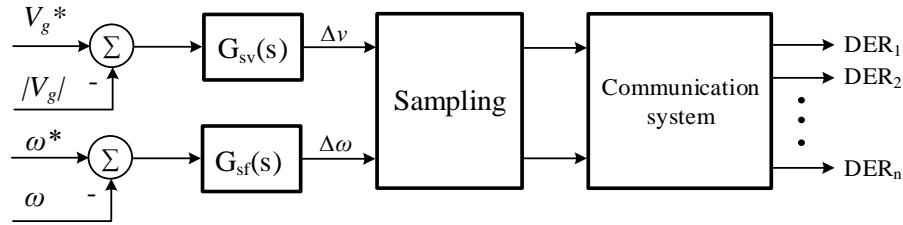


Figure 2.14 centralized secondary voltage and frequency control

$$\begin{aligned}\Delta\omega &= k_{sfp}(\omega^* - \omega) + k_{sfi} \int (\omega^* - \omega) \\ \Delta v &= k_{svp}(V_g^* - |V_g|) + k_{svi} \int (V_g^* - |V_g|)\end{aligned}\tag{2. 26}$$

where  $k_{sfp}$ ,  $k_{svp}$ ,  $k_{sfi}$  and  $k_{svi}$  are the proportional and integral gains of the PI controller. Then the droop control equations in (2.1) take the following form:

$$\begin{aligned}\omega_i &= \omega^* - m_i P_{oi} + \Delta\omega \\ V_i &= V^* - n_i Q_{oi} + \Delta v\end{aligned}\tag{2. 27}$$

Figure 2.15 shows the grid feeding VSC which has a similar current control loop to that of the grid forming VSC. The grid feeding mode is usually employed in the grid-connected operation of microgrids. However, if it is operated in islanded mode, there must be another grid forming device in the AC subgrid (such as a grid forming VSC or conventional synchronous generator-based

DER) to form the reference frame and control the voltage and frequency. The primary goal is to inject/absorb active and reactive setpoint powers, although it can be equipped with the reverse droop technique in islanded operation to support the AC subgrid during the grid voltage and frequency fluctuations as follows:

$$\begin{aligned} P_{ref} &= P^* - m_r(\omega - \omega^*) \\ Q_{ref} &= Q^* - n_r(V - V^*) \end{aligned} \quad (2.28)$$

where the superscript ‘\*’ represents the setpoint values and  $m_r$  and  $n_r$  are the reverse droop coefficients and are defined by:

$$\begin{aligned} m_r &\geq \frac{P_{max} - P_{min}}{\omega^*} \\ n_r &\geq \frac{V_{max} - V_{min}}{V^*} \end{aligned} \quad (2.29)$$

and the subscript *max* and *min* refer to maximum and minimum values of power rating of VSC and voltage range at the VSC output terminal. In the grid-connected mode of microgrid  $m_r = n_r = 0$ .

The grid feeding VSC is synchronized with the main grid (or AC subgrid) by the PLL [29]. The PLL has a park transformation block. It detects the phase angle  $\theta_s$  between the *abc* and *dq* system and smoothly drives  $v_q$  to zero to make  $v_d$  aligned with the *abc* reference through a feedback control system. figure 2.16 illustrates the standard structure of the PLL. The quality of PLL control is crucial for stable operation and accurate power delivery. The grid feeding VSC is suitable for constant power exchange by the grid in applications such as energy storage, RES with maximum power tracking (e.g. PV systems). If the PLL operates in the steady state,  $v_q = 0$  then the *dq* current references for grid feeding VSC are defined as below:

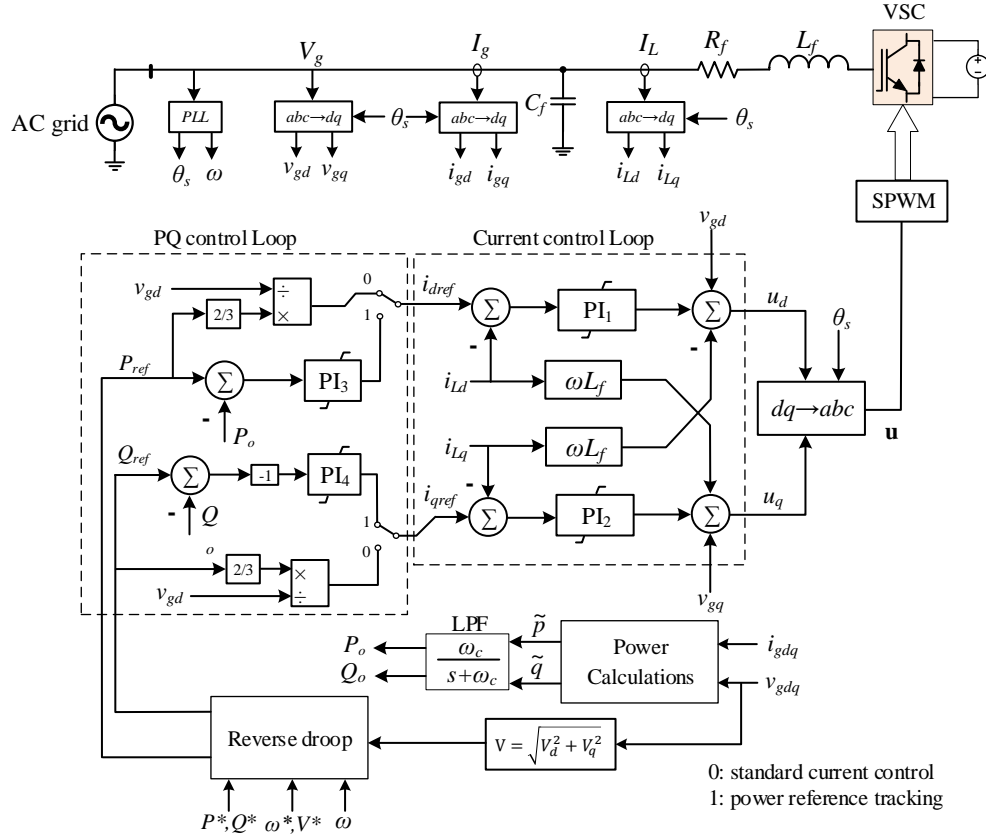


Figure 2.15 The control diagram of a grid feeding VSC

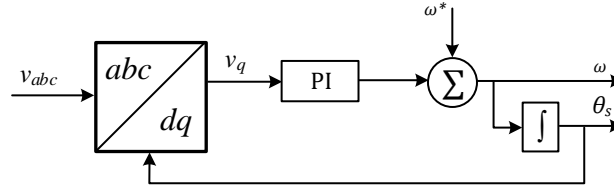


Figure 2.16 The standard structure of the PLL

$$i_{dref} = \frac{2 P_{ref}}{3 v_{gd}}$$

$$i_{qref} = -\frac{2 Q_{ref}}{3 v_{gd}}$$
(2. 30)

If the current control loop is fast enough, it is guaranteed that output active and reactive powers track  $P_{ref}$  and  $Q_{ref}$  independently. Alternatively, the  $dq$  current references can be generated using PI controllers. In this case, the error between the output powers and reference values is passed



through PI controllers. The current control loop must be fast enough to separate the transient operation of the current and power loops. Figure 2.15 depicts both schemes. The current control loop modeling and controller design are already presented earlier. The mathematical modeling of the PQ control loop will lead to nonlinear dynamics as active/reactive powers are the product of voltages and currents. Therefore, the best method to determine the PQ loop PI gains is to tune the parameters by the standard method of tuning PI parameters.

The grid feeding mode can be modified to form a VSC for controlling the DC side terminal voltage. This control mode is suitable for ILC converter and combined operation of DC RES and energy storage. Since the active power exchange between DC and AC subgrid is proportional to DC subgrid voltage, the  $d$  axis in the VSC decoupled control can perform the DC voltage reference tracking. Figure 2.17 shows the  $d$  axis reference current generating block diagram for a VSC with a DC voltage control scheme in which  $V_{dc}$  and  $V_{dc\text{ref}}$  represent DC subgrid (or DC-link) voltage and its reference value, respectively. The  $q$  axis can still track the reference reactive power or be set to zero to maximize the active power capacity of the VSC and to operate at unity power factor, depending on the application.

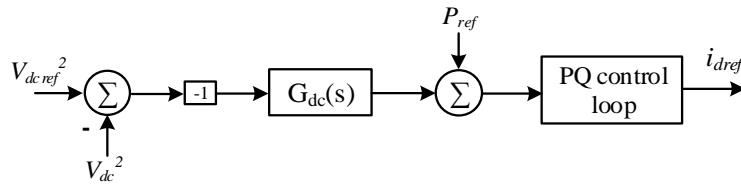


Figure 2.17  $d$  axis reference current generating in DC-link voltage control scheme

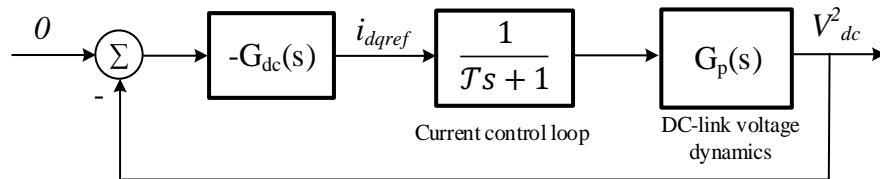


Figure 2.18 an equivalent linearized model of the DC-link voltage control dynamics

Figure 2.18 shows the equivalent linearized model of the DC-link voltage control dynamics.  $G_{dc}(s)$  is the DC-link voltage controller and  $G_p(s)$  represents the DC-link voltage dynamics as follows [20]:

$$G_p(s) = -\frac{2}{C_f} \frac{\frac{2L_f P_{ref0}}{3V_{gd}^2} s + 1}{s} \quad (2.31)$$

where  $P_{ref0}$  and  $V_{gd}$  are the steady-state values of active power flow reference and  $d$ -axis component of the grid voltage in the AC side which is equal to the magnitude of the AC voltage since in steady-state  $V_{gq} = 0$ . Note that VSC does not control the AC side voltage.  $G_{dc}(s)$  is, in general, a lead-integral type controller for the stability of the full-scale operation. However, a PI controller can also be implemented that works fine for a wide range of operating conditions. Reference [20] conducts a detailed design of the controller based on the phase margin criteria.

### 2.3.1.2 DC-DC converter control schemes

As described earlier, the DC-DC converters are employed in DC subgrid to control the voltage and power in DC DERs and certain loads. Here, we briefly discuss a conventional dual loop current/voltage control scheme based on PI compensators, that is widely used for different types. Also, the single loop current (power) control scheme is presented. The transfer functions of DC-DC converters are obtained using averaging approximation techniques over one switching period. References [43] and [44] provide detail of the converter transfer functions and different types of controllers for various applications. Buck and boost converters are two basic unidirectional topologies that are widely used in microgrid applications. The half-bridge bidirectional type is also composed of two buck and boost converters [see figure 2.4]. The averaging approximation results in a two-input two-output small-signal model of the converter represented by the following system of transfer function equations in the  $s$ -domain applicable to both buck and boost topologies:

$$\begin{bmatrix} e_2(s) \\ i_L(s) \end{bmatrix} = \begin{bmatrix} G_{11} & G_{12} \\ G_{21} & G_{22} \end{bmatrix} \begin{bmatrix} d(s) \\ e_1(s) \end{bmatrix} \quad (2.32)$$

where  $e_1(s)$  and  $e_2(s)$  are input and output voltage variables respectively,  $i_L(s)$  and  $d(t)$  are the inductor current and duty ratio. The duty ratio  $d(s)$  and converter input voltage  $e_1(s)$  are the independent input controls in a general form. However, here the input voltage is assumed to be constant during converter operation, hence the duty ratio is the only control input.  $G_{11} - G_{22}$  are converter small-signal transfer functions that are briefly discussed here.

$G_{11}$  and  $G_{21}$  are respectively duty-to-output voltage and duty-to-inductor current transfer functions.  $G_{12}$  and  $G_{22}$  are transfer functions of input voltage to, respectively, output voltage and inductor current that feed-forward  $e_1(t)$ , as a disturbance, to the output variable. However, they are neglected here, since  $e_1(t)$  is assumed to be constant. For the boost converter we have:

$$G_{11} = \left. \frac{e_2(s)}{d(s)} \right|_{e_1=0} = \alpha_0 \frac{\alpha_1 s^2 + \alpha_2 s + \alpha_3}{\alpha_4 \alpha_5 s^2 + \alpha_4 \alpha_6 s + \alpha_4^2} \quad (2.33)$$

$$G_{21} = \left. \frac{i_L(s)}{d(s)} \right|_{e_1=0} = \alpha_7 \frac{C(R_l + r_c)s + 1}{\alpha_4 \alpha_5 s^2 + \alpha_4 \alpha_6 s + \alpha_4^2} \quad (2.34)$$

where:

$$\begin{aligned} \alpha_0 &= -R_l E_1 (R_l + r_c), \quad \alpha_1 = LC r_c (R_l + r_c), \\ \alpha_2 &= C r_L r_c^2 (1 + D') + [C R_l (r_L D' - R_l D'^2 + r_L) - C r_L D' + L] r_c + L R_l \\ \alpha_3 &= (R_l - D' + r_c + R_l D' + r_c D') r_L - R_l^2 D'^2, \quad \alpha_4 = R_l D' (R_l D' + r_c) + r_L (R_l + r_c) \\ \alpha_5 &= LC (R_l + r_c)^2, \quad \alpha_6 = [L + C (R_l r_L + r_c r_L + R_l D' r_c)] (R_l + r_c) \\ \alpha_7 &= E_1 (R_l + r_c) [(1 - r_c - R_l) r_L + r_c R_l + D' R_l^2] \end{aligned} \quad (2.35)$$

where  $D = 1 - D' \in [0..1]$  and  $E_1$  are the DC value of duty ratio and the input voltage  $e_1$  in the steady-state operation.  $C$ ,  $L$ ,  $r_c$  and  $r_L$  are respectively the output capacitor, inductor, and their equivalent series resistance (ESR).  $R_l$  is the equivalent converter load resistance connected to the output terminal. The ESR of the power switch and diode are neglected for simplicity. In boost

converter  $V_L$  is the input and  $V_H$  is the output voltage. The voltage gain ratio of the boost converter is given as:

$$M_{boost} = \frac{V_H}{V_L} = \frac{1}{1-D} \quad (2.36)$$

which indicates that  $1 < M_{boost} < \infty$ . In practice  $D_{min} < D < D_{max}$  to protect the converter against overcurrent and overvoltage. For a buck converter we have:

$$G_{11} = \frac{e_2(s)}{d(s)} \Big|_{e_1=0} = \beta_0 \frac{s + \frac{1}{Cr_c}}{s^2 + \beta_1 s + \beta_2} \quad (2.37)$$

$$G_{21} = \frac{i_L(s)}{d(s)} \Big|_{e_1=0} = \frac{E_1}{L} \frac{s + \beta_3}{s^2 + \beta_1 s + \beta_2} \quad (2.38)$$

$$\beta_0 = \frac{E_1 R_l r_c}{L(R_l + r_c)}, \beta_1 = \frac{L + C(R_l r_L + r_L r_c + R_l r_c)}{LC(R + r_c)}, \beta_2 = \frac{(R + r_L)}{LC(R + r_c)}, \beta_3 = \frac{1}{C(R_l + r_c)} \quad (2.39)$$

In buck converter  $V_H$  is the input and  $V_L$  is the output voltage. The voltage gain ratio of the buck converter is given as:

$$M_{buck} = \frac{V_L}{V_H} = D_{buck} \quad (2.40)$$

which indicates that  $0 < M_{buck} < 1$ . In practice  $D_{min} < D_{buck} < D_{max}$  to protect the converter against overcurrent and overvoltage.

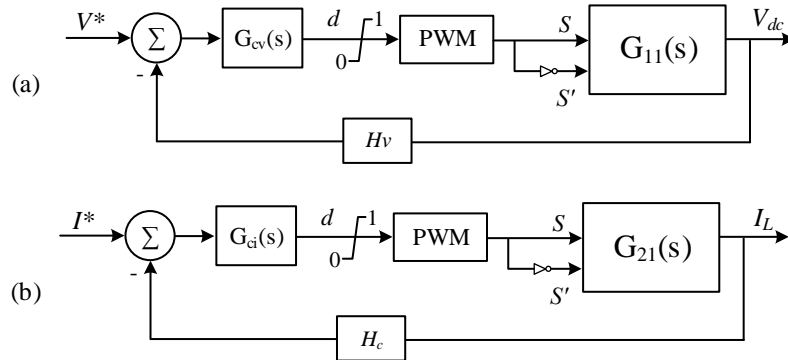


Figure 2.19 plant model of the DC-DC converter control schemes; (a) voltage control, (b) current control

The transfer functions are used to design the controllers for the different applications. Figure 2.19 shows the plant model of the single loop current and voltage control schemes applicable to the DC-DC converters depicted in Figure 2.4.  $I_L$  is the inductor current,  $d$  is the duty ratio,  $S$  and  $S'$  are the switching pulses applied to power electronic switching devices in the case of the bidirectional converter. If a unidirectional (buck or boost) converter is used  $S'$  is terminated.  $G_{cv}(s)$  and  $G_{ci}(s)$  are the compensators and  $H_v$  and  $H_c$  are feedback sensor transfer functions, respectively that are usually combined with an LPF to suppress the switching harmonics.  $V^*$  and  $I^*$  are voltage and current reference values. Power reference determines the current setpoint  $I^*$ :

$$I^* = \frac{P_{ref}}{V_{in}} \quad (2.41)$$

where  $P_{ref}$  is the reference power and  $V_{in}$  and  $V_{dc}$  are, respectively, the input and output voltages of the converter in boost, buck, or bidirectional operation. PI (or lag type) controllers are widely used for  $G_{cv}(s)$  and  $G_{ci}(s)$  implementation due to the large disturbance rejection. Although the PI controller relatively reduces converter response (hence its bandwidth), it reduces the switching noise in the feedback signal. Reference [44] provides a theoretical and practical basis to design controllers for DC-DC converters. The current control scheme is suitable for constant power control in energy storage applications, while the voltage control is used to control the DC bus voltage where no other devices are used to do so (like ILC).

Unidirectional converters are usually used for power conversion from primary energy sources like solar PV, fuel cell in DC, or hybrid microgrids. While, as mentioned earlier, BDC connects the energy storage to the grid. Figure 2.20 shows a dual-loop current/voltage control which is a commonly used scheme for BDC applications.  $G_v$  and  $G_c$  are designed such that the overall dynamic of the current loop is faster than the voltage loop. Hence, the bandwidth of the voltage

control loop is placed at least one decade below the current control loop. Then it can be guaranteed that  $I_L$  tracks the reference  $I_{L_{ref}}$  during the voltage transients.  $G_v$  and  $G_c$  are usually, PI controllers.  $R_v$  is the virtual resistance described earlier and  $H_v$  is the voltage feedback sensor's transfer function which is usually combined with an LPF to suppress the switching harmonics.  $V_{dc}$  and  $V_{dc}^*$  are the converter output voltage and its reference value.

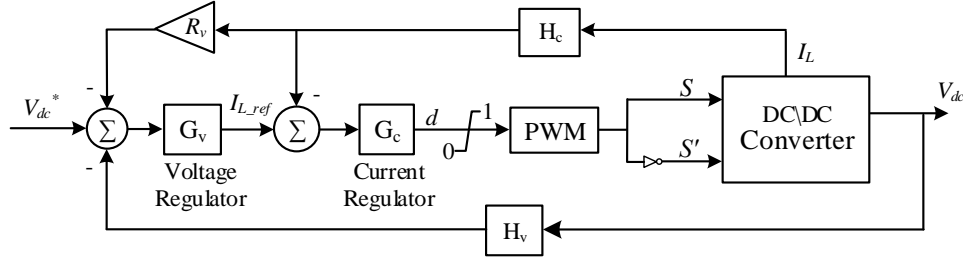


Figure 2.20 DC-DC converter dual-loop control

### 2.3.1.3 Interlinking Converter

ILC is the power bridge between AC and DC subgrids. It has a key role in maintaining the HMG's stability and power balance between AC and DC subgrid. The ILC is a VSC-based converter with a specific control strategy. Its control strategy depends on the control objectives in subgrids. If there exist DERs running in voltage control (or voltage source) mode like energy storage devices, synchronous machine-based generators (e.g., diesel, microturbines, etc.), and fuel cells with dispatchable primary sources in both subgrids, then the reference power of ILC aligned with  $d$  axis (in  $dq$  frame control) can be controlled by a normalized droop control technique to simultaneously control the frequency of the AC subgrid and DC voltage of the DC subgrid [45] [46][47]:

$$V_{dc_{pu}} = \frac{V_{dc} - 0.5(V_{dc}^{max} + V_{dc}^{min})}{0.5(V_{dc}^{max} - V_{dc}^{min})} \quad (2.42)$$

$$f_{ac_{pu}} = \frac{V_{dc} - 0.5(V_{dc}^{max} + V_{dc}^{min})}{0.5(V_{dc}^{max} - V_{dc}^{min})} \quad (2.43)$$

The error and its sign between normalized AC grid frequency and DC grid voltage define the amount of power that should be transferred between subgrids to make a power balance:

$$P_{ILC}^{ref} = K_{ILC} (V_{dc_{pu}} - f_{ac_{pu}}) \quad (2.44)$$

where  $K_{ILC}$  is the droop coefficient of ILC active power,  $V_{dc_{pu}}$  and  $f_{ac_{pu}}$  are normalized values of DC subgrid voltage and AC subgrid frequency, respectively. the *max* and *min* values refer to maximum and minimum allowable voltage and frequency. However, if there is no voltage source in any of the subgrids, the control strategy of ILC will be altered to a regular VSC. For instance, if there is no voltage source at the DC subgrid, the ILC will be a grid feeding VSC to control DC subgrid voltage (as the main function), shown in figure 2.17. It can also support the AC grid by reactive current control. Likewise, if the AC subgrid lacks the voltage source, the ILC performs as a grid forming VSC, working as a voltage source for the AC subgrid, shown in figure 2.10.

## 2.4 Fault Ride Through Capability of HMGs

Unlike the conventional electric power grids, which were mainly established for centralized utilization of fossil fuel energy resources, the microgrids are developed to decentralize the electric power generation through the DERs, especially from renewable energy sources [4][45]. The FRT capability is not trivial in isolated microgrids integrating various DERs. Grid codes emphasize that the DERs should remain connected during the temporary faults to deliver active and reactive powers [40]. According to these requirements, DERs must compensate reactive power to support grid voltage during a fault [48]. However, currently, there is not a unique code requirement issued for autonomous microgrids. Thus, the FRT requirements should be considered rigorously. Because of high penetration of renewable energies in microgrids, the voltage support and frequency stability

services should be provided by the fast response inverter-interfaced DERs such as ESS, ILCs, etc.

Different FRT schemes have been proposed and analyzed in the literature. However, only a few research studied the FRT issues related to HMGs. Authors in [49] and [50] investigated the FRT capability of HGM during faults in AC and DC sub-grids by employing additional droop controls in the DER and ILC inverter control loops. Nevertheless, insignificant improvement in AC sub-grid voltage was observed. In [40], a negative sequence droop control is proposed to inject negative sequence power in DERs to improve the LVRT. In addition, current limiting devices like the Superconducting Fault Current Limiter (SFCL) [51] have been proposed to enhance FRT capability in microgrids.

Many studies have dealt with the FRT improvement in the case of individually grid-connected Wind Turbines Generator (WTG) system only. A Modulated Series Dynamic Braking Resistor (MSDBR) along with a reference voltage calculation methodology is proposed in [52], however, it does not consider the current magnitude rise in fault detection algorithm. Several strategies based on the Bridge Type Fault Current Limiter (BFCL) have been proposed in [48], [53], [54] for the FRT capability improvement in WTGs. The work in [55] proposes efficient current limiting strategies to be employed in inverter-control systems to limit the inverter output current during grid faults. Authors in [56] proposed an add-on voltage controller which works based on symmetrical sequence components of inverter terminal voltage and current to adjust inverter voltage reference signal during fault.

So far, a few studies have investigated current limiting schemes to employ outgoing feeders to improve the entire HMG FRT performance. In fact, in such an HMG, a combination of current-limiting devices and voltage control is required to effectively suppress the fault current along with a reactive current compensation to recover the entire microgrid voltage. A FRT capability scheme



is proposed in chapter 3 in which a modulated series breaking resistor in coordination with reactive current control in ILC is utilized that controls the fault currents and improves the FRT capability of HMG.

## **2.5 Disturbance Resiliency of HMGs**

The low-voltage-ride-through (LVRT) capability and resiliency against grid disturbances are significant issues in islanded microgrids where high penetration of RES with various dynamic properties are introduced. The requirements of grid codes mandate that DERs must compensate reactive power to support grid voltage during a significant disruption [14]. The IEEE 1547-2018 standard obligates DER to modulate active power in proportion to the rate of change of frequency (ROCOF) [57].

Several studies have been conducted on the LVRT and disturbance resilience issues related to microgrids, and different schemes have been proposed and analyzed. Baghaee *et al* proposed a robust decentralized voltage control in [58] to improve small/large-signal stability in the islanded microgrid. A negative sequence droop control methodology is proposed in [40], to inject negative sequence power in DERs to improve the LVRT performance. Furthermore, fault current limiting devices like the Superconducting Fault Current Limiter (SFCL) [51] have been proposed to enhance the LVRT capability in microgrids. The authors in [50] evaluated the LVRT capability of HGM during separate faults in AC sub-grid (ACg) and DC sub-grids (DCg) using additional droop controls in the DER and ILC loops. A coordinated control strategy between ILC and MSDBR was reported in [14] to efficiently improve the LVRT capability of HMG under high penetration of RES during ACg faults. Nevertheless, none of these studies considered energy storage tuning to tackle the grid disturbances.

Power management and dynamic control of HMGs with a specific focus on stability issues

and voltage/frequency regulation have been studied in previous literature. The work in [59] provides a systematic small-signal stability analysis of islanded HMG and proposes a synthetic droop-based control approach to coordinate ACg and DCg through ILC control. The authors in [60] proposed a decentralized power management mechanism for an HMG with multiple subgrids having different rated voltages and frequencies. Research studies in [61] and [62] concentrated on single and multiple ILC control strategies to establish improved power-sharing and frequency controllability in HMGs. Nevertheless, these studies consider only general inverter-interfaced DERs with constant DC voltage sources as primary generation resources and no significant RES penetrations are considered. Furthermore, an effective and realistic energy storage device is not examined in these studies.

Due to the high penetration level of renewable energy resources in microgrids, the voltage support and frequency regulation services may be provided by the fast-response inverter-interfaced DERs such as energy storage systems, ILCs, etc. They can be effectively employed to provide frequency regulation and power oscillation damping during and after grid disturbances. Chapter 3 investigates a coordinated control of BESS and reactive current control of wind turbines to increase the resiliency of HMG against grid disruptions.

## **2.6 A Survey on Conventional Bidirectional DC-DC Converter**

In an HMG, the DC side BESS is connected to the grid through a BDC to control grid voltage or power. The converter is driven to exchange energy between the battery bank and grid to control grid voltage or power mismatches due to power under/oversupply. The conventional BDC frequently used in the literature for energy storage applications [63][64][65][66] is composed of a half-bridge converter and works as a separate Buck converter in step-down mode and Boost converter in step-up mode, with two controllable semiconductor switches. Figure 2.4(c) shows the

conventional, non-isolated BDC with some drawbacks, as noted below:

(i) Usually, one controller is used to control the converter in both modes, whereas two converters (Buck and Boost) exhibit two distinctive characteristics that cannot be controlled with one controller, since the controller usually designed based on one converter structure to operate in one mode cannot properly handle grid voltage and load disturbances in both modes.

(ii) The bidirectional operation does not have symmetrical voltage gain. This asymmetry originates from the different circuit structures in both modes. Therefore, the converter should work with different duty ratios in both modes, resulting in an asymmetric and relatively slow control response during power flow direction changeover. This issue is addressed to some extent by selecting a small enough battery voltage compared to the grid voltage, resulting in a high voltage difference between the two sides; otherwise, the Buck operation would not be as effective. However, this potential difference results in high current peaks in both switching operations, leading to high current ripples, particularly in heavy load levels. This issue is usually tackled by selecting a large inductor, thereby incurring a higher capital cost.

(iii) Both step-up and step-down switches are simultaneously modulated in both modes, resulting in increased converter switching losses that restrict the converter to low power density levels.

Other issues regarding conventional BDC are reported in the literature [67][68] from different viewpoints, although this chapter does not aim to address them. Previous studies proposed several isolated and non-isolated bidirectional topologies to improve the dynamic performance, gain, efficiency, and operability of BDCs for energy storage and renewable applications.

Resonant converters were of interest in some previous research as they provide the possibility

of zero-current/voltage soft-switching operation. Non-isolated, resonant-type, bidirectional converters were proposed to increase the overall voltage gain using coupled inductors and clamping capacitor circuits operating in zero-voltage-switching (ZVS) conditions [69][70]. An isolated, three-port, inductor-capacitor-inductor (LCL)-resonant converter operating in zero-current-switching (ZCS) condition was also implemented in [71] with the capability of integrating photovoltaic (PV) source to energy storage. However, these resonant converters add complexity and cost to both power and control stages and incur more loss due to additional circuit components. In addition, no control strategies were presented that symmetrically worked for both modes in bidirectional applications.

A relatively high voltage gain was achieved for step-down operation using a switched-capacitor cell augmented to a conventional half-bridge [72]. However, this configuration was an improved version of the half-bridge converter, making only a slight improvement only in voltage gain at the cost of additional components with a control design working asymmetrically for both modes. The non-isolated converter in [67] and its improved high-efficiency topology in [73] provided soft-switching operation, employing a 1:1 ideal transformer and pulse-frequency modulation to accommodate load variation and reduced switching loss, and achieve high efficiency. The implemented digital controller used a single loop Proportional-Integral (PI) controller that worked for both modes, with applications in residential energy storage systems.

Research work in [74] proposed a non-isolated BDC employing two conventional Boost converters to achieve the squared value of voltage gain of that of the conventional BDC. Although functional improvements in voltage gain, switching operation, and converter efficiency were obtained in the mentioned literature, the problem of bidirectional asymmetry in voltage gain and control scheme persists. Furthermore, no validating evaluations were conducted for bidirectional

applications under the load/generation uncertainties and DC bus voltage variations. Chapter 4 proposes a novel bidirectional DC-DC converter that has symmetric configuration and eliminates drawbacks of the conventional converter.

## **2.7 Energy Storage Location in HMGs**

There are several objectives to select the energy storage location and size in microgrid applications, and state-of-the-art algorithms have been proposed [75]. Thus far, many studies have researched in these contexts regarding BESS type. The objectives range from optimal power flow [76]-[77], capital cost [78], operation cost [79], power quality [80] and decarbonization objectives [81] to energy loss reduction [82],[83] and grid control objectives [84]. However, none of the mentioned works studied the microgrid's dynamic performance under the influence of the BESS location, specifically of HMGs operating with AC grid BESS (ACB) or DC grid BESS (DCB). In fact, the current research in the literature pays attention to the long-term operation of BESS circumventing transient operation optimality for the siting study [79].

The ILC in HMGs plays a substantial role in the power flow balance between ACg and DCg. In most of the cases found in the literature, the ILC active power reference is generated pursuant to various objectives. When voltage sources exist in both subgrids, e.g., energy storage devices running in voltage control mode a normalized droop-control method fulfills the primary service to simultaneously control the ACg frequency and DCg voltage [60]. In this method, the ILC power reference is generated based on the sign and magnitude of the error between normalized ACg frequency and DCg voltage applying a droop gain that can be used in a single ILC [85] or utilized locally for global active power-sharing between parallel ILCs [86] and reactive power sharing between ACg and DCg [39]. Any mismatch between normalized variables drives the ILC to exchange active power from the higher magnitude variable to the lower magnitude one.

However, the control strategy of ILC alters if there is no voltage source in either of the sub-grids. If the ILC runs in the grid feeding mode (like a grid-connected ILC) and no other sources control the DC bus voltage, it controls the DCg voltage at the connecting bus [87] which is the conventional active power control method in high-voltage DC (HVDC) systems [88]. Likewise, if the DCg voltage is controlled by an energy source and there is no voltage source in ACg at the connecting bus, the ILC performs as a grid forming converter [46] to controls the voltage and frequency. Recently, a multifunctional ILC was proposed that works in both grid-forming and grid-feeding control mode employing a large bandwidth triple-loop controller which is capable of transitioning between grid-connected and islanded operation [89]. However, none of the recently mentioned literature considered energy storage devices and their dynamic models in their studies.

The real-world microgrids include the RESs that usually operate in maximum power point tracking (MPPT) mode through grid-feeding converters. They are typically collocated with grid-forming DERs such as BESS, fuel cells, and diesel generators (DG) that have a dispatchable primary source. However, the existing control methodologies and example cases found in literature neglect the cooperation of these DERs. As a rare example, coordinated control of current-controlled and voltage-controlled inverters was proposed to share the reactive power and to regulate voltage harmonics [90]. Nevertheless, it is only applied to AC microgrids with low inertia generating sources.

Despite the considerable number of studies conducted on HMGs, to the best of the authors' knowledge, no single research paid attention to or compared the influence of BESS location in ACg and DCg pursuing the dynamic performance characteristics during grid contingencies. In practical HMGs with centralized BESS, the optimal storage location and size should be determined by the economic objectives and its dynamic impact. In small/medium-sized HMGs with

aggregated load/generation nodes, a consolidated BESS may be linked to the point of common coupling (PCC) of AC or DC subgrid, or to the critical load bus to supply energy storage services to the whole HMG. For a typical HMG design including the BESS devices at ACg and DCg [91][14], the grid operators might be concerned to realize the impact of storage location on the performance of the grid operating with only one storage device online. In this context, when running with ACB or DCB, the HMG exhibits dissimilar dynamic performance during different operating conditions and disturbances due to the storage location and the ILC control strategy that differs correspondingly. Consequently, a substantial analysis is required to examine the effect of storage location and corresponding ILC control strategy on the HMG dynamics. Chapter 5 conducts a performance evaluation of the impact of BESS location for two separate HMG case studies through comprehensive time-domain simulations and index-based performance.

## **2.8 Evaluation of PV Operating as PV-Supercapacitor Energy Storage**

Among RESs, the PV system has been considered to be the most promising due to its inherent features such as no presence of moving parts, low maintenance and operation cost, etc. [92][93]. Typically, a grid-connected photovoltaic (PV) system consists of a PV array/panel, a DC-DC boost converter with an MPPT controller, a DC-link capacitor, a battery energy storage (BES) system, and a DC/AC inverter, as shown in Figure 2.21 below. Since at night or on a cloudy day, the PV panel does not produce any real power, the BES provides power to the grid at that time. In recent years, due to its cost-effectiveness, supercapacitor energy storage (SES) has been extensively used for dynamic performance enhancement of power grids [94][95]. The SES can control both active and reactive powers quickly and simultaneously. Literature shows the applications of the SES system with the PV system as well [96][97][98]. The SES unit encompasses a supercapacitor, a bidirectional DC-DC converter (BDC), a DC-link capacitor, and a VSC, as shown in Figure 2.22.

However, a close similarity is found between the PV system and the SES unit in terms of their components. Except for the PV panel, MPPT controller, the BES, and the supercapacitor, both systems have the same type and number of components.

Based on this fact, it is interesting to explore whether the existing PV system components can be utilized as an SES unit during both nighttime and daytime and cloudy situations. It will be great if the PV-SES unit can be used for dynamic performance improvement including power fluctuations minimization, transient stability, power quality, power oscillation damping, increasing power transmission capacity of the grid-connected network that may have other DERs such as wind generator, diesel generator, etc., and various flexible loads.

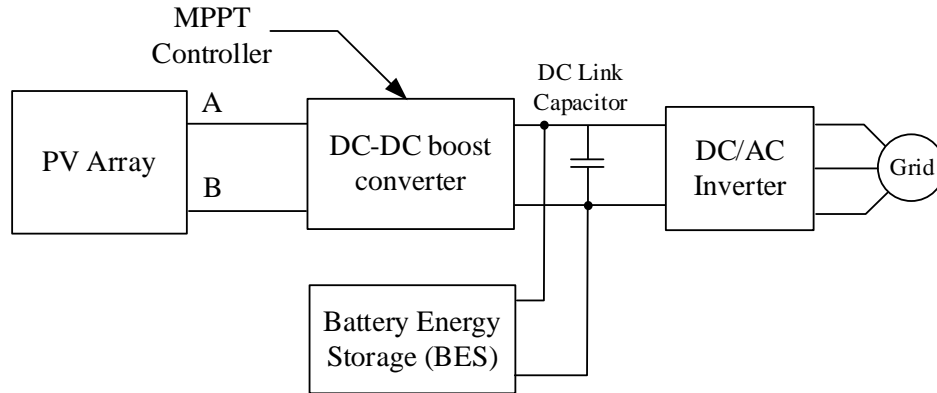


Figure 2.21 Basic schematic of the PV system with BES

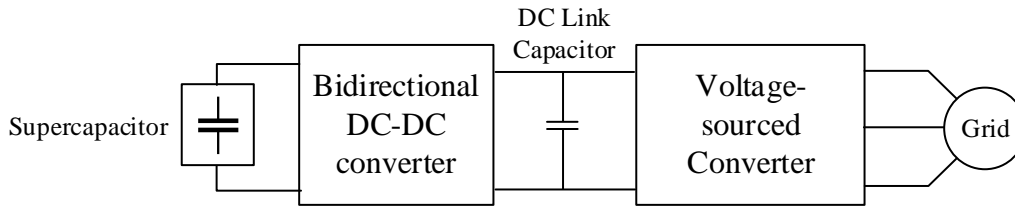


Figure 2.22 Supercapacitor energy storage unit.

Currently, the LVRT capability of the PV system is maintained by the reactive power control of the inverter [99][100][101]. Also, various MPPT techniques are being developed considering the partial shading of the PV panel [102][103]. The BES is used to compensate for power fluctuations



of the PV system [104]. However, there are significant shortcomings, limitations, and challenges of the existing PV system technology and controls, such as i) the basic PV system operation is limited to daytime use only; ii) the inverter can control only reactive power, but not the active power, since the operation is unidirectional, and the system is limited to inject the PV power at any time. This means the inverter can have a limited control on the grid voltage, but not the real power or the frequency; and iii) the BES can control high energy density power fluctuations, but not the high power density fluctuations. To address the aforementioned limitations and issues, chapter 6 proposes to design and operate a cost-effective PV-SES that integrates supercapacitor as a high power energy storage system.

## **2.9 Chapter Conclusion**

This chapter provided a thorough literature review on microgrid and HMG basic control techniques, control hierarchies, and structures. In addition, solid background of structures and controllers of widely used converters in microgrids was discussed. In the next chapters the main parts of the research are presented, where a more specific and detailed explanation of each study will be elaborated.

## **Chapter 3 Disturbance Resiliency and Fault Ride Through Capability of Hybrid Microgrids**

### **3.1 Introduction**

Due to the small generation reserve margin between load and generation, the stability and service continuity in islanded hybrid microgrids are easily compromised during grid disruptions and stochastic load/generation variations. The issue is more challenging when the HMG encompasses various DERs exhibiting diverse dynamic properties such as high/low inertia renewable energies, conventional generation sources, and frequency-dependent and non-linear loads. So, it is important to damp the system oscillations as fast as possible to maintain the stability and ride through the faults by supplying reactive power to keep the service continuity. This chapter evaluates the fault ride-through capability and disturbance resiliency enhancement of hybrid microgrids by coordinated control of different devices such as SDBR, ILC, and BESS.

### **3.2 Fault ride through evaluation of the Hybrid AC/DC Microgrids [14]**

Based on the background provided in section 2.4 of chapter 2, this section proposes coordination of Modulated SDBR (MSDBR) control and reactive current control in ILC for the FRT capability enhancement of an HMG. A fault detection logic is proposed based on the current rise rate and positive sequence voltage sag level. Independently switched three-phase MSDBR controls the current magnitude to keep the HMG stable. Also, a supplementary voltage control loop in ILC is activated to recover the voltage sag and swells during the fault. To demonstrate the effectiveness of the proposed strategy, both symmetrical and asymmetrical faults are considered on the line connecting the load in the AC sub-grid.

### 3.2.1 HMG Structure and Control systems for FRT Evaluation

The configuration of the islanded HMG under the study is shown in Figure 3.1. The Medium Voltage (MV) AC sub-grid power system contains a Doubly Fed Induction Generator (DFIG) based variable speed wind generator. A Diesel Generator (DG) is connected in parallel with the DFIG to provide steady-state reactive power service and backup power on-grid demand. The wind-diesel generation system is collocated with a BESS to provide peak shaving service during wind speed fluctuations. The constant AC loads are connected via short distribution lines. The DC sub-grid comprises Photovoltaic (PV) solar panels, a peak shaving BESS for mitigating solar irradiance fluctuations, and constant DC loads. The complete system parameters are given in the chapter appendix.

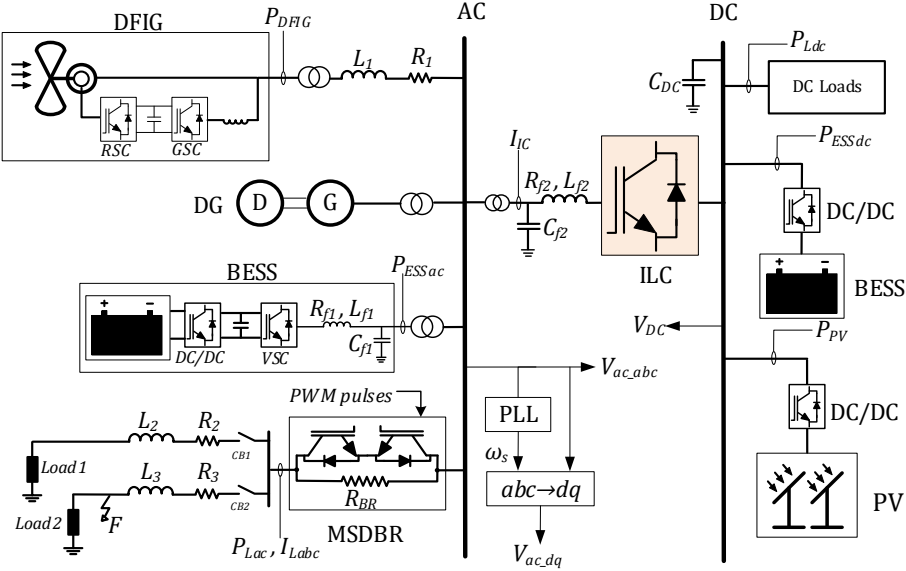


Figure 3.1 Hybrid AC/DC Microgrid structure under the study.

#### A. DFIG

The DFIG model in this work is a widely used model introduced in publications [48][54][105] with complete detailed modeling of Rotor Side Converter (RSC) and Grid Side Converter (GSC). The DFIG reactive power generation has been set to zero, and no DC chopper and crowbar are

used.

### B. PV

The PV model used is a generic model with an ideal single diode and equivalent circuit of parallel and series resistance [106]. A DC/DC boost converter and Perturb & Observe (P&O) based Maximum Power Point Tracking (MPPT) algorithm is integrated to extract the highest possible power in different ambient conditions and PV output voltages.

### C. BESS

Battery storage devices are based on the dynamic models introduced in [107], [108]. The battery flow of power is controlled using a buck/boost converter in both AC and DC sub-grids. A VCS-based two-level inverter is used to connect the storage system to the AC sub-grid. The VSC control includes a dual loop decoupled control system in  $dq$  synchronous reference frame [20]. The reference power set points are calculated based on load powers and power generation from renewable resources, as shown below.

$$P_{ESSac} = P_{Lac} - P_{DFIG} - P_{DG} \quad (3.1)$$

$$P_{ESSdc} = P_{Ldc} - P_{PV} \quad (3.2)$$

where  $P_{ESSac}$  and  $P_{ESSdc}$  are power references of AC and DC BESS, respectively.  $P_{Lac}$  and  $P_{Ldc}$  are AC and DC load powers, respectively.  $P_{DFIG}$ ,  $P_{DG}$  and  $P_{PV}$  are DFIG, DG, and PV output powers, respectively. Power references are applied to DC/DC converters control system to extract buck/boost duty cycles.

### D. DG

The DG is modeled considering the conventional salient pole synchronous generator, IEEE type 1 exciter, and governor control system [109]. The reference mechanical power is produced considering both generator active power and mechanical rotational speed feedbacks.

### E. ILC

The ILC is a VSC-based three-level inverter constructed of 12 IGBTs with an antiparallel diode and is controlled using a dual-loop decoupled  $dq$  reference frame [20] to regulate the DC sub-grid voltage. The ILC will contribute to AC voltage control during AC sub-grid faults. Fig. 3.2 shows the control diagram of the ILC.

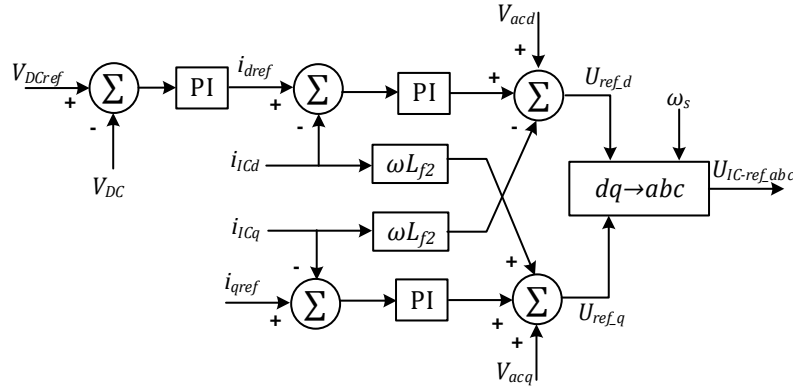


Figure 3.2 ILC control block diagram.

### 3.2.2 Proposed MSDBR-ILC Coordinated Control Algorithm

#### 3.2.2.1 MSDBR control algorithm

In this work, the MSDBR is in series with distribution load feeders shown in figure 3.1. The MSDBR is comprised of a high-power braking-resistor in parallel with two IGBTs in an anti-series arrangement for each phase. During the normal operating condition, a constant gate signal is applied to gates to keep the IGBT switched on to maintain the flow of load current. To suppress the fault current magnitude at the AC sub-grid, the MSDBR is controlled by appropriate PWM signal pulses to emulate a variable resistor.

**1) Fault detection logic-** Figure 3.3 shows the logic diagram of the fault detection algorithm for each phase. The fault is assumed to happen in load connecting lines, i.e., at point F in Figure 3.1. Any fault on the system causes sudden voltage sags on the affected phases. Thus, the algorithm

considers a per-phase current rise rate  $r_i$  and an under-voltage threshold level  $u_i$  defined by the protection scheme. The value of  $r_i$  must ensure that a significant current amount has been taken to set the fault signal, otherwise, normal microgrid disturbances such as step load change and islanding or DER plug-and-play operations will result in misdetection. On the other hand, the appropriate under-voltage index is needed to compensate for the effect of line impedance when a fault happens. In this work,  $u_i = 0.95\text{pu}$ ,  $r_i = 0.2\text{pu}/t_d$  and  $t_d = 1\text{ms}$  are chosen.

Figure 3.3 Per-phase fault detection logic diagram.

positive sequence voltage recovery at the threshold value. The logic will continuously monitor positive sequence voltage. The deactivation signal is triggered once the positive sequence voltage is recovered and a predefined threshold level is reached. Then the SW1 and SW2 return to the normal state. To perform a continuous transition from pulsed MSDBR to normal operation and to avoid sudden voltage and current change, a slew-rate limiting action is applied during deactivation. The actual value of braking resistance, when the MSDBR is activated, depends on the duty cycle, as shown below.

$$R_{MSDBR} = (1 - D)R_{BR} \quad (3.3)$$

where  $D$  and  $R_{BR}$  are the duty cycle and shunt resistance values in each phase, respectively.

**3) Duty cycle calculation-** The duty cycle is calculated based on pre-fault load power. This value defines the percentage of the switching cycle that the IGBT is switched on. When the IGBT is switched off, the current flows through the shunt resistance to suppress the fault current. To maintain the AC sub-grid voltage around pre-fault value, the duty cycle is determined according to pre-fault operating conditions. Greater load power means that the microgrid is operating in a greater balance of active and reactive powers. Therefore, the duty cycle should be adjusted in such a way as the braking resistor dissipates an amount of active power that is proportional to generating power in DERs to maintain the system stability during the fault. Here it is assumed that the pre-fault reactive load is less than the active load, and therefore the duty cycle is calculated as:

$$D = \begin{cases} 1 - \frac{P_{pre}}{P_{rated}} & I_{Lac} > 0 \\ d_0 & I_{Lac} \cong 0 \end{cases} \quad (3.4)$$

where  $P_{pre}$  and  $I_{Lac}$  are the pre-fault active load and current, respectively, at fault initiation moment.  $P_{rated}$  is the total rated active power capacity of DFIG and DG in the AC sub-grid.  $d_0$  is the

maximum value of duty cycle in case of no-load condition and is obtained from the relationship between the maximum allowable short-time line current setting  $I_{max}$  and pre-fault AC sub-grid voltage, as shown below.

$$d_0 = 1 - \frac{V_{phpre}}{R_{BR}I_{max}} \quad (3.5)$$

where  $V_{phpre}$  is the RMS pre-fault AC sub-grid phase voltage in the corresponding phase.

### 3.2.2.2 Coordination control with ILC

A coordinated control strategy with the contribution of ILC is proposed to mitigate the AC voltage oscillations during fault. It is assumed that the ILC does not regularly contribute to AC sub-grid voltage and frequency regulation to keep a stable voltage in the DC side. In this work, however, the ILC will only participate in the AC voltage control following the MSDBR activation during fault. It aims to control the post-fault voltage sags and swells in the AC sub-grid. Figure 3.3 represents the block diagram of the outer control loop in the ILC. It produces a reference reactive current  $i_{qref}$  to be applied in the  $q$ -axis in the ILC control diagram in Figure 3.2. The control block takes the pre-fault value of the AC grid in  $dq$  frame to generate the reference voltage  $V_{ref}$ .

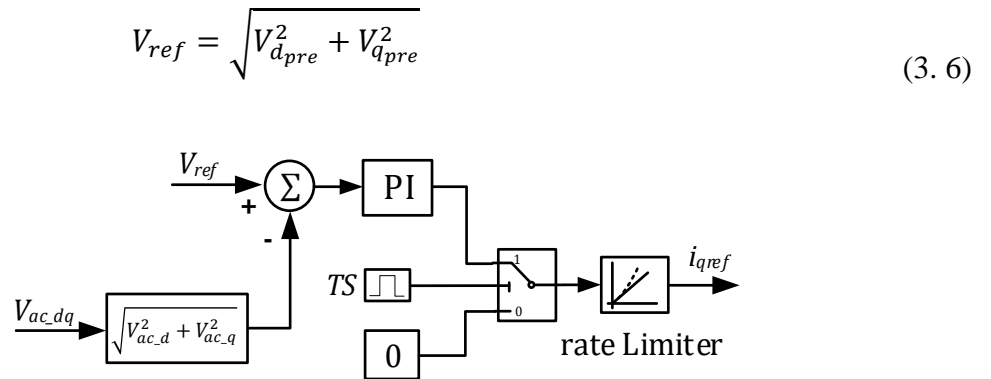


Figure 3.4 Block diagram of q-axis outer loop in ILC control system.

The activation/deactivation signal  $TS$  enables the controller operation. During the normal



condition,  $i_{qref}$  is equal to zero, which means the reactive power set point is zero and the ILC does not inject or absorb any reactive power into the AC sub-grid. A rate limiter controls the rise and slew rate of reference current to avoid sudden changes in the AC voltage.

### ***3.2.3 Performance Evaluation and analysis***

In this study, the HMG system is simulated in the MATLAB/Simulink environment with detailed models for all power electronic devices. The sample time for discrete-time simulations is chosen as 5 $\mu$ s. The wind speed and solar irradiance are kept constant during the fault scenarios.

#### ***3.2.3.1 Effectiveness of Proposed FRT Scheme During 3LG Fault***

In this case, a %100 three-line-to-ground (3LG) fault is applied at point **F** in HMG shown in Figure 3.1 for 134ms (8 cycles) at  $t_f=0.116$ s. The performance of the proposed FRT scheme has been compared with that of the without FRT scheme, as shown in Figure 3.5. Results show that the proposed MSDBR effectively suppresses the fault current level to below 1.05pu (1 MVA, 4.16 kV base). The modulation started at 0.119s that proves the quickness of the detection algorithm. Since the current has limited, no large voltage sag happens, and the ILC properly performs voltage regulation during the fault through the controlled reactive power injection. Figure 3.6 illustrates the total three-phase power dissipated by the MSDBR during the fault. This figure shows how the resistor should withstand against the fault current at the initiation moment and during the fault.

#### ***3.2.3.2 Effectiveness of Proposed FRT Scheme During 1LG Fault***

In this part, the proposed FRT scheme is analyzed against a one-line-to-ground (1LG) fault as an asymmetrical disturbance. The fault is applied at the same instance (at 0.116s) with the same duration (134ms) on phase *b*. Figure 3.7 shows the system dynamic responses. It has been shown that the proposed detection algorithm effectively identifies and suppresses the fault current magnitude. Since the ILC contributes to voltage regulation, the voltage at the DC sub-grid encounters

low amplitude fluctuations. The DC link voltage oscillations in DFIG (Figure 3.7.e) during fault are due to the negative sequence AC voltage that rotates in the reverse direction with double grid frequency and results in torque ripples.

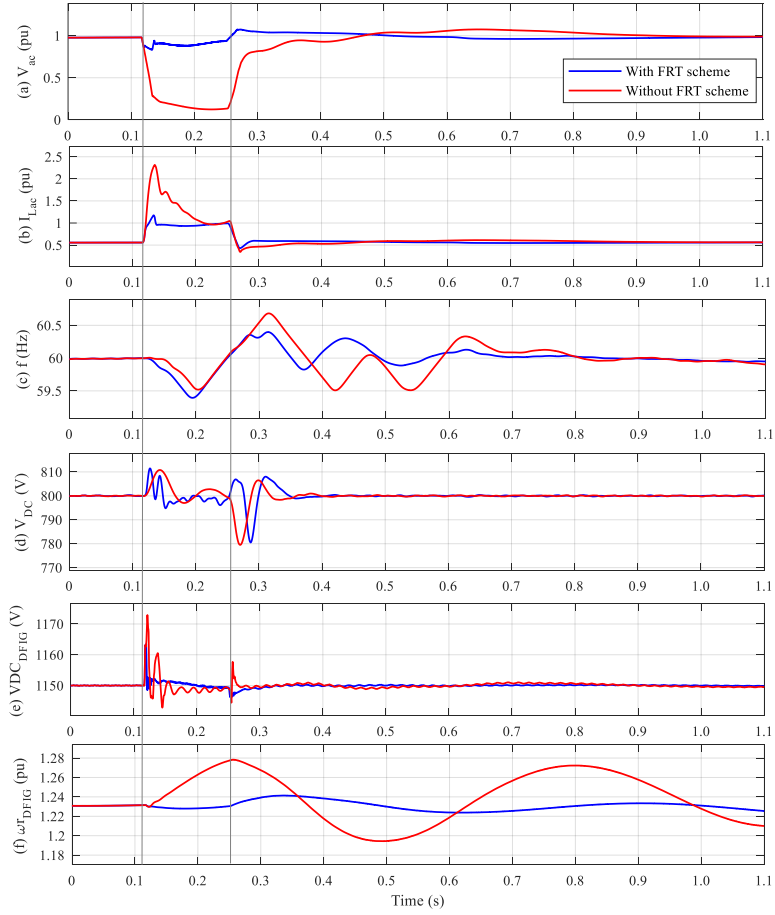


Figure 3.5 system dynamic response to a 3LG fault at point F. Red (without FRT), Blue (with FRT).

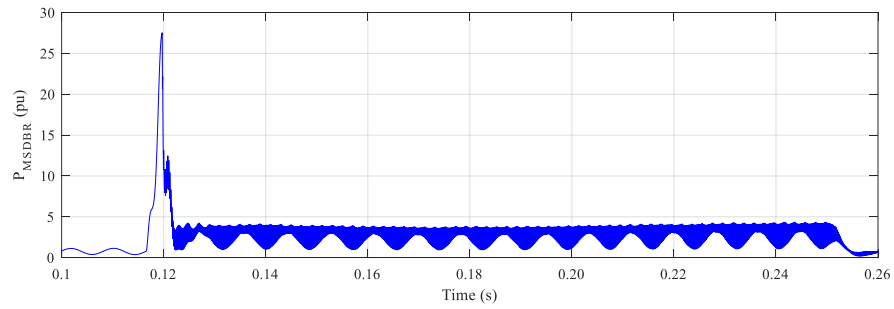


Figure 3.6 The total power dissipated by MSDBR during a 3LG fault.

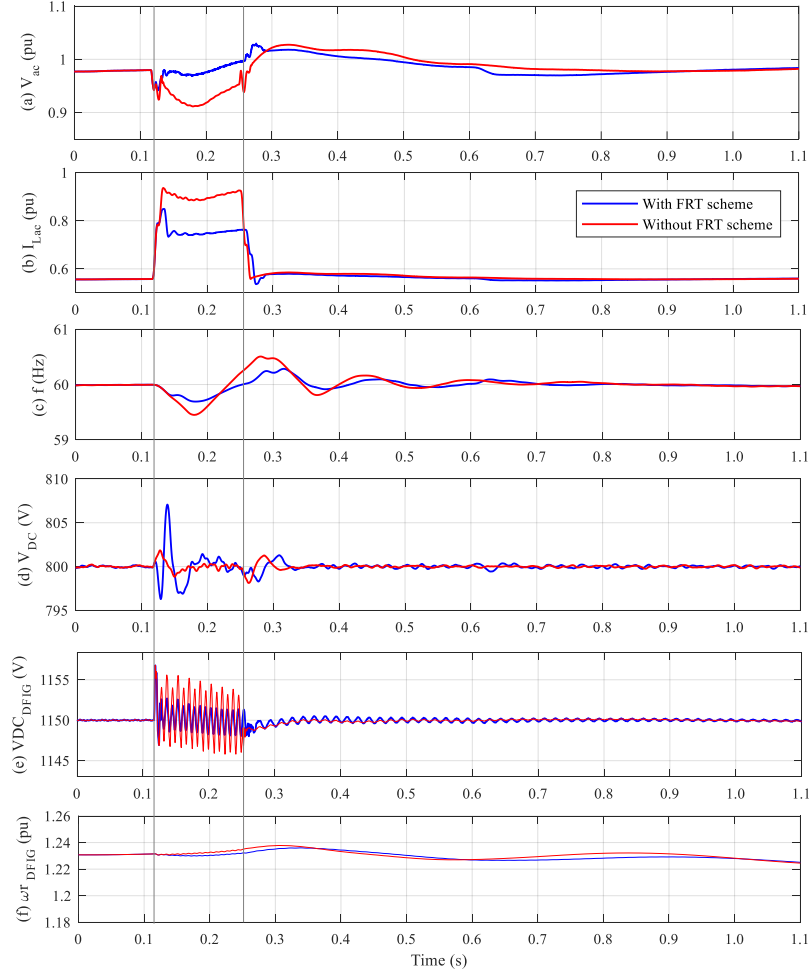


Figure 3.7 System dynamic response to a 1LG fault at point F. Red (without FRT), Blue (with FRT).

### 3.2.3.3 Index-based performance evaluation

To precisely analyze and compare the performance of the proposed FRT algorithm with that without the FRT scheme, an index-based performance evaluation is presented. The index is defined as:

$$index = \int_{t_f}^{t_1} |x - x_{ref}| dt \quad (3.7)$$

where  $x$  represents the parameter to be evaluated (e.g. voltage, current),  $x_{ref}$  is the reference value,  $t_f$  and  $t_1$  are evaluation time range. Here  $x_{ref}$  is considered the pre-fault parameters. The lower index

value means better system performance. Table 1 shows the index values for various parameters. Here, WO and W refer to without FRT and with FRT schemes, respectively. It has been shown that the proposed FRT scheme has significantly improved the essential HMG parameters for both 3LG and 1LG faults, with the exception that the DC sub-grid voltage  $V_{DC}$  and DFIG mechanical rotation  $\omega_r$  have not been enhanced in case of 1LG fault.

Table 3.1. Index-based performance evaluation

	3LG			1LG		
	WO	W	improvement	WO	W	improvement
$V_{ac} (pu)$	0.16	0.03	81%	0.018	0.011	51%
$I_{Lac} (pu)$	0.134	0.068	49%	0.053	0.034	52%
$f (Hz)$	0.164	0.11	33%	0.1	0.06	66%
$V_{DC} (V)$	1.14	1.08	5.4%	0.17	0.34	-49.7%
$VDC_{DFIG}$	0.78	0.32	59%	0.46	0.31	47.7%
$\omega_{rDFIG}(pu)$	0.023	0.003	83.6%	0.0024	0.0028	-13%

### 3.3 Disturbance Resilience Enhancement of Islanded Hybrid Microgrid Using Energy Storage [15]

Modern microgrids are gradually evolving from conventional power systems, where interconnected sub-grids govern power distribution with high penetration of RES and energy storage systems [110]. Conventional electric power grids were mainly established for centralized utilization of fossil fuel energy resources, while microgrids are developing to decentralize electric power generation through the DERs [4].

Following the background provided in chapter 2, this section investigates the resilience enhancement of the HMG against grid disturbances using a BESS connected to ACg, and this is the originality of this work. The BESS can be utilized for several ancillary purposes in microgrids, i.e., peak shaving, dynamic local voltage support, short-term frequency smoothing, and grid contingency support [14]. In this study, the BESS control system is adopted to contribute to

oscillations damping during grid disturbances. Another salient feature of this work is that a coordinated LVRT scheme is also provided in the wind turbine generator to support the reactive current requirements during faults. Case studies have been simulated in the MATLAB\Simulink environment. To evaluate the robustness of the proposed control mechanism, step load change conditions, wind speed/solar irradiance variations, and fault analysis on both ACg and DCg, have been considered.

### ***3.3.1 HMG Structure and Control systems***

Figure 3.7 shows the structure of the islanded HMG under the study, which is the base system shown in Figure 3.1 for FRT analysis. The AC and DC subgrids contain corresponding AC and DC loads and generation sources. An ILC links two subgrids to provide a bidirectional bridge for exchanging active power. The complete system parameters are given in chapter appendix [14].

#### ***3.3.1.1 AC subgrid***

The medium voltage ACg power system contains a DFIG-based variable speed wind generator. The DFIG model used in this work is a widely reported model introduced in [54] with complete detailed switching modeling of GSC control systems in  $dq$ -frame [20]. The RSC/GSC control, drive train, and details of blade pitch angle regulator can be found in [111].

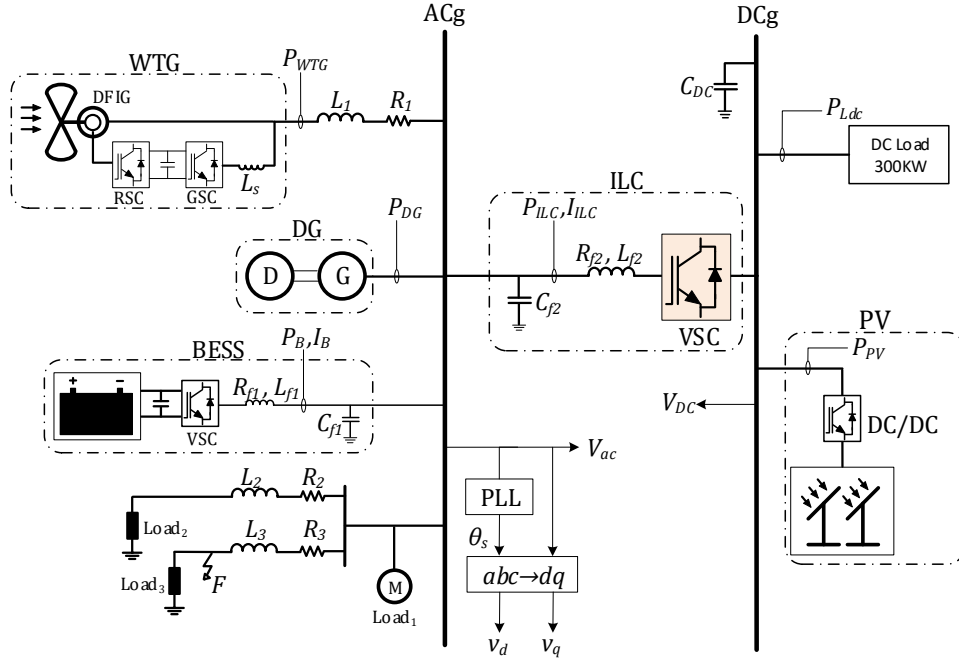


Figure 3.8 Hybrid AC/DC Microgrid structure under the study.

The wound-rotor induction machine is modeled using 4<sup>th</sup> and 2<sup>nd</sup> order for electrical and mechanical parts, respectively. A DG is in parallel with the wind turbine to provide dispatchable power requirements and is modeled considering the conventional salient pole synchronous generator [112], IEEE type 1 exciter [113], and speed governor control system shown in Figure 3.8. The DG establishes the synchronous reference frame for the DFIG and grid-following BESS.

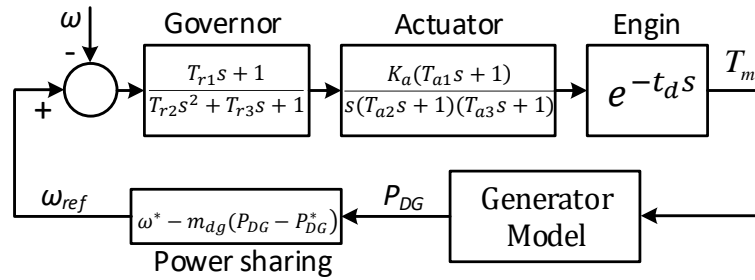


Figure 3.9 DG speed governor model.

In Figure 3.8,  $T_{ri}$  and  $T_{ai}$  are regulator and actuator time constants respectively and  $K_a$  is actuator gain,  $\omega$  and  $P_{DG}$  are measured frequency and DG output power respectively. The notation

‘\*’ refers to corresponding set-points.  $m_{dg}$  is power-sharing droop coefficient and  $t_d$  is engine delay.

The BESS includes a battery bank and a VSC-based inverter. The battery is a widely-used dynamic charge/discharge model of Li-ion experimentally verified in [114]. The detailed switching model of power electronic switches is used to reflect transient dynamics and non-linear properties of VSC [20]. Details of the BESS control system are discussed in section III. The power management unit calculates BESS power set-point  $P_B^*$  based on load powers and power generation from DERs, as follows:

$$P_B^* = \sum P_L - \sum P_G \quad (3.8)$$

$$P_L = P_{Lac} + P_{loss} + P_{ILC}, \quad P_G = P_{DFIG} + P_{DG}$$

where  $P_L$  and  $P_G$  are total load and generation active powers,  $P_{Lac}$ ,  $P_{loss}$ ,  $P_{ILC}$ ,  $P_{DFIG}$  and  $P_{DG}$  are respectively total AC load power, distribution losses, ILC power, DFIG, and DG powers. In this study, power signals are calculated and updated in the power management unit within time intervals that are longer than the simulation sampling frequency. Power signals are assumed to be sent and received once in every five simulation sample times. The detailed control system of BESS is given in section III. The reference direction of BESS power is from the battery to the grid, and ILC power is from ACg to DCg. Losses can be calculated by  $\sum_{i=1}^3 R_i |I_i|^2$ , where  $I_i$  are distribution line currents in ACg; losses in DCg are neglected. Load<sub>2</sub> and load<sub>3</sub> are modeled as constant power loads. A dynamic (frequency-dependent) AC load (load<sub>1</sub>) that is modeled as an induction motor [18] is also considered to emulate a more realistic HMG.

### 3.3.1.2 DC subgrid

The DC sub-grid (DCg) comprises Photovoltaic (PV) solar panels, constant and DC loads.

The PV model used is a generic model with an ideal single diode and equivalent circuit of parallel and series resistance [106]. A DC/DC boost converter along with an MPPT algorithm is integrated to extract the highest possible solar power in different ambient conditions and PV output voltages.

### 3.3.1.3 ILC

The ILC is modeled as a controlled DC-voltage power port using a VSC-based three-phase, three-level inverter [14][20]. The ILC performs as a DCg voltage controller and does not contribute to ACg voltage and frequency control. Any fluctuation in DCg voltage will be reflected in the ILC power flow to be regulated by the BESS. Similarly, any surplus/deficiency of power supply will render to increase/decrease DCg voltage that will be regulated by the ILC. The reference generating control signals of the VSC in  $dq$ -frame are given by:

$$\begin{aligned} u_{dILC} &= v_d + i_{qILC}\omega L_{f2} + \left(\frac{K_{i1ILC}}{s} + K_{p1ILC}\right)(i_{dref} - i_{dILC}) \\ u_{qILC} &= v_q - i_{dILC}\omega L_{f2} + \left(\frac{K_{i1ILC}}{s} + K_{p1ILC}\right)(i_{qref} - i_{qILC}) \\ i_{dref} &= \left(\frac{K_{i2ILC}}{s} + K_{p2ILC}\right)(V_{DCref}^2 - V_{DC}^2) \end{aligned} \quad (3.9)$$

where  $K_{ij}$  and  $K_{pj}$  are inner and outer loop regulator parameters ( $j = 1,2$ ), respectively. All  $v$  and  $i$  parameters on the right-hand side of (3.9) are the measured output voltages and currents of the ILC and the subscript ' $ref$ ' refers to reference values. By setting  $i_{qref} = 0$ , the ILC will be disengaged from reactive current generation and control on the ACg side. The reference  $u_{dqILC}$  is transformed to three-phase quantities using  $dq \rightarrow abc$  transformation.

### 3.3.2 BESS and Coordinated LVRT Scheme

#### 3.3.2.1 BESS control

The VSC used in BESS is implemented using a three-phase, three-level inverter [20]. The



VSC control includes a droop-based dual-loop control system in  $dq$ -frame which is implemented in grid-following mode and illustrated in Figure 3.10. Instantaneous BESS active and reactive powers are calculated based on the output  $dq$  current and terminal voltages:

$$\begin{aligned} p_B &= \frac{3}{2} [v_d i_{dB} + v_q i_{qB}] \\ q_B &= \frac{3}{2} [v_q i_{dB} - v_d i_{qB}] \end{aligned} \quad (3.10)$$

and average active and reactive powers are achieved using low pass filter (LPF) shown in Fig. 3.10 where  $\omega_c$  is the cut-off frequency of the filter.

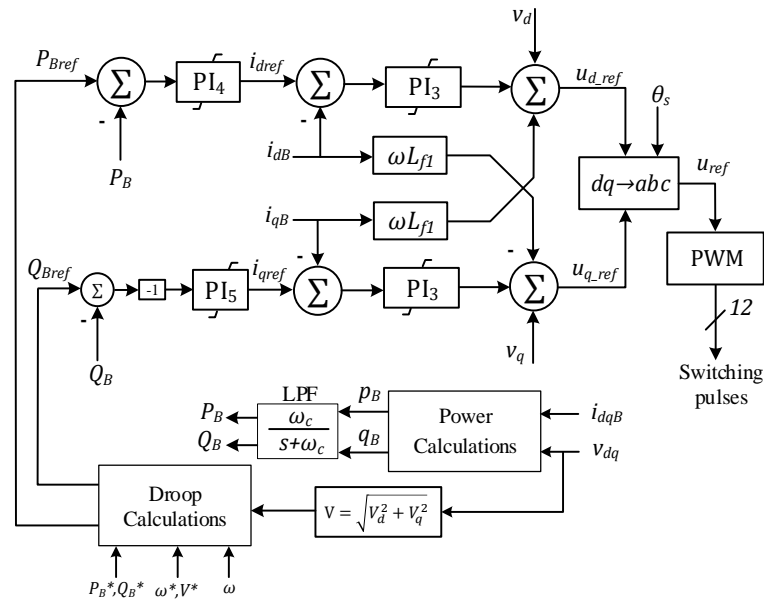


Figure 3.10 BESS control block diagram

The conventional droop control is obtained using  $\omega - P$  and  $V - Q$  droops:

$$\begin{aligned} \omega_{ref} &= \omega^* - m(P - P^*) \\ V_{ref} &= V^* - n(Q - Q^*) \end{aligned} \quad (3.11)$$

where ‘\*’ superscript denotes rated set points and  $m$  and  $n$  are droop gains. Since the BESS is mainly used in grid-following mode, the droop equations in (3.11) are not directly used. To enable the BESS to contribute to active/reactive power-sharing during system voltage and frequency

deviations, (3.11) is revised to (3.12) to form the BESS reference active/reactive powers:

$$\begin{aligned} P_{Bref} &= P_B^* - m_B(\omega - \omega^*) - m_\sigma \frac{d\omega}{dt} \\ Q_{Bref} &= Q_B^* - n_B(V - V^*) \end{aligned} \quad (3.12)$$

$$m_B \geq \frac{P_{Bmax} - P_{Bmin}}{\omega^*}, n_B \geq \frac{Q_{Bmax} - Q_{Bmin}}{V^*} \quad (3.13)$$

where  $V$  is the ACg voltage magnitude,  $m_B$ ,  $n_B$  and  $m_\sigma$  are BESS droop and ROCOF coefficients, respectively, and  $Q_B^*$  can be either set to a constant value to support ACg reactive power requirement or to zero to increase the BESS capacity of absorbing/injecting active power to the maximum rated value. While the BESS provides PQ service, the droop characteristics in (3.12) ensure that it responds to the voltage and frequency fluctuations as well as ROCOF.

### 3.3.2.2 Coordinated LVRT Scheme in DFIG

During grid faults and severe voltage sags, the electromagnetic torque inside the DFIG declines to low levels. This means that the DFIG does not supply active power during the fault. Grid codes mandate that the DFIG should stay connected and provide reactive power during low voltages. Therefore, inspired by [115], a coordinated control strategy of DFIG is adopted here to compensate for the reactive current requirement during the severe voltage drops. It is assumed that 1/3<sup>rd</sup> of output current is supplied by the GSC and 2/3<sup>rd</sup> of it is supplied by the stator. In normal operating condition, the reactive set point in RSC,  $Q_r^*$ , is set to zero. While during the fault, the DFIG should supply reactive current, and set points are changed according to DFIG terminal voltage magnitude:

$$Q_r^*(pu) = \begin{cases} 0, & V_t \geq 0.9 \\ -\frac{2}{3} \times (0.2)(0.8 - V_t), & 0.5 < V_t < 0.9 \\ -\frac{2}{3} \times 0.8, & V_t \leq 0.5 \end{cases} \quad (3.14)$$

The GSC and RSC maximum current should not be more than 0.8 and 0.9 pu, respectively.

### 3.3.3 Performance Evaluation and analysis

In this research, as already mentioned, the time-domain simulation of the HMG shown in Fig.1 is performed in the MATLAB/Simulink environment that runs on an HPC-based computing cluster facility. Due to the detailed switching models of power electronic devices, the sample time for discrete-time simulations is chosen  $T_s = 5\mu s$  and the sampling frequency for all parameters is equal to  $5T_s$ . The power stage data are taken from [14]. All other controller parameters are given in the chapter appendix. Three major case studies are considered which are discussed below. Simulations are performed for a system with (**W**) and without (**WO**) BESS and the LVRT scheme discussed in the previous sections.

#### 3.3.3.1 Step load change analysis

In this case, two load change scenarios are evaluated. First, a step load change is assumed in load<sub>1</sub> (induction motor) in ACg. Motor data is given in the Appendix.  $P_{DG}^*$  is set to 0.33 pu based on DG's rated power for all cases. Initially (case A1), the motor is run with 1.0 pu of rated torque. At 14.5s the following changes occur in torque value in 1.5s intervals: [0.1, 1.2, 0.8]. Next (case A2), the step load change happens at 14s in DC load from the initial value of 300KW to the following values: [180, 250, 140] KW in 1.5s intervals. Figures 3.11 and 3.12 show dynamic responses of the system corresponding to these simulation cases. The fast charge /discharge operation along with the reference adjustment in BESS strictly rejects the power generation disturbance in the case of **W**. Although the system **WO** recovers also to the reference values in a longer time, the frequency passes beyond the upper bound level due to the high inertia of DFIG. And in both cases, it gets stable in a higher frequency due to declined load level and power-sharing mechanism in DG.

### 3.3.3.2 Power generation variation analysis

In this part, the performance of the proposed scheme is analyzed against intermittent wind and irradiation levels. First (case B1), the wind speed changes from the initial value of 14m/s (which gives rated power output) to the following values in 2s intervals accordingly: [8.5, 11.2, 17, 12.5] m/s. The DFIG output changes based on wind speed variation and pitch angle control action. In the next simulation (case B2), solar irradiance in PV changes at 14s from the initial value of 1pu based on 1100W/m<sup>2</sup> to the following values in 2s intervals accordingly: [0.6, 1.4, 0.9] pu applying an appropriate ramp-rate. The PV power output changes based on irradiance values and the MPPT perturbations. Figures 3.13 and 3.14 depict the results of essential HMG parameters for these cases. As it is expected, the BESS compensates for load/generation mismatches through a quick response of charge/discharge operation and thus keeps the load curve flat.

### 3.3.3.3 Fault analysis

In this section, the LVRT capability of the proposed scheme is evaluated against HMG faults under heavy load conditions. First (case C1), a three-line-to-ground (3LG) short circuit, is applied for 150ms duration at  $t_f = 14s$  at location **F** in ACg shown in Figure 3.8. Next (case C2), a pole-to-pole fault is applied in DCg bus for 100ms duration at  $t_f = 14s$ . The dynamic response of both cases is delineated in Figure 3.15. In the case of ACg fault, the system **W** effectively controls fluctuations inside the limits. Although the system **W** can recover from DCg fault, it cannot bind the voltage magnitude inside the 1.2 pu limit for the specified time limit of 0.16s outlined in IEEE 1547- 2018 [57].

### 3.3.3.4 Index-Based Performance Evaluation

To have a clear understanding and closer look at the performance of the discussed method, an

index-based performance evaluation is presented to quantify the excursion level of parameters.

The index is defined as:

$$index = \int_{t_f}^{t_1} |x - x_{ref}| dt \quad (3.15)$$

where  $x$  represents the parameter to be evaluated (e.g., voltage, frequency),  $x_{ref}$  is the steady-state pre-disturbance value of parameters,  $[t_f \ t_1]$  is the evaluation time range and is chosen  $[14 \ 25]$ s for all cases. The lower index value means better system performance. Table 3.2 shows the index values for some critical HMG parameters for selected cases. PoI represents the percentage of improvement.

Table 3.2. Index-based performance evaluation

	Case A2			Case B2			Case C1		
	WO	W	PoI	WO	W	PoI	WO	W	PoI
$V_{ac}$ (pu)	0.039	0.017	%55	0.082	0.016	%79	0.30	0.21	%28
$F$ (Hz)	6.1	0.23	%96	7.5	0.31	%95	6.02	0.65	%89
$V_{DC}$ (V)	6.6	6.2	%5	10.0	9.4	%6	9.8	8.1	%17

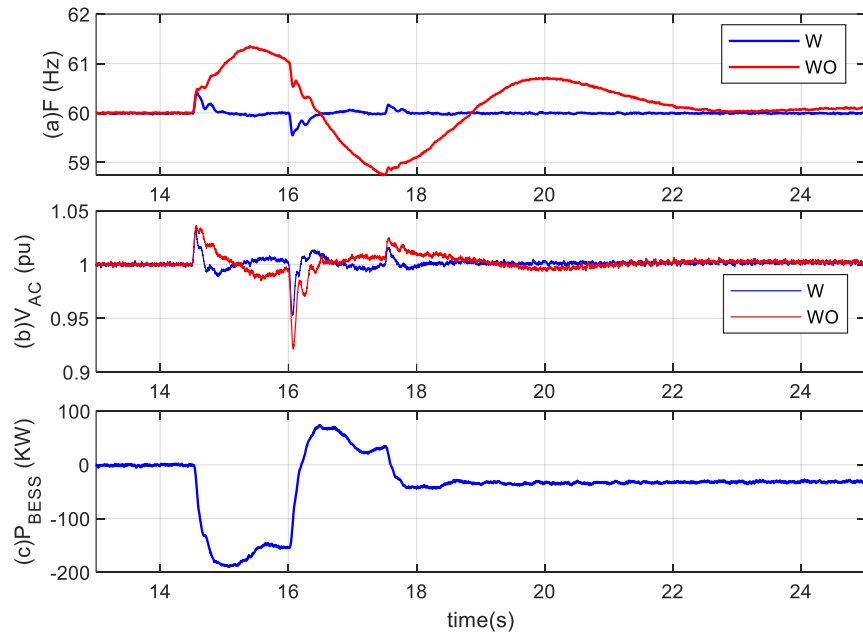


Figure 3.11 Step load change in Load<sub>1</sub> (case A1) ; (a) ACg frequency, (b) ACg voltage magnitude and (c) BESS power in case of **W**

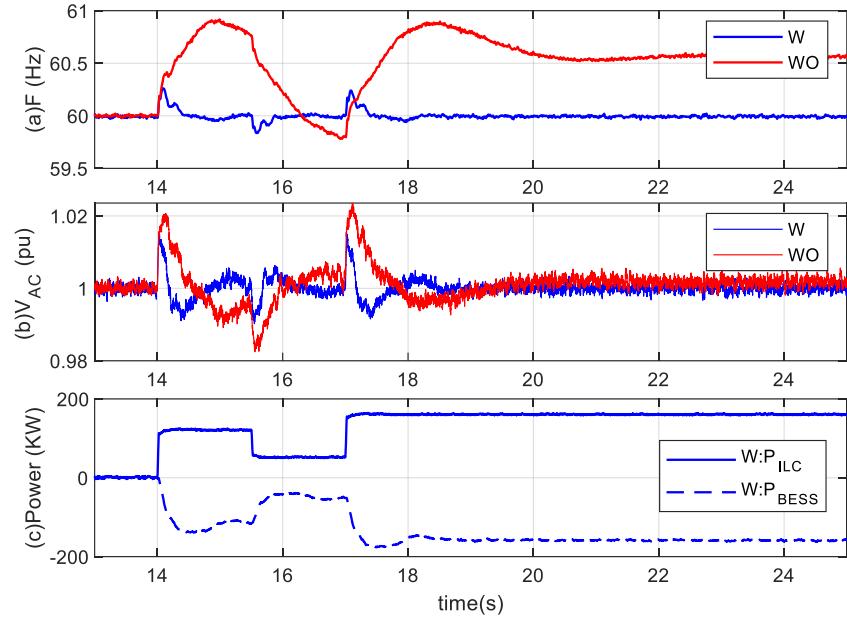


Figure 3.12 Step load changes in DC Load (case A2); (a) ACg frequency, (b) ACg voltage magnitude, (c) ILC and BESS power in case of **W**

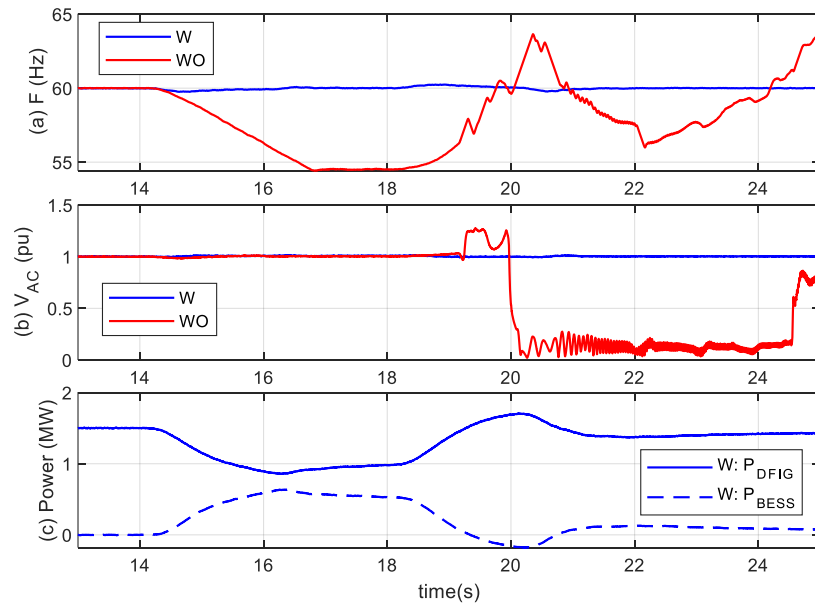


Figure 3.13 Wind speed fluctuation (case B1): a) ACg frequency, b) ACg voltage magnitude and c) DFIG and BESS power in case of **W**

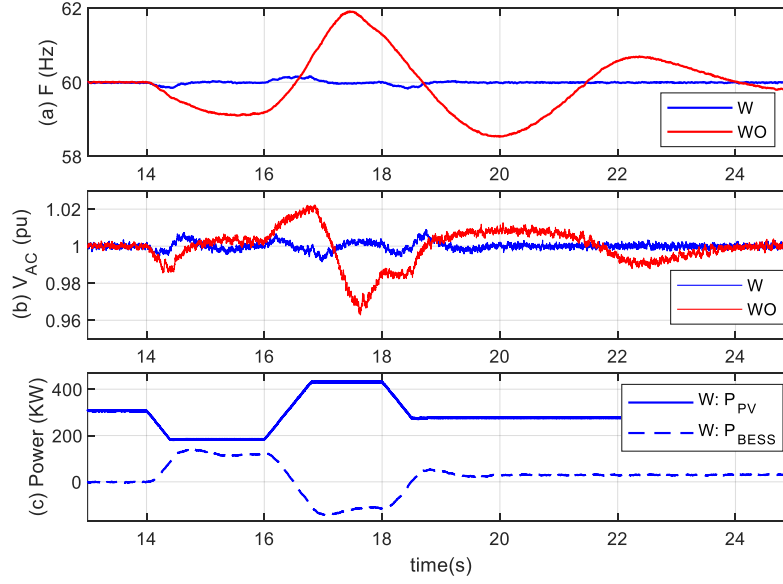


Figure 3.14 Solar irradiance variation (case B2): (a) ACg frequency, (b) ACg voltage magnitude, (c) PV and BESS output power in case of **W**

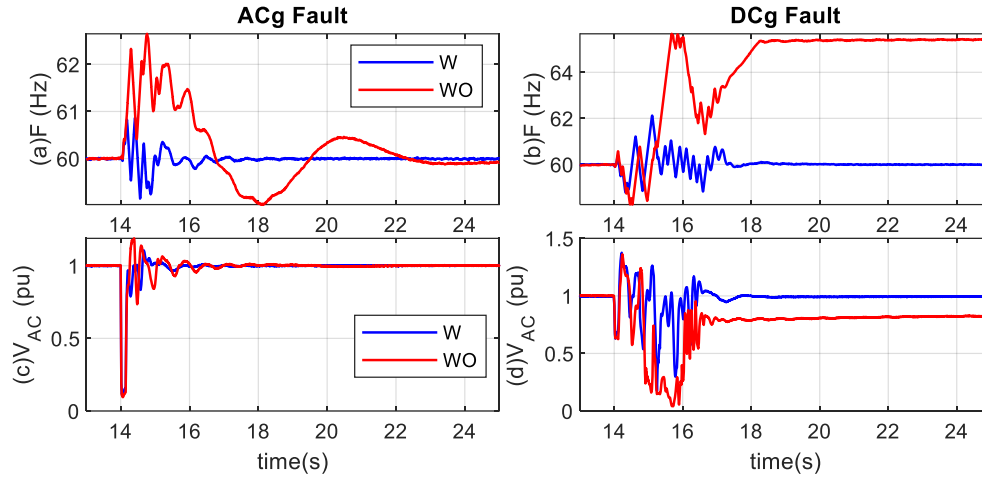


Figure 3.15 Fault analysis (cases C1 and C2); (a) and (b) ACg frequency, (c) and (d) ACg voltage magnitude during ACg and DCg faults respectively.

### 3.4 Chapter Conclusion

In this chapter, a coordinated control strategy was proposed to enhance the FRT capability of an islanded hybrid AC/DC microgrid. In addition, a coordinated control strategy of the droop-based BESS and LVRT scheme in DFIG was proposed to enhance the disturbance resilience of the islanded HMG with a high level of RES penetration. The following remarks are concluded

from the simulation results for both studies:

*a-1)* The coordinated MSDBR control along with the reactive current control loop in the ILC, effectively suppresses the fault current during both symmetrical and asymmetrical faults.

*a-2)* With the proposed FRT, not only do the DERs remain connected but also unaffected loads are able to continue the service.

*a-3)* The proposed method can recover the positive sequence voltage and reduce negative and zero sequence voltage components. Furthermore,

*b-1)* The proposed strategy for disturbance resiliency enhancement effectively minimizes power fluctuations generated from intermittent RES to maintain a relatively flat load profile.

*b-2)* The proposed coordinated control of BESS along with the reactive current control compensation in DFIG RSC effectively improves the LVRT capability during ACg fault.

In the next chapters, the study will be extended to design a novel bi-directional DC-DC converter for energy storage applications in DC and hybrid microgrids.

### **3.5 Chapter Appendix**

#### ***3.5.1 System parameters for both studies***

Table 3.3 presents the system's data for the power stage.



Table 3.3 System data for power stage

<b>DFIG</b>			
Rated Power	1.67 MVA	Turbine inertia constant	4.32
Rated Voltage	575 V	Shaft spring constant	1.11
Stator $R_s, L_s$	0.023, 0.18 pu	Shaft mutual damping	1.5
Rotor $R'_r, L'_r$	0.016, 0.16 pu	DC Link Capacitor	10 mF
Inertia constant	0.685 s	Rated DC-link Voltage	1150 V
Friction factor	0.01 pu	Pole pairs	3
<b>PV</b>			
Module	SunPower	Model: SPR-315E-WHT-D	
Parallel strings	128	Series modules per string	8
<b>DG</b>			
Rated Power:	800 KVA	$X_d, X_q$	2.59, 2.36 pu
Rated Voltage	460 V	Inertia constant, Friction	0.1716s, 0.0133pu
Stator Resistance $R_s$	0.014 pu	Pole pairs	2
<b>AC BESS</b>			
Rated Voltage	950 V	AC Filter: $R_{fl}, L_{fl}, C_{fl}$	1.9m $\Omega$ , 0.5mH, 250 $\mu$ F
Rated Capacity	500 Ah	DC link Voltage, Capacitor	750V, 5mF
		VSC carrier frequency	1980 Hz
<b>DC BESS</b>			
Rated Voltage	690 V	Rated Capacity	688 Ah
<b>IC</b>			
DC Voltage, $C_{DC}$	800V, 50 mF	VSC carrier frequency	1980 Hz
AC Filter: $R_{f2}, L_{f2}, C_{f2}$	1.9m $\Omega$ , 0.5mH, 2500 $\mu$ F		
<b>MSDBR</b>			
$R_{BR}$	1.213 pu	PWM switching frequency	5 KHz
<b>HMG Loads and Lines</b>			
Base Voltage ( $V_{AC}$ )	4.16 KV	Load 1,2	0.85pu, PF=0.83
Base Power	1MVA	System frequency	60 Hz
L1, L2, L3	1.9, 1.3, 1.9 mH	R1, R2, R3	0.2, 0.1384, 0.2 $\Omega$

### 3.5.2 Parameters of the system controllers:

DG:  $T_{r1} = 0.2, T_{r2} = 0.02, T_{r3} = 0.2, T_{a1} = 0.25, T_{a2} = 0.009, T_{a3} = 0.0386, t_d = 10ms, K_a = 25, m_{dg} = 0.05$

ILC:  $K_{i1} = 7.5, K_{p1} = 0.42, K_{i2} = 50, K_{p2} = 6$

BESS: PI<sub>3</sub>-  $K_{i3} = 20, K_{p3} = 0.3$ , PI<sub>4</sub>-  $K_{i4} = 2, K_{p4} = 0.05$ , PI<sub>5</sub>-  $K_{i5} = 10, K_{p5} = 0.025, m_B = 75, n_B = 5, m_\sigma =$

$0.05, \omega_c = 20 \frac{rad}{s}, P_{Bmax} = 1MW, P_{Bmin} = -1MW, Q_{Bmax} = 0.4MVar, Q_{Bmin} = -0.4MVar, Q_B^* = 0.2MVar$

Induction motor: 460V, 205KW, 1780 RPM, 1100N.m

## Chapter 4 A Novel Bidirectional DC-DC Converter for Energy Storage Applications [116]

### 4.1 Introduction

Hybrid microgrids (HMGs) are evolving from the concept stage to real-world practice, as they combine the functionalities of both AC and DC load/generation systems into a synthetic power distribution system. [13][117]. It is imperative to regulate system oscillations with faster dynamics and reliable controllers. Converter-interfaced battery energy storage systems (BESS) [15] are well demonstrated to be the most reliable, technically suitable, and economically available solutions to manage voltage/frequency deviations and to enhance the dynamic performance of microgrids [118].

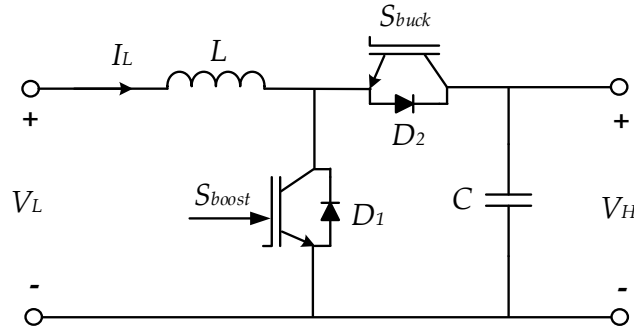


Figure 4.1 Conventional bidirectional DC-DC converter.

Based on the background provided in section 2.6 of chapter 2, to overcome the drawbacks of the conventional DC-DC converter (see Figure 4.1) this chapter proposes a novel bidirectional DC-DC converter for BESS applications in hybrid and DC microgrids (see Figure 4.2). Several noteworthy features of the proposed converter are as follows:

- (i) It employs two Boost converters in back-to-back topology and has a minimum additional component compared with other proposed converter configurations.

(ii) Compared to the conventional type, the proposed converter has three more diodes and one more inductor and capacitor. Since there is no Buck operation and the battery voltage can be raised to higher levels, the converter inductors have less inductance and current capacity due to the reduced battery current.

(iii) The proposed configuration has two voltage levels on the battery side in two modes of operation. The converter exhibits similar dynamic characteristics in both modes of operation, hence, one single controller can be designed and implemented.

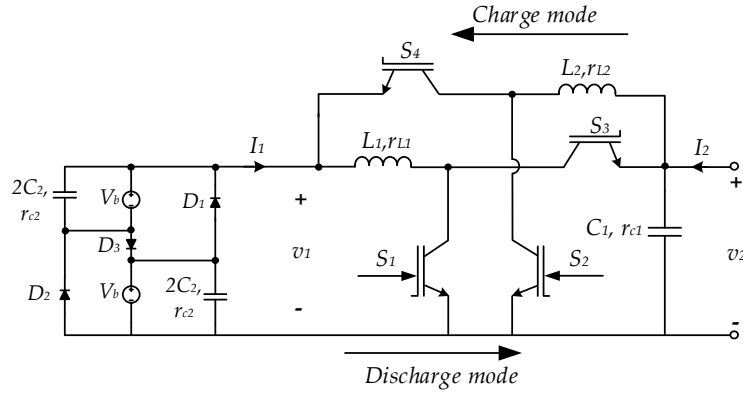


Figure 4.2 Proposed bidirectional DC-DC converter.

Table 4.1 presents a summarized comparison of the salient features of the proposed BDC in this paper and other BDCs submitted in previously discussed research works. The proposed converter is suitable for voltage and power control in DC microgrids or DC subgrids of HMGs, specifically for high-voltage/high-power applications. The proposed BDC is employed in HMG, as shown in Figure 4.3, and its efficacy is evaluated by the time-domain simulations presented in section 4.4. The HMG in Figure 4.3 comprises AC and DC subgrids interconnected through an ILC and two DERs, as well as a BESS in a DC subgrid. More details are given in section 4.4.

Table 4.1. Comparison between proposed, conventional, and other bidirectional DC-DC converters (BDCs).

	Proposed	Conventional	[69]	[72]	[67]/ [73]	[74]	[70]
Voltage gain in discharge mode	$\frac{1}{1-D}$	$\frac{1}{1-D}$	$\frac{2G_1^{(1)}}{1-D_{boost}}$	$\frac{1+D}{1-D}$	$\frac{1}{1-D}$	$\left(\frac{1}{1-D}\right)^2$	$\frac{2+D}{1-D}$
Voltage gain in charge mode	$\frac{1}{1-D}$	$D$	$\frac{1}{2}D_{buck}G_2^{(1)}$	$\frac{1-D}{1+D}$	$D$	$D^2$	$\frac{(1-D)D}{2D^2+1}$
Symmetrical scheme	✓	✗	✗	✗	✗	✗	✗
Control complexity	low	low	high	low	medium	low	high
Component count:	-	-	-	-	-	-	-
Inductors	2	1	3	2	3/3	2	1
Capacitors <sup>(2)</sup>	0	0	3	2	2/2	1	2
Switching devices	4	2	4	3	2/4	4	3
Diodes <sup>(3)</sup>	3	-	-	-	-	-	3
Coupled inductors	-	-	-	-	1/1	-	1

<sup>(1)</sup>  $G_1, G_2$  are functions of switching frequency, load resistance, and reactance of the resonant circuit parameters.

<sup>(2)</sup> Input/output capacitors are not counted. <sup>(3)</sup> Body diodes are not considered

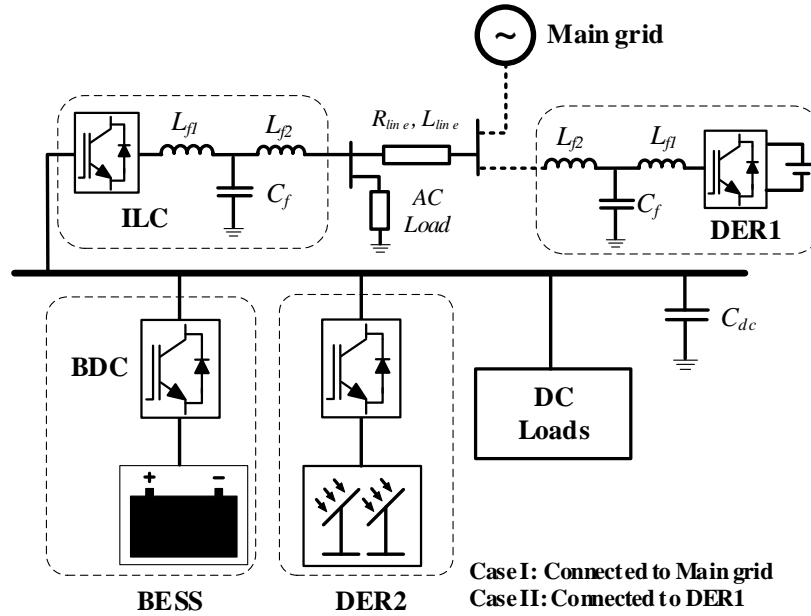


Figure 4.3 Hybrid microgrid under the study.

## 4.2 Proposed DC-DC Converter for BESS System

### 4.2.1 Principle of Operation

The proposed converter is composed of two Boost converters in a back-to-back configuration. Therefore, there is the only step-up mode in both directions. The objective is to make a

bidirectional converter that:

- Works symmetrically with the same dynamic properties in both directions.
- Has equally high DC gain in both discharge and charge modes.
- Does not have much power loss compared with the conventional type.
- Has a robust yet straightforward controller that fits both modes.

The proposed configuration has two battery voltage levels in two modes of operation, i.e., in discharge mode  $v_1 < v_2$  and in charge mode  $v_1 > v_2$ , as shown in Figure 4.2. This is made by employing two battery sections with equal voltage levels, which work in parallel in discharge mode and series in charge mode. Although two battery levels are used, in practice, battery packs are made up of several cells connected in series and parallel to achieve the desired voltage and current. Hence, this would not be a limitation.  $S_1$  and  $S_2$  are modulating switches that are separately controlled by the pulse width modulator (PWM) driver in discharge and charge mode, respectively.

Equal parameters make the base case for two modes. However, the different input/output operational voltages and the converter external network result in different converter dynamics during bidirectional operation. Thus, some adjustments in the power stage and control loops are needed to make a symmetrical bidirectional operation. In this study, it is assumed that  $r_{L1} = r_{L2} = r_L$  and  $r_{c1} = r_{c2} = r_c$ , where  $r_L$  and  $r_c$  are equivalent series resistance (ESR) of the inductor and the capacitor. ON-state resistance ( $r_{on}$ ) of power switches and diodes are neglected in the theoretical analysis for simplicity [43][119][120] but are included in the simulation analysis for accuracy.

**Discharge mode operation:** Figure 4.4 shows the converter circuit in discharge mode. In this mode,  $S_1$  is modulated to boost  $v_2$ , while  $S_3$  is kept ON and  $S_4$  is kept OFF.  $D_1$  and  $D_2$  are in forward-bias and  $D_3$  is in reverse-bias during Boost operation to configure two battery sections in parallel

connection to allow current  $I_1$  to flow from  $v_1$  toward  $v_2$  (see Figure 4.4a). Consequently, battery sections with parallel capacitors are all in parallel connection and  $v_1 = V_b - V_d$ , where  $V_b$  is the battery voltage in each section and  $V_d$  is the voltage drop across the diode ( $D_1$  and  $D_2$ ) in forward bias (see Figure 4.4b). Due to the low order of magnitude,  $V_d$  can be neglected in high-voltage applications, i.e.,  $v_1 \approx V_b$ . However, this should not be the case in low-voltage applications.

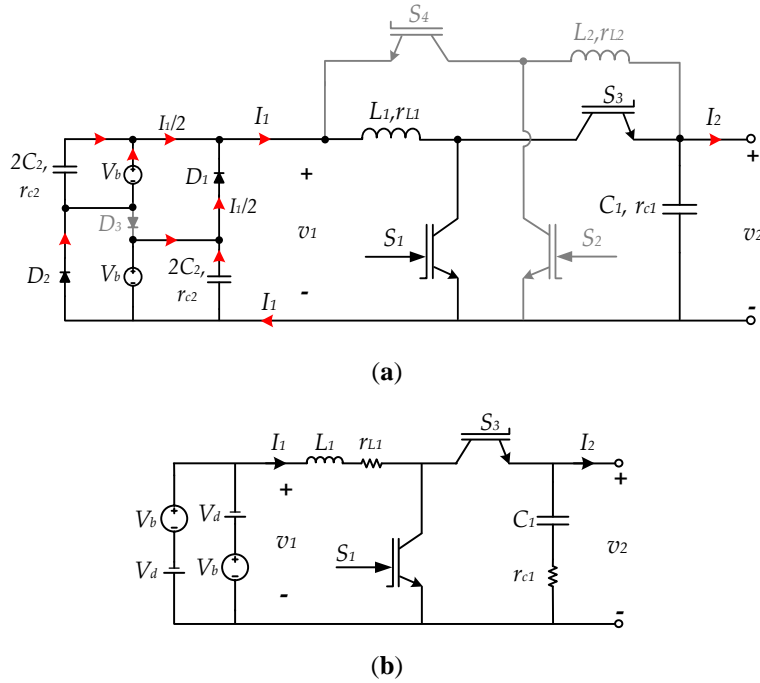


Figure 4.4 Discharge mode circuit. (a) Current flow diagram; (b) equivalent circuit.

**Charge mode operation:** In charge mode, (see Figure 4.5),  $S_2$  is modulated to boost  $v_1$ , while  $S_4$  is kept ON and  $S_3$  is kept OFF.  $D_1$  and  $D_2$  are in reverse-bias and  $D_3$  is in forward-bias during Boost operation to configure two battery sections in series connection and to allow current  $I_2$  to flow from  $v_2$  toward  $v_1$  (see Figure 4.5a). As a result, battery sections with parallel capacitors are in series connection with  $D_3$  in between. If  $D_3$  is moved to the lower part of the series connection such that the same current ( $I_1$ ) flows through it, the circuit configuration remains the same, hence,  $v_1 = 2V_b + V_d$ , as shown in Figure 5b. It can be shown that  $I_x = 0$  and the symmetrical

combination of the two battery sections and parallel capacitors are equivalent to one section in parallel with the equivalent capacitor and its ESR, as shown on the left side of Figure 5b. Also,  $C_2$  can be removed since the battery charge level is high enough to keep  $v_1$  constant.

In mode changeover state, inductors are fully discharged before the current flow direction changes. Hence,  $S_3$  and  $S_4$  are switched under zero current conditions. Figure 4.6 shows a simulation instance of inductor currents and  $S_3$  and  $S_4$  switching conditions during a power flow direction change.

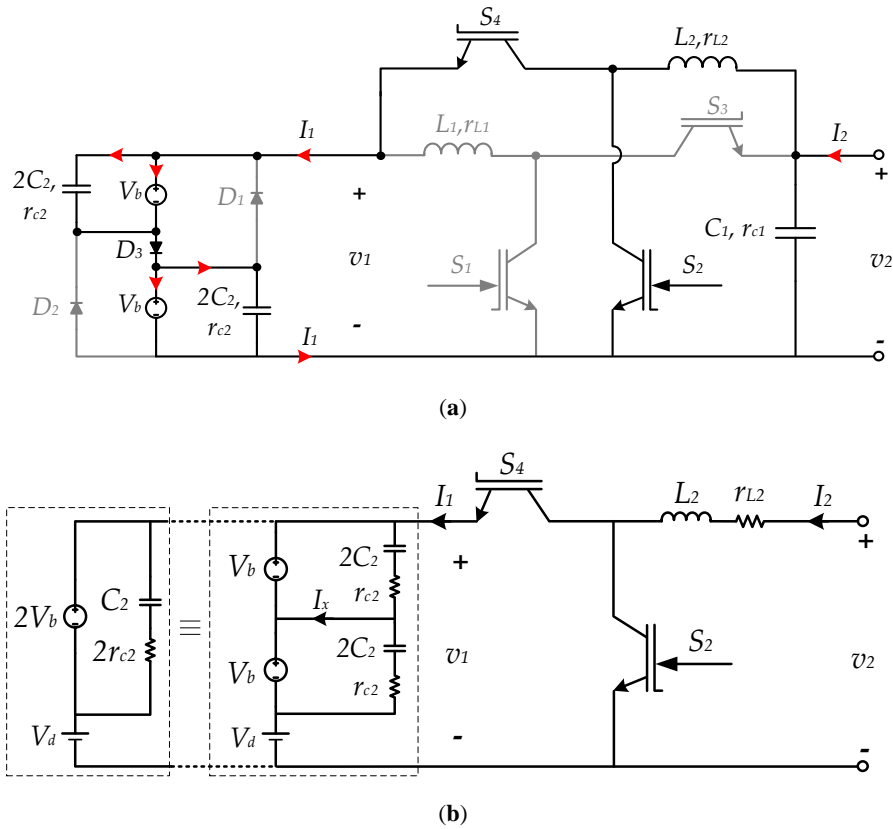


Figure 4.5 Charge mode circuit. (a) Current flow diagram; (b) equivalent circuit.

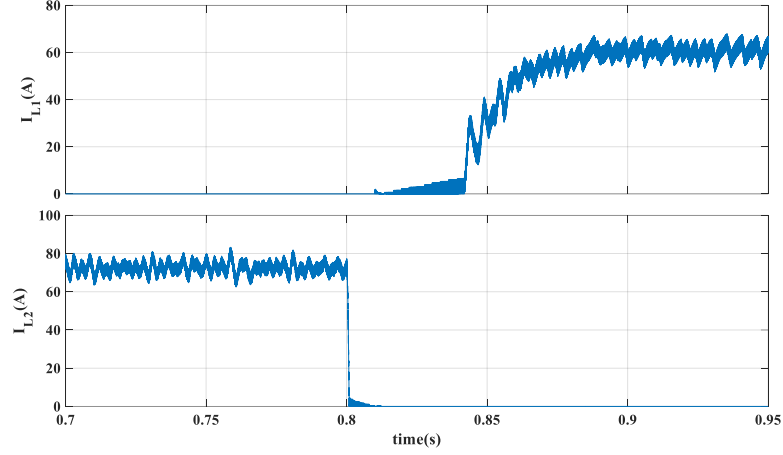


Figure 4.6 Inductor currents and  $S_3$ – $S_4$  switching conditions during a flow direction change.

Comparing two modes, the only discrepancy in the converter structure is the value of capacitor ESR equal to  $2r_c$  in charge mode, which is negligible due to its order of the value. Also, since the values of the capacitor ESR are not proportional to its capacity, the series combination resistance is less than  $2r_c$ . In addition,  $r_c$  does not affect the steady-state operation of the converter. It should be noted that since  $S_3$  and  $S_4$  are not continuously modulated, their conduction loss is significantly lower than the switching loss [121]. Also, they should be implemented by devices without body diodes such as IGBTs. However,  $S_1$  and  $S_2$  can be implemented by either IGBTs or MOSFETs. Although IGBTs might be suitable for high power/high voltage applications, MOSFETs have lower switching and conduction losses and can work with higher switching frequencies. The maximum stress voltage on all switches is equal to  $2V_b$  and  $V_b$  for all diodes.

**Battery voltage selection:** To realize the discharge and charge mode voltage equalization, for a given DC grid rated voltage  $V_{dc}$ , such that  $v_2 = V_{dc}$  in steady-state, the rated value of battery voltage  $V_b$  in each section is determined such that the equal steady-state duty ratio is maintained.



$$\begin{cases} V_{dc} = \frac{V_b}{1-D} & \text{discharge mode} \\ 2V_b = \frac{V_{dc}}{1-D} & \text{charge mode} \end{cases} \quad (4.1)$$

Then,  $\frac{V_b}{V_{dc}} = \frac{V_{dc}}{2V_b}$ , which yields:

$$V_b = \frac{V_{dc}}{\sqrt{2}} \quad (4.2)$$

#### 4.2.1 Converter Transfer Functions

In order to design the converter controllers, a linearized model of the converter is derived based on the state-space averaging for continuous conduction mode (CCM) [119][43]. Since the converter has the same structure (but inequivalent parameter values) in both modes, one equivalent model is derived that is valid for both modes, as depicted in Figure 4.7.

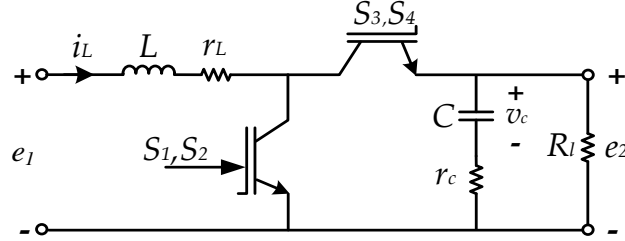


Figure 4.7 Equivalent Boost converter circuit;  $e_1$  and  $e_2$  represent input and output voltages, respectively and  $R_l$  represents the converter equivalent load in each mode.

Averaging takes place over one switching interval  $T_s = \frac{1}{f_s}$ , with  $f_s$  being the PWM switching frequency with ON- and OFF-state subintervals for  $S_1, S_2$  switches. Averaged affine continuous-time state-space representation of the converter is given by

$$\begin{cases} \dot{x}(t) = \mathcal{A}x(t) + \mathcal{B}u(t) \\ y(t) = \mathcal{C}x(t) \end{cases} \quad (4.3)$$

where  $x(t) = [i_L(t) \quad v_c(t)]^T$  is the state vector,  $u(t)$  is the converter input voltage  $e_1$ ,  $i_L$  is the

inductor current,  $v_c$  is the capacitor voltage, and  $y(t)$  is the output.  $\mathcal{A}$ ,  $\mathcal{B}$ , and  $\mathcal{C}$  are the averaged state transition, input, and output matrices. The converter input voltage ( $v_1$  in discharge mode and  $v_2$  in charge mode) is assumed to stay constant during Boost operation. With this assumption,  $i_L$  represents the input current in both modes. Writing the network equations during ON/OFF-state sub-intervals and establishing state-space equations, we obtain [43]

$$\mathcal{A} = \begin{bmatrix} -\frac{1}{L} \left( r_L + \frac{d' r_c R_l}{r_c + R_l} \right) & -\frac{d'}{L} \left( 1 + \frac{r_c}{r_c + R_l} \right) \\ \frac{d' R_l}{C(r_c + R_l)} & -\frac{1}{C(r_c + R_l)} \end{bmatrix} \quad (4.4)$$

$$\mathcal{B} = \begin{bmatrix} \frac{1}{L} \\ 0 \end{bmatrix} \quad \mathcal{C} = \left[ d' R_l \left( 1 - \frac{R_l}{r_c + R_l} \right) \quad \frac{R_l}{r_c + R_l} \right]$$

where  $d \in [0,1]$  is the duty ratio variable and  $d' = 1 - d$ .  $R_l$  represents the load resistance estimated based on the converter network discussed hereafter. Averaged value matrices are obtained by combining the corresponding subintervals matrices over one switching period. For the affine system (4.3) with the initial state  $x(0) = x_0$ ,  $\mathcal{A}$  is stable and nonsingular, such that  $x(t)$  converges to equilibrium point  $X = -\mathcal{A}^{-1}\mathcal{B}u$  [122]. Let  $u = e_1$  and  $y = e_2$ , then linearizing (4.3) results in a two-input, two-output, small-signal model of the converter, represented by the following system of transfer function equations in the  $s$ -domain:

$$\begin{bmatrix} e_2(s) \\ i_L(s) \end{bmatrix} = \begin{bmatrix} G_{11} & G_{12} \\ G_{21} & G_{22} \end{bmatrix} \begin{bmatrix} d(s) \\ e_1(s) \end{bmatrix} \quad (4.5)$$

where

$$G_{11} = \frac{e_2(s)}{d(s)} \Big|_{e_1=0} = \alpha_0 \frac{\alpha_1 s^2 + \alpha_2 s + \alpha_3}{\alpha_4 \alpha_5 s^2 + \alpha_4 \alpha_6 s + \alpha_4^2} \quad (4.6)$$

$$G_{12} = \frac{e_2(s)}{e_1(s)} \Big|_{d=0} = \frac{R_l C D' r_c (R_l + r_c) s + R_l D' (R_l + r_c)}{\alpha_5 s^2 + \alpha_6 s + \alpha_4} \quad (4.7)$$

$$G_{21} = \frac{i_L(s)}{d(s)} \Big|_{e_1=0} = \alpha_7 \frac{C (R_l + r_c) s + 1}{\alpha_4 \alpha_5 s^2 + \alpha_4 \alpha_6 s + \alpha_4^2} \quad (4.8)$$

$$G_{22} = \frac{i_L(s)}{e_1(s)} \Big|_{d=0} = \frac{C (R_l + r_c)^2 s + (R_l + r_c)}{\alpha_5 s^2 + \alpha_6 s + \alpha_4} \quad (4.9)$$

$$\begin{aligned} \alpha_0 &= -R_l E_1 (R_l + r_c) \\ \alpha_1 &= L C r_c (R_l + r_c) \\ \alpha_2 &= C r_L r_c^2 (1 + D') + [C R_l (r_L D' - R_l D'^2 + r_L) - C r_L D' + L] r_c + L R_l \\ \alpha_3 &= (R_l - D' + r_c + R_l D' + r_c D') r_L - R_l^2 D'^2 \\ \alpha_4 &= R_l D' (R_l D' + r_c) + r_L (R_l + r_c) \\ \alpha_5 &= L C (R_l + r_c)^2 \\ \alpha_6 &= [L + C (R_l r_L + r_c r_L + R_l D' r_c)] (R_l + r_c) \\ \alpha_7 &= E_1 (R_l + r_c) [(1 - r_c - R_l) r_L + r_c R_L + D' R_l^2] \end{aligned} \quad (4.10)$$

where  $D = 1 - D'$  is the steady-state value of duty ratio. Expression (4.5) states that duty ratio  $d(s)$  and converter input voltage  $e_1(s)$  are the independent input controls in the general form. However, the input voltage is assumed here to be approximately constant during Boost operation. Hence, the duty ratio is the only control input. In (4.6)–(4.10),  $E_1$  is the DC value of the input voltage  $e_1$  in the steady-state operation. It should be noted that the value of the input voltage is not the same during the two modes.

#### 4.2.3 Estimation of the Equivalent Load Resistance

Unlike the conventional notion of the unidirectional DC-DC converters, the bidirectional DC-DC converter used in microgrids does not have an explicit load resistance ( $R_l$ ) connected to the output terminal. However, the dynamic value of  $R_l$  depends on the parameters of the network external to

the converter (see Figure 4.8), which vary during charge and discharge mode operation and are essential parameters for transfer function realization. Conventional methods of calculating transfer functions [19][43][44][119] are based on known values of load resistance. In contrast, in a BDC, the actual value of the load resistance mainly depends on the input/output terminal voltages. This subsection provides a novel yet simple approach to calculating this parameter.

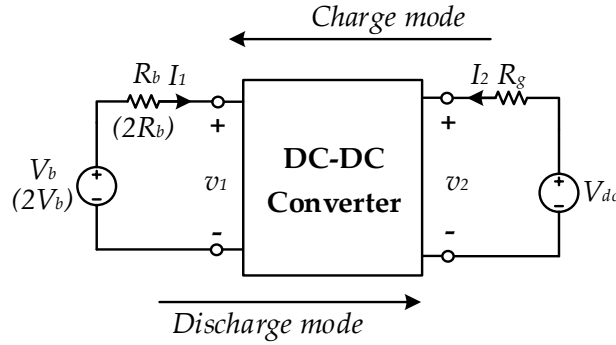


Figure 4.8 Converter connection network. (·) stands for charge mode operating parameters.

The following network equations hold for the discharge mode (see Figure 4.8):

$$\begin{cases} v_1 = V_b - R_b I_1 \\ v_2 = V_{dc} + R_g I_2 \end{cases} \quad (4.11)$$

where  $I_2 = D' I_1$  and  $v_1 = D' v_2$ . In discharge mode, the equivalent load ( $R_l^{dch}$ ) is seen from the  $v_2$  terminal and  $I_2$  flows toward the grid. From (4.11), we obtain

$$\begin{aligned} R_l^{dch} &= \frac{v_2}{I_2} = \frac{R_g v_2}{v_2 - V_{dc}} \\ &= \frac{V_b R_g D' + R_b V_{dc}}{D'(V_b - D' V_{dc})} \end{aligned} \quad (4.12)$$

It is useful to express the load as a function of the voltage ratio  $\frac{V_{dc}}{V_b}$  to reflect its variation with respect to both battery and DC grid voltage variations. Dividing the nominator and denominator of (4.12) by  $V_b$ , we obtain

$$R_l^{dch} = \frac{R_g D' + R_b M}{D'(1-D'M)} \quad (4.13)$$

where  $M = \frac{V_{dc}}{V_b}$ . It should be noted, according to (2),  $M = \sqrt{2}$  for the nominal values of  $V_{dc}$  and  $V_b$ .

In recent equations,  $R_b$  and  $R_g$  are the total battery side and grid side resistances, respectively.

Similarly, the following network equations satisfy the charge mode:

$$\begin{cases} v_1 = 2V_b + 2R_b I_1 \\ v_2 = V_{dc} - R_g I_2 \end{cases} \quad (4.14)$$

where  $I_1 = D' I_2$  and  $v_2 = D' v_1$ . In charge mode, the equivalent load resistance ( $R_l^{ch}$ ) is seen from the  $v_1$  terminal and  $I_1$  flows toward the battery. From (4.13), we obtain

$$\begin{aligned} R_l^{ch} &= \frac{v_1}{I_1} = \frac{2R_b v_1}{v_1 - 2V_b} \\ &= \frac{2R_b D' V_{dc} + 4R_g V_b}{D'(V_{dc} - 2D' V_b)} \end{aligned} \quad (4.15)$$

Expressed as a function of voltage ratio, (4.15) becomes

$$R_l^{ch} = \frac{2R_b D' M + 4R_g}{D'(M - 2D')} \quad (4.16)$$

The superscripts *ch* and *dch* refer to charge mode and discharge mode parameters, respectively. The maximum loading (corresponding to the minimum load resistance) occurs for the maximum grid voltage  $V_{dc}^{max}$  and minimum battery voltage  $V_b^{min}$  in charge mode and the minimum grid voltage  $V_{dc}^{min}$  and maximum battery voltage  $V_b^{max}$  in discharge mode. Figure 4.9 shows a profile of equivalent load resistance vs. variation of voltage ratio for the test case presented in Table 4.2. The power stage parameters of the converter can be designed based on conventional ripple-based [19] or optimization-based [123] methods.

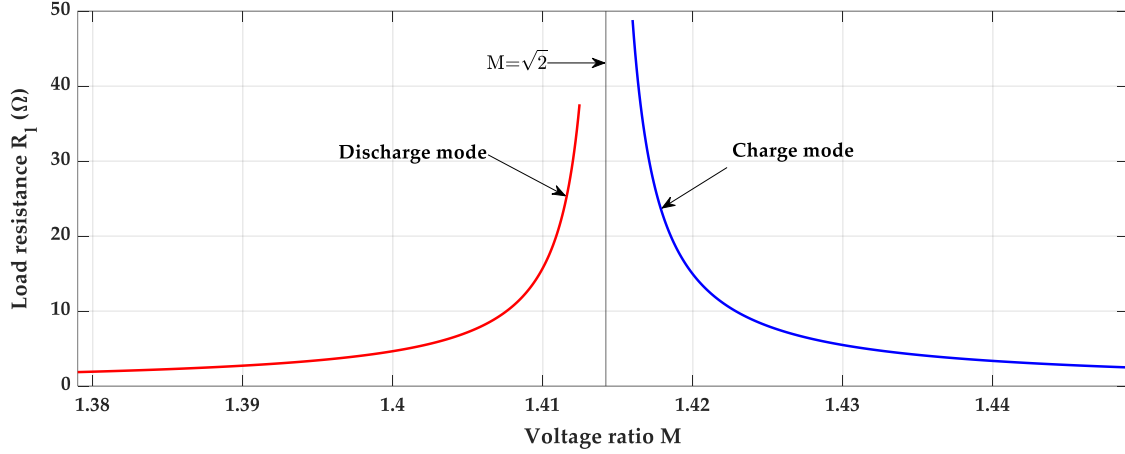


Figure 4.9 Load resistance variation for the test case presented in Table 4.2.

Table 4.2 Parameters of the proposed BDC.

$C_1$	500 $\mu$ F	$C_2$	300 $\mu$ F	$r_c$	10 m $\Omega$
$L_1$	0.45 mH	$L_2$	0.72 mH	$r_L$	0.5 m $\Omega$
$V_b$	565 V	$V_{dc}$	800 V	$\omega_{fi}$	500 $\frac{\text{rad}}{\text{s}}$
$R_b$	11 m $\Omega$	$R_g$	25 m $\Omega$	$f_s$	50 kHz
$k_{pi}, \omega_{ci}$	0.0003, 8340 $\frac{\text{rad}}{\text{s}}$		$k_{pv}, \omega_{cv}$	0.00199, 196 $\frac{\text{rad}}{\text{s}}$	
$K_{PWM}$	1	$H_v$	1	$H_c$	1
Battery:	Capacity	300 Ah	Type	Li-ion	$r_{on} = 5 \text{ m}\Omega$

#### 4.2.4 Power Stage Adjustment

Although the equal values of the inductor and capacitor for charge and discharge mode Boost converters theoretically result in similar dynamics, the external network causes unequal loading for each mode, resulting in small discrepancies that deteriorate the dynamic performance when working as a bidirectional converter. Therefore, an adjustment in the internal configuration is needed to tackle this discrepancy. Figure 4.10 shows the bode plot of the open-loop transfer function of the unadjusted Boost converters in both modes of operation for  $G_{11}(s)$  for the converter parameters shown in Table 4.2. There are two significant differences between the two modes,

i.e., the quality factor and high/low-frequency gains. This section deals with the former to provide equal dynamic performance. The latter is discussed in the next section.

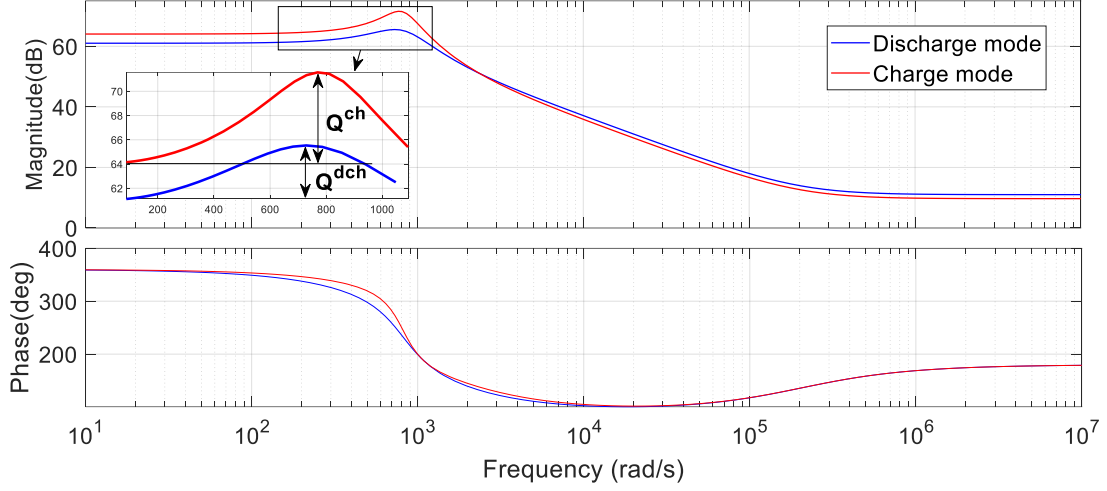


Figure 4.10 Bode plot of unadjusted converter for open-loop  $G_{11}(s)$  with zoomed-in magnitude.

From the characteristic equation of the system given in (6) and (8) and comparing with the standard form of a second-order system's equation [19][44], the quality factor  $Q$  and corresponding resonant frequency  $\omega_r$  are defined as

$$Q =: \frac{1}{\alpha_6} \sqrt{\alpha_4 \alpha_5} \quad \omega_r =: \sqrt{\frac{\alpha_4}{\alpha_5}} \quad (4.17)$$

The quality factor in frequency response corresponds to time-domain overshoot and is correlated to the damping ratio  $\delta$ , as in  $Q = \frac{1}{2\delta}$ . In general, with the symmetrical form of the proposed bidirectional converter, the discharge mode has a smaller quality factor due to the higher loading and can be chosen as the reference. Hence, equating the quality factor in discharge mode with that of the value in the charge mode yields the adjusted  $L_2$  and  $C_2$ .

$$\left(\frac{1}{\alpha_6}\sqrt{\alpha_4\alpha_5}\right)^{ch} = Q^{dch} \quad (4.18)$$

In addition, to maintain the same resonant frequency, we use

$$\left(\sqrt{\frac{\alpha_4}{\alpha_5}}\right)^{ch} = \omega_r^{dch} \quad (4.19)$$

Substituting coefficients (4.10) into (4.17) for the charge mode using the rated values of load resistance  $R_l^{ch}$  and input voltage  $E_1^{ch}$  in (4.18) and (4.19) yields

$$Q^{dch^2} L_2^2 + Q^{dch^2} \gamma^2 C_2^2 + (Q^{dch^2} \gamma - \alpha_4) \alpha_4 L_2 C_2 = 0$$

$$\omega_r^{dch^2} (R_l^{ch} + r_c)^2 L_2 C_2 - \alpha_4 = 0 \quad (4.20)$$

$$\gamma = R_l^{ch} r_L + r_c r_L + R_l^{ch} D' r_c$$

subject to

$$L_{2min} < L_2 < L_{2max} \text{ and } C_{2min} < C_2 < C_{2max}$$

where (4.20) is a bivariate quadratic system of equations that can be solved for  $L_2$  and  $C_2$ . The minimum values of the inductor and the capacitor are obtained based on ripple criteria. An estimation of the maximum values can be roughly calculated based on the ratio of load resistances, such that  $\frac{L_{2max}}{L_1} \cong \frac{R_l^{ch}}{R_l^{dch}}$  and  $\frac{C_1}{C_{2max}} \cong \frac{R_l^{ch}}{R_l^{dch}}$ . Figure 4.11 shows the bode plot of the adjusted converter with equal quality factors for the converter's case, as presented in Table 4.2.



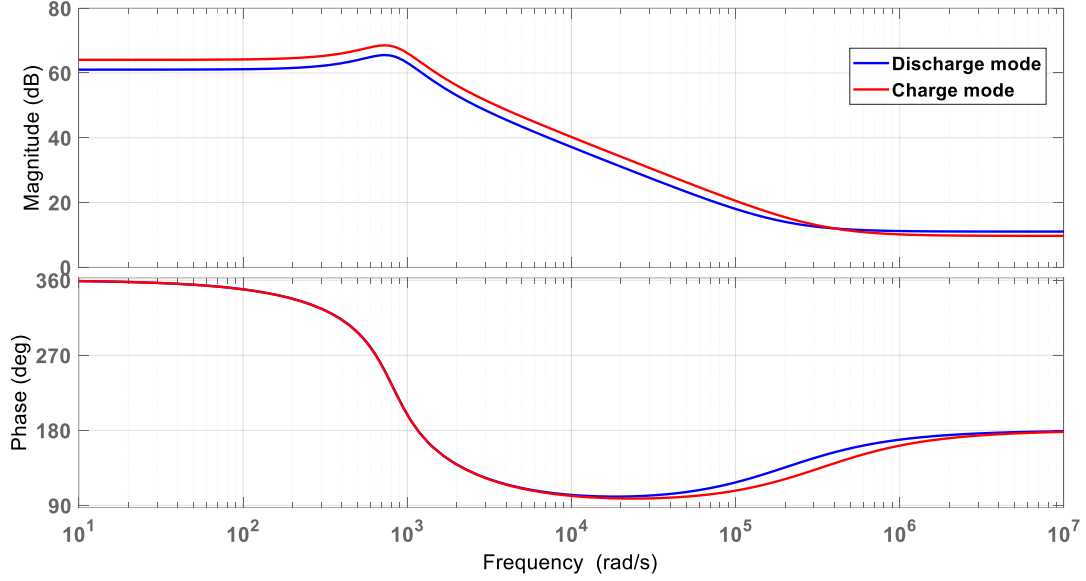


Figure 4.11 Bode plot of the adjusted converter for open-loop  $G_{11}(s)$ .

### 4.3 Control System

The transfer functions derived in the earlier sections can be utilized to design different schemes of closed-loop controllers based on the linearized models. The BESS in the DC grid is usually used in the grid-forming operation to control DC grid voltage. In contrast, in grid-following operation, power is injected/absorbed to track the reference power signals defined by the power management system (PMS). The power mode control is designed based on the current controller using a reference power to generate the reference current. Here, a design approach is presented based on the frequency response of the open/closed-loop gain transfer function for the proposed BDC controller design presented in subsection 4.3.1. Subsection 4.3.2 briefly discusses the conventional BDC controller scheme as a background framework for the comparison made in Section 4.4.

#### 4.3.1 Proposed Converter Controller

##### 4.3.1.1 Current Control Mode

Figure 4.12a illustrates a block diagram of the small-signal model of the converter with the

current controller.  $G_{ci}$ ,  $K_{PWM}$ , and  $H_c$  are the compensator, the PWM gain, and the feedback sensor's transfer function, respectively.

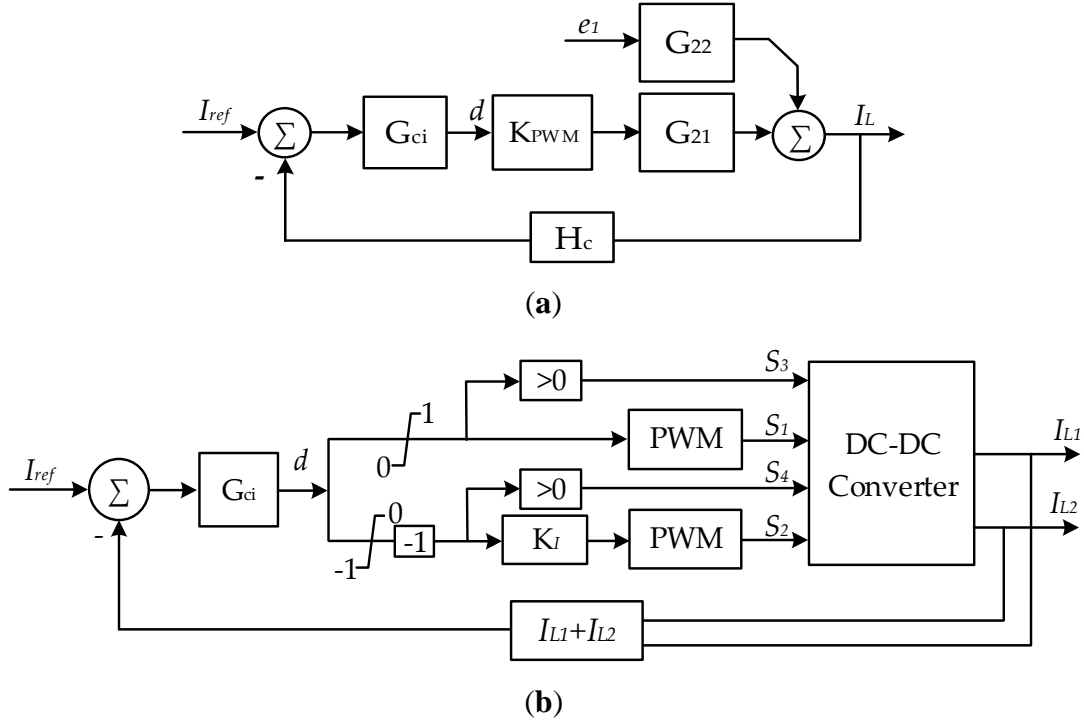


Figure 4.12 Current controller block diagram of the proposed converter. (a) Closed-loop small-signal model based on the discharge mode parameters for reference; (b) plant model.

Figure 4.13a shows the bode plot of the open-loop  $G_{21}$  for both modes with adjustment made in the power stage for the case study presented in Table 4.2, which has a similar phase but dissimilar gain. Before the controller is designed, another adjustment is needed to obtain equal bidirectional gain dynamics. The overall behavior of  $G_{21}$  is like a single real pole, which is  $\frac{G_{210}}{\frac{s}{\omega_{b21}} + 1}$ , where  $\omega_{b21}$  is the cut-off frequency and  $G_{210} = \frac{\alpha_7}{\alpha_4^2}$  is the DC gain. By neglecting ESRs,  $G_{210} \cong \frac{2E_1}{R_l D'^3}$  is obtained in terms of converter rated values for the Boost converter, as depicted in Figure 4.6. In the low frequency,  $|G_{21}(s)| = G_{210}$ , whereas in the high frequency, the gain decreases with a slope of  $-20 \frac{dB}{dec}$ .

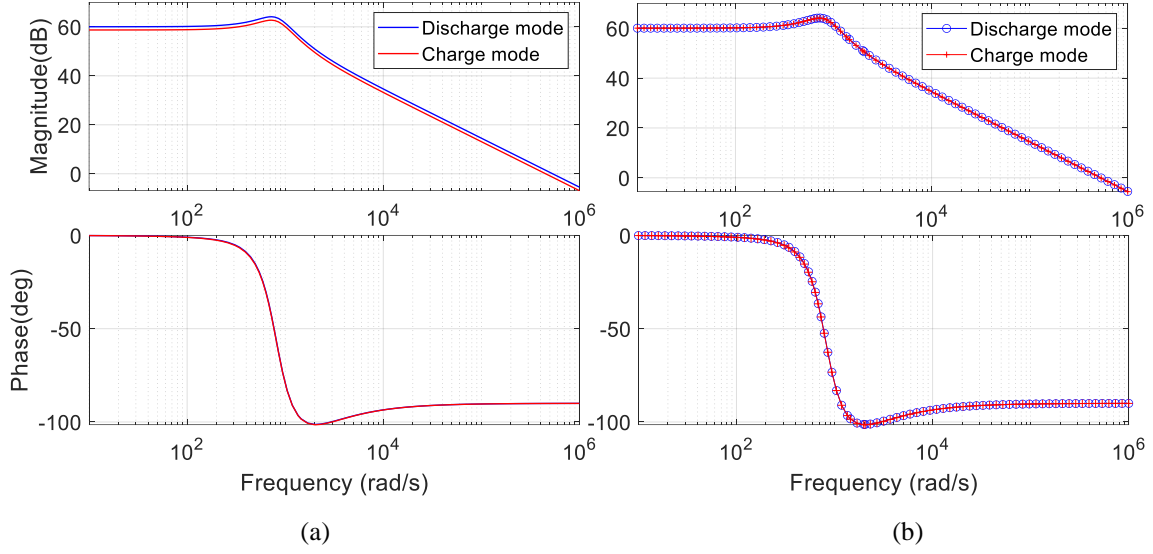


Figure 4.13 Bode plots of duty ratio-to-inductor current  $G_{21}(s)$ . (a) uncompensated charge mode gain; (b) compensated charge mode gain.

The adjustment made in the earlier section guarantees equal bidirectional bandwidth for  $G_{21}$ . Therefore, to have the same bidirectional gain crossover frequency, the following equity should be supported:

$$\begin{aligned}
 G_{21_0}^{ch} &= G_{21_0}^{dch} \\
 \Rightarrow \frac{2V_{dc}}{R_l^{ch} D'^3} &= \frac{2V_b}{R_l^{dch} D'^3}
 \end{aligned} \tag{4.21}$$

Selecting the discharge mode as a reference, gain coefficient  $K_I$  is obtained from (4.21) for the charge mode current control loop.

$$K_I = \frac{V_b R_l^{ch}}{V_{dc} R_l^{dch}} \tag{4.22}$$

Figure 4.13b shows the bode plot of both modes for the open-loop  $G_{21}$  after applying gain adjustment, yielding analogous bidirectional dynamics. The closed-loop current controller can be designed based on the discharge mode parameters, which is the reference mode. For sufficient

disturbance rejection during load variation, we choose the lag type controller for  $G_{ci}$ . Although the lag controller relatively reduces converter response (hence its bandwidth), it reduces the switching noise in the feedback signal. Inspired by the method discussed in [19], the compensator transfer function is given by

$$G_{ci}(s) = k_{pi} \left( 1 + \frac{\omega_{ci}}{s} \right) \quad (4.23)$$

where  $k_p$  is the proportional gain and  $\omega_{ci}$  is the controller's zero, which is selected at least one decade below the closed-loop gain crossover frequency  $\omega_{c21}$  to maintain an adequate phase margin and therefore system stability. On the other hand, to suppress switching harmonics,  $\omega_{c21}$  is placed well below the switching frequency  $f_s$ . The approximate practical proportions  $\omega_{c21} = \frac{2\pi f_s}{4}$  and  $\omega_{ci} = \frac{\omega_{c21}}{10}$  are chosen for this work. The unity value of the loop gain of the compensated current control loop occurs at  $\omega_{c21}$ , i.e.,  $|L(j\omega_{c21})| = K_{PWM}|G_{ci}(j\omega_{c21})G_{21}(\omega_{c21})H_c(j\omega_{c21})| = 1$ . The value of the controller gain is  $|G_{ci}| = 1.1k_{pi}$  at this frequency. Then, the compensator's coefficient is obtained as follows:

$$k_{pi} = \frac{1}{1.1K_{PWM}|G_{21}(j\omega_{21})H(j\omega_{21})|} \quad (4.24)$$

Since the approach is practical, further tuning might be needed to ensure closed-loop stability, limited overshoot, and reasonable phase margin. The reference current  $I_{ref}$  is calculated based on the reference power  $P_{ref}$  acquired from PMS. In the current (power) control mode, it is assumed that other devices in the grid control the grid voltage. The sign of  $P_{ref}$  determines the converter operation mode as follows:

$$\begin{cases} P_{ref} > 0, I_{ref} = \frac{P_{ref}}{v_2} & \text{Charge mode} \\ P_{ref} < 0, I_{ref} = \frac{-P_{ref}D'}{\eta v_2} & \text{Discharge mode} \end{cases} \quad (4.25)$$

where  $\eta$  is the converter efficiency in discharge mode and can be calculated for a Boost converter; if ESRs are neglected,  $\eta = 1$ .  $P_{ref}$  is a reference signal obtained from PMS to compensate for real-time load/generation power mismatch or constant charging.

#### 4.3.1.2 Voltage Control Mode

As Figure 4.11 shows, due to the asymmetric property of the converter in two modes, the high- and low-frequency gain values are not the same for the open-loop duty ratio-to-output voltage  $G_{11}(s)$ . Gain equalization further results in bidirectional dynamic symmetry. For the voltage control loop with discharge mode being the target frequency response, the following equations hold:

$$\begin{aligned} \lim_{\omega \rightarrow 0} |G_{11}^{dch}(j\omega)| &\approx \lim_{\omega \rightarrow 0} |G_v(j\omega) \cdot G_{11}^{ch}(j\omega)| \\ \lim_{\omega \rightarrow \infty} |G_{11}^{dch}(j\omega)| &\approx \lim_{\omega \rightarrow \infty} |G_v(j\omega) \cdot G_{11}^{ch}(j\omega)| \end{aligned} \quad (4.26)$$

where  $G_v(s)$  should be a filter with negligible change in phase to match the asymptotic low- and high-frequency gains of charge mode to that of discharge mode. We consider a pair of real pole/zero, given by

$$G_v(s) = K_v \frac{s + \omega_z}{s + \omega_p} \quad (4.27)$$

where  $K_v$ ,  $\omega_z$  and  $\omega_p$  are the filter's high-frequency gain, zero, and pole, respectively, and should be designed to match bidirectional dynamics for  $G_{11}$ . The filter should reduce low-frequency gain and raise high-frequency gain while causing an insignificant change in phase to obtain the target

frequency response. For a Boost converter, neglecting ESRs results in  $|G_{11}| = \frac{E_1}{R_l D' C}$  as  $\omega \rightarrow \infty$  and  $|G_{11}| = \frac{E_1}{D'^2}$  as  $\omega \rightarrow 0$ . Therefore, the criteria outlined in (4.26) determine the following asymptotes:

$$\begin{aligned} K_v &= \lim_{\omega \rightarrow \infty} \frac{|G_{11}^{dch}(j\omega)|}{|G_{11}^{ch}(j\omega)|} = \frac{V_b R_l^{ch} C_2}{V_{dc} R_l^{dch} C_1} \\ K_v \frac{\omega_z}{\omega_p} &= \lim_{\omega \rightarrow 0} \frac{|G_{11}^{dch}(j\omega)|}{|G_{11}^{ch}(j\omega)|} = \frac{V_{dc}}{V_b} \\ \frac{\omega_z}{\omega_p} &= \frac{V_{dc}^2 R_l^{dch} C_1}{V_b^2 R_l^{ch} C_2} \end{aligned} \quad (4.28)$$

this implies the filter gain rolls off from a nonzero DC gain in  $\omega_z$  and rolls on to a nonzero asymptotic gain in  $\omega_p$ , with a slope of  $K_v \frac{\omega_p - \omega_z}{\sqrt{2} \omega_p} > 0$ ,  $\omega_z < \omega_p$ . The maximum phase angle of  $\phi_m = \tan^{-1} \left( \frac{\omega_p - \omega_z}{2\sqrt{\omega_p \omega_z}} \right)$  occurs at the frequency of  $\omega_m = \sqrt{\omega_p \omega_z}$ . Proper choice of  $\omega_z$  (and  $\omega_p$ ) results in a suitable gain fit and insignificant phase angle discrepancy between two modes. Since the adjustment made in the power stage in the previous section guarantees the same bidirectional cut-off frequency, a good approximation is to equate the zero with the cut-off frequency of  $G_{11}(s)$ , i.e.,  $\omega_z = \omega_{c11}$ . Figure 4.14 compares the bode plots of the power stage-adjusted transfer function  $G_{11}(s)$  for gain compensated and uncompensated charge mode for the case study presented in Table 4.2. In this example, a maximum of  $\phi_m = 14.8^\circ$  occurs in the phase angle at  $\omega_m = 46.64 \frac{\text{krad}}{\text{s}}$ , which negligibly changes the charge mode gain and phase in this vicinity but makes an overall frequency response fit regarding the discharge mode.

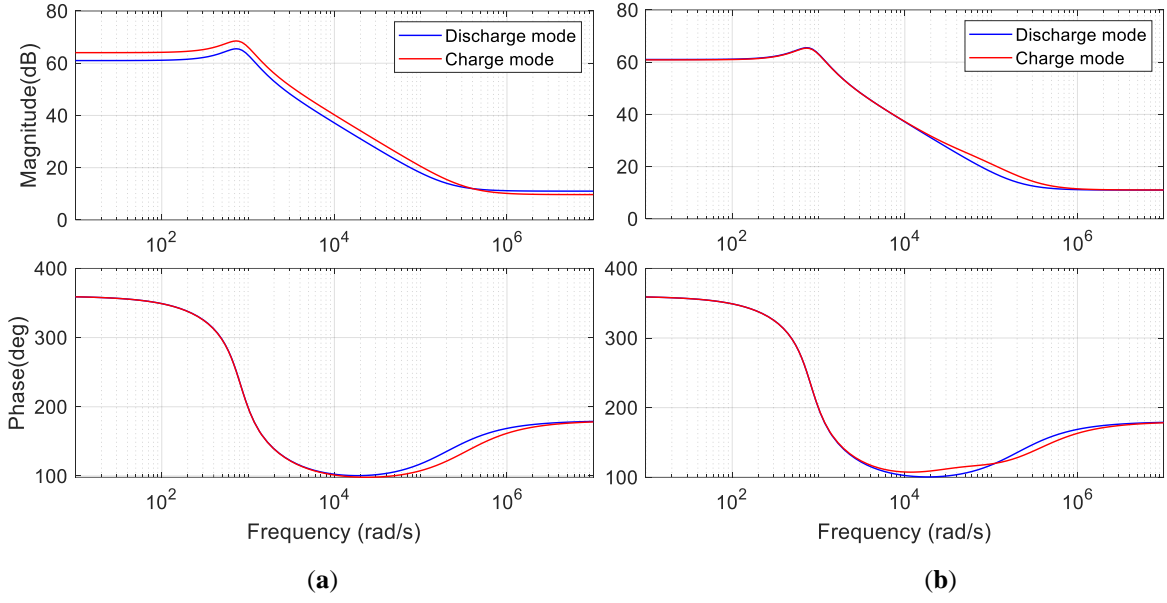


Figure 4.14 Bode plots of duty ratio-to-output voltage ( $v_2$ ),  $G_{11}(s)$ . (a) Uncompensated charge mode; (b) compensated charge mode.

Figure 4.15a shows the small-signal model of the converter based on the linearized model for the voltage controller based on the discharge mode parameters. In the voltage control mode, the objective is to control the grid voltage by tracking the reference value  $V_{ref}$  which is given by

$$V_{ref} = V^* + R_g \bar{I}_2$$

$$\bar{I}_2 = \frac{\omega_{fi}}{s + \omega_{fi}} I_2 \quad (4.29)$$

where  $V^*$  is the voltage set point of the converter at the connection terminal  $v_2$  that, in general, is equal to  $V_{dc}$ , and  $\omega_{fi}$  is the cut-off frequency of a low-pass filter to suppress converter current-switching harmonics. The following transfer function is given for the voltage compensator, a lag type controller analogous to that of the current controller counterpart:

$$G_{cv}(s) = K_{pv} \left( 1 + \frac{\omega_{cv}}{s} \right) \quad (4.30)$$

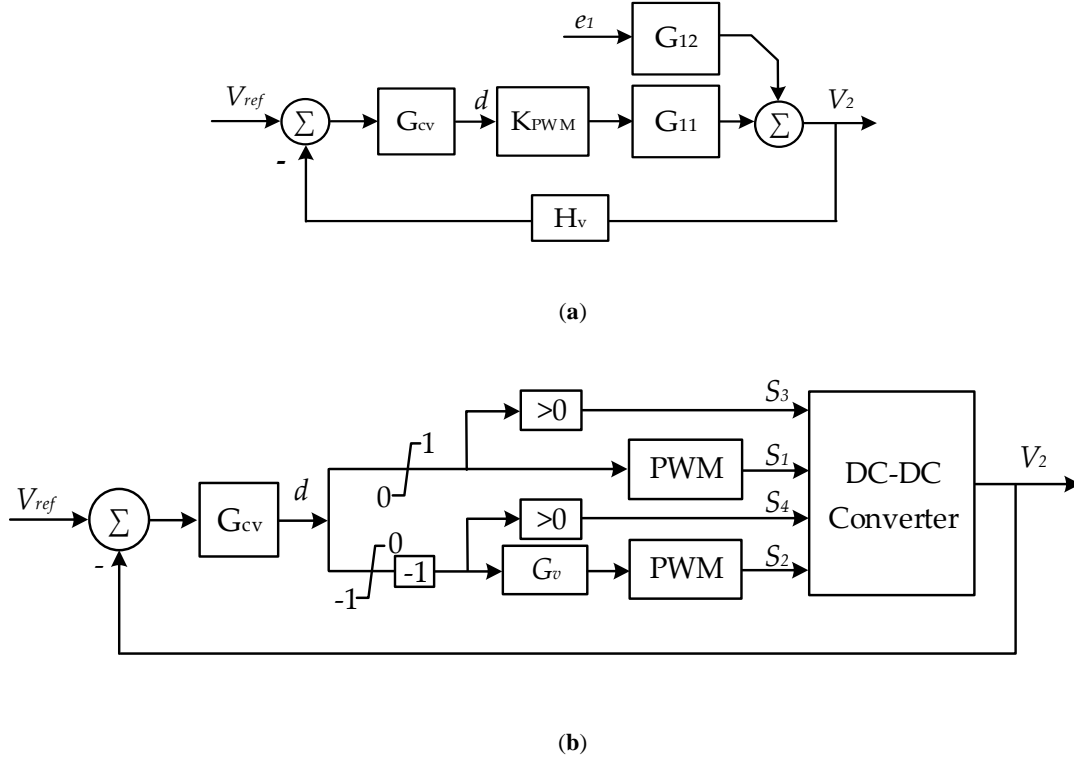


Figure 4.15 Voltage controller block diagram of the proposed converter. (a) Closed-loop small-signal model based on the discharge mode parameters as the reference; (b) plant model.

where  $K_{pv}$  and  $\omega_{cv}$  are the controller's proportional gain and zero obtained in an analogous way to that of the current controller in the previous section. It should be noted that the voltage controller must be much slower than the current controller, resulting in a lower bandwidth since, as observed in Figure 4.14,  $G_{11}$  has one pole which is not rejected at high frequency. On the other hand, this single loop voltage control is relatively faster than the conventional design dual-loop scheme in response to grid voltage variations. As the DC grid voltage gets stiffer, the dynamics of the BDC in voltage control mode tend to be more oscillatory, particularly under heavy loads. This property of BDC makes it disparate from the unidirectional converter, where the steady-state duty ratio  $D$  varies based on the load value. In a bidirectional converter,  $D$  is a constant defined by the grid and battery voltages given in (1) and (2). Note that the battery voltage does not change significantly across the operational range of state of charge (SoC). Figure 16 shows the battery voltage variation



for the typical minimum and maximum ranges of SoC under four loading conditions. Therefore, there should be a maximum limit for the inductor value to restrict the magnitude of the voltage oscillations in  $v_2$  during heavy loading. This situation results in a tradeoff between inductor current ripples and voltage oscillations in the full load.

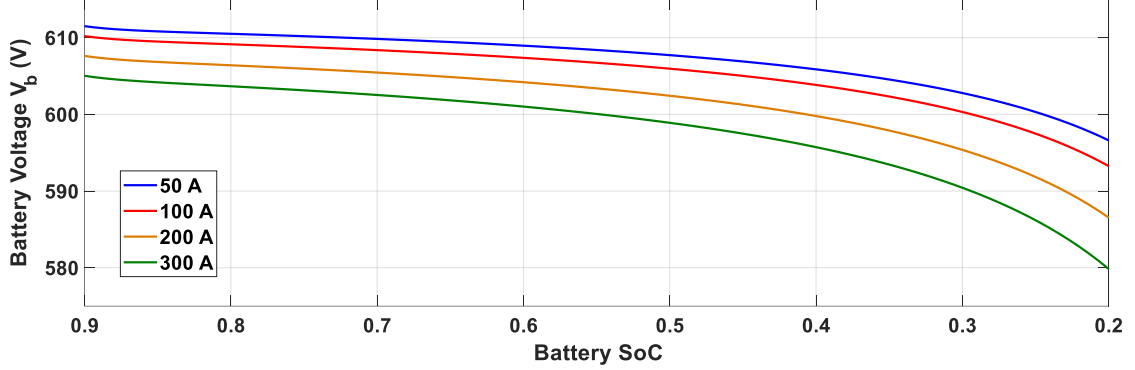
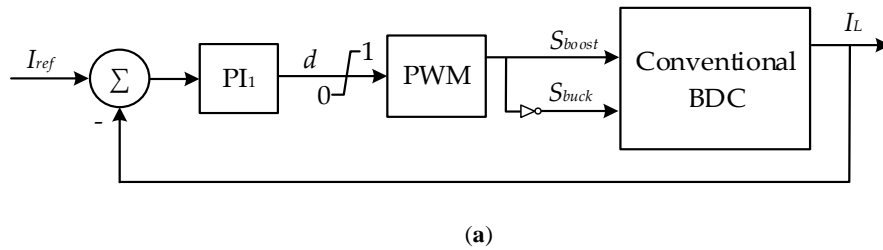


Figure 4.16 Battery voltage vs. state of charge (SoC) for different loading conditions.

### 4.3.2 Conventional BDC Controller

The power stage diagram in Figure 4.1 is used for the conventional BDC, with the parameters equal to the discharge mode of the proposed BDC. The control system of the conventional BDC is a single loop PI controller [72][124] for the current control mode displayed in Figure 4.17a, and a dual-loop PI-based control [125] for the voltage control mode illustrated in Figure 4.17b. Table 4.3 presents all the parameters of conventional BDC. The variables  $k_p$  and  $k_i$  in Table 4.3 refer to the proportional and integral gains, respectively, of the PI controllers illustrated in Figure 4.17.



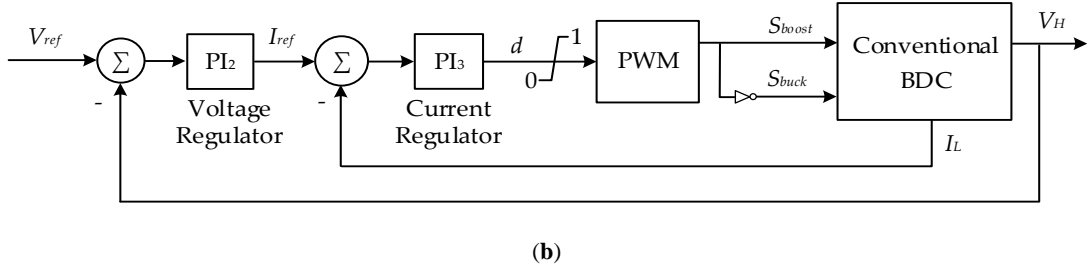


Figure 4.17 Conventional BDC control systems used for comparison analysis. (a) Current control; (b) voltage control.

Table 4.3. Conventional BDC parameters.

$C$	500 $\mu\text{F}$	$L$	0.45 mH	$V_b$	200 V
$r_c$	10 m $\Omega$	$r_L$	0.5 m $\Omega$	$R_b$	11 m $\Omega$
PI <sub>1</sub> :	$k_{pi}$	0.0003	$k_{i1}$	0.1	$r_{on} = 5 \text{ m}\Omega$
PI <sub>2</sub> :	$k_{p2}$	0.008	$k_{i2}$	0.8	
PI <sub>3</sub> :	$k_{p3}$	0.09	$k_{i3}$	5	
Battery:	Capacity	1700 Ah	Type	Li-ion	

#### 4.4 Simulation Results

In this section, the effectiveness of the proposed converter is evaluated and compared with that of the conventional type for the converter case presented in Table 4.2. The case study HMG includes a three-phase 460 V/60 Hz AC grid and an 800 V DC grid power system, as shown in Figure 3, with the parameters presented in Table 4. It is simulated using detailed switching models for power electronic devices by applying a sampling frequency of 2 MHz for discrete time-domain simulations performed in the MATLAB\Simulink environment. In total, three instances are simulated using the test systems for two separate cases, as detailed below.

**Case I—Grid-connected HMG:** In this state, the DC grid is connected to the main grid through a grid-following ILC. In the voltage control mode, the BDC controls the DC grid voltage, while ILC tracks the reference powers. In the current control mode, this scheme switches between BDC and

ILC.

Table 4.4 Grid parameters.

$C_f$	2500 $\mu$ F	$C_{dc}$	2.5 mF	$R_{line}$	70 m $\Omega$
$L_{f1}$	0.4 mH	$L_{f2}$	8 $\mu$ H	$L_{line}$	63 $\mu$ H
$V_{AC}$	460 V	DER1	250 kW	DER2	307 kW
DC Load	1.6~4 $\Omega$	AC Load	1.053 $\Omega$	ILC	250 kW

**Case II—Islanded HMG:** In this state, Case I is modified to form an islanded HMG. In the voltage control mode of BDC, the ILC is a grid-forming VSC, and DER1 is a grid-following generation source to supply reference active/reactive powers. All control systems of VSCs in ILC and DER1 are well-established structures adopted from [29].

A narrow-band dead zone is implemented in both converters' control systems to prevent discontinuous conduction mode (DCM) operation. An equal value of ON-state resistance ( $r_{on} = 5 \text{ m}\Omega$ ) is applied for all power switches and diodes in both converter types. DER2 is modeled as a solar PV connected via a DC-DC converter to the DC bus to track the maximum power point. Figures 4.18–4.20 show the dynamic response of the system to the separate pulsed changes in DC load in Case I for current and voltage control modes, respectively. At first, the DC load demands 370 kW power. For the voltage control mode, starting from 0.5 seconds, four subsequent step changes occur, i.e., [170 216 244 334] kW, in 0.3 s intervals. For the current control mode, three subsequent pulsed variations take place, i.e., [257 130 590] kW, in 0.5 s intervals. In the current control mode, the controller effort is lighter than that of the voltage control mode, despite the heavier load change. The significant performance of the proposed BDC can be observed in mode changeovers from discharge to charge mode and vice versa. Although the conventional BDC works well in Boost operation, it has deficient performance during Buck mode.

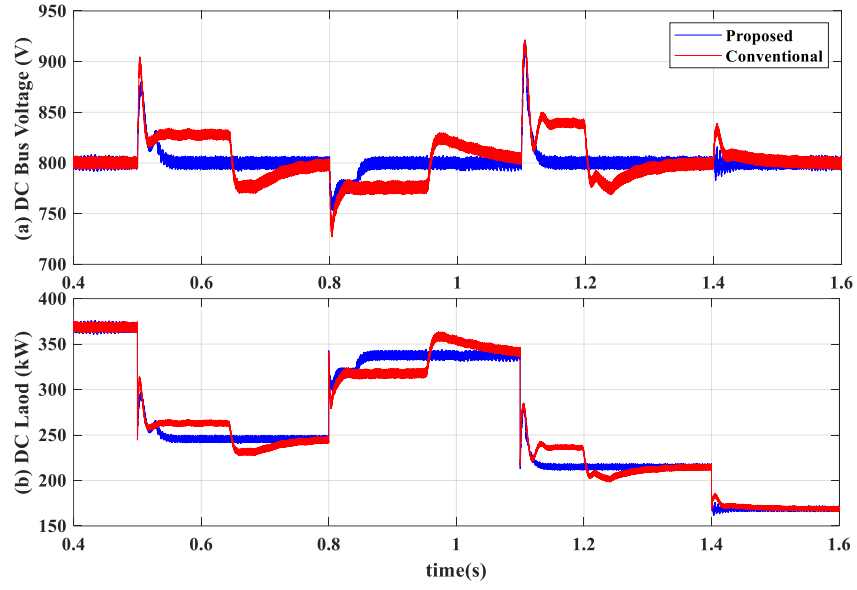


Figure 4.18 Converter response to pulsed DC load change for Case I with voltage control mode.

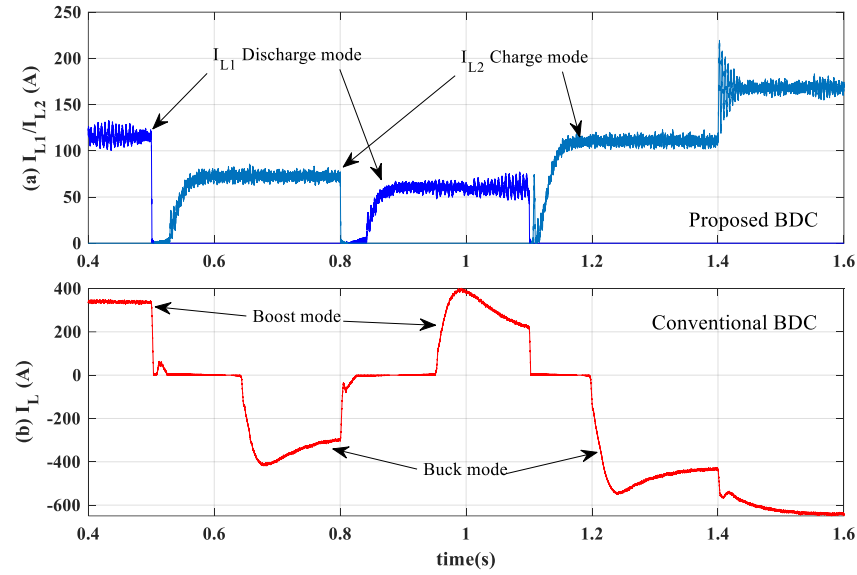


Figure 4.19 Inductor currents in voltage control mode for Case I.

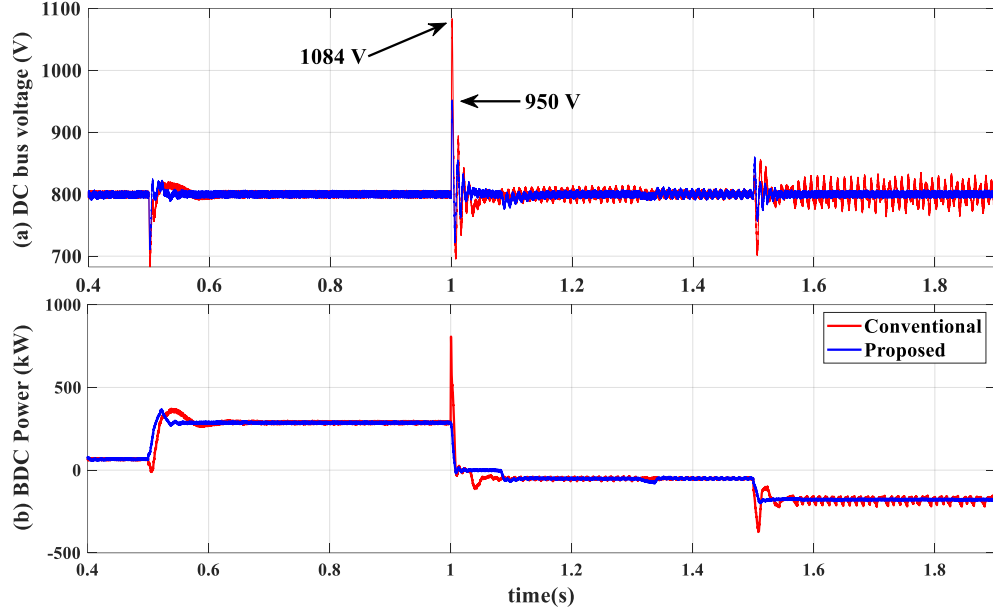


Figure 4.20 Converter response to pulsed DC load changes for Case I with the current controller.

Figure 4.21 illustrates the system's dynamic response to the active power generation variations in DER1 for Case II with BDC in the voltage control mode. Initially, DER1 generates 150 kW of active power, causing ILC to exchange 50 kW power from the DC side to the AC side. Starting from second 1, four subsequent power generation disturbances, i.e., [100 200 250 300] kW, occur in 150 ms intervals in DER1. This power fluctuation in the AC side propagates to the DC side by exchanging power in ILC, as shown in Figure 4.21. Like Case I, the mode changeover performance in the proposed BDC is superior to that of the conventional type, resulting in a faster response to grid voltage variations.

## 4.5 Chapter Conclusion

This chapter proposed a novel bidirectional DC-DC converter for energy storage applications in DC microgrid and HMG systems composed of two back-to-back Boost converters in the power stage adjusted to symmetrical operation, as well as an equal gain ratio in both charge and discharge modes. Systematical methodologies were implemented based on the frequency response of

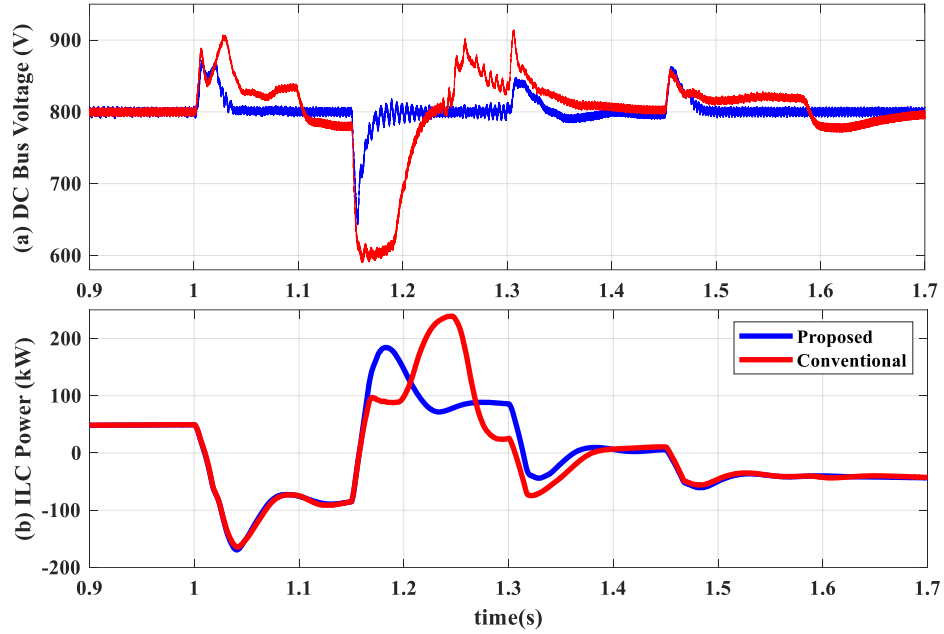


Figure 4.21 System response to power generation variation in DER1 in Case II with BDC in voltage control.

converter plant models in charge and discharge modes. A novel approach was proposed to estimate the equivalent load resistance for each operation mode, which is a key parameter in open-loop transfer functions rendering the converter loading to not be equal during two modes. The efficacy of the proposed converter was evaluated and compared with that of the conventional type via two case studies for voltage and current mode controllers, respectively. The simulation results demonstrated that the proposed converter exhibited superior performance in handling power and voltage fluctuation in the DC grid. The battery voltage (low-voltage side) must be selected in proportion to DC bus voltage (high-voltage side), representing the only limitation of this converter.

## **Chapter 5 Performance Analysis of Hybrid Microgrids Under Influence of Energy Storage Location [126]**

### **5.1 Introduction**

The recent advancement in storage technology has made it possible to use several types of energy storage systems in various scales in power and energy applications[127],[128]. However, the BESS is the most viable solution thanks to its efficacy [129] (in terms of operation and maintenance, energy efficiency and density, and reliability), low environmental pollution [78], and fast ramp rate [130]. Therefore, it is a suitable option for primary frequency control in microgrids and utility-scale applications [131].

Following an introductory literature review in section 2.7 in chapter 2, this chapter performs a comparative study to examine the influence of the location of aggregated BESS system on the dynamic performance of the islanded HMGs based on a heuristic approach. The present study is an extension of a recently published research in [118]. Two general case studies (i.e., an industrial and a fully converter-based islanded HMGs) are considered for simulation purposes. The major contributions of this chapter are as follows:

- The HMG performance is examined when separately operating with ACB and DCB for the same operating conditions.
- A new bidirectional DC-DC converter is employed for DCB, which enhances grid performance.
- A highly non-linear and dynamically complex power system with a combination of high penetrated RES, high inertia generation, and frequency-dependent AC load is included for an industrial case study to emulate an actual HMG.

## 5.2 HMG case studies and their configurations

As mentioned in the previous section, this paper considers two case studies to conduct a comparative analysis to substantiate the results. The control strategies implemented in each BESS type in each case study are such that the BESS has the maximum response to voltage/frequency deviations in the grid. It should be noted that, in addition to BESS dynamics, the ILC control strategy contributes to the HMG dynamic performance. The ILC roles will be discussed for each case study.

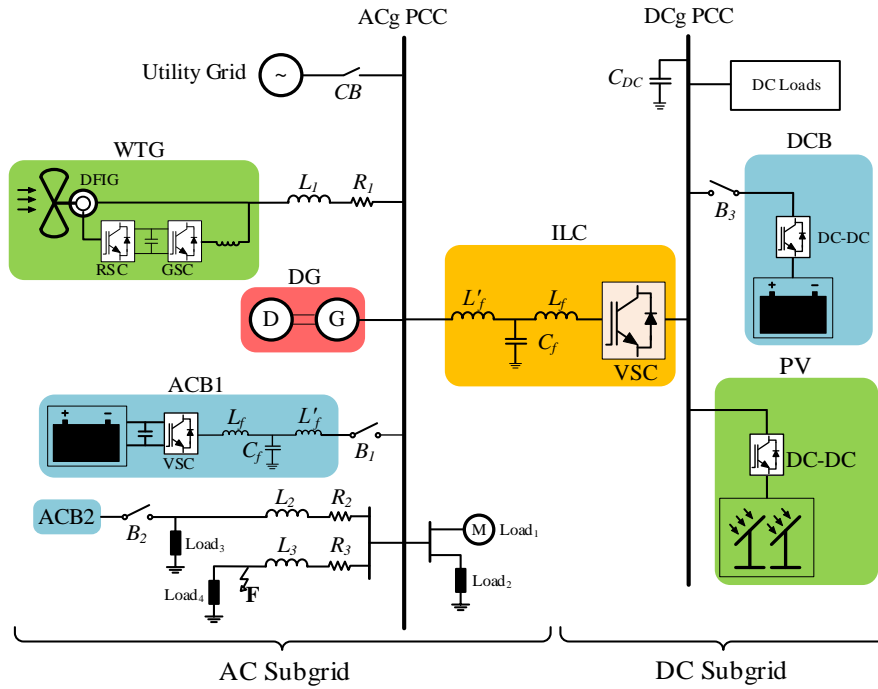


Figure 5.1 Hybrid AC/DC microgrid in Case Study I.

### 5.2.1 Case Study I: An Industrial HMG

The first case is a relatively aggregated HMG thread where DERs and BESS are directly connected to AC and DC PCCs (see Figure 5.1). This case study is an improved version of the test system used in the previous chapter. This case contains a high penetration of RES, a combination of high and low inertia DERs as well as a frequency-dependent load to realize a real-world industrial HMG.



The AC subgrid includes a variable speed Wind Turbine Generator (WTG) as the main RES, a DG to provide baseload and reactive power regulation, three constant loads, and an induction motor to represent the frequency-dependent load. The DC subgrid incorporates a Photovoltaic (PV) solar power generation and a DC load with constant resistance. All grid components are modeled based on well-known full-scale models of rotating devices and power electronics converters found in the literature [15]. Except for ACB and ILC that communicate with power management system (PMS) through ultra-low-bandwidth communication links to transmit the active power signals, all other DERs are controlled by primary level control exploiting local measurements. There are three candidate locations for this case study illustrated in Figure 5.1. When switch B1 is closed, and B2 and B3 are open, the HMG operates with ACB1. When B2 is closed, and B1 and B3 are open, it works with ACB2. Also, when B3 is closed, and B1 and B2 are open, it runs with the DCB.

In this case study, the DG works as a voltage source, and its governor and automatic voltage regulator have the minimum response to frequency and voltage deviations. A conventional droop control with power reference tracking is implemented in DG to generate setpoint active/reactive powers as follows:

$$\begin{cases} \omega_{DG}^{ref} = \omega_{DG}^* - m_{DG}(P_{DG} - P_{DG}^*) \\ V_{DG}^{ref} = V_{DG}^* - n_{DG}(Q_{DG} - Q_{DG}^*) \end{cases} \quad (5.1)$$

where  $\omega_{DG}$  and  $V_{DG}$  are frequency and voltage at DG terminal, respectively, and superscripts ‘*ref*’ and ‘\*’ represent their reference and setpoint values.  $m_{DG}$  and  $n_{DG}$  are droop coefficients that are tuned to obtain a minimum ramp-rate for power-sharing during the transients.  $P_{DG}$  and  $Q_{DG}$  are DG active and reactive power outputs, respectively, and superscript ‘\*’ represents their setpoint values.

The control strategy of ILC depends on BESS location, i.e., ACB or DCB (see Figure 5.2). When operating with ACB (i.e., sw1 switched on ACB in Figure 5.2), the BESS works as a grid-feeding VSC to maintain active and reactive power balance between load and generation through reverse droop-based control [90] and indirectly regulates the DCg voltage via ILC. In this state, the ILC works as a grid-following VSC to control the DCg voltage. Since PV runs in the current source mode to track maximum power point (MPP), the ILC is the only voltage source in DCg. Power fluctuations in DCg result in DCg voltage variation that is controlled by ILC, accordingly.

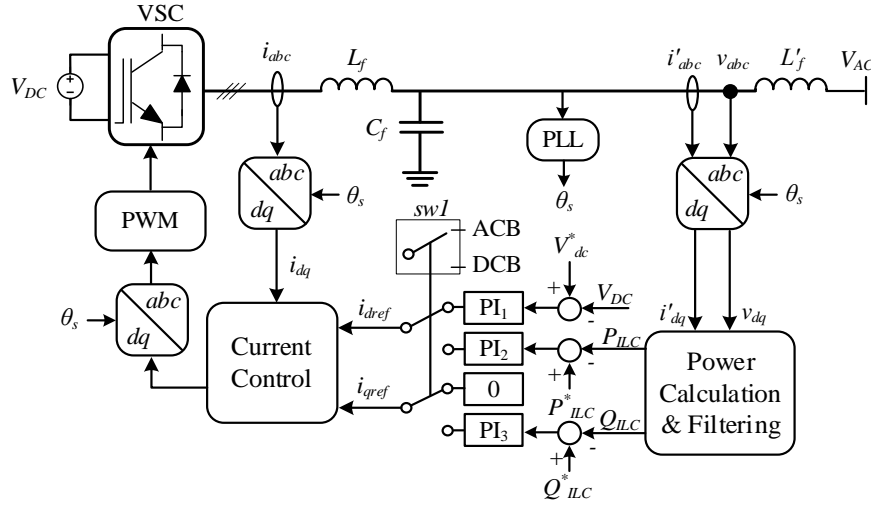


Figure 5.2 ILC control system for Case I with both BESSs and Case II with ACB only.

On the other hand, during the operation with DCB (i.e., sw1 switched on DCB in Fig. 2), the DCB works as a voltage source in DCg, and ILC controls the active and reactive power balance in ACg as follows:

$$P_{ILC}^* = \sum_{i \in S_L} P_{L_i} + \sum_{j \in S_I} P_{loss_j} - \sum_{k \in S_G} P_{G_k} \quad (5.2)$$

where  $P_{ILC}^*$  is the ILC reference power,  $P_{L_i}$ ,  $P_{loss_j}$  and  $P_{G_k}$  are the active power of AC loads, transmission losses, and active power generations in ACg, respectively, and  $S_L = \{1..4\}$ ,  $S_I = \{1..3\}$  and  $S_G = \{WTG, DG\}$ . All other elements of ILC control in Figure 5.2 can be found in the literature

and are not discussed here for brevity. The BESS control strategy and its power references will be discussed in section 3 with more details.

### 5.2.2 Case Study II: A Fully Converter-based HMG

The modern microgrids evolve into fully converter-based systems in which all DERs are connected to the grid through low-inertia power electronic converters. Case study II, unlike Case study I, deals with an islanded 6-bus HMG with four distributed DERs and local loads shown in Figure 5.3, all controlled by local measurements (primary control), and no communication link is implemented. DER1 and DER4 are candidate locations for the BESS.

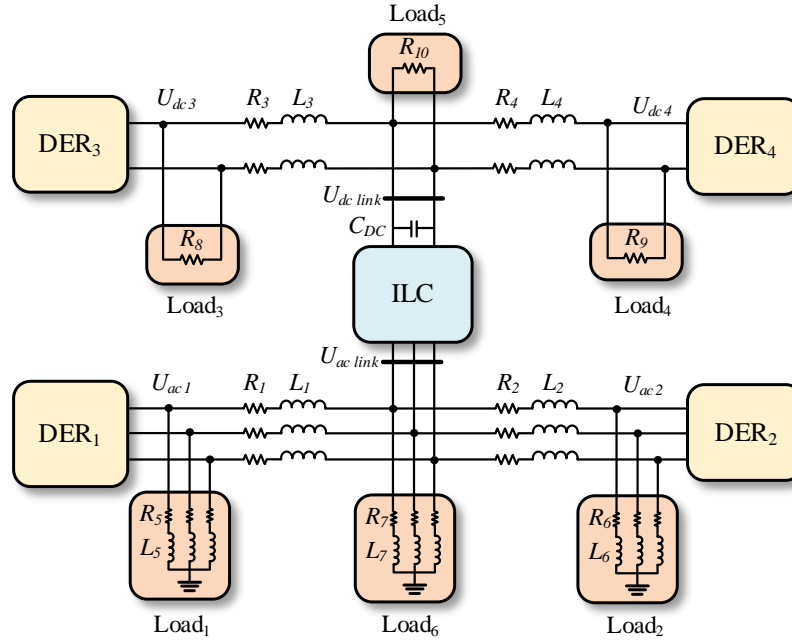


Figure 5.3 Case II Hybrid microgrid; DER1 and DER4 are the candidate locations for BESS

For the case with AC BESS, DER1 serves as ACB, and its VSC works in grid-forming mode to control the voltage and frequency at its terminal. In this state, ILC operates in grid-following mode, like Case I with ACB, shown in Figure 5.2, to control the DC link's voltage and is considered the voltage source for DCg. When operating with DC BESS, DER4 serves as DCB, and its converter works as a voltage source to control the DC voltage at its terminal. In this state, ILC runs

in grid-forming mode and serves as a voltage source for ACg, i.e., its role swaps with DER1 in the ACB case.

All non-BESS DERs in both operating cases (DER2 and DER3 in both BESS cases, and DER1 and DER4 with DCB and ACB, respectively) are constant power RESs running in grid-feeding mode to track MPP (MPPT source). Therefore, the voltage (and frequency in ACg) in all non-BESS buses will have small deviations from setpoint values. The primary sources for non-BESS DERs are modeled as constant DC voltage sources connected through VSCs and DC-DC boost converters for DERs in ACg and DCg, respectively. Figures 5.4 and 5.5 show the power stage and control diagram of non-BESS DERs utilized in this paper. The MPPT system provides these DERs with the reference current/power depending on available renewable energy and ambient conditions. Table 5.1 summarizes the role of DERs in each BESS operating case.

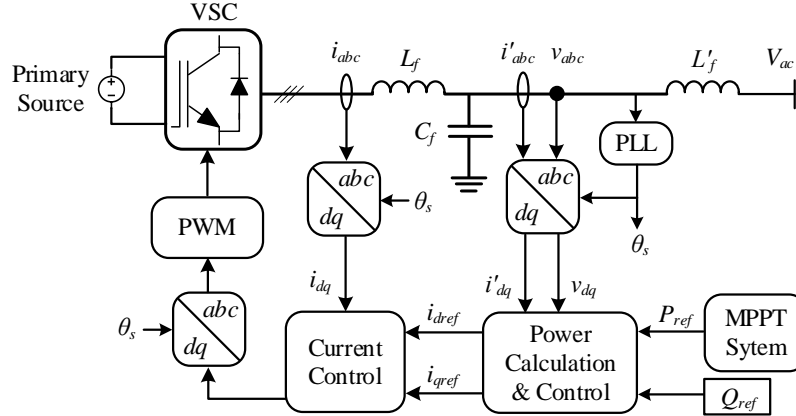


Figure 5.4 Power stage and control diagram of non-BESS DERs in ACg in Case II [29].  $V_{aci}$  is the terminal voltage and  $i \in \{1,2\}$ .

### 5.3 BESS Modelling

#### 5.3.1 Battery Model

The ACB and DCB have the same capacity in terms of energy density. This study considers the battery state of charge (SoC) for modeling. In this paper, we use a dynamic model of the

Table 5.1 DERs' role in Case study II

Operating case	ACB	DCB
DER1	AC BESS	MPPT source
DER2	MPPT source	MPPT source
DER3	MPPT source	MPPT source
DER4	MPPT source	DC BESS
ILC	DC link control	AC link control

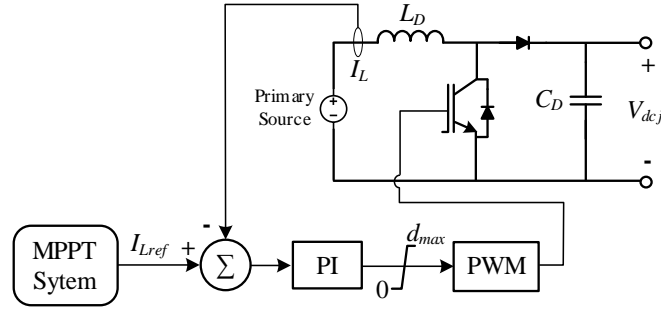


Figure 5.5 Power stage and control diagram of non-BESS DERs in DCg in Case II.  $V_{dcj}$  is the terminal voltage and  $j \in \{3,4\}$ .

lithium-ion battery that has been experimented with and analyzed in [132] and is widely utilized in the literature. The model involves an internal constant source in series with battery resistance. Equations (5.3) to (5.5) represent the non-linear dynamic of the battery voltage in charge and discharge mode, respectively:

$$V_b^{ch} = E_0 - K_p \left( \frac{i_b t}{SoC} + \frac{\bar{i}_b}{0.9 - SoC} \right) - R_b i_b + A e^{-B i_b t} \quad (5.3)$$

$$V_b^{dch} = E_0 - K_p \frac{i_b t + \bar{i}_b}{SoC} - R_b i_b + A e^{-B i_b t} \quad (5.4)$$

$$SoC(t) = SoC(0) - \frac{1}{Q} \int_0^t i_b(t) dt = SoC(0) - \frac{i_b t}{Q} \quad (5.5)$$

with the variables delineated as below:

$E_0, R_b$ : Battery internal voltage source (V) and resistance ( $\Omega$ ),

$K_p$ : polarization constant  $\left( \frac{V}{Ah} \right)$ ,

$i_b, \bar{i}_b$ : actual and filtered battery output current (A),

$i_b t, Q$ , and  $SoC$  : actual battery charge, battery capacity (Ah) and state of charge in the range of [0 1],

$A$  and  $B$  : exponential zone voltage and time constant ( $Ah^{-1}$ ).

The subscripts *ch* and *dch* refer to charge mode and discharge modes. The operation of the battery is normally constrained between the minimum and maximum  $SoC$  ( $SoC_{min}, SoC_{max}$ ) to prolong the battery lifecycle.  $SoC(0)$  is the initial value of  $SoC$  at the beginning of the charge/discharge process. It should be noted that, since the battery  $SoC$  range restricts its operation, the load shedding or generation curtailment might be needed in cases that the battery runs out of charge or overcharges. Ref. [133] proposed an autonomous power management strategy based on local measurements to keep  $SoC$  in a safe range while efficiently utilizing RES.

### 5.3.2 AC BESS

In both case studies, the ACB comprises a battery connected to ACg via a VSC-based converter and an LCL harmonic filter. In Case study I, as mentioned earlier, the ACB works as a grid-feeding converter with a reverse droop control technique to inject/absorb reference active and reactive powers (see Figure 5.6). The reverse droop is given by [12]:

$$\begin{cases} P_{ACB}^{ref} = P_{ACB}^* - m_{ACB}(\omega - \omega^*) \\ Q_{ACB}^{ref} = Q_{ACB}^* - n_{ACB}(V - V^*) \end{cases} \quad (5.6)$$

where  $P_{ACB}^{ref}$  and  $Q_{ACB}^{ref}$  are the ACB reference active and reactive powers, respectively,  $m_{ACB}$  and  $n_{ACB}$  are reverse droop coefficients,  $\omega$ , and  $V$  are the measured ACg angular frequency and voltage amplitude, and superscript ‘\*’ denotes their setpoint values.  $\omega$  is measured by the phase-locked loop (PLL), and  $V$  is the magnitude of  $dq$  voltage components at the ACB terminal. The setpoint

value of active power is obtained from the PMS system through ultra-low-bandwidth communication links and is the power mismatch between loads and generation:

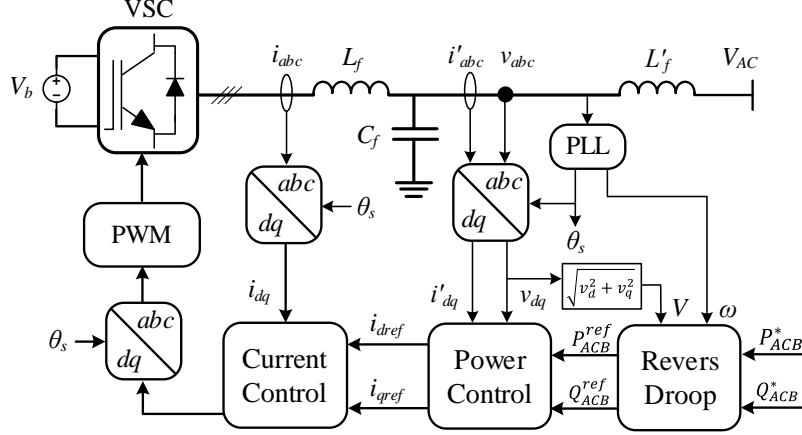


Figure 5.6 The VSC control diagram used in ACB control in Case I

$$P_{ACB}^* = \sum_{i \in S_L} P_{L_i} + \sum_{j \in S_I} P_{loss_j} - \sum_{k \in S_G} P_{G_k} - P_{ILC} \quad (5.7)$$

where  $P_{ILC}$  is the ILC output power, and its reference direction is from DCg to ACg. The setpoint value of reactive power can also be calculated similarly or set to a constant value. In this paper, the constant value is used. For the islanded operation, the battery reference power is calculated by power mismatch between load and generation. If HMG runs in the grid-connected mode in Case I (i.e., CB closed in Figure 5.1), depending on PMS strategy, ABC's setpoint power can be set to a constant value to constantly charge the battery from the grid.

In Case study II, the ACB is a grid-forming converter and controls the ACg voltage and frequency using local measurements at its terminal. Its control system is composed of the well-known standard voltage and current control loops implemented in  $dq$  frame [134],[20], shown in Figure 5.7. In this figure,  $V^*$  and  $\omega^*$  are the setpoint ACg voltage and frequency, respectively. As mentioned earlier, when operating with ACB in case study II, ILC controls the DC link voltage.





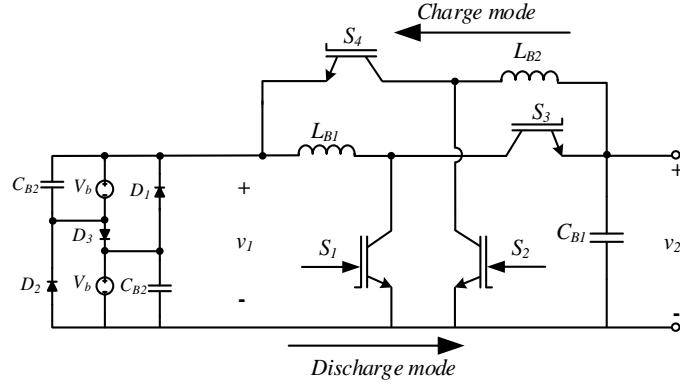


Figure 5.8 Power stage block diagram of DC-DC converter utilized in DCB [116] in both cases.  $v_2$  is the DCB output terminal that is connected to DCg PCC and  $V_{dc4}$  in the Case I and Case II, respectively.

Figure 5.9 displays the converter controller in the voltage-controlled mode suitable for the DCB working as a voltage source in DCg. The controller is a proportional-integral (PI) regulator designed based on the converter frequency response and the equivalent load resistance.  $G_v$  is a pair of pole/zero to match the gain frequency response in both modes.  $V_{dc}^*$  is the setpoint value of DCg voltage. The voltage level of each battery section is proportional to DCg voltage as given by:

$$V_b = \frac{V_{dc}^*}{\sqrt{2}} \quad (5.8)$$

where  $V_b$  is the battery voltage level. More details about the converter can be found in [116].

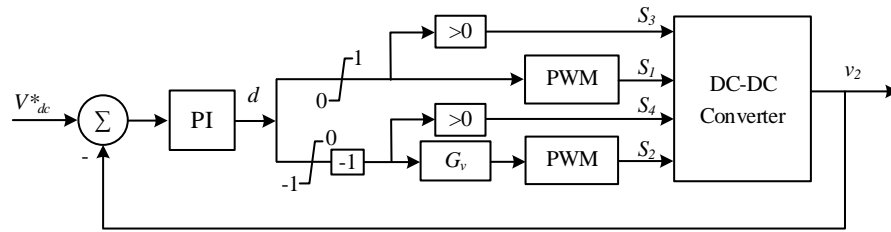


Figure 5.9 Control system diagram of the bidirectional DC-DC converter.  $v_2$  is the DCB output terminal voltage that is connected to DCg PCC and  $V_{dc4}$  in Case I and II, respectively

## 5.4 Simulation Results and Discussion

This section performs and discusses the comparative analysis of case studies undergoing

various operating conditions. The HMGs shown in Figures 5.1 and 5.3 and their control architectures are simulated in MATLAB\Simulink environment by discrete time-domain simulations exerting sampling frequency of  $F_s = 200kHz$ . Besides, the sampling frequency of power signals in Case study I is equal to  $\frac{F_s}{20}$ . Several grid events are applied to case studies to evaluate the HMG's transient performance corresponding to the BESS location. Tables 5.5 to 5.10 in the appendix present system data as well as initial parameters of both case studies.

#### 5.4.1 Case Study I analysis

Case study I has two candidate locations for ACB and one place for DCB, shown in Figure 5.1. All BESSs have the same power rating. All initial operating conditions of Case I are given in Table 5.4 in the chapter appendix.

##### 5.4.1.1 Islanding

Although this study emphasizes the islanded operation of HMG, the first simulation case in this part presents the influence of BESS location on the microgrid's performance during islanding events. Before islanding, the utility grid charges the batteries as much as 200kW (i.e.,  $P_{ACB}^* = P_{ILC}^* = -200kW$ ). Also, the generates 0.15 pu active power based on its rated power. Power set-points switch to (2) and (7) after islanding incidence. Fig. 5.10 exhibits the system's critical parameters in reaction to the islanding event at 14s for three locations of ACB and DCB separately. The frequency reduction following islanding indicates that the HMG runs with insufficient power generated by DERs, corroborated by the new operating points of all BESSs. Results demonstrate that the HMG with all three locations has almost the same dynamic performance. The unbalance of load/generation power in ACg causes an instantaneous drop in  $V_{dc}$  (Figure 5.10 c) in initial moments during DCB operation. The power shortage is transferred from DCg to ACg by ILC

operation that makes a brief reduction in  $V_{DC}$  that is efficiently restored by DCB.

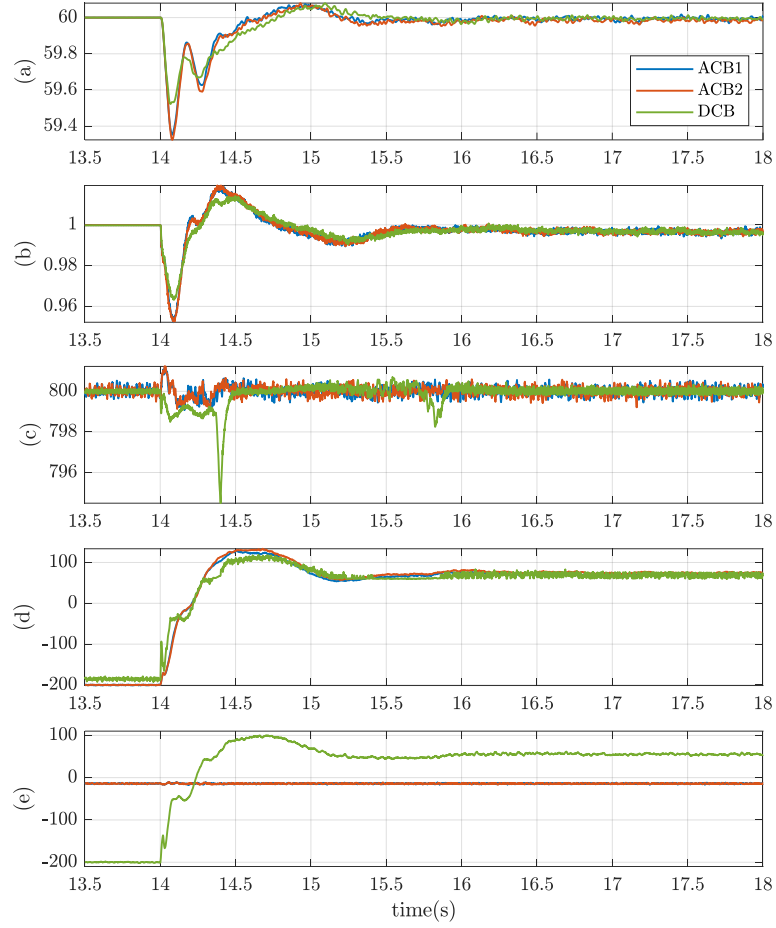


Figure 5.10 System response to Islanding incidence simulation in Case I; (a) ACg frequency (Hz), (b) ACg voltage (pu), (c) DCg Voltage (V), (d) BESS power (kW) and (e) ILC power (kW).

#### 5.4.1.2 Random fluctuation in wind speed

This part simulates a string of random changes in wind speed affecting the power generation in WTG. The HMG works in oversupply mode since the DC load power has changed from 307kW to 128 kW, causing the BESS to charge. At  $t = 14s$ , a stepwise wind velocity variation is simulated from its initial value of 14m/s (yielding the rated power in WTG) to the following quantities occurring in 1s intervals consecutively: [9.8, 15, 18.2 and 14] m/s. Figure 5.11 demonstrates the system's dynamic response to this disruption. WTG's output power depends not only on wind

speed but also on MPPT and blade pitch-angle control effort. All BESSs preserve the ACg voltage and frequency by compensating for the oversupply and undersupply energy during wind speed fluctuation with equal performance. The DCg voltage does not undergo a significant variation.

#### 5.4.1.3 Disruption in dynamic load

In this part, the performance of the HMG is evaluated against pulse-wise variation of a high inertia frequency-dependent load. The power generation in HMG is more than load and BESSs are charging. The frequency-dependent load (Load1), which is modeled by a 205kW induction motor, initially runs with 0.91 pu of rated mechanical torque (i.e., 1100 N.m). The following stepwise variations occur in motor load torque in 1s intervals starting from  $t = 14$ s consecutively: [0.2, 1.2, and 0.91] pu.

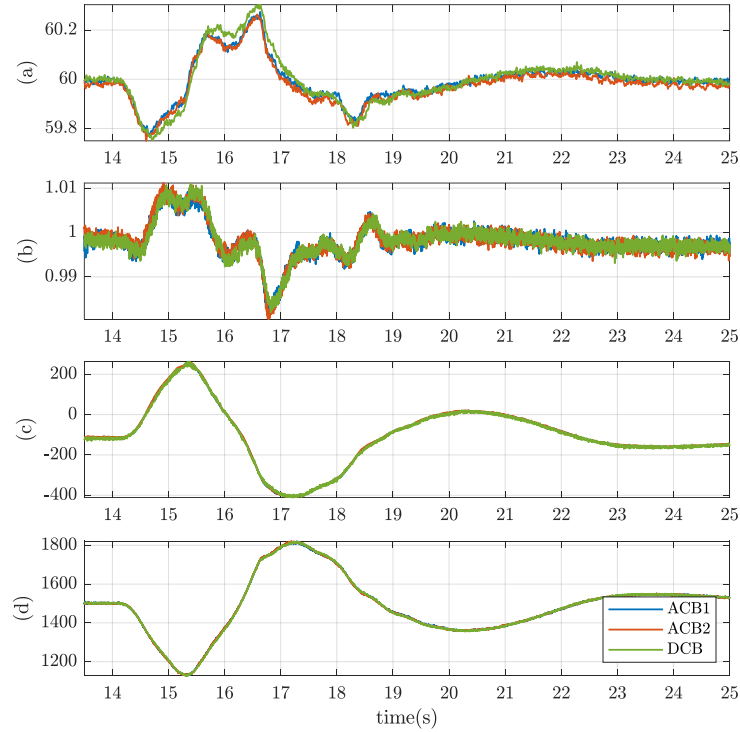


Figure 5.11 Disturbance in wind speed in Case I; (a) ACg frequency (Hz), (b) ACg voltage (pu), (c) BESS output power (kW), and (d) WTG output power (kW).

Figure 5.12 illustrates the crucial parameters of the HMG during this event. All BESSs and ILC can maintain the frequency and voltages at normal ranges by quick responses to dynamic load variation. Note here that, since the DC load is initially changed from 307kW to 128kW, a large amount of active power is transferred from DCg to ACg by ILC when operating with ACBs. In the HMG operating with DCB, the BESS instantly absorbs a part of the power and the remaining power is transferred from DCg to ACg to keep a power balance in ACg.

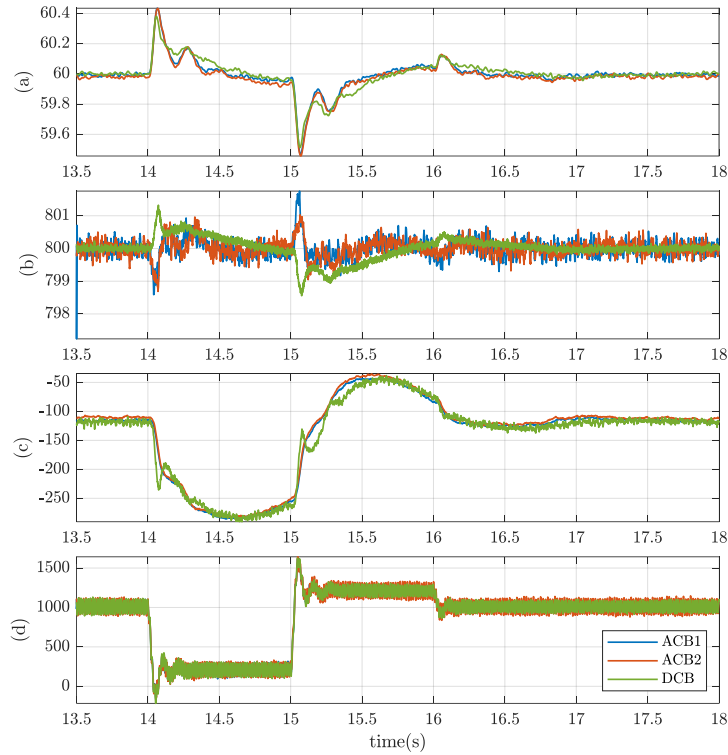


Figure 5.12 The step change in frequency-dependent load in Case study I; (a) ACg frequency (Hz), (b) DCg voltage (V), (c) BESS output power (kW), and (d) Mechanical torque of induction motor (N.m).

#### 5.4.1.4 Random variation of solar irradiance

This part evaluates and compares the system's performance against randomly altered solar irradiance perturbing power generation in PV. Initial conditions are similar to disturbance cases discussed in parts B and C. The solar irradiance level is  $1000 \frac{W}{m^2}$  in the beginning, that yields to 305kW output power while the MPPT system is ON. The following solar irradiance variation

applying an appropriate ramp-rate occurs starting from  $t = 14s$  within 2s intervals consecutively:  $[1400 \ 600 \ 1000] \frac{W}{m^2}$ . Figure 5.13 depicts the dynamic reaction of critical parameters of the HMG to this incidence. Even though all BESSs in both subgrids can handle the power generation disturbance, the DCB performs robustly to maintain the DCg voltage and ACg frequency at stable conditions. Since the ILC regulates the DCg voltage when running with ACB, excessive or insufficient power should be exchanged with ACg through DCg voltage regulation. The power interchange in ILC prompts DCg voltage excursions by charging/discharging energy in the DCg capacitor ( $C_{dc}$ ) on one side and the battery of ACB on the other side. However, the DCB carries out this process dissimilarly. The bidirectional converter of DCB directly exchanges the energy with the battery that results in a relatively flat voltage profile.

#### 5.4.1.5 Fault analysis and LVRT evaluation

The BESS is not generally employed to cope with the grid faults. However, in this part, a performance analysis is implemented to study the LVRT capability of HMG and BESS in handling the extreme conditions of fault situations with high penetration of RESs. In this simulation, separate fault events are applied in ACg and DCg when operating with each BESS. For ACB1 and ACB2, a 3-line-to-ground (3LG) high-impedance short circuit occurs at  $t_f = 14s$  at the ending terminal of line 3 (location **F** in Figure 5.1) and is cleared after 150ms with no circuit breaker operation. All the DERs remain connected to HMG during and after the fault to accomplish the LVRT requirements. Likewise, for DCB operation, a pole-to-pole short circuit with a fault resistance of  $50m\Omega$  happens at  $t_f = 14s$  on the DC PCC for 100ms. The dynamic response of the system to these extreme conditions is illustrated in Figures 5.14 and 5.15. The system with all BESSs is able to recover to a normal operating condition after the ACg fault event. However, the DCB has superior performance compared to ACB1 and ACB2 in damping system oscillations and

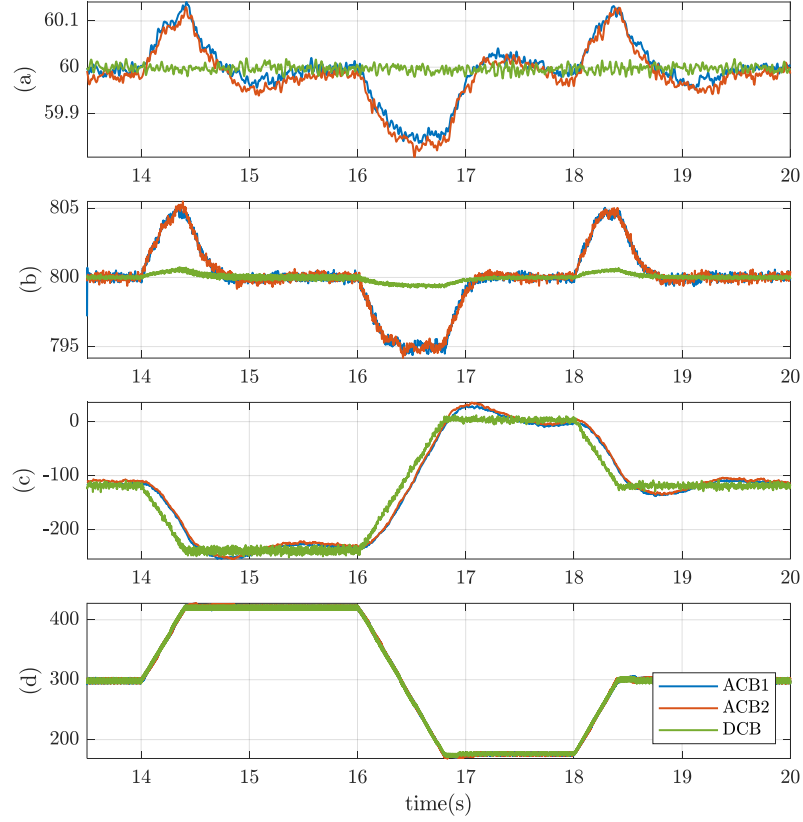


Figure 5.13 Random variation of Solar Irradiance; (a) ACg frequency ( $Hz$ ), (b) DCg voltage ( $V$ ), (c) BESS output power ( $kW$ ) and (d) PV output power ( $kW$ )

limiting DCg voltage during both fault incidences. ACB2, in the case of ACg fault, is conditionally successful in maintaining stability since the ACg frequency reaches the values ( $61.5\ Hz$ ) that, depending on the grid codes, will likely lead to the system shut down due to trip operation in protective devices.

In the case of DCg fault, the system with DCB performs remarkably better than that of ACB1 and ACB2 in controlling grid voltage swells. The system with ACB1 can recover to normal operation; however, it cannot bound DCg voltage excursions to an acceptable range. The magnitudes of  $V_{AC}$  and  $V_{DC}$  for the system with ACB1 reach the quantities greater than 1.2 and 1.6 pu, respectively, that are immeasurably higher than the acceptable ranges resulting in operation of protective devices. The HMG with ACB2, as the simulation results show, due to the severity of the

disturbance and the high inertia of the microgrid, a power oscillation takes place between high inertia energy sources and loads such that the system is unable to damp the oscillations and recover to a stable point and consequently the system collapses.

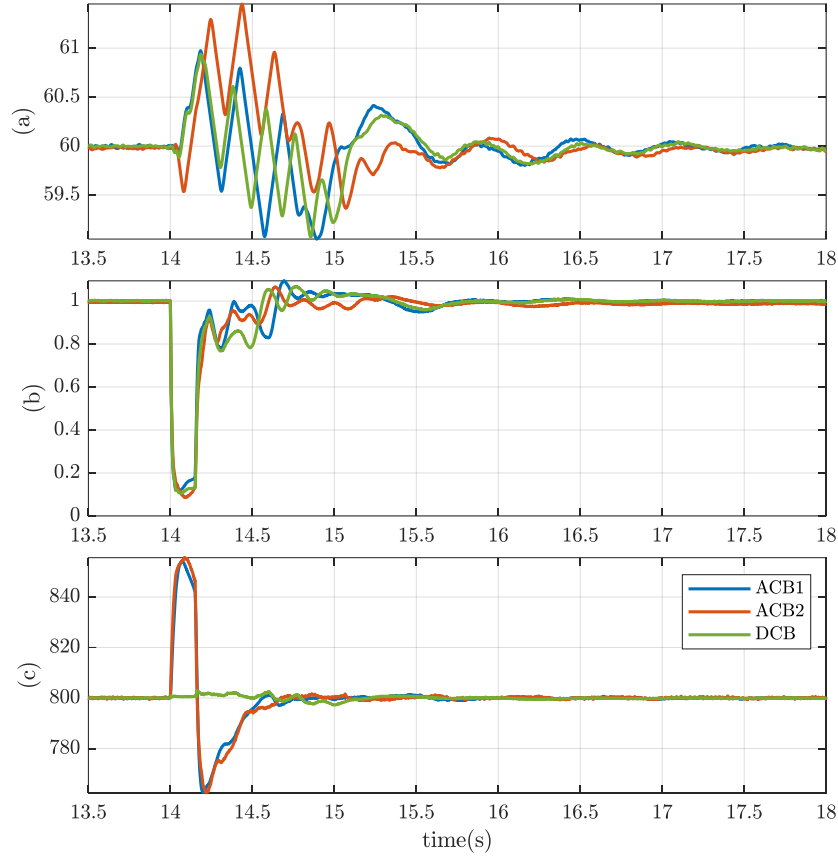


Figure 5.14 Dynamic response to a 3LG fault event in ACg of Case I; (a) ACg frequency (Hz), (b) ACg voltage (pu), (c) DCg voltage (V).

#### 5.4.2 Case Study II Analysis

For Case study II, one candidate site is considered for each subgrid. As presented in Table 1, the candidate locations for BESS are DER1 and DER4 shown in Figure 5.3. DERs are controlled using their local measurements, and no secondary control is implemented. For this case, three separate events are simulated. All system parameters and initial operating conditions of Case II are given in Tables 5.5 to 5.7 in the chapter appendix.



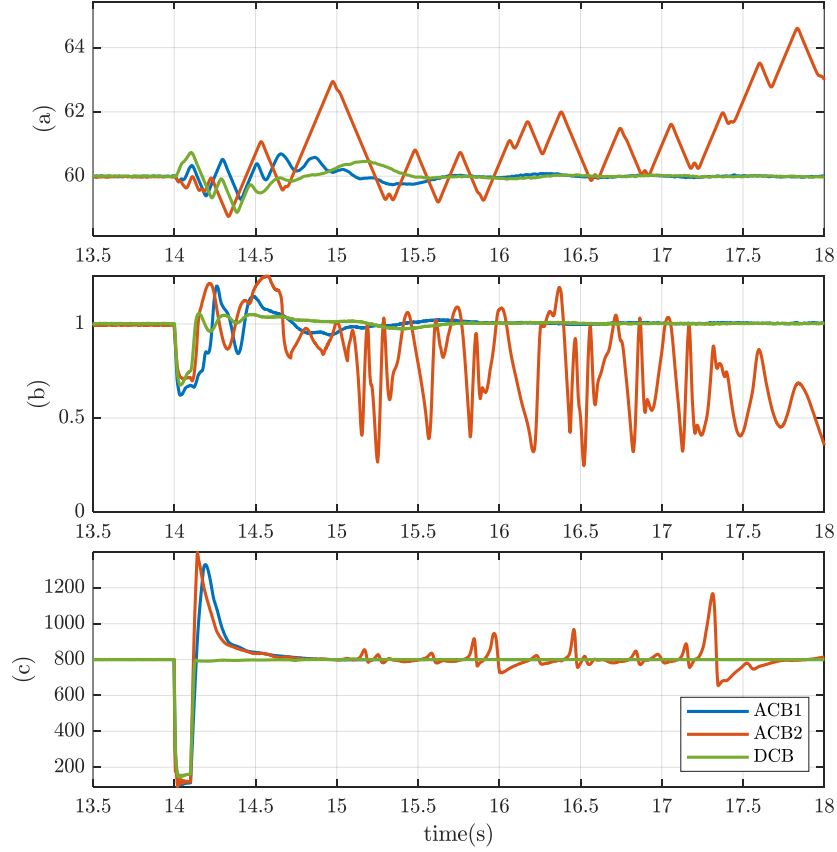


Figure 5.15 Dynamic response to fault event in DCg in Case I; (a) ACg frequency, (b) ACg voltage, (c) DCg voltage.

#### 5.4.2.1 Load/generation variation in DCg.

In this part, some stepwise changes in load and generation happening in DCg are simulated as follows: (i) DER3 reference power changes from the initial value of 100kW to the following magnitudes [50, 100, 150] kW within the next time range [1, 1.3, 1.6] s, respectively, and (ii) the load resistance in Load5 changes from its initial value  $10\Omega$  to the following values [5, 20, 10]  $\Omega$  within the subsequent time range [1.9, 2.2, 2.5] s, respectively. Figure 5.16 shows the dynamic response of the critical parameters of the system to these disturbances. The overall performance for both BESSs is the same, though the ACB's performance is superior to its counterpart in DCg in controlling the DC link voltage peaks. It is to note that, in the case of operation with DCB, the ILC works as a voltage source for ACg and controls the AC link voltage and frequency at their nominal

values. Whereas, in the case of ACB, the ILC works as a current source for ACg with no regulation on voltage and frequency. Consequently, the AC link voltage has a little excursion from its nominal value. Similarly, in the case of DCB, the DC link voltage has deviations from its nominal value as there is no voltage source at the DC link bus.

#### 5.4.2.2 Load/generation variation in ACg.

This part simulates some random load/generation variations in Load1 and DER2 in ACg as follows. (i) the reference power in DER2 changes from the initial value of 150kW to the following [200, 175, 125] kW within the following time range [1, 1.3, 1.6] s, respectively. (ii) the load impedance in Load1 changes from its initial value  $7.76 + j2.26\Omega$  to the following values  $[3.88 + j1.13, 7.76 + j2.26, 2.58 + j0.75] \Omega$  within the next time ranges [1.9, 2.2, 2.5] s, respectively. Figure 5.17 presents the dynamic response of the HMG to these disruptions for critical variables of the system. The response is similar to the last part, but the magnitude of peaks in DC link voltage for generation steps are more critical. These spikes happen due to the power flow direction change in the bidirectional DC-DC converter used in DCB.

#### 5.4.2.3 Fault event and LVRT analysis

Like the analysis carried out in Case study I, this part evaluates the system's LVRT capability in response to ACg and DCg faults in Case study II. First, a high impedance ( $R_{fac} = 200m\Omega$ ) 3LG fault occurs in ACg near Load2 and DER2 at  $t_{f1} = 1s$  for 83ms. Then, a high resistance ( $R_{fdc} = 2.5\Omega$ ) pole-to-pole fault takes place in DC link bus in DCg at  $t_{f2} = 1.9s$  for 70ms. The operation of protective devices is not simulated in this event. Also, only the non-BESS DERs are limited by their rated powers to allow BESSs to contribute to LVRT swings freely. Fig. 18 shows the results of this simulation. Since the system is made up of low inertia DERs, these faults can be considered as high-power pulsed loads occurring for a short duration. As can be seen, the system's

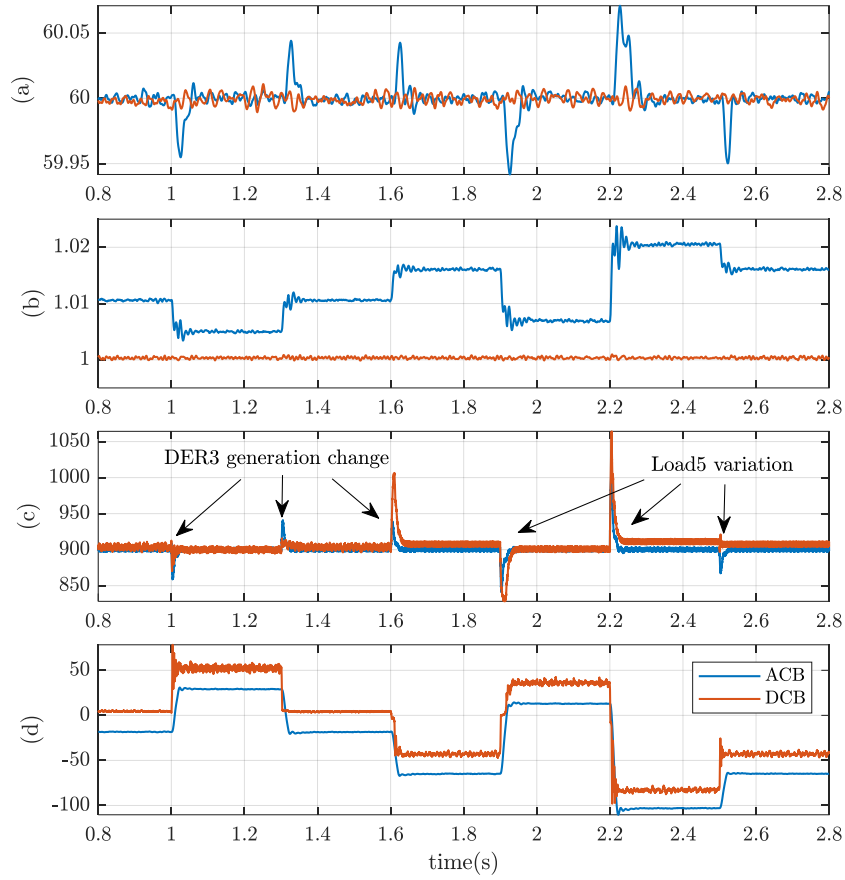


Figure 5.16 Load/generation variation in DCg in Case II, (a) AC link frequency (Hz), (b) AC link voltage magnitude (pu), (c) DC link voltage (V), and (d) BESS output power (kW).

performance operated with ACB is superior to that of the DCB, although in both BESS cases, the system recovers to the normal operating point. In the real case, the protective devices will operate in the system operated with DCB. However, the ACB power critically reaches high values above the rated capacity of the ACB converter. This operation in the real case depends on the maximum withstand levels of the battery, the converter's switching devices, and short circuit current magnitudes. The batteries typically have charge/discharge withstand levels of 2.5 to 3 times the nominal current for a short duration. Therefore, within these ranges, the critical factor in determining BESS's LVRT capability would be the converter rating and its transient short circuit capability. For the evaluation, the system is simulated under different fault resistances in ACg and DCg,

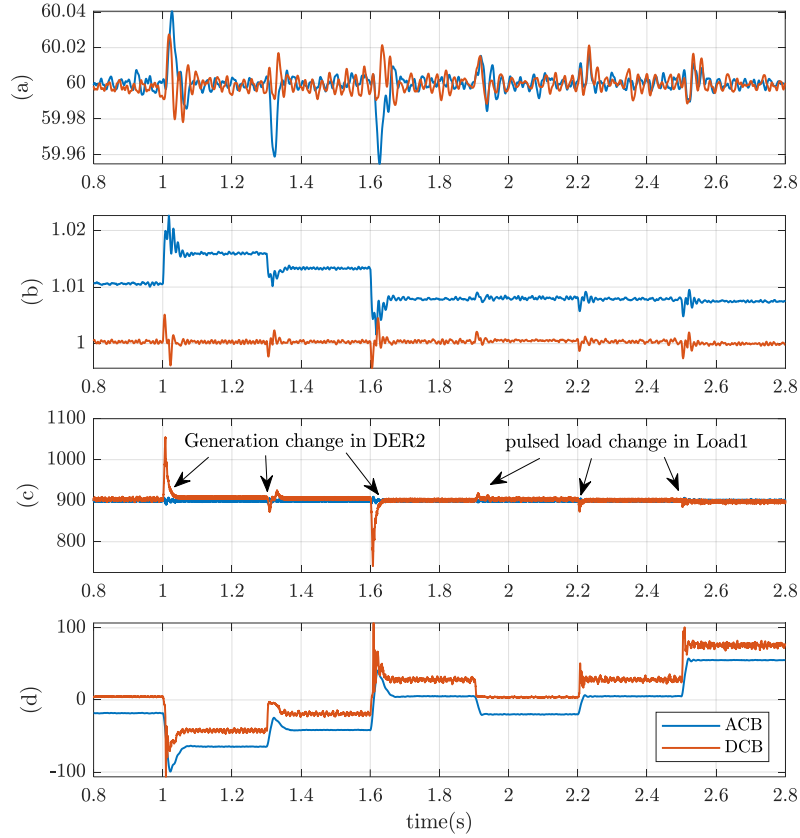


Figure 5.17 Load/generation variation in ACg in Case II, (a) AC link frequency (Hz), (b) AC link voltage magnitude (pu), (c) DC link voltage (V) and (d) BESS output power (kW).

Figure 5.19 shows the result of this analysis for more critical cases. For the lowest resistance value, both BESSs have a poor performance that is expected. The DCB controller halts during ACg fault. In the case of ACB, the fault excites the system's oscillatory mode, and ACB is unable to damp the oscillations. It is noteworthy that the control strategy and the controller's bandwidth have a significant effect on the BESS capability in handling the oscillations occurring during and after instantaneous voltage sags like faults. Although the BESS is not mainly placed for coping with severe low voltages and faults, it indeed undergoes intense fault currents. Particularly in microgrids where it operates as a voltage source, and there is no high inertia DER running as a voltage source to share the fault current. In this study, we have tuned the parameters of the PI controllers of BESSs that optimally work for a wide range of BESS loading.

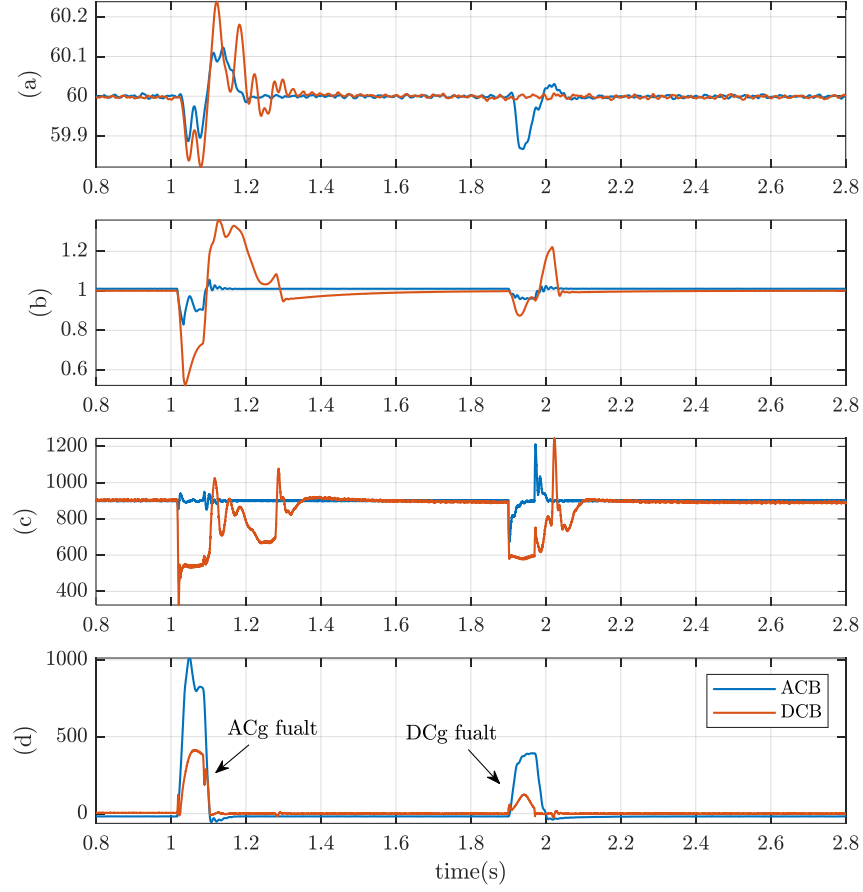


Figure 5.18 Evaluation of fault event in Case II. (a) AC link frequency ( $Hz$ ), (b) AC link voltage magnitude (pu), (c) DC link voltage ( $V$ ), and (d) BESS output power ( $kW$ ).

### 5.4.3 Index-based performance analysis

The previous parts in this section provided comparisons through illustrative tools. This part, however, presents a performance analysis based on numerical indices obtained from simulations which give more insights on the excursion level of a specific parameter such that the lower index value implies the better performance. The index is defined as [15]:

$$index = \int_{t_1}^{t_2} |X - X_{ref}| dt \quad (5.9)$$

where  $X$  and  $X_{ref}$  represent the parameter under the evaluation and its reference or steady-state value and the range between  $t_1$  and  $t_2$  is the evaluation period. The essential parameters of the

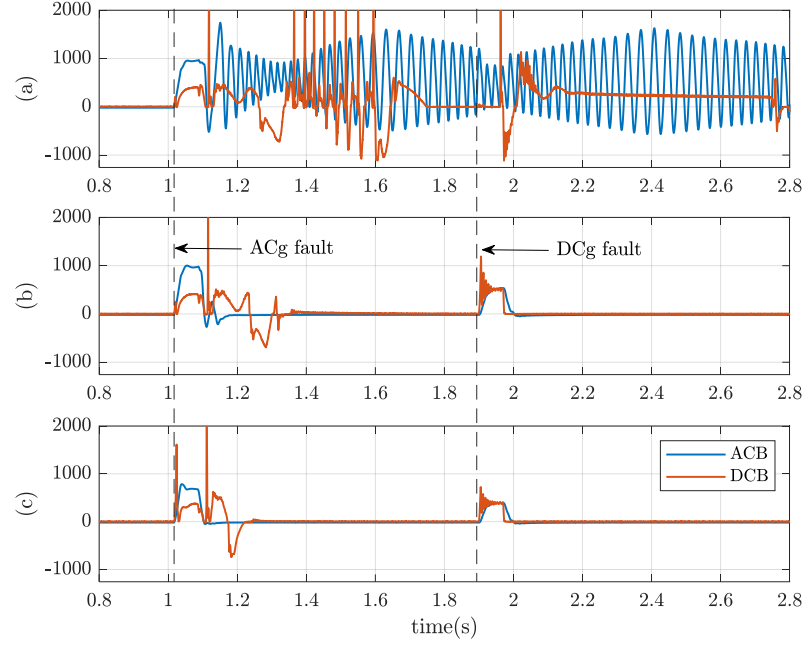


Figure 5.19 BESS output power for high impedance faults occurring in both subgrids of Case II with different values of resistances to emulate different levels of voltage sags; (a)  $R_{fac} = 120m\Omega$  ,  $R_{fdc} = 1.25\Omega$  (b)  $R_{fac} = 150m\Omega$  ,  $R_{fdc} = 1.5\Omega$  and (c)  $R_{fac} = 180m\Omega$  ,  $R_{fdc} = 2\Omega$ , where  $R_{fac}$  and  $R_{fdc}$  represent fault resistance of ACg and DCg faults, respectively.

HMG which have equal reference values when operating with different BESSs for both study cases are evaluated for selected disturbances and presented in tables 5.2 to 5.4. These parameters are ACg and DCg voltage and frequency at PCC or ILC links nodes. As was mentioned earlier, the lower index values indicate better performance. The numerical results in table 2 demonstrate that in Case study I, the HMG equipped with DCB has dominantly lower index values in critical disruption cases.

For Case study II, although the indices of AC link voltage for ACB are higher than that of DCB in generation/load disturbance cases, the overall performance quality is dominated by ACB. Due to the grid-following type of control in ILC in the case of ACB operation, the steady-state value of the AC link voltage has a little error (see figs. 5.17 and 5.18) from its nominal value which is inside the normal operating range and its transient performance is good.

Table 5.2 index values of disturbances for key parameters of the HMG in Case study I

	Dynamic load disturbance in ACg (14-18s)			Solar irradiance variation in DCg (14-20s)			Fault in ACg (14-18s)			Fault in DCg (14-18s)		
<b>BESS</b>	<b>ACB1</b>	<b>ACB2</b>	<b>DCB</b>	<b>ACB1</b>	<b>ACB2</b>	<b>DCB</b>	<b>ACB1</b>	<b>ACB2</b>	<b>DCB</b>	<b>ACB1</b>	<b>ACB2</b>	<b>DCB</b>
$U_{AC}$	0.0449	0.0442	0.0452	0.0421	0.0409	0.0424	0.2206	0.235	0.2401	0.1363	1.003	0.0706
$U_{DC}$	1.1069	1.098	1.0318	8.3792	8.5275	1.1214	14.89	16.013	1.955	155.65	231.7	71.92
$f_{AC}$	0.2297	0.2771	0.2595	0.2588	0.2937	0.0381	0.6926	0.7514	0.626	0.4585	4.615	0.5123

Table 5.3 Index values of disturbances happening in ACg for key parameters of the HMG in Case study II

	Generation change (0.8-1.8s)		Load variation (1.8-2.8s)		Fault (0.8-1.8s)	
<b>BESS</b>	<b>ACB</b>	<b>DCB</b>	<b>ACB</b>	<b>DCB</b>	<b>ACB</b>	<b>DCB</b>
$U_{ac\ link}$	0.8634	0.0845	0.6773	0.0809	2.0158	18.2
$U_{dc\ link}$	1.5555	8.2	1.4643	3.0156	2.5945	61.92
$f_{ac\ link}$	0.0045	0.0042	0.0028	0.0032	0.0127	0.025

Table 5.4 Index values of disturbances happening in DCg for key parameters of the HMG in Case study II

	Generation change (0.8-1.8s)		Load variation (1.8-2.8s)		Fault (1.8-2.8s)	
<b>BESS</b>	<b>ACB</b>	<b>DCB</b>	<b>ACB</b>	<b>DCB</b>	<b>ACB</b>	<b>DCB</b>
$U_{ac\ link}$	0.7544	0.0415	1.6788	0.0414	0.9968	3.7742
$U_{dc\ link}$	2.3553	5.3979	3.0175	9.5727	7.3171	44.33
$f_{ac\ link}$	0.0046	0.0031	0.0064	0.0026	0.0089	0.0031

## 5.4 Chapter Conclusion

This chapter analyzed and compared the dynamic performance of HMGs when operated with an aggregated battery energy storage device connected to either ACg or DCg through a heuristic approach. Two different microgrid case studies were considered for evaluations, i.e., an industrial HMG with high penetration of RES dynamics and high inertia elements and a converter-based microgrid. A recently reported novel bidirectional DC-DC converter was employed in DCB to improve the dynamic response of HMG. Besides, several operating conditions and grid disturbances were applied for comparative analysis. The following conclusions can be drawn based on the comparative analysis performed in this study:

- The comparison showed that in an industrial microgrid (Case study I) with high inertia

DERs, the DCB has relatively better performance during large signal disruptions, e.g., grid voltage dips. Particularly, the index-based analysis shows that DCg voltage index for HMG with DCB, as a key performance indicator, has 40.7%, 41%, and 26.5% lower values compared to the average value of those of ACB1 and ACB2 in case of solar irradiance, ACg fault, and DCg fault disruptions respectively, where a lower index value indicates superior performance. Similarly, ACg frequency and voltage for HMG with DCB have 40.3% and 41.25% lower index values in comparison to the average value of that of the ACB1 and ACB2 in case of solar irradiance, and DCg fault disruptions respectively.

Conversely, a converter-based microgrid with low inertia sources (Case study II) equipped with ACB outperforms the microgrid equipped with DCB. Specifically, the DCg voltage index for HMG with ACB has roughly 68%, 34.6%, and 92% lower values compared to those of DCB for generation, load, and fault disruptions respectively, happening in ACg. Likewise, it has 39%, 52%, and 71.6% lower index values compared to those of DCB occurring in DCg accordingly.

b) The BESS controller and its bandwidth, as well as the ILC control strategy, have great importance when the energy storage runs as a voltage source in either sub-grid of HMG.

c) This research could be beneficial to the industry, designers, and microgrid operators to know about the influence of the energy storage location on HMG performance that is usually overlooked during the siting analysis since the optimal location is always selected pursuant to economic and power flow objectives.

d) Although this study covered only two HMG cases, whether the results can be generalized to all cases or not, similar research is needed along with other objectives.

This study can be extended to HMGs with distributed energy storage devices where there are



several candidate locations for BESS. In that case, analytical approaches like small-signal and stability analysis may preferably be used instead of heuristic methods.

## 5.5 Chapter Appendix

Table 5.5 System parameters in the case study I

$V^*, V_{DG}^*$	460 V(L-L)	$V_{ref}(\text{DC})$	800 V
$\omega^*, \omega_{DG}^*$	$\frac{314\text{rad}}{s}$	$C_{DC}$	10mF
$L_1, L_3$	1.9mH	$R_1, R_3$	207m $\Omega$
$L_2$	1.3mH	$R_2$	138m $\Omega$
$L_{f1}$	375 $\mu$ H	$L'_{f1}$	75 $\mu$ H
$L_{f2}$	250 $\mu$ H	$L'_{f2}$	50 $\mu$ H
$C_{f1}$	1200 $\mu$ F	$C_{f2}$	1500 $\mu$ F
$m_{ACB}$	75	$n_{ACB}$	10
$m_{DG}$	0.05	$n_{DG}$	0.15
Load 1	205kW	Load 2	355kW + j112kVar
Load 3	4560kW + j112kVar	Load DC	307 kW

Table 5.6 BESS parameters in the case study I

ACB1 and ACB2			
$E_0$	950 V	$f_{pwm}$	5 kHz
$Q$	500 Ah	$P_{conv}$	500kW
$R_b$	15m $\Omega$	$K_p$	0.013
$A$	73.3	$B$	0.122
DCB			
$E_0$	565 V	$f_{pwm}$	10 kHz
$Q$	420 Ah	$P_{conv}$	500 kW
$L_{B1}, L_{B2}$	0.45, 0.72mH	$C_{B1}, C_{B2}$	500, 300 $\mu$ F
$R_b$	10m $\Omega$	$K_p$	0.0092
$A$	43.6	$B$	0.145

Table 5.7 Initial values in the case study I

DG:	$P_{DG} = 0.15pu, Q_{DG} = 0.47pu$ (rating:800kVA)	
PV:	$P_{PV} = 1pu$ (rating:305kW)	Irradiance: 1000W/m <sup>2</sup>
WTG:	$P_{WTG} = 1pu$ (rating:1500kW)	Wind speed: 14m/s
Load 1	$P_M = 0.91 pu$ (at 205kW base)	
$P_{ACB}^*, P_{ILC}^*$	-200kW before islanding	

Table 5.8 System parameters in the case study II

Grid Parameters			
$V^*(ACg)$	460 V(L-L)	$V_{dc}^*(DCg)$	900 V
$\omega^*$	$\frac{314red}{s}$	$C_{DC}$	1000 $\mu F$
$R_1, L_1$	25m $\Omega$ , 45 $\mu H$	$R_2, L_2$	20m $\Omega$ , 36 $\mu H$
$R_3, L_3$	47m $\Omega$ , 65 $\mu H$	$R_4, L_4$	25m $\Omega$ , 45 $\mu H$
$R_5, L_5$	7.76 $\Omega$ , 6mH	$R_6, L_6$	3.38 $\Omega$ , 3mH
$R_7, L_7$	3.38 $\Omega$ , 3mH	$R_8, R_9, R_{10}$	30, 20, 10 $\Omega$
BESS circuit parameters			
ACB	$L_f, L'_f, C_f$	450 $\mu H$ , 90 $\mu H$ , 1200 $\mu F$	
DCB	$L_{B1}, L_{B2}, C_{B1}, C_{B2}$	450 $\mu H$ , 720 $\mu H$ , 1200 $\mu F$ , 750 $\mu F$	
Non-BESS circuit parameters			
DER1,2 & ILC	$L_f, L'_f, C_f$	400 $\mu H$ , 80 $\mu H$ , 1200 $\mu F$	
DER3,4	$L_D, C_D$	1mH, 250 $\mu F$	

Table 5.9 BESS parameters in the case study II

ACB			
$E_0$	900 V	$f_{pwm}$	5 kHz
$Q$	300 Ah	$P_{conv}$	270 kW
$R_b$	25m $\Omega$	$K_p$	0.02
$A$	70	$B$	0.2
DCB			
$E_0$	636 V	$f_{pwm}$	20 kHz
$Q$	212 Ah	$P_{conv}$	270 kW
$R_b$	20m $\Omega$	$K_p$	0.016
$A$	49.3	$B$	0.226

Table 5.10 Initial values in the case study II

Operating with ACB	
DER2	150kW/60kVar
DER3, DER4	100kW, 75kW
Operating with DCB	
DER1	50kW/0kVar
DER2	150kW/60kVar
DER3	100kW

# **Chapter 6 Solar Photovoltaic (PV) System as Supercapacitor Energy Storage**

## **6.1 Introduction**

An introductory evaluation regarding merging PV system with a high power energy storage like supercapacitor was given in chapter 2. To overcome the limitations and challenges discussed in section 2.7, this chapter proposes to design and operate the grid-connected PV system as an SES during nighttime or intermittent cloud insolation conditions as well as during daytime. According to the proposed approach, a partially charged supercapacitor (by the grid power) will be connected between points A and B at the PV panel terminal (see Figure 2.21). At nighttime, the PV panel will be disconnected naturally. Consequently, the charged supercapacitor connected as the input to the DC-DC converter and the rest of the components (except the MPPT controller and BES) will constitute the SES unit that can be used for dynamic performance improvement. During the daytime, following any disturbances like any faults in the network, the PV panel will be disconnected for a very short time, and the SES unit will control both reactive and active powers, thereby providing both voltage and frequency support to the grid. Once the power grid stability is maintained, the PV panel will be connected back and operate normally. Thus, the proposed system can provide a seamless and robust operation of the grid-connected PV system.

In summary, the main benefits of the proposed approach are as follows.

- The proposed PV system not only works in its typical mode of operation but also can improve the system stability whenever needed (i.e., whenever there are any disturbances in the grid). And this is the additional advantage that can be achieved from the same PV system just by momentarily connecting a supercapacitor/battery at the PV panel terminal.

- To handle any disturbances (fault, load change, etc.) at the grid side, typically an auxiliary control device such as STATCOM, SVC, fault current limiter, any extra energy storage device (like a full supercapacitor energy storage unit as shown in Figure 2.22 or a full battery energy storage system) is connected at the grid point, and the system stability is maintained. However, as per the proposed approach, since the same PV system is being used, it saves the cost of adding any auxiliary control devices at the grid point. In other words, this technology will achieve significant cost savings due to the use of existing PV system components as the SES unit.

In this study, a new controller has been designed to open and close the switches of the PV and SES systems. Small-signal stability analysis for the proposed PV-SES system has been conducted. In order to show the effectiveness of the proposed PV-SES unit, extensive simulations have been performed. Both voltage and frequency disturbances have been considered at the grid side.

## **6.2 Proposed PV-Supercapacitor Energy Storage (SES) System Modeling**

### ***6.2.1 Principle of Operation***

The operation of the proposed PV-Supercapacitor (PVSC) concept can be better explained in Figure 6.1. As shown on the rightmost side of this figure, there is a PCC grid point where there can be other power sources such as synchronous generators, wind generators, other PV systems, etc., connected to power the loads or the customers. To handle any disturbances (fault, load change, etc.) at the grid side, typically an auxiliary control device is connected at the grid point or the DC link point, and the system stability is maintained. Now, according to the proposed concept, during any random disturbances at the grid side, usage of any full supercapacitor storage system or full battery energy storage system at the grid side or the DC link point will not be needed. According to this concept, if suddenly any disturbance happens at the grid side (it can be any time like

nighttime/daytime/cloudy weather), then the PV panel will be momentarily disconnected by the switch SW1 and the supercapacitor switch SW2 will be closed (assuming the SC has already some charge). Then the supercapacitor together with the bidirectional DC-DC converter, DC link capacitor, and voltage-sourced converter (VSC) will constitute the full supercapacitor energy storage unit/system (like Figure 2.22) that can tackle the sudden fault, load change, at the grid side. Since the PV panel is getting disconnected for a short moment, certainly other power sources connected at the grid point will continue providing power to the customers at that time. Once the grid becomes stable, immediately the PV panel will be connected back by closing the switch SW1 and will operate normally (during sunny time) and the SC switch SW2 will be disconnected. Therefore, the utility integrated PV system can operate as a supercapacitor or battery energy storage system. It should be noted that in the proposed PVSC system the BDC works in voltage control mode and the VSC works in grid-forming control mode with a conventional synchronous generator-based droop control that can track the reference power. This reference power is defined by either MPPT system in PV mode operation or another value in energy storage mode of operation. The next part explains how the algorithm controls the switches SW1 and SW2 and VSC reference power.

It is to note here that the proposed PVSC system will have the capabilities to operate in the following two modes:

**i) PV system mode:** In this mode, the proposed PV system will provide power to the grid, as usual, assuming there is sufficient solar irradiance (sunlight).

**ii) Energy storage mode:** Once there are any grid disturbances such as faults, load change, etc. (irrespective of daytime, nighttime, cloudy situations), the same PV system changes to the energy storage (supercapacitor/battery) mode through the switches, and by controlling active and reactive powers it improves the transient stability, fault-ride through capability, voltage sag, etc.,

of the grid. Once the grid stability is maintained, it changes back to the usual PV system mode above.

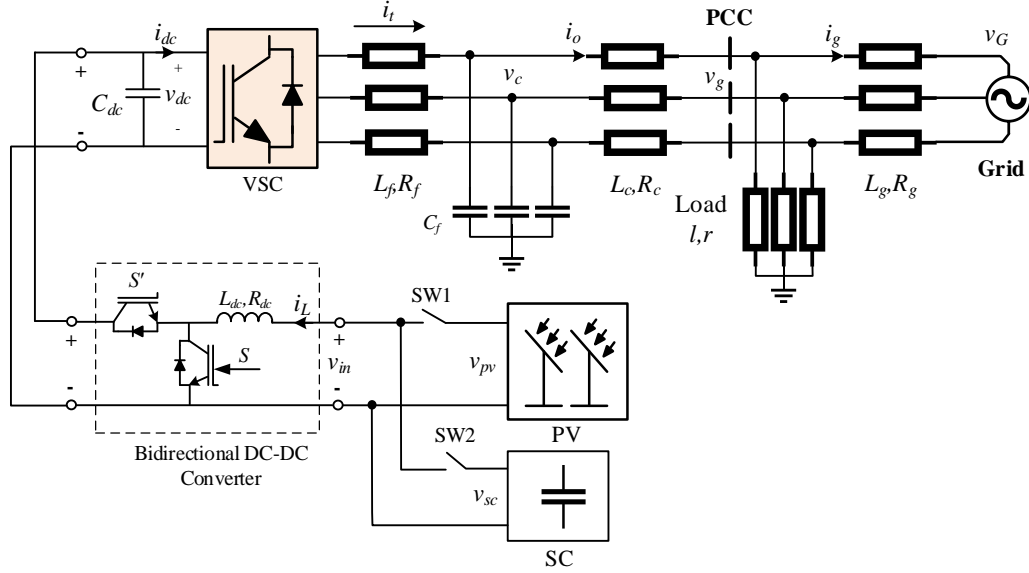


Figure 6.1 Proposed PV-Supercapacitor energy storage system (power stage).

### 6.2.2 Operation Algorithm

Figure 6.2 shows the flowchart of the control algorithm of the proposed PVSC system. It is assumed that a disturbance detection algorithm (DDA) generates a control signal ( $u$ ) with two values of 0, indicating normal operation, and 1 indicating detected disturbance along with other measurements controls the switching states of SW1 and SW2 as well. This study does not intend to design and analyze the DDA as it is out of the scope of this paper. It can be based on the monitoring of the combination of the real-time values or rate of change of grid parameters at PCC.

During the daytime, while no disturbance is detected, the system is working like a regular PV system to inject the maximum power generated by solar irradiance. Therefore, SW1 is closed (on), and SW2 is open (off), and the VSC reference power ( $P_{VSC}^{ref}$ ) is set to PV maximum power ( $P_{mpp}$ ). Once a disturbance is detected by DDA such that  $u = 1$ , first SW1 is opened and then SW2 is immediately closed. In the moment of changeover from PV to SC, the last value of the PV voltage

$(v_{pv}^{t-})$  is saved to be applied in the next changeover from SC back to PV. In addition, a flag is toggled to 1 to indicate that changeover from PV to SC is occurred. The system will continue to handle the transient stability until the operating condition comes back to a normal situation and DDA issues the signal  $u = 0$ .

It should be noted that, during the transient period that SC is switched on, the reference power is kept on the previous value of  $P_{VSC}^{ref}$  to have a smooth changeover by supplying the same power. At the end of the transient operation, the stored energy in SC is examined by checking its voltage. The transient period is usually short enough (in the order of few seconds) to assume that the solar irradiance remains unchanged and the same  $P_{mpp}$  is generated. The SC voltage ( $v_{sc}$ ) must be close to  $v_{pv}^{t-}$  to ensure that changeover from SC to PV is smooth and the PV gets back to its operating point once it had prior to the changeover. It should be noted that due to employing the MPPT system,  $v_{pv}$  does not vary significantly for a wide range of solar irradiance levels. For example, for the PV under the study in this paper, it is in the range of  $257 < v_{pv} < 273$  for a vast range of irradiance level between 100 to  $1000 \frac{W}{m^2}$ . Consequently, the SC is charged/discharged from the grid at the end of the transient period to ensure that  $v_{sc}$  is in this range by applying appropriate charge/discharge power reference ( $P_{ch}, P_{dch}$ ) to VSC. Before changeover to PV, if the SC is over-charged (i.e.,  $v_{sc} > v_{pv}^{t-}$ ), the VSC will continue to discharge power to the grid, and if it is under-charged (i.e.,  $v_{sc} < v_{pv}^{t-}$ ), the algorithm will change  $P_{VSC}^{ref}$  to  $P_{ch}$ . A small value of  $\varepsilon$  is added to  $v_{pv}^{t-}$  as a dead band to avoid chattering. The process of smooth power reference variation will be discussed in the next parts. during the nighttime or full cloudy weather while the irradiance level is below the operation threshold the system works as a regular SC energy storage and VSC reference power is set to zero ( $P_{VSC}^{ref} = 0$ ).

### 6.3 Components models and control systems

The details of the control systems and power stage of the VSC, BDC, supercapacitor, and PV are well studied in the literature. Here, a theoretical background is briefly provided that is vital for the small-signal analyses discussed in the next section. This study considers a detailed switching model (DSM) of the components for time-domain analyses and a nonlinear mathematical model (NMM) for stability analyses.

#### 6.3.1 PV

Figure 6.3 (a) and (b) show the current source model [106] and its equivalent Thevenin model [135] of the PV module, respectively. The voltage-current ( $V$ - $I$ ) characteristic of a PV array consisting of  $N_s$  series modules and  $N_p$  parallel strings is defined by the following nonlinear expressions:

$$i_{pv} = I_{spv} - I_d - \frac{v_{pv} + R_{spv}i_{pv}}{R_p} \quad (6.1)$$

$$I_d = I_0 \left[ \exp\left(\frac{v_{pv} + R_{spv}i_{pv}}{nV_{TH}}\right) - 1 \right] \quad (6.2)$$

$$I_s = \frac{S}{S_r} [I_{s,r} + \alpha_I(T - T_r)] \quad (6.3)$$

where  $I_{spv} = N_p I_s$  and  $I_0 = N_p I_{0,d}$  are PV and diode saturation current of the array,  $V_{TH} = \frac{N_c k T}{q}$  is the diode thermal voltage,  $k$  is Boltzmann constant,  $N_c$  is the number of cells per module, and  $n$  is the diode ideality factor, respectively.  $I_s$  and  $I_{0,d}$  are individual module's photogenerated current and diode saturation current, and  $R_p$  and  $R_{spv}$  are the equivalent series and parallel



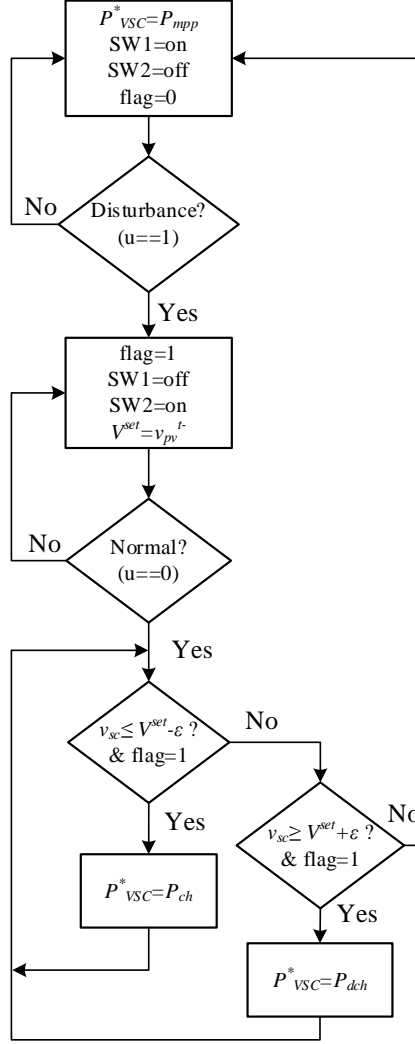


Figure 6.2 The control algorithm of the proposed PVSC system during daytime

resistances of the array, respectively.  $I_{s,r}$  is photogenerated current at nominal conditions ( $25^\circ\text{C}$  and  $1000\text{W}/\text{m}^2$ ),  $\alpha_I$  is a current-temperature coefficient,  $S$ , and  $T$  are irradiation level ( $\text{W}/\text{m}^2$ ) and ambient temperature (in Kelvin) with  $S_r$  and  $T_r$  being their nominal values. The nonlinear model in Figure 6.3a can be approximated by its tangent to achieve a Thevenin equivalent model (Figure 6.5.b), around the equilibrium point ( $V_{pv}, I_{pv}$ ) of the PV:

$$V_{spv} = v_{pv} + R_{pv}i_{pv} \quad (6.4)$$

where  $R_{pv}$  is the PV source static resistance and is defined by  $R_{pv} \triangleq \frac{V_{pv}}{I_{pv}}$  at equilibrium point and

$V_{spv}$  is the equivalent internal voltage source.

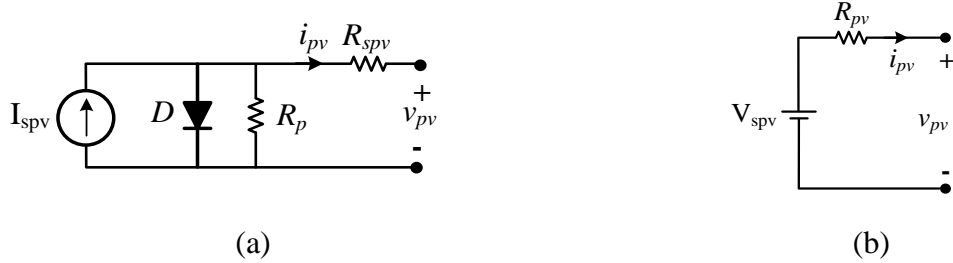


Figure 6.3 Figure 5. PV module equivalent circuit, a) current source model, Thevenin equivalent

With the known values of  $R_{spv}$  and  $R_p$ , and using (6.1), the PV power is calculated by:

$$P_{pv} = v_{pv} i_{pv} \quad (6.5)$$

and the maximum PV power ( $P_{mp}$ ) and the corresponding value of the voltage at this point can be obtained by equating the power expression to zero at maximum point ( $mp$ ) [136]:

$$\left. \frac{dP_{pv}}{dv_{pv}} \right|_{mp} = 0 \quad (6.6)$$

These PV power and voltage values can be used for the control system which will be discussed in the next section. The PV manufacturers usually supply the  $I$ - $V$  and  $P$ - $V$  characteristics of the module for different operating points [106]. However, one can estimate the maximum power point parameters using (6.6) if the module parameters are known. Figure 6.4 shows the  $P$ - $V$  characteristics of the PV array used in this study for different values of solar irradiation. As can be seen, the range of the PV voltage when tracking maximum point is narrow enough to safely connect it to a pre-charged SC with the voltage at the same range.

### 6.3.2 Supercapacitor

Figure 6.5 shows the equivalent model of the SC [137]. In this study, the capacitor element of the SC is modeled as an internal voltage source, with a parallel self-discharge resistance ( $R_{psc}$ )

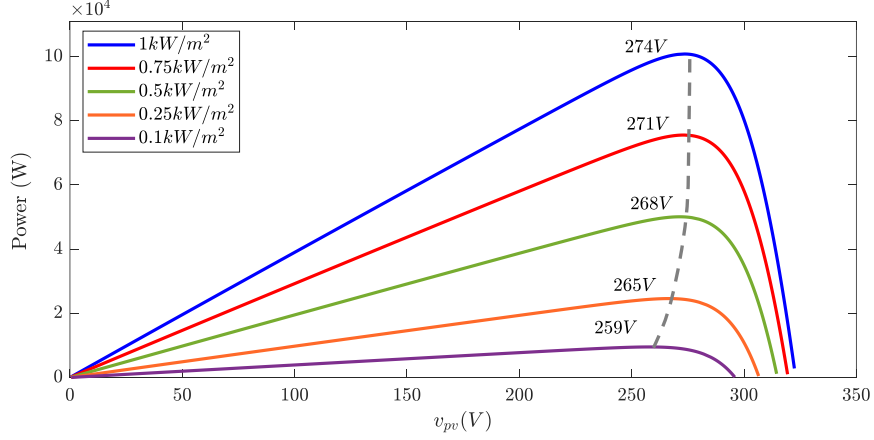


Figure 6.4  $P$ - $V$  characteristics of the PV array under the study, for different levels of irradiance and rated temperature (25°C).

and series resistance ( $R_{ssc}$ ). The incremental/decremental energy in the internal capacitor depends on the power absorbed/injected and the duration of the SC in operation:

$$E_{sc}(t) = \int V_{csc}(t) i_{csc}(t) dt \quad (6.7)$$

where

$$i_{csc} = i_{sc} + \frac{V_{csc}}{R_{psc}} \quad (6.8)$$

is the internal capacitor current. Then the current value of  $V_{csc}$  can be calculated by:

$$V_{csc}(t) = \sqrt{\frac{2(E_{sc,0} - E_{sc}(t))}{C_{sc}}} \quad (6.9)$$

where  $E_{sc,0} = \frac{1}{2} C_{sc} V_{csc,0}^2$  is the initial energy stored in the internal capacitor with the initial voltage  $V_{csc,0}$ . Figure 6.5(b) represents the nonlinear model of the SC to be used in NMM.

### 6.3.3 Bidirectional DC-DC Converter

The BDC is a half-bridge converter [137][138] and controls the DC link voltage where VSC is connected to its DC side. Unlike the regular PV systems where a boost converter along with the

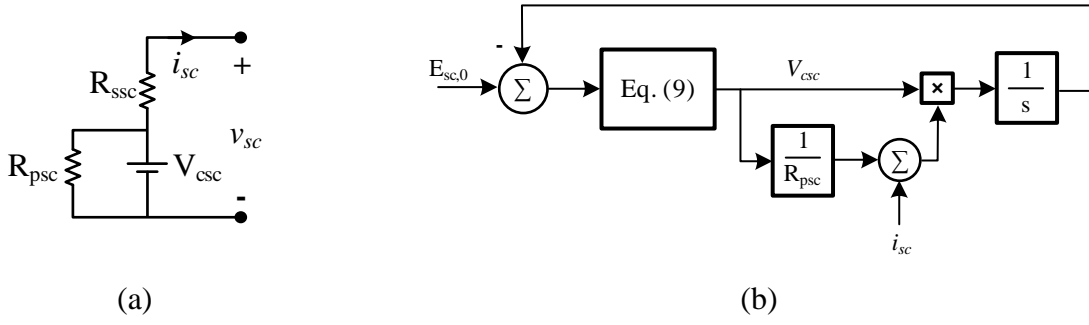


Figure 6.5 Supercapacitor model, (a) circuit model, and (b) nonlinear model diagram

VSC works in current source mode (or grid-supporting mode) and it does not control the voltage and frequency, the proposed system aims to implement the voltage source mode (or grid forming mode) where the BDC controls the DC link voltage and the VSC controls voltage and frequency at its terminal in AC side. The regular PV system injects the PV active power and can have limited control on reactive power. The dynamics of the BDC is expressed in terms of inductor current ( $i_L$ ) and DC-link capacitor voltage ( $v_{dc}$ ):

$$\begin{cases} \frac{di_L}{dt} = -\frac{R_{dc}i_L}{L_{dc}} + \frac{1}{L_{dc}}[v_{in} - f(d)v_{dc}] \\ v_{dc} = \frac{1}{C_{dc}} \int f(d)i_L dt \end{cases} \quad (6.10)$$

where  $L_{dc}$ ,  $R_{dc}$  and  $C_{dc}$  are, respectively, the inductor and DC link capacitor parameters,  $v_{in}$  is the converter input voltage that can be either connected to  $v_{pv}$  (when operating with PV) and  $v_{sc}$  when operating with SC, and  $f(d)$  is defined by:

$$\begin{cases} f(d) = d & \text{buck mode} \\ f(d) = 1 - d & \text{boost mode} \end{cases} \quad (6.11)$$

where  $d$  is the duty cycle generated by the control system. It should be noted that when operating with SC,  $f(d)$  can take both values in (11) depending on charge or discharge operation. However, during the operation with PV, where the converter works in boost mode,  $f(d) = d$ . Figure 6.6,

on the left-hand side, shows the equivalent circuit model of the BDC power stage. The dynamics of the inductor current ( $i_L$ ) has a little difference when operating with PV and SC. For the BDC connected to PV we have:

$$\frac{di_L}{dt} = -\frac{(R_{dc} + R_{spv})i_L}{L_{dc}} + \frac{1}{L_{dc}}[V_{spv} - f(d)v_{dc}] \quad (6.12)$$

where  $f(d) = 1 - d$ . And for the BDC connected to SC it holds:

$$\frac{di_L}{dt} = -\frac{(R_{dc} + R_{ssc})i_L}{L_{dc}} + \frac{1}{L_{dc}}[V_{csc} - f(d)v_{dc}] \quad (6.13)$$

The diagram of the nonlinear dynamic model of the BDC combined with PV and SC is separately expressed in the Laplace domain and represented in Figure 6.7 which will be used for linearization purposes. The control system of BDC is discussed in the next part.

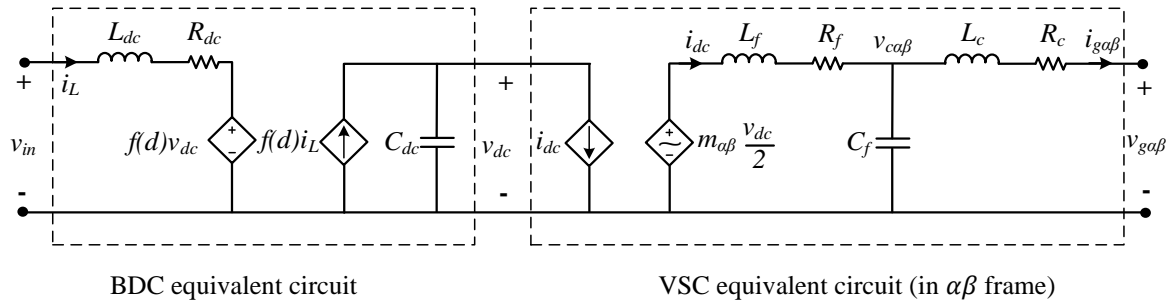
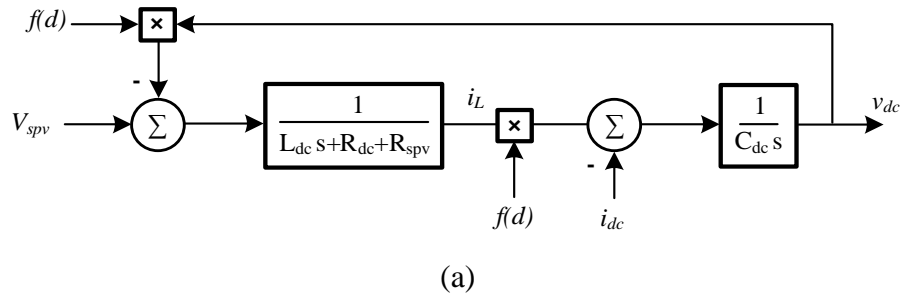


Figure 6.6 Equivalent circuit model for power stage of the BDC and VSC



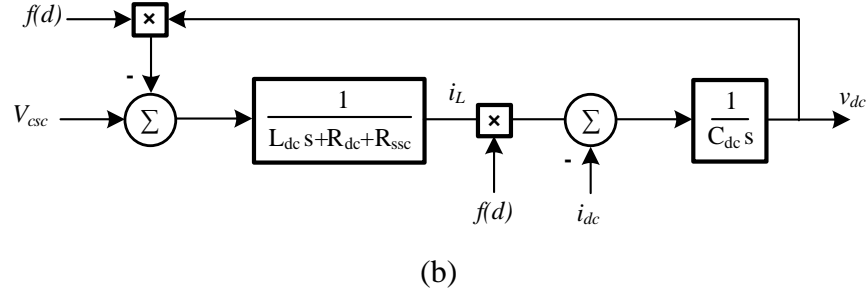


Figure 6.7 Diagram of the nonlinear model of the BDC combined with: (a) PV and (b) SC models.

### 6.3.4 VSC, Load and Transmission Line

The VSC is a two-level three-phase inverter [20] with an LCL circuit [139] working as a second-order filter. It should be noted, although the control system of the VSC is implemented in the rotating reference frame (RRF) or  $dq$  to interact with DC parts of the system, its power stage is modeled in the stationary reference frame (SRF) or  $\alpha\beta$  to reflect the frequency interactions with power grid [21]. The following expressions represents the VSC dynamics in  $\alpha\beta$  frame:

$$\begin{aligned}
 \frac{di_{t\alpha\beta}}{dt} &= \frac{1}{L_f} (-R_f i_{t\alpha\beta} + v_{t\alpha\beta} - v_{c\alpha\beta}) \\
 v_{c\alpha\beta} &= \frac{1}{C_f} \int (i_{t\alpha\beta} - i_{o\alpha\beta}) dt \\
 \frac{di_{o\alpha\beta}}{dt} &= \frac{1}{L_c} (-R_c i_{o\alpha\beta} + v_{c\alpha\beta} - v_{g\alpha\beta}) \\
 v_{t\alpha\beta} &= m_{\alpha\beta} \frac{v_{dc}}{2}
 \end{aligned} \tag{6.14}$$

where  $m_{\alpha\beta}$  is the control signal input to VSC and  $v_{t\alpha\beta}$  is the converter AC terminal voltage and all other parameters are introduced in Figure 6.1. Variables with subscription  $\alpha\beta$  are orthogonal space vectors where the component  $\alpha$  is aligned with the phase  $a$  of the corresponding variable in  $abc$  reference frame.

The load is a combination of resistive and inductive elements. Although the series combination of the load is considered in the time domain modeling, its parallel combination is presented in the Laplace domain in Figure 6.8 where  $R'_l$  and  $L'_l$  represent the parallel equivalent of the load

elements. The following expressions define the dynamics of the load and transmission line in  $\alpha\beta$  frame:

$$\begin{aligned} \frac{d}{dt} (i_{o\alpha\beta} - i_{g\alpha\beta}) &= \frac{1}{L_l} [-R_l(i_{o\alpha\beta} - i_{g\alpha\beta}) + v_{g\alpha\beta}] \\ \frac{di_{g\alpha\beta}}{dt} &= \frac{1}{L_g} (-R_g i_{g\alpha\beta} + v_{g\alpha\beta} - v_{G\alpha\beta}) \end{aligned} \quad (6.15)$$

where  $v_{G\alpha\beta}$  is the constant vector of grid voltage. The  $\alpha\beta$  vectors of the grid voltage can be converted from  $abc$  reference frame using Clark transformation [20][31]. The complete dynamic model of the VSC, load, and transmission line is derived from (6.14) and (6.15) and represented in Figure 6.8. This model along with the dynamic models of the other components will be used in NMM for linearization and stability analyses.

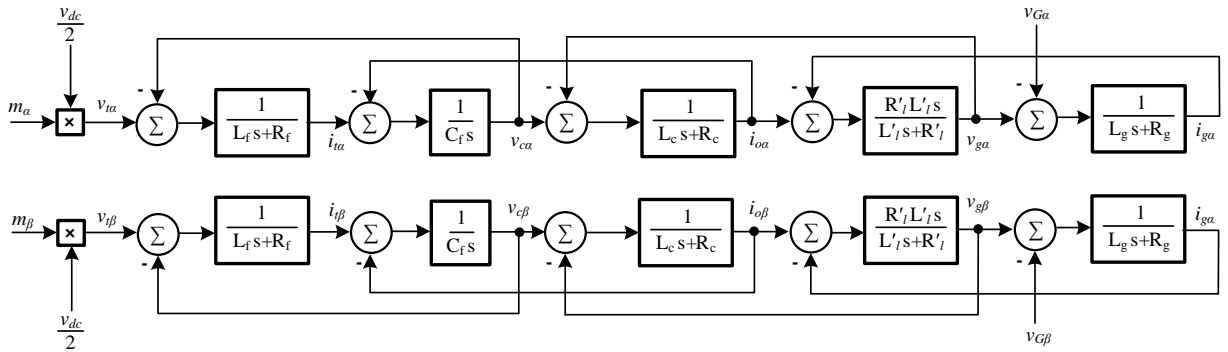


Figure 6.8 The complete dynamic model of the VSC, load and transmission line represented in  $\alpha\beta$  frame

## 6.4 Control systems

The control systems are designed and implemented such that the combination of the BDC and VSC operates in voltage source or grid-forming mode.

### 6.4.1 BDC control

When operating with PV, the BDC turns into a unidirectional converter whose function is to

transfer the PV power to VSC while ensuring the DC link voltage remains on its reference value. However, during the operation with SC, it performs as a bidirectional converter to exchange power with VSC. This changeover is facilitated in the control algorithm by switching between signals and measurements. The BDC is controlled by a cascaded voltage-current control framework [135][116] where the current loop bandwidth is much greater than that of the voltage loop. Hence the controllers can be separately designed.

Figure 6.9 shows the BDC control diagram when operating with SC, where  $k_{pv}$ ,  $k_{iv}$ ,  $k_{pc}$  and  $k_{ic}$  are, respectively, the proportional and integral gains of the PI regulators in voltage and current loops. Also,  $\omega_{c1}$  is the bandwidth of the low pass filter (LPF) to suppress the switching noise of current measurement ( $\tilde{i}_L$ ).  $v_{dc}$  and  $v_{dc}^*$  are the DC link voltage measurement and its reference value.

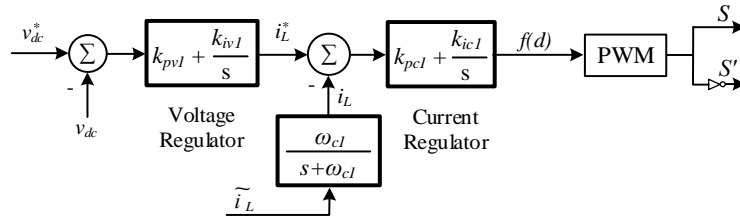


Figure 6.9 BDC control diagram when operating with SC

The operation of BDC, when connected to PV, requires the controller to track the maximum power point voltage at PV terminals ( $v_{mp}$ ) as the reference.  $v_{mp}$  along with the corresponding power ( $P_{mp}$ ) (see Figure 6.4) are generated by the MPPT system. Inspired by [135], the control system in Figure 6.9 is reconfigured to control the converter input voltage as feedback provided that the output voltage ( $v_{dc}$ ) remains on its reference value ( $v_{dc}^*$ ). We have:

$$f(d) = 1 - \frac{1}{v_{dc}^*} (v_{pv} - [k_{pc}(i_L^* - i_L) + k_{ic} \int (i_L^* - i_L) dt]) \quad (6.16)$$



which is represented in Figure 6.10. It should be noted that all controller parameters will remain the same during the changeover from PV to SC and vice versa.

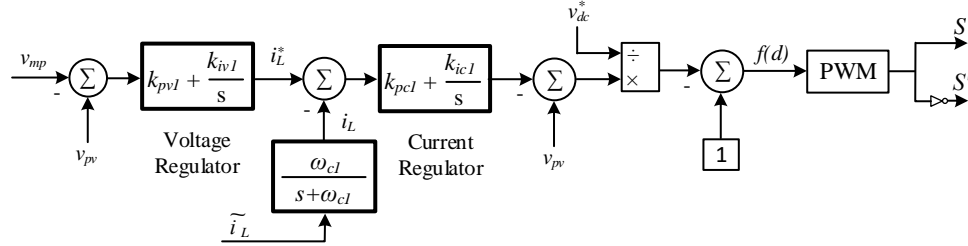


Figure 6.10 BDC control system when connected to PV.

Note that  $P_{mp}$  is applied to VSC reference power ensuring that the power transferred from DC link to AC side is equal to PV output power hence the DC link voltage remains constant during the operation of PV with different irradiance levels.

#### 6.4.2 VSC Control

The VSC has a droop controlled dual loop voltage/current control system implemented in  $dq$  frame which is well studied in the literature [20][140] and is shown in figure 6.11. Voltage and current loop controllers are realized using PI regulators, where the bandwidth of the voltage loop is selected at least one decade below the current loop bandwidth.

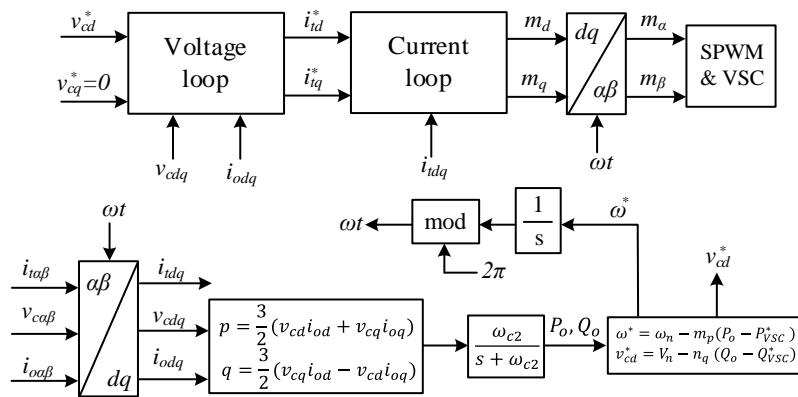


Figure 6.11 The VSC control system diagram

In Figure 6.11,  $\omega_n$  and  $V_n$  are nominal values of the system frequency and voltage magnitude,  $m_p$  and  $n_q$  are droop control coefficients,  $P_o$ ,  $Q_o$ ,  $P_{VSC}^*$  and  $Q_{VSC}^*$  are the output active and reactive power and their references, respectively. It should be noted since the VSC is connected to the grid and the frequency is a global variable, the steady-state error of the frequency is zero and VSC tracks the reference active power, which is defined by the control algorithm. However, as the voltage is a local variable there would be a trade off between tracking the reference reactive power or voltage magnitude. The voltage and current control loops are expressed in (6.17) and (6.18), respectively:

$$\begin{aligned} i_{td}^* &= k_{pv2}(v_{cd}^* - v_{cd}) + k_{iv2} \int (v_{cd}^* - v_{cd})dt + i_{od} - \omega_n C_f v_{cq} \\ i_{tq}^* &= k_{pv2}(v_{cq}^* - v_{cq}) + k_{iv2} \int (v_{cq}^* - v_{cq})dt + i_{oq} + \omega_n C_f v_{cd} \end{aligned} \quad (6.17)$$

$$\begin{aligned} m_d &= k_{pc2}(i_{td}^* - i_{td}) + k_{ic2} \int (i_{td}^* - i_{td})dt + v_{cd} - \omega_n L_f i_{tq} \\ m_q &= k_{pc2}(i_{tq}^* - i_{tq}) + k_{ic2} \int (i_{tq}^* - i_{tq})dt + v_{cq} + \omega_n L_f i_{td} \end{aligned} \quad (6.18)$$

where  $k_{pv2}$ ,  $k_{iv2}$ ,  $k_{pc2}$  and  $k_{ic2}$  are proportional and integral gains of the PI regulators.

## 6.5 Nonlinear Mathematical Model and Small-Signal Analyses

In this section, the proposed system's stability is analyzed through a complete nonlinear mathematical model (NMM) of all components and their interactions.

### 6.5.1 NMM

The NMM is suitable for fast linearization analysis with high accuracy where the system's dynamic complexity grows with the number of components. It can be considered as a reduced order average model that retains the system's dynamic with high accuracy. The NMM can be formed by interconnecting all component's dynamic models. The dynamic interaction between AC and DC parts is established by power balance in DC link between BDC and VSC as follows. Neglecting the power transfer loss in VSC we have:

$$P_{DC} = v_{dc}i_{dc} \quad (6.19)$$

$$P_{AC} = \frac{3}{2}(v_{td}i_{td} + v_{tq}i_{tq}) \quad (6.20)$$

where  $P_{DC}$  and  $P_{AC}$  are input and output power of the VSC respectively. Substituting  $v_{td} = \frac{m_{dq}}{2}v_{dc}$  in (6.20) and equating right-hand sides of the (6.19) and (6.20) it holds:

$$v_{dc}i_{dc} = \frac{3}{2}\left(\frac{m_d}{2}v_{dc}i_{td} + \frac{m_q}{2}v_{dc}i_{tq}\right) \quad (6.21)$$

$$i_{dc} = \frac{3}{4}(m_d i_{td} + m_q i_{tq}) \quad (6.22)$$

in which  $i_{dc}$  is expressed in terms of  $dq$  quantities of the modulation indices and VSC output terminal current ( $i_{tdq}$ ). Figure 6.12 shows the NMM of the proposed PVSC system which can be easily utilized for deriving linearized state-space models and transfer functions for any sets of input/output signals. these models and transfer functions can be used for examining the stability of the system under different operating points and parameter variations as well as control system design. As can be seen, the NMM is purely based on mathematical models with no implementation of circuits.

### 6.5.2 Small-Signal Analyses

Reference [140] provides a systematic approach to derive the small-signal state-space model of a grid-forming VSC with a constant voltage DC source as an energy source. The same methodology can be used for deriving a combined small-signal model of the PVSC system. However, this study, instead of implementing a tedious linearization approach, utilizes the NMM model and Simulink Control Design (SCD) tool [141] to obtain the small-signal model. Once the NMM model shown in Figure 6.12 is formed, the SCD tool is used to carry out classical linear control analyses. The resulting linearized system is represented by the state-space form:

$$\begin{cases} \dot{x}(t) = \mathcal{A}x(t) + \mathcal{B}u(t) \\ y(t) = \mathcal{C}x(t) \end{cases} \quad (6.23)$$

where  $x, u$  and  $y$  are the small-signal vectors of state variables, input, and output signals, and  $\mathcal{A}, \mathcal{B}$ , and  $\mathcal{C}$  are state transition, input, and output matrices of the system. The eigenvalues of matrix  $\mathcal{A}$  represent poles of the system. For a given operating point, if all poles of the system (6.23) are in the left half-plane of the Real/Imag plane, the system is stable [142] or asymptotically stable.

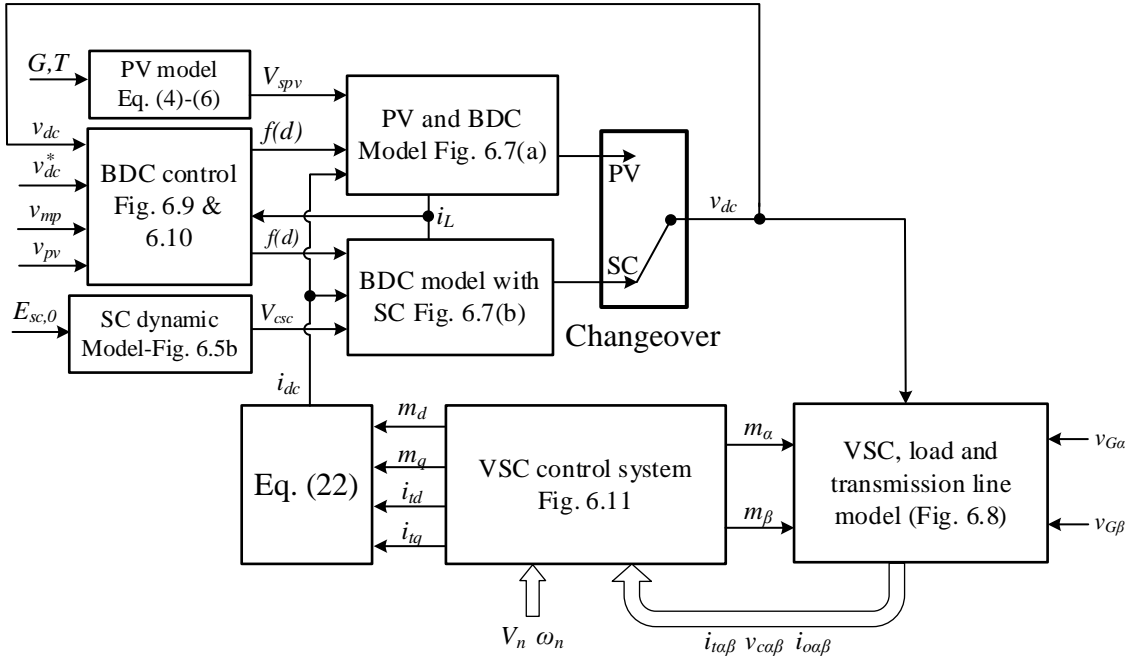


Figure 6.12 Nonlinear Mathematical Model of the proposed PVSC system

This part aims to examine the stability boundaries of the PVSC system for variation of some parameters in each operating point. Figure 6.13 shows the map of the dominant poles of the linearized PVSC system for the case under the study around the nominal operating point represented in Tables 6.1 to 6.3. The initial operating point values are obtained from the steady-state operation of the system under nominal conditions. The figure represents the influence of variation of active power droop coefficient  $0.01 < m_d < 0.1$  when operating with SC. The linearized model has 23 state variables. The displacement of the pole pair shown in figure 6.13 indicates that while the

system stability elevates with increasing  $m_d$ , the system step response would be more aggressive with higher overshoots during the load or power reference changes. Therefore, there should be a trade-off in selecting this parameter.

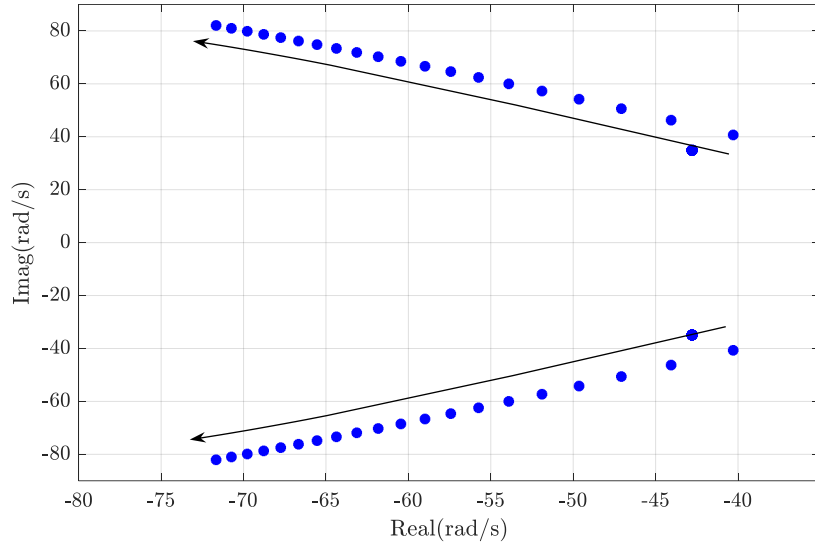


Figure 6.13 Replacement of dominant poles of the linearized PVSC system for variation of active power droop  
 $0.01 < m_d < 0.1$

The same analysis can be conducted for determining the stability boundaries for variation of control parameters. Figure 6.14 (a) and (b) illustrates the dominant poles' displacement trajectory for the variation of integral gain of the voltage control loop ( $k_{iv1}$ ) and integral gain of the current control loop ( $k_{ic1}$ ) of BDC control system. These figures demonstrate how increasing or decreasing integral gains in BDC affects the stability and step response of the system.

Similarly, the dominant pole displacement in response to integral gain variation in VSC voltage control ( $k_{iv2}$ ) loops are depicted in Figure 6.15.

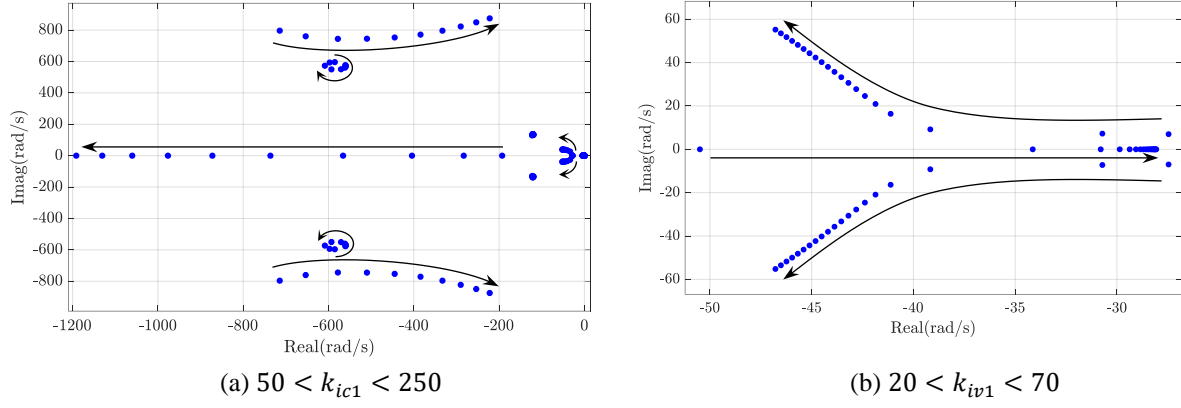


Figure 6.14 pole map of the PVSC small-signal model for the variation of DC-DC control system parameters; (a) variation of  $k_{ic1}$  and (b) variation of  $k_{iv1}$ .

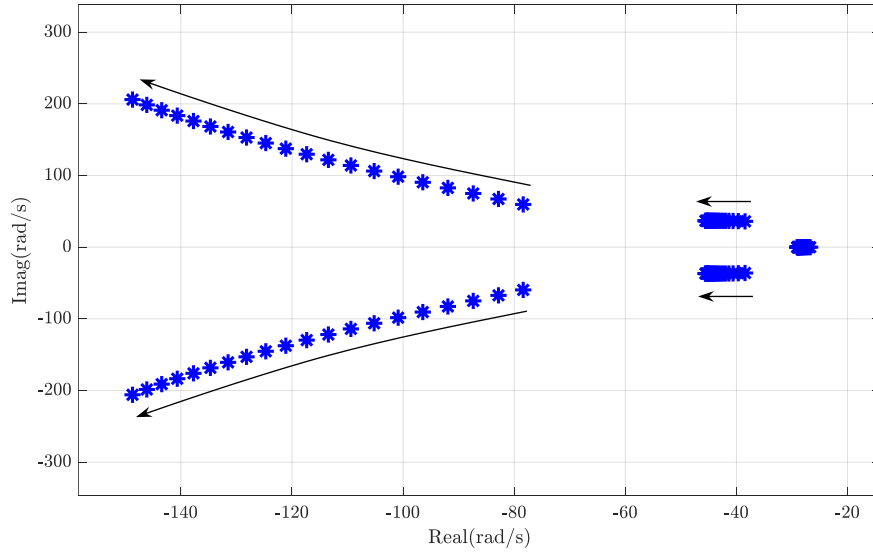


Figure 6.15 Pole displacement map in response to integral gain variation in VSC voltage control ( $k_{iv2}$ ) loops,  $188 < k_{iv2} < 560$ .

## 6.6 Simulation Results and Discussions

This section implements the time-domain simulation of the proposed PVSC system shown in Figure 6.1 and analysis the effectiveness of the system in response to grid disruptions. The test system data are represented in Tables 6.1 to 6.3.

Table 6.1 Parameters of the PVSC system under the study

$v_G$	460 V(L-L)	$v_{dc}^*$	1000 V
$\omega_n$	314 rad/s	$V_n$	460/ $\sqrt{3}$ V
$L_f$	1.6mH	$R_f$	4.76m $\Omega$
$L_c$	64 $\mu$ H	$R_c$	0.5m $\Omega$
$L_g$	18mH	$R_g$	102mH
$l'$	56.1mH	$r'$	2.16mH
$L_{dc}$	1mH	$R_{dc}$	45mH
$C_f$	2.5mF	$C_{dc}$	2mF
$m_p$	0.025	$n_q$	0
$k_{pv1}$	1	$k_{pv2}$	1.673
$k_{pc1}$	1.15	$k_{pc2}$	3.2
$k_{iv1}$	39	$k_{iv2}$	374.6
$k_{ic1}$	150	$k_{ic2}$	11.28
$\omega_{c1}$	30 rad/s	$\omega_{c2}$	2000 rad/s

Table 6.2 PV parameters

PV Module <sup>1</sup> : SunPower SPR-315E-WHT-D			
$N_s$	5	$N_p$	64
$V_{mp}$ <sup>2</sup>	54.7 V	$I_{mp}$ <sup>2</sup>	5.76 A
$R_{pv}$	0.1484m $\Omega$		
$T_r$	298K	$S_r$	1000 W/m <sup>2</sup>

<sup>1</sup> Individual module's parameters are extracted from this PV model

<sup>2</sup>  $V_{mp}$  and  $I_{mp}$  are voltage and current at maximum power point per module, respectively.

Table 6.3 SC parameters

$C_{sc}$	25F	$V_{rated}$	530V
$R_{ssc}$	0.9m $\Omega$	$R_{psc}$	950 $\Omega$
$V_{csc,0}$	257~274 V	$I_{mp}^*$	5.76 A

### 6.6.1 Validation of dynamic accuracy of NMM

**A.1 Examining NMM conformity:** To examine the validation of NMM, this part simulates and compares NMM and DSM in the normal operating conditions where there are some step changes in reference values with no external disturbances. It should be noted that the ambient conditions in PV are kept constant during simulations. Figure 6.16 (a) and (b) compare the system

response to a step change in nominal voltage of AC terminal ( $V_n$ ) for  $v_c$  and VSC control signals  $m_{dq}$ . The nominal voltage decreases and increases by %5 in 1-second interval. As it is shown, with negligible error in  $m_{dq}$  signals, both systems have similar dynamics. Also, Figure 6.17 illustrates  $v_{dc}$  response to  $\pm\%5$  consecutive step changes in DC link reference voltage  $v_{dc}^*$ . Finally, figure 6.18 compares the response of VSC output power ( $P_o$ ) to  $+\%25$  step change in its reference power ( $P_{VSC}^*$ ). It can be concluded from figures 18 to 20, that the NMM model conforms with that of the DSM dynamics and can be used for small signal analysis.

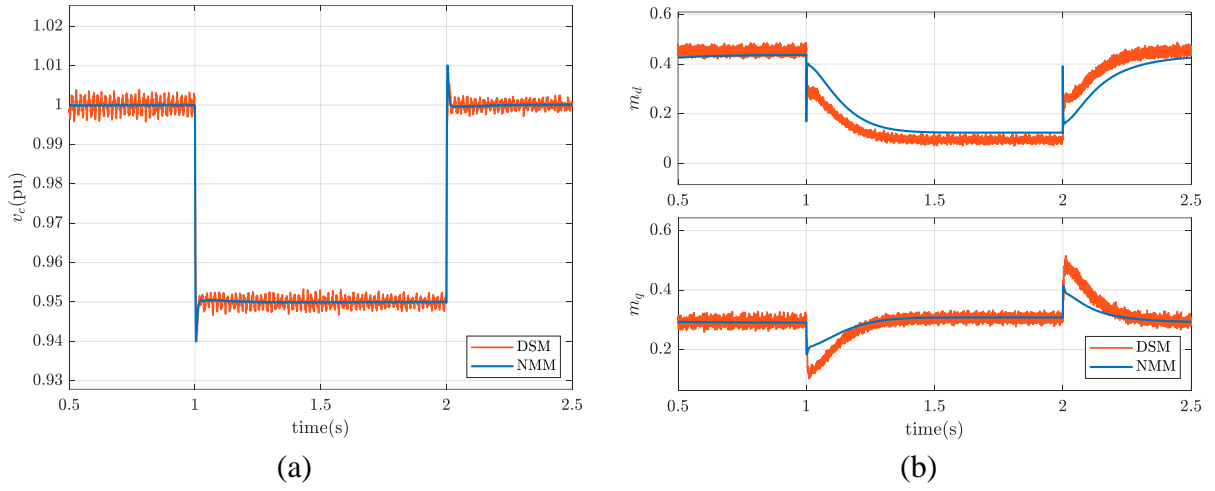


Figure 6.16 Comparison of NMM to that of the DSM for a step change in AC nominal voltage; (a)  $v_c$  and (b)  $m_{dq}$

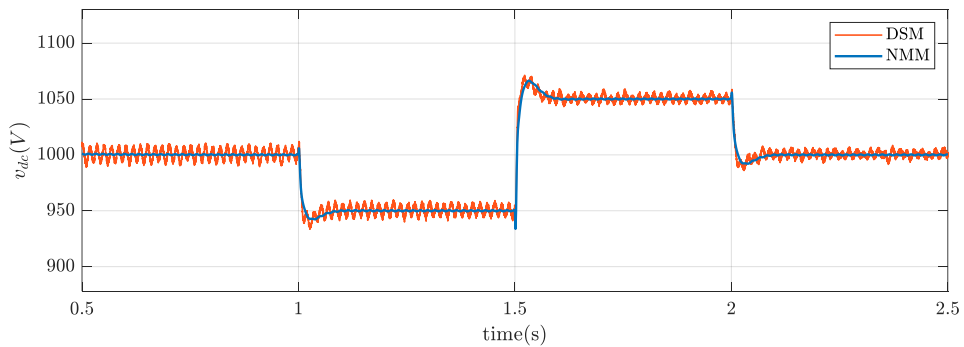


Figure 6.17 Comparison of NMM dynamics to that of the DSM for a step change in DC link reference voltage  $v_{dc}$



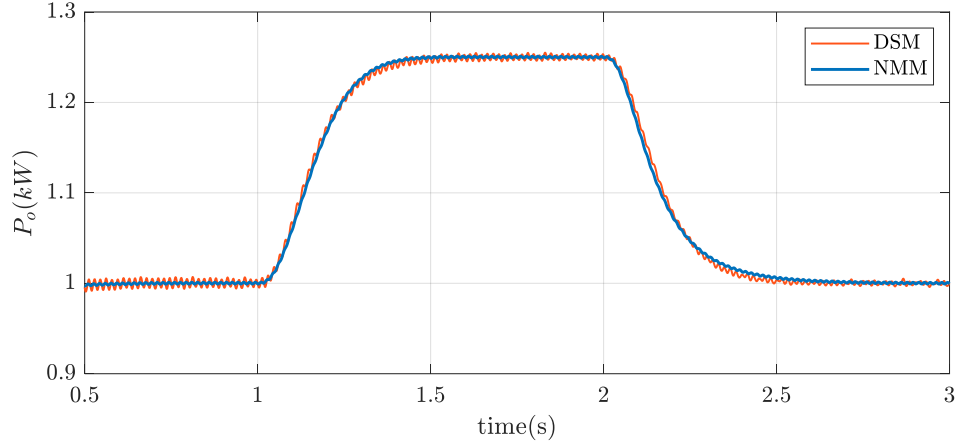


Figure 6.18 Comparison of NMM dynamics to that of the DSM for step change in  $P_{vsc}^*$

**A.2 Changeover between PV and SC:** Figures 6.19 and 6.20 show the magnitude of  $v_{sc}$  and  $v_{dc}$  in response to changeover between PV and SC in DSM, where the changeover takes place with maximum and minimum values of  $v_{pv}$  to emulate the worse cases with maximum voltage difference. In this case, a fictitious disturbance signal is triggered by DDA for  $2 \leq t \leq 3s$ . The control algorithm performs the procedure. In both cases, the SC gets discharged to keep the reference output power. For the case started with  $v_{pv}^{min}$ , the system turns back to PV with  $v_{pv}^{t-}$  where  $v_{pv}^{t-}$  refers to the PV voltage at the initial changeover moment. However, for the case started with  $v_{pv}^{max}$ , the algorithm charges the SC to prepare it for the next changeover with  $v_{pv}^{t-}$ . It is confirmed that the changeover with maximum difference between  $v_{pv}$  and  $v_{sc}$  during the system operation has no negative impact on the system's performance hence the proposed PVSC system can be safely used for handling grid disturbances, discussed in the next part.

### 6.6.2 Effectiveness of Proposed PVSC System to Maintain Voltage Stability

This part evaluates the effectiveness of the proposed system to maintain voltage stability during the main grid's voltage sags and swells. The proposed PVSC is compared with a regular PV system (RPS) with the same nominal values in which the VSC has a grid-feeding control mode

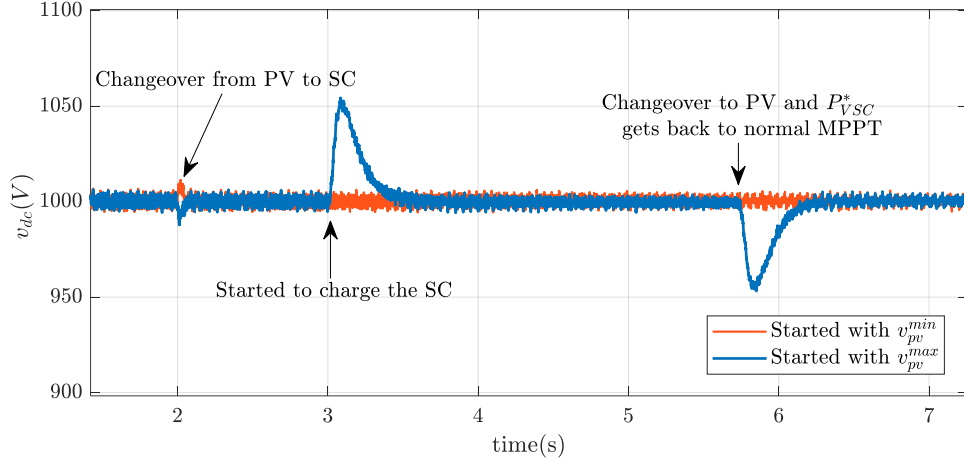


Figure 6.19 DC link voltage during the changeover between PV and SC

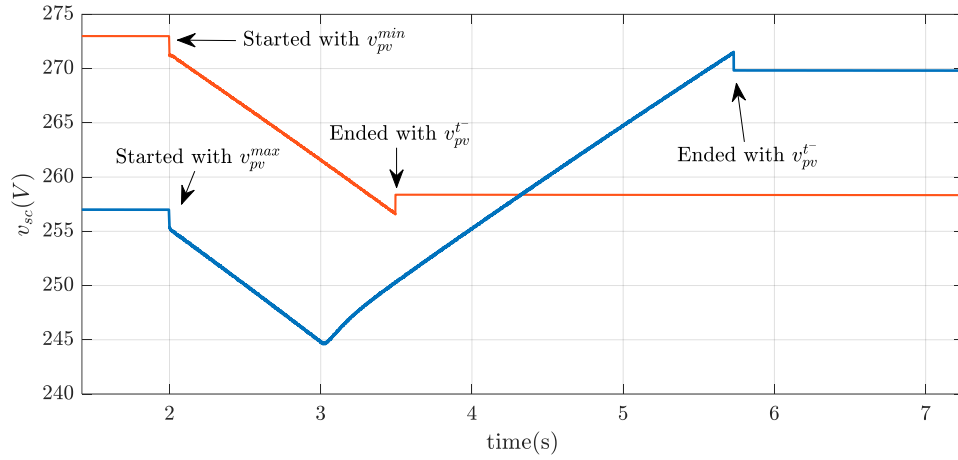


Figure 6.20 SC terminal voltage during the changeover between PV and SC;  $v_{pv}^{t-}$  refers to the PV voltage at the changeover moment.

[29] (or current source) where maximum PV power is injected into the grid with no response to grid voltage/frequency deviations. In the RPS, the VSC controls DC link voltage and the DC-DC converter tracks the PV maximum power [101]. In this case, a voltage disruption with  $\pm 0.05$  pu in 1s intervals takes place in the main grid voltage magnitude. Figure 6.21 compares the performance of the proposed PVSC and RPS for voltage and frequency at the VSC terminal in response to this disruption. It is assumed that the DDA enables/disables the unnormal condition signal with a 50ms delay. As can be seen, the SC remains connected after the system returns to normal

condition to charge the SC and gets prepared for the next event. Although in the case of PVSC the frequency at the VSC terminal has transients during the voltage disturbances and SC operations, the voltage is kept perfectly at its nominal value guaranteeing the power quality for the local load.

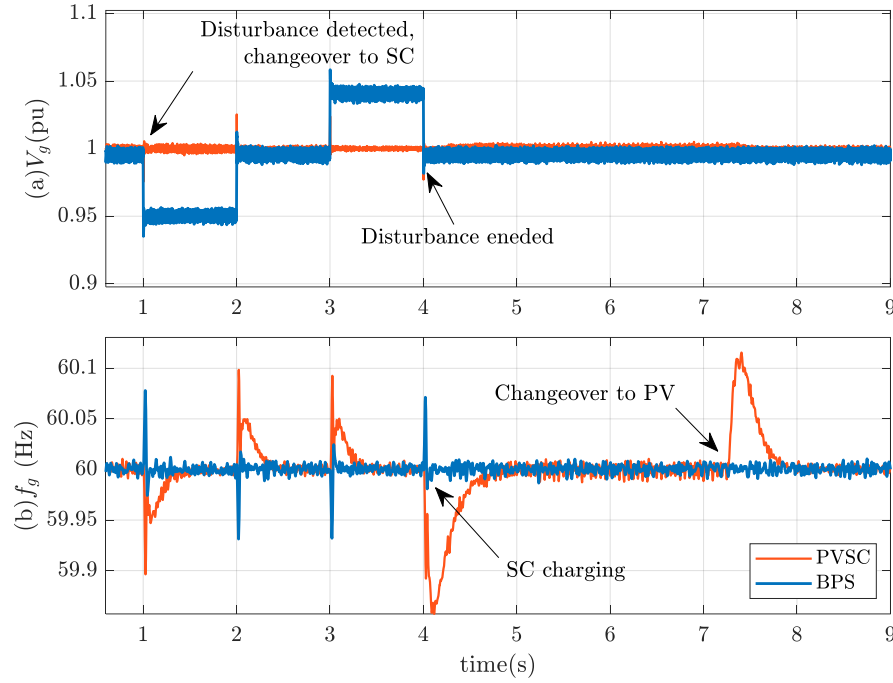


Figure 6.21 Performance evaluation of proposed PVSC compared to regular PV system during voltage disruption in main grid; (a) VSC output voltage, (b) VSC output frequency

### 6.6.3 Stepwise Load Variation and Weak Integration to Grid

This part assumes that the PV system is weakly integrated to main grid with higher transmission line impedance ( $4L_g, 4R_g$ ). A  $\pm 25\%$  step load disruption (both active and reactive power) occurs at the local load during  $1 < t < 3$  that causes some transients. The DDA enables/disables the unnormal condition signal with 50ms delay. It is assumed that RPS generates a constant reactive power. As shown in figure 6.22, since the RPS does not control the voltage and frequency, load variation causes voltage excursions from its nominal value and a low magnitude frequency swing is observed in RPS's terminal. In contrast, PVSC damps the load variation transients by controlling voltage and frequency.

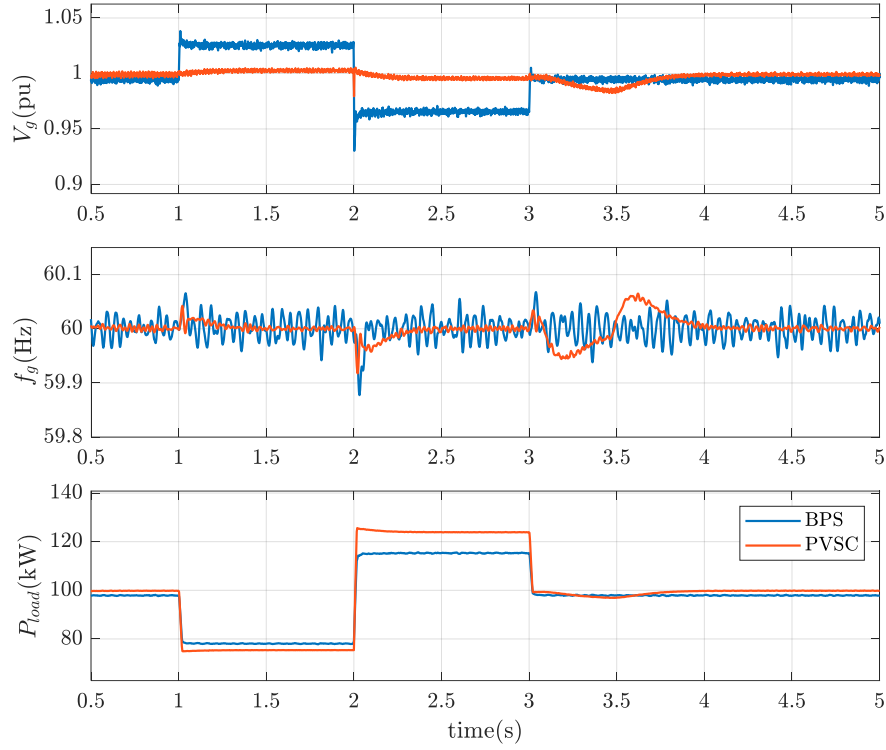


Figure 6.22 Stepwise load variation and weak integration to grid

#### 6.6.4 Performance Comparison Between the Proposed PVSC and Conventional SC

This part investigates the performance of the proposed PVSC in an islanded microgrid and compares it with the case that the basic PV system is collocated with a conventional supercapacitor (shown in Figure 6.23). In figure 6.23, when the dashed lines are open, the conventional SC is not in use and the remaining system represents the BPS; and when the dashed lines are closed the conventional SC is in use and the system represents the BPS collocated with a conventional SC (BPS-SC). To make the islanded microgrid, the grid models in Figures 2.21 and 6.1 are replaced with a droop-controlled grid-forming energy source (DER1) whose primary energy supply can be any source with DC voltage. All components of the microgrid in the three models have the same ratings.

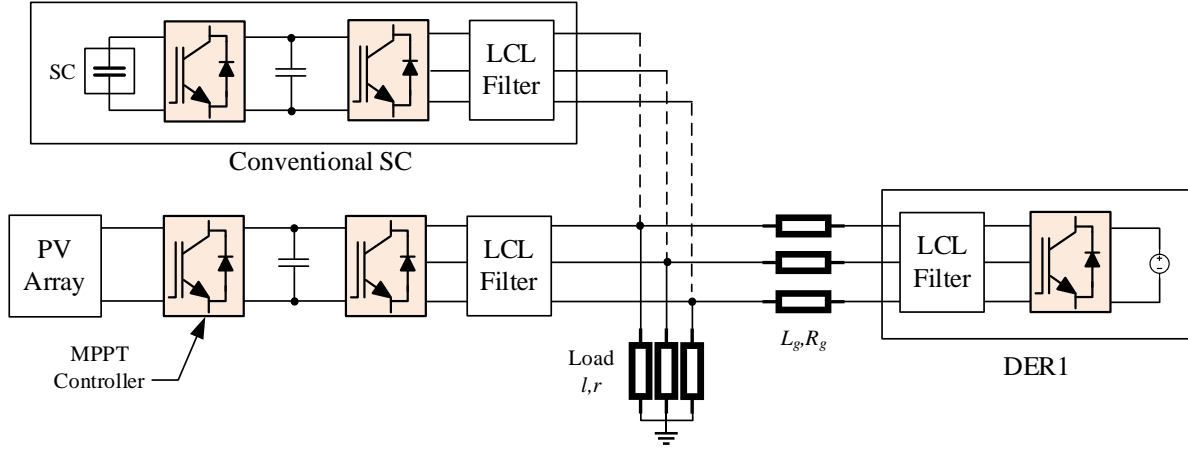


Figure 6.23 Islanded microgrid representation with the BPS and BPS-SC. The open dashed lines represent BPS, and the closed dashed lines represent BPS-SC.

**The step change in local load:** In this section, some stepwise load changes consecutively occur in the local load, similar to the disruptions considered in part C, where the nominal load is 100kW and the PV works with the max irradiance level. Figure 6.24 shows the performance of the three system models i.e., the BPS which is the basic system, the BPS collocated with a conventional SC (BPS-SC), and the proposed PVSC for essential system parameters. It is assumed that the DDA system activates and inactivates the SC operation with a 50ms delay. It is demonstrated that the BPS system is unable to maintain the load power at the demand level, due to the voltage magnitude excursion from its nominal value. Also, figure 6.25 shows the output power of the PV energy storage system. The power balance is made by both systems. However, the PVSC gets charged from the DER1 to maintain the minimum level of the SC charge available for the next disturbance. The charging process ends at  $t=4.62s$ . For a short duration, the load and SC charge power are supplied by the DER1. It is well demonstrated that the performance of the proposed cost-effective system is almost similar to the conventional system in maintaining the load demand.

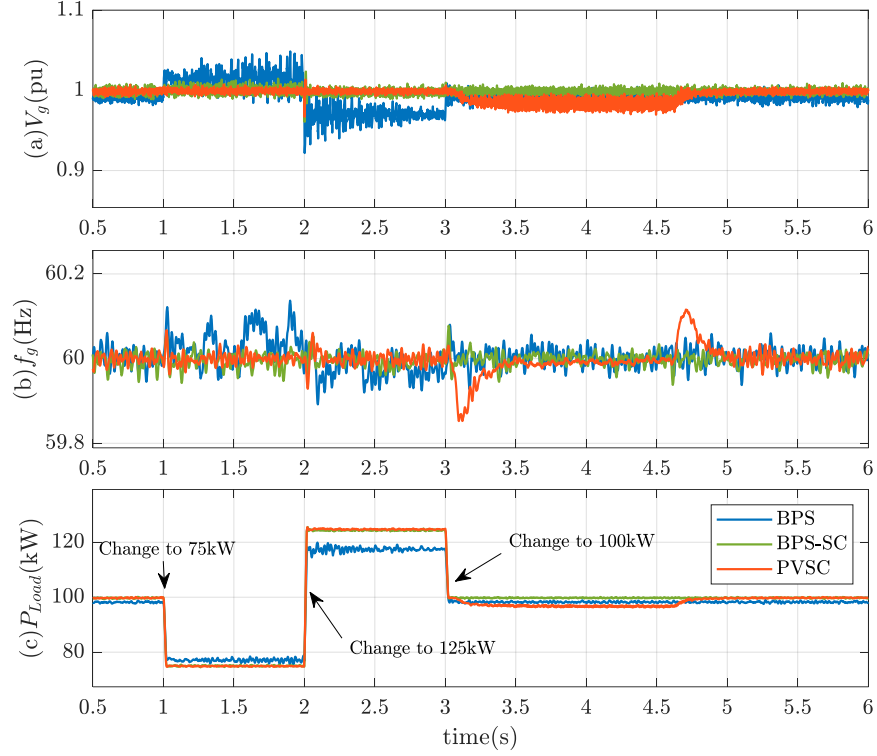


Figure 6.24 Step load change in local load. (a) and (b) grid voltage and frequency at load point and (c) load power.

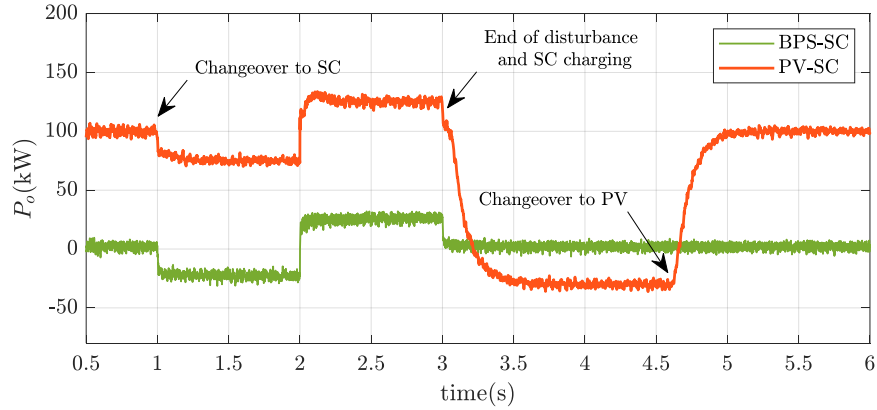


Figure 6.25 Output active power in PV energy storage systems for load change disturbance.

**Fault Analysis:** In this section, a 3-line-to-ground (3LG) short circuit with  $0.35\Omega$  impedance takes place in the middle of the distribution line connecting the PV system to DER1 at  $t=1$ s for the duration of 83ms. Figure 6.26 demonstrates the effectiveness of the proposed system in handling

the fault disturbance in an isolated microgrid and compares it to the conventional system.

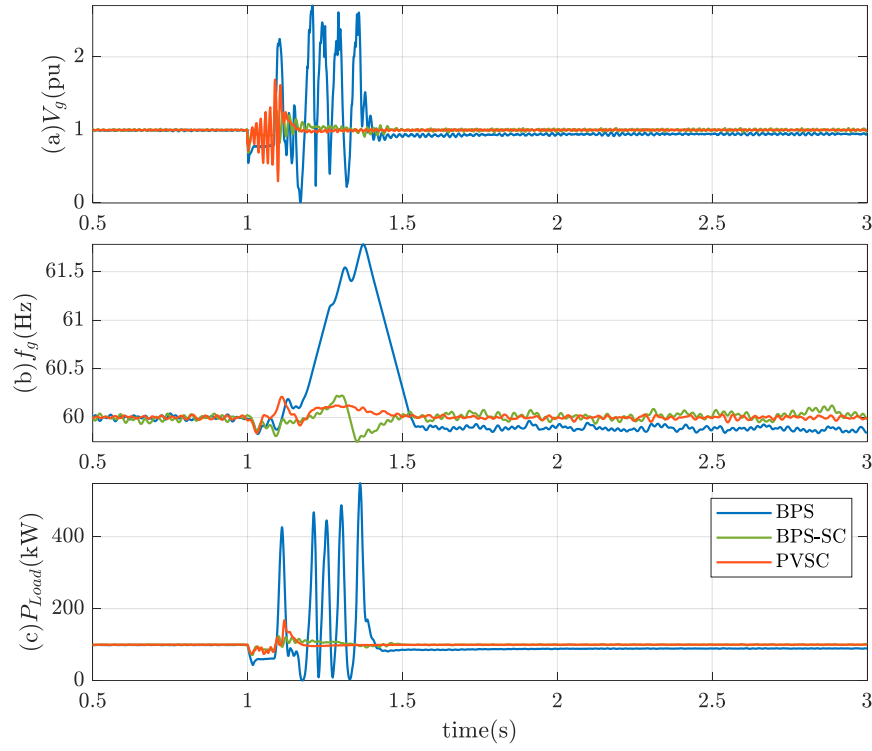


Figure 6.26 Fault analysis evaluation, (a) and (b) grid voltage and frequency at load point, and (c) load power.

### 6.6.5 Cost-Effectiveness of the Proposed Approach

The proposed PV-SC system saves costs as it combines the functionality of energy storage and a regular PV system. To enable a PV system with energy storage capability through the traditional methods (i.e., integrating an energy storage device with its converters and control systems) extra devices and systems are needed. It can be either integrating the PV and energy storage device in DC link and using a common VSC to connect to the AC grid or using two separate VSCs, one for PV and another for the energy storage device. Either way, the cost of this integration would be higher than the PV-SC system. Compared to a regular PV system, the proposed PV-SC system has one extra switching device in DC-DC converter that reconfigures it to a BDC, and two non-modulating switches for changeover operations between PV and SC with a little increase in converter's

capacity.

## 6.7 Chapter Conclusion

This chapter proposed a cost-effective and integrated PV-Supercapacitor (PV-SC) system for dynamic performance enhancement of grid-connected PV systems. It was assumed that a disturbance detection algorithm detects the potential disruptions in the point of common coupling and triggers the SC operation. A control algorithm directs the changeover operations between PV and SC, and VSC power reference allocation. The following remarks can be concluded from this study:

- The traditional PV system that runs in grid-feeding mode, has no means to control the voltage and frequency at the load terminal since it works in current source mode. It is shown in this study, the traditional PV system can be equipped with a high-power density energy storage device i.e., supercapacitor, and run as a voltage source (i.e., grid-forming mode) to carry out the high-power demand storage services along with the ancillary ones.
- During the daytime, the irradiance level is more than the threshold level, and the proposed PV-SC system works as a PV-Energy storage device, while during the nighttime or cloudy weather, it works as an energy storage device.
- A nonlinear mathematical model was developed to analyze the stability boundaries and to design the controller parameters where its dynamic accuracy was compared to that of a detailed switching model.
- The system performance was evaluated for different grid disturbance cases. Simulation results demonstrate the effectiveness of the proposed system in maintaining voltage stability and LVRT capability.



## Chapter 7 Conclusion, Contributions, and Future Work

### 7.1 Conclusion and Contributions

This dissertation presented several studies conducted in the area of control of hybrid microgrids as well as conventional AC and DC microgrids. In terms of the level or type of the research in the field, one study focused on devising a new device at the level of power and control stage and the rest concentrated on designing control methodologies and algorithms for the whole microgrid. The research approach was based on analyzing the existing methods, identifying the gaps or drawbacks, and finding the right solutions. The methodologies were validated through computer simulations. The following findings are briefly concluded:

- This research proposed a coordinated control algorithm between MSDBR and reactive current control loop in ILC in hybrid microgrids where the fault current in load feeder in AC subgrid is effectively suppressed during both symmetrical and asymmetrical faults, improving the fault ride-through capability of the whole microgrid. With the proposed coordinated algorithm, not only do the DERs remain connected but also unaffected loads are able to continue the service.
- A simple reverse droop control methodology in BESS along with coordinated reactive current compensation in wind turbine generators is proposed that enhances the disturbance resiliency of a high inertia HMG with a high penetration level of renewable energies. The simulation results demonstrated that the proposed control constructively improved the LVRT capability of HMG during AC subgrid faults.
- This study proposed a novel bidirectional DC-DC converter for energy storage applications in DC and hybrid microgrids. Contrary to the conventional half-bridge converter, the proposed converter has a symmetrical configuration and dynamic in both charge and discharge modes of

operation resulting in improved performance. The simulation results for two case studies (i.e., an islanded and a grid connector HMG) demonstrated the proposed converter exhibits superior performance in handling power and voltage fluctuation in the DC grid. The battery voltage (low-voltage side) must be selected in proportion to DC bus voltage (high-voltage side), representing the only limitation of this converter.

- This work evaluated and compared the influence of the location of an aggregated BESS on the dynamic performance of the islanded HMGs where the candidate locations are ACg or DCg. Two case studies i.e., an industrial high-inertia HMG and a low-inertia distributed converter interfaced HMG, were considered. It was demonstrated through the simulations that both BESSs separately employed in sub-grids maintain the transient stability of HMGs against microgrid contingencies during small-signal disturbances. However, during large-signal disruptions in microgrids, the performance is remarkably different. In industrial HMG with high-inertia DERs, the DC BESS has relatively better performance during large signal disruptions. On the contrary, a low-inertia HMG equipped with AC BESS outperforms the microgrid equipped with DC BESS. The study showed that the BESS controller and the ILC's control strategy, have key roles when the energy storage runs as a voltage source in either sub-grid of HMG.

- This study proposed a cost-effective approach to integrating a high-power density energy storage system i.e., supercapacitor to a grid-connected conventional PV that uses one DC-DC converter for both systems. The proposed system works as a PV-SC system to handle the grid disturbances and improve the power quality for a sensitive load during daytime and sunny weather, as well as works as regular energy storage during nighttime and cloudy weather. To analyze the stability of the system, a nonlinear mathematical modeling approach was developed, and its dynamic structure was validated. The time-domain simulation of the detailed switching

model demonstrated that the proposed system effectively maintained the power quality during grid voltage sags and severe load changes.

It is to note here that all models in this study have been simulated in MATLAB/Simulink environment which is a well-known and widely accepted software tool for simulating control and power systems. The obtained results closely match with realistic situations, as the accuracy of basic model blocks and function blocks found in the software library and toolboxes has been numerically validated previously by the software developer.

## **7.2 Future Work**

The researcher is interested to pursue this research or recommends extending this research in the following directions:

- Due to the complexity and nonlinear nature of power electronics devices, the associated control methodologies should be validated through laboratory experimental setups. It is highly recommended to validate the simulation results by the experimental emulation, at least for studies conducted in chapters 4 and 6. The experiments can be conducted either by Hardware-in-the-loop (HIL) or scaled-down prototype systems.
- The Study of BESS location can be extended to HMGs with distributed energy storage devices where there are multiple candidate locations for BESS. In that case, the analytical approaches may preferably be used instead of heuristic methods.
- This study covered only the control of microgrids transients. However, the study can be further extended to explore the issue and solutions of HMG power management with distributed energy storage systems.
- To continue the study of the nonlinear mathematical modeling in chapter 6, it can be further

extended to the synthetic microgrids encompassing both grid forming and grid feeding DERs that the dynamics of the primary DC source are included in the study.

- The effectiveness of the novel bidirectional DC-DC converter should be evaluated in more realistic HMGs, including diverse generation sources like wind turbine generators and diesel generators employing advanced controllers. Furthermore, as a necessary complement to this study, the experimental verification of the proposed DC-DC converter should be performed in future research.

- In the modern environment of smart grids, there is a significant cyber integration between physical systems with a high volume of data generation, transmission, and utilization. This study can be extended to explore cybersecurity threats, their adversary effects, and possible solutions for hybrid microgrids, considering the study of communication failure and latency for hierarchical control. In addition, the study can be further developed by applying statistical and artificial intelligence methods and tools such as machine learning for energy storage optimization, renewable power management, disturbance detection, and protection of HMGs by utilizing data analytics of power systems.

## Bibliography

- [1] R. H. Lasseter, "MicroGrids," in *2002 IEEE Power Engineering Society Winter Meeting. Conference Proceedings (Cat. No.02CH37309)*, 2002, vol. 1, pp. 305–308, doi: 10.1109/PESW.2002.985003.
- [2] J. Tollefson, "California wildfires and power outages cause disruptions for scientists," *Nature*, vol. 575, no. 7781, pp. 16–16, Nov. 2019, doi: 10.1038/d41586-019-03302-z.
- [3] B. Storrow, "Why the Deep Freeze Caused Texas to Lose Power," *Scientific American*, 2021. <https://www.scientificamerican.com/article/why-the-deep-freeze-caused-texas-to-lose-power/>.
- [4] A. Gupta, S. Doolla, and K. Chatterjee, "Hybrid AC–DC Microgrid: Systematic Evaluation of Control Strategies," *IEEE Trans. Smart Grid*, vol. 9, no. 4, pp. 3830–3843, Jul. 2017, doi: 10.1109/TSG.2017.2727344.
- [5] X. Liu, P. Wang, and P. C. Loh, "A hybrid AC/DC microgrid and its coordination control," *IEEE Trans. Smart Grid*, 2011, doi: 10.1109/TSG.2011.2116162.
- [6] Z. Li and M. Shahidehpour, "Small-signal modeling and stability analysis of hybrid AC/DC microgrids," *IEEE Trans. Smart Grid*, vol. 10, no. 2, pp. 2080–2095, 2019, doi: 10.1109/TSG.2017.2788042.
- [7] M. Farrokhhabadi *et al.*, "Microgrid Stability Definitions , Analysis , and Examples," vol. 35, no. 1, pp. 13–29, 2020, doi: 10.1109/TPWRS.2019.2925703.
- [8] A. Di Giorgio, F. Liberati, A. Lanna, A. Pietrabissa, and F. Delli Priscoli, "Model Predictive Control of Energy Storage Systems for Power Tracking and Shaving in Distribution Grids," *IEEE Trans. Sustain. ENERGY*, vol. 8, no. 2, 2017, doi: 10.1109/TSTE.2016.2608279.
- [9] Y. J. A. Zhang, C. Zhao, W. Tang, and S. H. Low, "Profit-maximizing planning and control of battery energy storage systems for primary frequency control," *IEEE Trans. Smart Grid*, vol. 9, no. 2, pp. 712–723, 2018, doi: 10.1109/TSG.2016.2562672.
- [10] S. Kotra and M. K. Mishra, "A supervisory power management system for a hybrid microgrid with HESS," *IEEE Trans. Ind. Electron.*, vol. 64, no. 5, pp. 3640–3649, 2017, doi: 10.1109/TIE.2017.2652345.
- [11] S. Buso, T. Caldognetto, and Q. Liu, "Analysis and Experimental Characterization of a Large-Bandwidth Triple-Loop Controller for Grid-Tied Inverters," *IEEE Trans. Power Electron.*, vol. 34, no. 2, pp. 1936–1949, 2019, doi: 10.1109/TPEL.2018.2835158.
- [12] M. Hasan Ali and M. Daviran Keshavarzi, "Mixed AC/DC System Stability under Uncertainty," in *Emerging Power Converters for Renewable Energy and Electric Vehicles*, 1st ed., M. R. Shah and M. H. Ali, Eds. Boca Raton: CRC Press, 2021.
- [13] A. Eisapour-Moarref, M. Kalantar, and M. Esmaili, "Power Sharing in Hybrid Microgrids Using a Harmonic-Based Multidimensional Droop," *IEEE Trans. Ind. Informatics*, vol. 16, no. 1, pp. 109–119, Jan. 2020, doi: 10.1109/TII.2019.2915240.
- [14] M. D. Keshavarzi and M. H. Ali, "FRT Capability Enhancement of Autonomous AC/DC Hybrid Microgrid by Coordinated MSDBR and Interlinking Converter Control Strategy," in *2019 IEEE Power & Energy Society Innovative Smart Grid Technologies Conference (ISGT)*, Feb. 2019, pp. 1–5, doi: 10.1109/ISGT.2019.8791661.
- [15] M. D. Keshavarzi and M. H. Ali, "Disturbance Resilience Enhancement of Islanded Hybrid Microgrid Under High Penetration of Renewable Energy Resources by BESS," in *2020 IEEE/PES Transmission and Distribution Conference and Exposition (T&D)*, Oct. 2020, vol. 2020-Octob,

- pp. 1–5, doi: 10.1109/TD39804.2020.9299957.
- [16] X. Lu, J. M. Guerrero, K. Sun, J. C. Vasquez, R. Teodorescu, and L. Huang, “Hierarchical control of parallel AC-DC converter interfaces for hybrid microgrids,” *IEEE Trans. Smart Grid*, vol. 5, no. 2, pp. 683–692, 2014, doi: 10.1109/TSG.2013.2272327.
  - [17] Z. Zhao, P. Yang, Y. Wang, Z. Xu, and J. M. Guerrero, “Dynamic Characteristics Analysis and Stabilization of PV-Based Multiple Microgrid Clusters,” *IEEE Trans. Smart Grid*, vol. 10, no. 1, pp. 805–818, 2019, doi: 10.1109/TSG.2017.2752640\_rfseq1.
  - [18] B. John, A. Ghosh, M. Goyal, and F. Zare, “A DC Power Exchange Highway Based Power Flow Management for Interconnected Microgrid Clusters,” *IEEE Syst. J.*, vol. 13, no. 3, pp. 3347–3357, 2019, doi: 10.1109/JSYST.2019.2911625.
  - [19] M. K. Kazimierczuk, *Pulse-Width Modulated DC-DC Power Converters*, 2nd ed. Chichester, West Sussex: John Wiley & Sons, Ltd., 2012.
  - [20] A. Yazdani and R. Iravani, *Voltage-Sourced Converters in Power Systems*. Hoboken, NJ, USA: John Wiley & Sons, Inc., 2010.
  - [21] J. C. Vasquez, J. M. Guerrero, M. Savaghebi, J. Eloy-Garcia, and R. Teodorescu, “Modeling, Analysis, and Design of Stationary-Reference-Frame Droop-Controlled Parallel Three-Phase Voltage Source Inverters,” *IEEE Trans. Ind. Electron.*, vol. 60, no. 4, pp. 1271–1280, Apr. 2013, doi: 10.1109/TIE.2012.2194951.
  - [22] M. Liserre, F. Blaabjerg, and S. Hansen, “Design and control of an LCL-filter-based three-phase active rectifier,” *IEEE Trans. Ind. Appl.*, vol. 41, no. 5, pp. 1281–1291, 2005, doi: 10.1109/TIA.2005.853373.
  - [23] A. C. Zambroni de Souza and M. Castilla, *Microgrids Design and Implementation*. Cham: Springer International Publishing, 2019.
  - [24] X. Sun, Y. Hao, Q. Wu, X. Guo, and B. Wang, “A Multifunctional and Wireless Droop Control for Distributed Energy Storage Units in Islanded AC Microgrid Applications,” *IEEE Trans. Power Electron.*, vol. 32, no. 1, pp. 736–751, 2017, doi: 10.1109/TPEL.2016.2531379.
  - [25] P. H. Divshali, A. Alimardani, S. H. Hosseini, and M. Abedi, “Decentralized cooperative control strategy of microsources for stabilizing autonomous VSC-based microgrids,” *IEEE Trans. Power Syst.*, vol. 27, no. 4, pp. 1949–1959, 2012, doi: 10.1109/TPWRS.2012.2188914.
  - [26] A. Bidram and A. Davoudi, “Hierarchical structure of microgrids control system,” *IEEE Trans. Smart Grid*, vol. 3, no. 4, pp. 1963–1976, 2012, doi: 10.1109/TSG.2012.2197425.
  - [27] T. Morstyn, B. Hredzak, and V. G. Agelidis, “Control Strategies for Microgrids with Distributed Energy Storage Systems: An Overview,” *IEEE Trans. Smart Grid*, vol. 9, no. 4, pp. 3652–3666, 2018, doi: 10.1109/TSG.2016.2637958.
  - [28] D. E. Olivares *et al.*, “Trends in microgrid control,” *IEEE Trans. Smart Grid*, vol. 5, no. 4, pp. 1905–1919, 2014, doi: 10.1109/TSG.2013.2295514.
  - [29] J. Rocabert, A. Luna, F. Blaabjerg, and P. Rodríguez, “Control of Power Converters in AC Microgrids,” *IEEE Trans. Power Electron.*, vol. 27, no. 11, pp. 4734–4749, Nov. 2012, doi: 10.1109/TPEL.2012.2199334.
  - [30] S. M. Ashabani and Y. A. I. Mohamed, “New Family of Microgrid Control and Management Strategies in Smart Distribution Grids Analysis, Comparison and Testing,” *IEEE Trans. Power Syst.*, vol. 29, no. 5, pp. 2257–2269, 2014, doi: 10.1109/TPWRS.2014.2306016.
  - [31] C. J. O’Rourke, M. M. Qasim, M. R. Overlin, and J. L. Kirtley, “A Geometric Interpretation of

- Reference Frames and Transformations: Dq0, Clarke, and Park,” *IEEE Trans. Energy Convers.*, vol. 34, no. 4, pp. 2070–2083, 2019, doi: 10.1109/TEC.2019.2941175.
- [32] M. Naderi, Y. Khayat, Q. Shafiee, T. Dragicevic, H. Bevrani, and F. Blaabjerg, “Interconnected Autonomous AC Microgrids via Back-to-Back Converters—Part I: Small-Signal Modeling,” *IEEE Trans. Power Electron.*, vol. 35, no. 5, pp. 4728–4740, May 2020, doi: 10.1109/TPEL.2019.2943996.
- [33] F. D. Mohammadi and H. K. Vanashi, “State-Space Modeling , Analysis , and Distributed Secondary Frequency Control of Isolated Microgrids,” *IEEE Trans. Energy Convers.*, vol. 33, no. 1, pp. 155–165, 2018, doi: 10.1109/TEC.2017.2757012.
- [34] B. Bahrani, S. Kenzelmann, and A. Rufer, “Multivariable-PI-Based dq Current Control of Voltage Source Converters With Superior Axis,” *Ieee Trans. Ind. Electron.*, vol. 58, no. 7, pp. 3016–3026, 2011, doi: 10.1109/TIE.2010.2070776.
- [35] W. Leonhard, *Control of Electrical Drives*, 3rd ed. Berlin, Heidelberg: Springer, 2001.
- [36] A. Bidram, A. Davoudi, F. L. Lewis, and J. M. Guerrero, “Distributed cooperative secondary control of microgrids using feedback linearization,” *IEEE Trans. Power Syst.*, vol. 28, no. 3, pp. 3462–3470, 2013, doi: 10.1109/TPWRS.2013.2247071.
- [37] M. A. Shahab, B. Mozafari, S. Soleymani, N. M. Dehkordi, H. M. Shourkaei, and J. M. Guerrero, “Stochastic Consensus-Based Control of Microgrids With Communication Delays and Noises,” *IEEE Trans. Power Syst.*, vol. 34, no. 5, pp. 3573–3581, 2019, doi: 10.1109/tpwrs.2019.2905433.
- [38] R. Zhang and B. Hredzak, “Distributed finite-time multiagent control for DC microgrids with time delays,” *IEEE Trans. Smart Grid*, vol. 10, no. 3, pp. 2692–2701, 2019, doi: 10.1109/TSG.2018.2808467.
- [39] H. J. Yoo, T. T. Nguyen, and H. M. Kim, “Consensus-based distributed coordination control of hybrid AC/DC microgrids,” *IEEE Trans. Sustain. Energy*, vol. 11, no. 2, pp. 629–639, 2020, doi: 10.1109/TSTE.2019.2899119.
- [40] X. Zhao, J. M. Guerrero, M. Savaghebi, J. C. Vasquez, X. Wu, and K. Sun, “Low-voltage ride-through operation of power converters in grid-interactive microgrids by using negative-sequence droop control,” *IEEE Trans. Power Electron.*, vol. 32, no. 4, pp. 3128–3142, 2017, doi: 10.1109/TPEL.2016.2570204.
- [41] R. Heydari *et al.*, “Robust High-Rate Secondary Control of Microgrids With Mitigation of Communication Impairments,” *IEEE Trans. Power Electron.*, vol. 35, no. 11, pp. 12486–12496, Nov. 2020, doi: 10.1109/TPEL.2020.2986368.
- [42] C. Ahumada, R. Cárdenas, D. Sáez, and J. M. Guerrero, “Secondary Control Strategies for Frequency Restoration in Islanded Microgrids With Consideration of Communication Delays,” *IEEE Trans. Smart Grid*, vol. 7, no. 3, pp. 1430–1441, 2016, doi: 10.1109/TSG.2015.2461190.
- [43] A. Ioinovici, *Power Electronics and Energy Conversion Systems*, vol. 1. West Sussex: WILEY, 2013.
- [44] R. W. Erickson and D. Maksimović, *Fundamentals of Power Electronics*, 2nd ed. Boston, MA: Springer US, 2001.
- [45] P. C. Loh, D. Li, Y. K. Chai, and F. Blaabjerg, “Hybrid AC-DC microgrids with energy storages and progressive energy flow tuning,” *IEEE Trans. Power Electron.*, vol. 28, no. 4, pp. 1533–1543, 2013, doi: 10.1109/TPEL.2012.2210445.
- [46] S. Peyghami, H. Mokhtari, and F. Blaabjerg, “Autonomous operation of a hybrid AC/DC microgrid with multiple interlinking converters,” *IEEE Trans. Smart Grid*, vol. 9, no. 6, pp. 6480–

- 6488, 2018, doi: 10.1109/TSG.2017.2713941.
- [47] P. C. Loh, D. Li, Y. K. Chai, and F. Blaabjerg, "Autonomous operation of hybrid microgrid with ac and dc subgrids," *IEEE Trans. Power Electron.*, vol. 28, no. 5, pp. 2214–2223, 2013, doi: 10.1109/TPEL.2012.2214792.
  - [48] M. Firouzi and G. B. Gharehpetian, "LVRT Performance Enhancement of DFIG-Based Wind Farms by Capacitive Bridge-Type Fault Current Limiter (CBFCL)," *IEEE Trans. Sustain. Energy*, vol. 9, no. 3, pp. 1118–1125, 2018, doi: 10.1109/TSTE.2017.2771321.
  - [49] L. Meegahapola, "Investigations on Fault ride through Capability of AC/DC Hbrid Microgrids during AC Network Faults," *2017 IEEE Power Energy Soc. Gen. Meet.*, pp. 5–9, 2017.
  - [50] L. Meegahapola, I. U. Nutkani, and B. McGrath, "Fault ride-through capability of AC/DC hybrid microgrids during AC and DC network faults," *IEEE Power Energy Soc. Gen. Meet.*, vol. 2018-Janua, pp. 1–5, 2018, doi: 10.1109/PESGM.2017.8274583.
  - [51] H. He *et al.*, "Application of a SFCL for Fault Ride-Through Capability Enhancement of DG in a Microgrid System and Relay Protection Coordination," *IEEE Trans. Appl. Supercond.*, 2016, doi: 10.1109/TASC.2016.2599898.
  - [52] P. H. Huang, M. S. El Moursi, and S. A. Hasen, "Novel Fault Ride-Through Scheme and Control Strategy for Doubly Fed Induction Generator-Based Wind Turbine," *IEEE Trans. Energy Convers.*, vol. 30, no. 2, pp. 635–645, 2015, doi: 10.1109/TEC.2014.2367113.
  - [53] G. Rashid and M. Hasan Ali, "Transient Stability Enhancement of Doubly Fed Induction Machine-Based Wind Generator by Bridge-Type Fault Current Limiter," *IEEE Trans. Energy Convers.*, vol. 30, no. 3, pp. 939–947, 2015, doi: 10.1049/iet-rpg.2015.0150.
  - [54] G. Rashid and M. H. Ali, "Nonlinear Control-Based Modified BFCL for LVRT Capacity Enhancement of DFIG-Based Wind Farm," *IEEE Trans. Energy Convers.*, vol. 32, no. 1, pp. 284–295, 2017, doi: 10.1109/TEC.2016.2603967.
  - [55] M. E. H. G. Iman Sadeghkhani, "A current limiting strategy to improve fault ride-through of inverter interfaced autonomous microgrids," *IEEE Trans. Smart Grid*, vol. 8, no. 5, pp. 2138–2148, 2017, doi: 10.1016/j.seta.2017.02.004.
  - [56] P. Piya, M. Ebrahimi, M. Karimi-Ghartemani, and S. A. Khajehoddin, "Fault Ride-Through Capability of Voltage-Controlled Inverters," *IEEE Trans. Ind. Electron.*, vol. 65, no. 10, pp. 7933–7943, 2018, doi: 10.1109/TIE.2018.2803765.
  - [57] M. Ropp, "Guide to the IEEE 1547-2018 standard and its impacts on cooperatives," 2019. [Online]. Available: <https://www.cooperative.com/topics/transmission-distribution/Pages/NRECA-Guide-to-IEEE-1547-2018-Standard-for-DER-Interconnections.aspx>.
  - [58] H. R. Baghaee, M. Mirsalim, G. B. Gharehpetian, and H. A. Talebi, "A Decentralized Robust Mixed H<sub>2</sub>/H<sub>∞</sub> Voltage Control Scheme to Improve Small/Large-Signal Stability and FRT Capability of Islanded Multi-DER Microgrid Considering Load Disturbances," *IEEE Syst. J.*, vol. 12, no. 3, pp. 2610–2621, 2017, doi: 10.1109/JSYST.2017.2716351.
  - [59] Z. Li and M. Shahidehpour, "Small-Signal Modeling and Stability Analysis of Hybrid AC/DC Microgrids," *IEEE Trans. Smart Grid*, 2018, doi: 10.1109/TSG.2017.2788042.
  - [60] Y. Xia, W. Wei, M. Yu, X. Wang, and Y. Peng, "Power Management for a Hybrid AC/DC Microgrid with Multiple Subgrids," *IEEE Trans. Power Electron.*, vol. 33, no. 4, pp. 3520–3533, 2018, doi: 10.1109/TPEL.2017.2705133.
  - [61] J. M. G. Baharizadeh, Mehdi, "An Improved power control strategy for hybrid AC-DC microgrids," *Electr. Power Energy Syst.*, vol. 95, 2017.



- [62] G. Qi, A. Chen, and J. Chen, "Improved Control Strategy of Interlinking Converters With Synchronous Generator Characteristic in Islanded Hybrid AC / DC Microgrid," *CPSS Trans. Power Electron. Appl.*, vol. 2, no. 2, pp. 149–158, 2017, doi: 10.24295/CPSSTPEA.2017.00015.
- [63] M. Corti, E. Tironi, and G. Ubezio, "DC networks including multiport DC/DC converters: Fault analysis," *IEEE Trans. Ind. Appl.*, vol. 52, no. 5, pp. 3655–3662, 2016, doi: 10.1109/TIA.2016.2572045.
- [64] X. Zhu, F. Meng, Z. Xie, and Y. Yue, "An Inertia and Damping Control Method of DC–DC Converter in DC Microgrids," *IEEE Trans. Energy Convers.*, vol. 35, no. 2, pp. 799–807, Jun. 2020, doi: 10.1109/TEC.2019.2952717.
- [65] S. Kotra and M. K. Mishra, "Design and Stability Analysis of DC Microgrid With Hybrid Energy Storage System," *IEEE Trans. Sustain. Energy*, vol. 10, no. 3, pp. 1603–1612, Jul. 2019, doi: 10.1109/TSTE.2019.2891255.
- [66] A. Khodamoradi, G. Liu, P. Mattavelli, T. Caldognetto, and P. Magnone, "Analysis of an Online Stability Monitoring Approach for DC Microgrid Power Converters," *IEEE Trans. Power Electron.*, vol. 34, no. 5, pp. 4794–4806, May 2019, doi: 10.1109/TPEL.2018.2858572.
- [67] Y. G. Choi, S. W. Lee, H. S. Lee, S. C. Lee, and B. Kang, "Increase in Power Conversion Efficiency of Bidirectional DC-DC Converter Using 1:1 Transformer and Pulse-Frequency Modulation Control," *IEEE Trans. Power Electron.*, vol. 33, no. 12, pp. 10539–10549, 2018, doi: 10.1109/TPEL.2018.2809682.
- [68] C.-C. Lin, G. W. Wu, and L.-S. Yang, "Study of a non-isolated bidirectional DC–DC converter," *IET Power Electron.*, vol. 6, no. 1, pp. 30–37, Jan. 2013, doi: 10.1049/iet-pel.2012.0338.
- [69] A. K. Rathore, D. R. Patil, and D. Srinivasan, "Non-isolated Bidirectional Soft-Switching Current-Fed LCL Resonant DC/DC Converter to Interface Energy Storage in DC Microgrid," *IEEE Trans. Ind. Appl.*, vol. 52, no. 2, pp. 1711–1722, 2016, doi: 10.1109/TIA.2015.2498127.
- [70] M. Aamir, S. Mekhilef, and H. J. Kim, "High-Gain Zero-Voltage Switching Bidirectional Converter With a Reduced Number of Switches," *IEEE Trans. Circuits Syst. II Express Briefs*, vol. 62, no. 8, pp. 816–820, 2015, doi: 10.1109/TCSII.2015.2433351.
- [71] J. Zeng, W. Qiao, and L. Qu, "An Isolated Three-Port Bidirectional DC-DC Converter for Photovoltaic Systems With Energy Storage," *IEEE Trans. Ind. Appl.*, vol. 51, no. 4, pp. 3493–3503, 2015, doi: 10.1109/TIA.2015.2399613.
- [72] O. Cornea, G. D. Andreescu, N. Muntean, and D. Hulea, "Bidirectional Power Flow Control in a DC Microgrid Through a Switched-Capacitor Cell Hybrid DC-DC Converter," *IEEE Trans. Ind. Electron.*, vol. 64, no. 4, pp. 3012–3022, 2017, doi: 10.1109/TIE.2016.2631527.
- [73] S.-H. Ham, Y.-G. Choi, H.-S. Lee, S.-W. Lee, S.-C. Lee, and B. Kang, "High-efficiency Bidirectional Buck–Boost Converter for Residential Energy Storage System," *Energies*, vol. 12, no. 19, p. 3786, Oct. 2019, doi: 10.3390/en12193786.
- [74] H. Ardi, A. Ajami, F. Kardan, and S. N. Avilagh, "Analysis and Implementation of a Nonisolated Bidirectional DC-DC Converter with High Voltage Gain," *IEEE Trans. Ind. Electron.*, vol. 63, no. 8, pp. 4878–4888, 2016, doi: 10.1109/TIE.2016.2552139.
- [75] B. Yang *et al.*, "Optimal sizing and placement of energy storage system in power grids: A state-of-the-art one-stop handbook," *J. Energy Storage*, vol. 32, no. May, p. 101814, 2020, doi: 10.1016/j.est.2020.101814.
- [76] S. W. Alnaser and L. F. Ochoa, "Optimal Sizing and Control of Energy Storage in Wind Power-Rich Distribution Networks," *IEEE Trans. Power Syst.*, vol. 31, no. 3, pp. 2004–2013, 2016, doi:

10.1109/TPWRS.2015.2465181.

- [77] E. Grover-Silva, R. Girard, and G. Kariniotakis, "Optimal sizing and placement of distribution grid connected battery systems through an SOCP optimal power flow algorithm," *Appl. Energy*, vol. 219, no. April, pp. 385–393, 2018, doi: 10.1016/j.apenergy.2017.09.008.
- [78] P. N. D. Premadasa and D. P. Chandima, "An innovative approach of optimizing size and cost of hybrid energy storage system with state of charge regulation for stand-alone direct current microgrids," *J. Energy Storage*, vol. 32, no. July, p. 101703, 2020, doi: 10.1016/j.est.2020.101703.
- [79] K. Hesaroor and D. Das, "Optimal sizing of energy storage system in islanded microgrid using incremental cost approach," *J. Energy Storage*, vol. 24, no. January, p. 100768, 2019, doi: 10.1016/j.est.2019.100768.
- [80] G. Carpinelli, F. Mottola, D. Proto, A. Russo, and P. Varilone, "A hybrid method for optimal siting and sizing of battery energy storage systems in unbalanced low voltage microgrids," *Appl. Sci.*, vol. 8, no. 3, 2018, doi: 10.3390/app8030455.
- [81] M. A. Hannan, M. Faisal, P. Jern Ker, R. A. Begum, Z. Y. Dong, and C. Zhang, "Review of optimal methods and algorithms for sizing energy storage systems to achieve decarbonization in microgrid applications," *Renew. Sustain. Energy Rev.*, vol. 131, no. May, p. 110022, 2020, doi: 10.1016/j.rser.2020.110022.
- [82] L. A. Wong, V. K. Ramachandaramurthy, S. L. Walker, P. Taylor, and M. J. Sanjari, "Optimal placement and sizing of battery energy storage system for losses reduction using whale optimization algorithm," *J. Energy Storage*, vol. 26, no. August, p. 100892, 2019, doi: 10.1016/j.est.2019.100892.
- [83] A. S. A. Awad, T. H. M. EL-Fouly, and M. M. A. Salama, "Optimal ESS Allocation for Benefit Maximization in Distribution Networks," *IEEE Trans. Smart Grid*, vol. 8, no. 4, pp. 1668–1678, 2017, doi: 10.1109/TSG.2015.2499264.
- [84] A. Giannitrapani, S. Paoletti, A. Vicino, and D. Zarrilli, "Optimal Allocation of Energy Storage Systems for Voltage Control in LV Distribution Networks," *IEEE Trans. Smart Grid*, vol. 8, no. 6, pp. 2859–2870, 2017, doi: 10.1109/TSG.2016.2602480.
- [85] A. A. Ejajal, M. A. Abdelwahed, E. F. El-Saadany, and K. Ponnambalam, "A Unified Approach to the Power Flow Analysis of AC/DC Hybrid Microgrids," *IEEE Trans. Sustain. Energy*, vol. 7, no. 3, pp. 1145–1158, 2016, doi: 10.1109/TSTE.2016.2530740.
- [86] J.-W. Chang, S.-I. Moon, G. Lee, and P.-I. Hwang, "A New Local Control Method of Interlinking Converters to Improve Global Power Sharing in an Islanded Hybrid AC/DC Microgrid," *IEEE Trans. Energy Convers.*, vol. 35, no. 2, pp. 1–1, 2020, doi: 10.1109/tec.2020.2967416.
- [87] M. Davari and Y. A. R. I. Mohamed, "Robust multi-objective control of VSC-based DC-voltage power port in hybrid AC/DC multi-terminal micro-grids," *IEEE Trans. Smart Grid*, vol. 4, no. 3, pp. 1597–1612, 2013, doi: 10.1109/TSG.2013.2249541.
- [88] L. Papangelis, M.-S. Debry, P. Panciatici, and T. Van Cutsem, "Coordinated Supervisory Control of Multi-Terminal HVDC Grids: a Model Predictive Control Approach," *IEEE Trans. Power Syst.*, vol. 32, no. 6, pp. 1–1, 2017, doi: 10.1109/TPWRS.2017.2659781.
- [89] Q. Liu, T. Caldognetto, and S. Buso, "Flexible Control of Interlinking Converters for DC Microgrids Coupled to Smart AC Power Systems," *IEEE Trans. Ind. Electron.*, vol. 66, no. 5, pp. 3477–3485, 2019, doi: 10.1109/TIE.2018.2856210.
- [90] S. Y. M. Mousavi, A. Jalilian, M. Savaghebi, and J. M. Guerrero, "Autonomous Control of Current-and Voltage-Controlled DG Interface Inverters for Reactive Power Sharing and

- Harmonics Compensation in Islanded Microgrids,” *IEEE Trans. Power Electron.*, vol. 33, no. 11, pp. 9375–9386, 2018, doi: 10.1109/TPEL.2018.2792780.
- [91] P. Lin *et al.*, “A Distributed Power Management Strategy for Multi-Paralleled Bidirectional Interlinking Converters in Hybrid AC/DC Microgrids,” *IEEE Trans. Smart Grid*, vol. 10, no. 5, pp. 5696–5711, Sep. 2019, doi: 10.1109/TSG.2018.2890420.
- [92] A. Kumar and V. Verma, “Performance Enhancement of Single-Phase Grid-Connected PV System under Partial Shading Using Cascaded Multilevel Converter,” *IEEE Trans. Ind. Appl.*, vol. 54, no. 3, pp. 2665–2676, 2018, doi: 10.1109/TIA.2017.2789238.
- [93] M. K. Hossain and M. H. Ali, “Fuzzy logic controlled power balancing for low voltage ride-through capability enhancement of large-scale grid-connected PV plants,” *2017 IEEE Texas Power Energy Conf. TPEC 2017*, no. February, 2017, doi: 10.1109/TPEC.2017.7868274.
- [94] M. R. Hossain, M. K. Hossain, M. H. Ali, Y. Luo, and R. Hovsapien, “Synchronous generator stabilization by thyristor controlled supercapacitor energy storage system,” *Conf. Proc. - IEEE SOUTHEASTCON*, pp. 1–6, 2017, doi: 10.1109/SECON.2017.7925264.
- [95] A. Anwar, M. H. Ali, and R. A. Dougal, “Supercapacitor energy storage for low-voltage ride through in a 13.8KV AC system,” *Conf. Proc. - IEEE SOUTHEASTCON*, pp. 189–192, 2010, doi: 10.1109/SECON.2010.5453890.
- [96] N. Li, J. Zhang, and Y. Zhong, “A novel charging control scheme for super capacitor energy storage in photovoltaic generation system,” *3rd Int. Conf. Deregul. Restruct. Power Technol. DRPT 2008*, no. April, pp. 2671–2675, 2008, doi: 10.1109/DRPT.2008.4523863.
- [97] A. Eroglu, T. Dey, K. Dey, and G. Whelan, “Supercapacitor implementation for PV power generation system and integration,” *Appl. Comput. Electromagn. Soc. J.*, vol. 33, no. 10, pp. 1140–1145, 2018, doi: 10.23919/ROPACES.2018.8364262.CITATIONS.
- [98] C. A. Ramos-Paja, G. Petrone, G. Spagnuolo, D. Gonzalez, and S. Sergio-Serna, “Current equalization of mismatched PV panels based on a capacitor energy storage,” *Proc. IEEE Int. Conf. Ind. Technol.*, vol. 2018-Febru, no. November, pp. 921–926, 2018, doi: 10.1109/ICIT.2018.8352301.
- [99] M. Sufyan, N. A. Rahim, B. Eid, and S. R. S. Raihan, “A comprehensive review of reactive power control strategies for three phase grid connected photovoltaic systems with low voltage ride through capability,” *J. Renew. Sustain. Energy*, vol. 11, no. 4, 2019, doi: 10.1063/1.5095185.
- [100] H. Jafarian, B. Parkhideh, J. Enslin, R. Cox, and S. Bhowmik, “On reactive power injection control of distributed grid-tied AC-stacked PV inverter architecture,” *ECCE 2016 - IEEE Energy Convers. Congr. Expo. Proc.*, 2016, doi: 10.1109/ECCE.2016.7855303.
- [101] R. K. Varma and E. M. Siavashi, “PV-STATCOM: A New Smart Inverter for Voltage Control in Distribution Systems,” *IEEE Trans. Sustain. Energy*, vol. 9, no. 4, pp. 1681–1691, 2018, doi: 10.1109/TSTE.2018.2808601.
- [102] A. Mohapatra, B. Nayak, and C. Saiprakash, “Adaptive Perturb Observe MPPT for PV System with Experimental Validation,” *1st IEEE Int. Conf. Sustain. Energy Technol. Syst. ICSETS 2019*, no. September, pp. 257–261, 2019, doi: 10.1109/ICSETS.2019.8744819.
- [103] M. K. Hossein and M. H. Ali, “Overview on Maximum Power Point Tracking (MPPT) Techniques for Photovoltaic Power Systems,” *Int. Rev. Electr. Eng.*, vol. 8, no. 4, 2013.
- [104] A. Saipet and S. Nuchprayoon, “On Controlling Power Ramping and Output of Grid-Connected Rooftop Solar PV Using Battery Energy Storage System,” *Proc. - 2019 IEEE Int. Conf. Environ. Electr. Eng. 2019 IEEE Ind. Commer. Power Syst. Eur. IEEEIC/I CPS Eur. 2019*, 2019, doi:

10.1109/EEEIC.2019.8783980.

- [105] S. Müller, M. Deicke, and D. W., & Rik Doncker, “Doubly fed induction generator systems for wind turbines,” *Ind. Appl. Mag. IEEE*, vol. 8, no. 3, pp. 26–33, 2002, doi: 10.1109/2943.999610.
- [106] M. Villalva, J. Gazoli, and E. Filho, “Comprehensive Approach to Modeling and Simulation of Photovoltaic Arrays,” *IEEE Trans. Power Electron.*, vol. 24, no. 5, pp. 1198–1208, 2009, doi: 10.1109/tpe.2009.2013862.
- [107] M. Farrokhhabadi, S. Konig, C. A. Canizares, K. Bhattacharya, and T. Leibfried, “Battery Energy Storage System Models for Microgrid Stability Analysis and Dynamic Simulation,” *IEEE Trans. Power Syst.*, vol. 33, no. 2, pp. 2301–2312, Mar. 2018, doi: 10.1109/TPWRS.2017.2740163.
- [108] Z. Wu, D. W. Gao, H. Zhang, S. Yan, and X. Wang, “Coordinated Control Strategy of Battery Energy Storage System and PMSG-WTG to Enhance System Frequency Regulation Capability,” *IEEE Trans. Sustain. Energy*, vol. 8, no. 3, pp. 1330–1343, 2017, doi: 10.1109/TSTE.2017.2679716.
- [109] P. Kundur, *Power System Stability and Control*. McGraw-Hill, Inc., 1994.
- [110] F. Nejatbakhs and Y. W. Li, “Overview of PowerManagement Strategies of Hybrid AC/DC Microgrid,” *IEEE Trans. POWER Electron.*, vol. 30, no. 12, pp. 7072–7089, 2015, doi: 10.1109/TPEL.2014.2384999.
- [111] K. Clark, N. W. Miller, and J. J. Sanchez-Gasca, “Modeling of GE Wind Turbine-Generators for Grid Studies,” 2010.
- [112] P. C. Krause, O. Wasynczuk, and S. D. Sudhoff, *Analysis of Electric Machinery and Drive Systems*, 3rd ed. Hoboken, New Jersey: John Wiley & Sons, Inc., 2013.
- [113] “IEEE Recommended Practice for Excitation System Models for Power System Stability Studies,” *IEEE Std 421.5-2005*. 2005, doi: 10.1109/IEEESTD.2006.99499.
- [114] O. Tremblay and L.-A. Dessaint, “Experimental Validation of a Battery Dynamic Model for EV Applications,” *World Electr. Veh. J.*, vol. 3, no. 2, pp. 289–298, Jun. 2009, doi: 10.3390/wevj3020289.
- [115] B. B. Ambati, P. Kanjiya, and V. Khadkikar, “A low component count series voltage compensation scheme for DFIG WTs to enhance fault ride-through capability,” *IEEE Trans. Energy Convers.*, vol. 30, no. 1, pp. 208–217, 2015, doi: 10.1109/TEC.2014.2351799.
- [116] M. Daviran Keshavarzi and M. H. Ali, “A Novel Bidirectional DC-DC Converter for Dynamic Performance Enhancement of Hybrid AC/DC Microgrid,” *Electronics*, vol. 9, no. 10, p. 1653, Oct. 2020, doi: 10.3390/electronics9101653.
- [117] A. Kirakosyan, E. F. El-Saadany, M. S. El Moursi, A. H. Yazdavar, and A. Al-Durra, “Communication-Free Current Sharing Control Strategy for DC Microgrids and Its Application for AC/DC Hybrid Microgrids,” *IEEE Trans. Power Syst.*, vol. 35, no. 1, pp. 140–151, Jan. 2020, doi: 10.1109/TPWRS.2019.2925779.
- [118] M. D. Keshavarzi and M. Hasan Ali, “Influence of Battery Energy Storage Location on the Dynamic Performance of Hybrid AC/DC Microgrid,” in *2020 2nd International Conference on Smart Power & Internet Energy Systems (SPIES)*, Sep. 2020, pp. 182–187, doi: 10.1109/SPIES48661.2020.9242947.
- [119] S. Mariéthoz *et al.*, “Comparison of Hybrid Control Techniques for Buck and Boost DC-DC Converters,” *IEEE Trans. Control Syst. Technol.*, vol. 18, no. 5, pp. 1126–1145, 2010.
- [120] A. Taheri, A. Ghasemian, and H. P. Ren, “Boost Converters’ Proximate Constrained Time-

- Optimal Sliding Mode Control Based on Hybrid Switching Model,” *Complexity*, vol. 2019, 2019, doi: 10.1155/2019/5834741.
- [121] S. Chakraborty *et al.*, “Scalable Modeling Approach and Robust Hardware-in-the-Loop Testing of an Optimized Interleaved Bidirectional HV DC/DC Converter for Electric Vehicle Drivetrains,” *IEEE Access*, vol. 8, pp. 115515–115536, 2020, doi: 10.1109/ACCESS.2020.3004238.
  - [122] A. Ghasemian and A. Taheri, “Constrained Near-Time-Optimal Sliding-Mode Control of Boost Converters Based on Switched Affine Model Analysis,” *IEEE Trans. Ind. Electron.*, vol. 65, no. 1, pp. 887–897, 2018.
  - [123] M. Veerachary and A. R. Saxena, “Optimized power stage design of low source current ripple fourth-order boost DC-DC converter: A PSO approach,” *IEEE Trans. Ind. Electron.*, vol. 62, no. 3, pp. 1491–1502, 2015, doi: 10.1109/TIE.2014.2361316.
  - [124] A. Elserougi, I. Abdelsalam, A. Massoud, and S. Ahmed, “A bidirectional non-isolated hybrid modular DC–DC converter with zero-voltage switching,” *Electr. Power Syst. Res.*, vol. 167, no. November 2018, pp. 277–289, 2019, doi: 10.1016/j.epsr.2018.11.009.
  - [125] M. Kwon and S. Choi, “Control Scheme for Autonomous and Smooth Mode Switching of Bidirectional DC-DC Converters in a DC Microgrid,” *IEEE Trans. Power Electron.*, vol. 33, no. 8, pp. 7094–7104, 2018, doi: 10.1109/TPEL.2017.2753845.
  - [126] M. Daviran Keshavarzi and M. Hasan Ali, “Performance Analysis of Hybrid AC/DC Microgrid Under Influence of Battery Energy Storage Location (Under review),” *Int. Trans. Electr. Energy Syst.*, pp. 1–19, 2021.
  - [127] U. Akram, M. Nadarajah, R. Shah, and F. Milano, “A review on rapid responsive energy storage technologies for frequency regulation in modern power systems,” *Renew. Sustain. Energy Rev.*, vol. 120, no. November 2019, p. 109626, 2020, doi: 10.1016/j.rser.2019.109626.
  - [128] S. Koohi-Fayegh and M. A. Rosen, “A review of energy storage types, applications and recent developments,” *J. Energy Storage*, vol. 27, no. November 2019, p. 101047, 2020, doi: 10.1016/j.est.2019.101047.
  - [129] A. R. Dehghani-Sanij, E. Tharumalingam, M. B. Dusseault, and R. Fraser, “Study of energy storage systems and environmental challenges of batteries,” *Renew. Sustain. Energy Rev.*, vol. 104, no. January, pp. 192–208, 2019, doi: 10.1016/j.rser.2019.01.023.
  - [130] J. Tan and Y. Zhang, “Coordinated Control Strategy of a Battery Energy Storage System to Support a Wind Power Plant Providing Multi-Timescale Frequency Ancillary Services,” *IEEE Trans. Sustain. Energy*, vol. 8, no. 3, pp. 1140–1153, 2017, doi: 10.1109/TSTE.2017.2663334.
  - [131] T. Zhao and Z. Ding, “Cooperative Optimal Control of Battery Energy Storage System under Wind Uncertainties in a Microgrid,” *IEEE Trans. Power Syst.*, vol. 33, no. 2, pp. 2292–2300, 2018, doi: 10.1109/TPWRS.2017.2741672.
  - [132] O. Tremblay, L. A. Dessaint, and A. I. Dekkiche, “A generic battery model for the dynamic simulation of hybrid electric vehicles,” *VPPC 2007 - Proc. 2007 IEEE Veh. Power Propuls. Conf.*, no. V, pp. 284–289, 2007, doi: 10.1109/VPPC.2007.4544139.
  - [133] D. Wu, F. Tang, T. Dragicevic, J. C. Vasquez, and J. M. Guerrero, “Autonomous active power control for islanded AC microgrids with photovoltaic generation and energy storage system,” *IEEE Trans. Energy Convers.*, vol. 29, no. 4, pp. 882–892, 2014, doi: 10.1109/TEC.2014.2358612.
  - [134] A. Esmaili, B. Novakovic, A. Nasiri, and O. Abdel-Baqi, “A Hybrid System of Li-Ion Capacitors and Flow Battery for Dynamic Wind Energy Support,” *Ieee Trans. Ind. Appl.*, vol. 49, no. 4, pp.

- 1649–1657, 2013, doi: 10.1109/TIA.2013.2255112.
- [135] L. Callegaro, M. Ciobotaru, D. J. Pagano, and J. E. Fletcher, “Feedback linearization control in photovoltaic module integrated converters,” *IEEE Trans. Power Electron.*, vol. 34, no. 7, pp. 6876–6889, 2019, doi: 10.1109/TPEL.2018.2872677.
  - [136] W. De Soto, S. A. Klein, and W. A. Beckman, “Improvement and validation of a model for photovoltaic array performance,” *Sol. Energy*, vol. 80, no. 1, pp. 78–88, 2006, doi: 10.1016/j.solener.2005.06.010.
  - [137] L. Wang, Q. S. Vo, and A. V Prokhorov, “Dynamic Stability Analysis of a Hybrid Wave and Photovoltaic Power Generation System Integrated Into a Distribution Power Grid,” *IEEE Trans. Sustain. Energy*, vol. 8, no. 1, pp. 404–413, 2017, doi: 10.1109/TSTE.2016.2602370.
  - [138] F. A. Inthamoussou, J. Pegueroles-Queralt, and F. D. Bianchi, “Control of a supercapacitor energy storage system for microgrid applications,” *IEEE Trans. Energy Convers.*, vol. 28, no. 3, pp. 690–697, 2013, doi: 10.1109/TEC.2013.2260752.
  - [139] A. Reznik, M. G. Simoes, A. Al-Durra, and S. M. Mueen, “LCL Filter design and performance analysis for grid-interconnected systems,” *IEEE Trans. Ind. Appl.*, vol. 50, no. 2, pp. 1225–1232, 2014, doi: 10.1109/TIA.2013.2274612.
  - [140] N. Pogaku, M. Prodanović, and T. C. Green, “Modeling, analysis and testing of autonomous operation of an inverter-based microgrid,” *IEEE Trans. Power Electron.*, vol. 22, no. 2, pp. 613–625, 2007, doi: 10.1109/TPEL.2006.890003.
  - [141] “Simulink Control Design Getting Started Guide,” *Mathwork.com*, 2020.  
[https://www.mathworks.com/help/pdf\\_doc/slcontrol/slcontrol\\_gsg.pdf](https://www.mathworks.com/help/pdf_doc/slcontrol/slcontrol_gsg.pdf).
  - [142] G. San, W. Zhang, X. Guo, C. Hua, H. Xin, and F. Blaabjerg, “Large-disturbance stability for power-converter-dominated microgrid: A review,” *Renew. Sustain. Energy Rev.*, vol. 127, no. May 2019, p. 109859, 2020, doi: 10.1016/j.rser.2020.109859.